University of Lille
Faculty of Sciences and Technologies

Doctoral School 104 - Science of the Matter, of the Radiation, and of the Environment

Doctoral Thesis

by

Yevheniia SMORTSOVA

to obtain the degree of

Doctor of Lille University

Discipline: Analytical, Physical and Theoretical Chemistry

Dye sensitized solar cells efficiency improvement: optimization of the electrolyte using ionic liquids/molecular solvents mixture and study of the photodynamic properties of organic indolinic derivative dyes

Date of defense: 04 December 2018

Rachel	**MEALLET-RENAULT**	**Referee**
	Professor, University of Paris-Sud	
Ralf	**LUDWIG**	**Referee**
	Professor, University of Rostock (Germany)	
Abdenacer	**IDRISSI**	**Supervisor**
	Professor, University of Lille	
Oleg	**KALUGIN**	**Co-supervisor**
	Professeur, Kharkiv National University (Ukraine)	
François-Alexandre	**MIANNAY**	**Co-supervisor**
	Assistant professor, University of Lille	
Maria	**ABRAHAMSSON**	**Examiner**
	Assistant professor, Chalmers University of Technology (Sweden)	
Thomas	**GUSTAVSSON**	**Examiner**
	CNRS research director, CEA Saclay	
Jean-Paul	**CORNARD**	**President**
	Professor, University of Lille	

Université de Lille
Faculté des Sciences et Technologies

Ecole Doctorale 104 - Sciences de la Matiére, du Rayonnement, et de l'Environment

Thèse de Doctorat

par

Yevheniia SMORTSOVA

pour l'obtention du titre de

Docteur de l'Université de Lille

Discipline: Chimie Analytique, Physique, et Théorique

Développement des perfomances des cellules solaires à photosensibilisateur: Optimisation du choix du mélange liquide ionique/solvant moléculaire et étude des caractéristiques photodynamiques des colorants dérivés de l'indoline par spectroscopie résolue en temps

Date de soutenance: 04 décembre 2018

Rachel	**MEALLET-RENAULT**	**Rapporteur**
	Professeur, Université Paris-Sud	
Ralf	**LUDWIG**	**Rapporteur**
	Professeur, Université de Rostock (Allemagne)	
Abdenacer	**IDRISSI**	**Directeur de thése**
	Professeur, Université de Lille	
Oleg	**KALUGIN**	**Co-directeur de thése**
	Professeur, Université nationale de Kharkiv (Ukraine)	
François-Alexandre	**MIANNAY**	**Co-encadrant**
	MCF, Université de Lille	
Maria	**ABRAHAMSSON**	**Examinateur**
	MCF, Université de Technologie de Chalmers (Suède)	
Thomas	**GUSTAVSSON**	**Examinateur**
	Directeur de recherche au CNRS, CEA Saclay	
Jean-Paul	**CORNARD**	**Président**
	Professeur, Université de Lille	

Acknowledgements

This work was performed at the University of Lille, in the Laboratory of Infrared and Raman Spectrochemistry (LASIR UMR 8516).

I wish to thank this institution and its director, Dr. Hervé Vezin for the possibility to pursue my PhD studies. I thank Lille University and the Région Haut-de-France for the financial support without which this work would not be possible.

My deepest gratitude is indeed due to my supervisors, Profs. Abdenacer Idrissi and Oleg Kalugin and Dr. François-Alexandre Miannay, for their wisdom, patience and scientific experience. I have learned and I continue to learn a lot from them. They know the debt of gratefulness I owe them for their work and the high esteem I have for them.

Prof. Rachel Meallet-Renault and Prof. Ralph Ludwig, the referees of this thesis, and the members of the jury: Dr. Thomas Gustavsson, Dr. Maria Abrahamsson and Prof. Jean-Paul Cornard are gratefully acknowledged for their time and effort to read this thesis.

My special thanks to the laser engineer, Julien Dubois, who helped me to master the time-resolved spectroscopy set-ups in LASIR. I can't also forget the PhD students Hanna Oher, Diksha Jani Thaviligadu, Pratima Bhurtun and also Ornella Laouadi who supported me during my work. I must also mention my teachers of French language who helped me to integrate in France.

Finally, I should thank my family for their understanding and love.

Abstract

Among all the renewable energy sources, solar energy is the most powerful source far ahead wind or geothermal energies. The first key component of DSSCs is the photosensitizer. It is through this component that the most important steps of photocurrent generation are possible: the photo-absorption, the charge separation in the dye and the electron injection into the semiconductor's conduction band and hole capture by the redox mediator in electrolyte. On the other hand, ionic liquids (ILs) have been proposed as electrolyte for DSSCs due to their peculiar properties: (1) vapor pressure is extremely low for many ionic liquids; (2) high thermal and chemical robustness; (3) excellent solubility of both inorganic and organic chemicals; (4) polarity and phase behaviour are changeable; (5) excellent electrochemical properties and (6) low melting point.

The objective of this thesis was to get a comprehensive understanding of the photophysics in the systems of indoline derivated dyes in molecular solvents (MS) and in the IL/MS mixtures. Firstly, the solvent dependence of the spectroscopic properties of the indoline derivated dyes D131, D102, D149 and D205 was studied by the steady-state UV-Vis absorption and fluorescence spectroscopy. Then, time-resolved spectroscopy was used to elucidate the photophysics of these dyes and its solvent dependence. These experiments helped to discern the particular influence of the hydrogen bond donor and acceptor ability of the solvent on the spectroscopic and photophysical properties of these dyes. The solvation dynamics was shown to play a major role in the excited state dynamics of these dyes. This process in IL/MS mixtures was elucidated using the classic fluorescent probe C153 by the means of time-resolved spectroscopy and MD simulations. The complex multi-regime solvation response in these systems was shown to be shaped by the strengthening of the hydrogen bonding between the probe and the mixture components. The results of this thesis work contribute to the fundamental understanding of the photodynamics of the sensitizer and the response of the electrolyte used in the DSSCs.

Résumé

Parmi toutes les nouvelles énergies renouvelables, l'énergie solaire est la plus puissante, loin devant les énergies éolienne ou géothermique. La première composante clé des dispositifs de cellules solaires dopées à colorants est le photosensibiliseur. C'est grâce à ce composant que la plupart des étapes de génération de photocourant sont rendues possibles: la photo-absorption, la séparation de charge au sein du photosensibliseur, l'injection électronique dans la bande de conduction du semi-conducteur et la régénération du photosensibiliseur par le couple rédox dans l'électrolyte. La deuxième composante clé est l'électrolyte. Les liquides ioniques (ILs) ont été utilisés, cette dernière décénie, en tant qu'électrolyte pour cellules solaires dopèées à colorants du fait de leurs remarquables propriétés chimiques: (1) une pression de vapeur extrêmement faible pour de nombreux ILs; (2) une haute stabilité thermique et chimique; (3) une excellente solubilité pour les composés organiques et inorganiques; (4) une polarité et un comportement de phase modulables; (5) d'excellentes propriétés électrochimiques et (6) un point de fusion bas.

L'objectif de cette thèse de doctorat est de comprendre les processus photophysiques ayant lieu au sein des colorants dérivés d'indolines utilisés comme photosensibiliseurs dans des solvants moléculaires (MS) et dans des mélanges liquide ionique/solvant moléculaire (IL/MS). Dans un premier temps, l'influence des solvants sur les propriétés spectroscopiques des sensibiliseurs dérivés d'indoline D131, D102, D149 et D205 a été étudiée par spectroscopie stationnaire d'absorption UV-visible et de fluorescence. Ensuite, des techniques de spectroscopies résolues en temps ont été utilisées pour sonder la photodynamique des états excités de ces colorants, ainsi que l'influence des solvants sur ces phénomènes. Ces expériences ont permis de mettre en évidence l'influence particulière des paramètres d'aptitude de donneur de liaison hydrogène et d'aptitude d'accepteur de liaison hydrogène sur les propriétés spectroscopiques et photophysiques de cette classe de colorants. Ces mesures de spectroscopies résolues en temps menées sur les colorants ont aussi montré un résultat important: le rôle majeur de la dynamique de solvatation dans la dynamique des états excités des sensibilseurs dérivés d'indoline. Pour comprendre ce phénomène dans les mélanges IL/MS, une sonde fluorescente classique, C153, a été étudiée par deux techniques de spectroscopies de fluorescence résolues en temps (fluorescence up-conversion et comptage de photons uniques corrélés en temps) ainsi que par des simulations de dynamique moléculaire. Les réponses de solvatation de ces mélanges, complexes et multi-régimes, se sont révélées être dirigées par le renforcement de la liaison hydrogène entre la sonde et les composants des mélanges (cations, anions, et molécules du solvant). Les résultats apportés par cette thèse contribuent à la compréhension des processus fondamentaux impliqués dans les mécanismes de photodésactivation des photosensibiliseurs et des réarrangements moléculaires ayant lieu dans des électrolytes utilisés dans les cellules solaires dopées à colorants.

Contents

List of abbrevations

ACN	acetonitrile
ADF	Angle distribution function
$BmimBF_4$	1-n-butyl-3-methylimidazolium tetrafluoroborate
CDF	Combined distribution function
CoR	Center of the ring
DAS	Decay associated spectra
DF	Deprotonated form
DMSO	dimethylsulfoxide
DSSC	Dyes sensitized solar cell
EEM	Excitation emission matrix
ESA	Excited state absorption
FWHM	Full width half maximum
GSB	Ground state bleach
GVD	Group velocity dispersion
HB	Hydrogen bond
HOMO	Highest occupied molecular orbital
IL	Ionic liquid
IRF	Instrument response function
LUMO	Lowest unoccupied molecular orbital
MeOH	Methanol
MS	Molecular solvent
NF	Neutral form
PC	Propylene carbonate
RDF	Radial distribution function
SE	Stimulated emission
SRF	Solvation response function
TA	Transient absorption
TCSPC	Time-correlated single photon counting
TDDFT	Time-dependent density functional theory
TRES	Time-resolved emission spectrum

The relevant structural formulas of organic molecules are assembled in Appendix G.

Introduction

Solar energy harvesting is a key concern in a modern research and development. DSSCs is a new type of a photovoltaic cell, a low-cost (0.5-1\$/W_p vs 0.7-1.29\$/W_p for silicone cells[1]) and stable at elevated temperatures (2000h at 60°[2]) alternative to conventional semiconductor devices. In order to deploy DSSCs to real life, they are assembled into modules and panels. In spite of low efficiency, their commercialisation is on the way (Solaronix Ltd., Dyesol, G-24 Ltd.). In view of the possibility to produce transparent devices, it was also proposed to extend their application to agriculture (e.g., greenhouse shading[3]). DSSCs work efficiently in diffused or low light and are weakly dependent on the angle of incidence, potentially suiting the indoor light harvesting.

A large improvement of dye-sensitized solar cells (DSSCs) efficiency was reported in 1991 in an article in Nature by Brian O'Regan and Michael Grätzel[4]. Although DSSCs were described much earlier[5], a considerable increase of cells efficiency to 7.1-7.9% made this article a legend of photovoltaics.

The schematic representation of the structure of DSSC is presented in fig. 1.

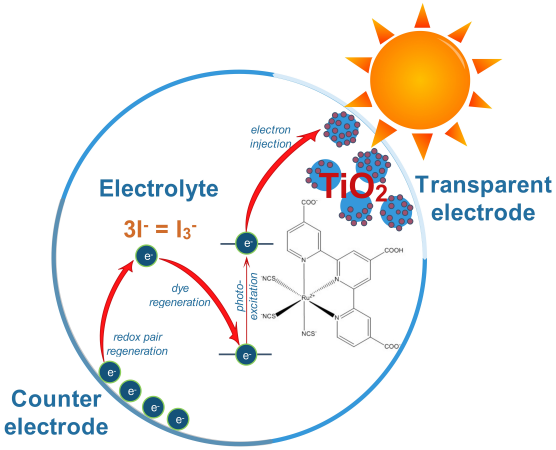

Figure 1: A scheme of DSSC.

A charge-transfer dye is absorbed on a transparent film, consisting of nanoparticles of n-type semiconductor (TiO_2, ZnO etc.). This film is deposited on a transparent conducting glass. An electrolyte between the sealed counterelectrode and coated semiconductor contains a redox couple. A principle difference between the DSSC and conventional semiconductor solar cell is that the processes of light harvesting and charge carrier transport are separated. Thus, the sensitizer, a charge-transfer dye, absorbs solar energy. Excited state electron energy level, higher than Fermi level of the semiconductor as well as charge-transfer character of the dye make the electron injection to the semiconductor possible. A redox couple transfers the charge

from the counterelectrode to the oxidized sensitizer.

Obviously, the performance of DSSCs depends largely on their components. An excellent review is available on this topic (see article [6] and the references within). The main performance characteristics are: (i) open-circuit voltage V_{OC}, (ii) short-circuit current J_{SC}, (iii) fill factor FF and overall efficiency η. These quantities are derived from measurements of $I-V$ curves[7]. In theory, an open-circuit voltage (V_{OC}) of DSSC is the difference between the Fermi level of the semiconductor and the Nernst potential of the redox couple. Also, an over-potential (0.2 eV [6] difference in energy between the charge transfer steps) is required to efficiently drive the processes of electron injection from LUMO to the metal oxide conduction band and dye regeneration. A short-circuit current (J_{SC}) of the device depends on the light harvesting and on the electron injection efficiency. The limits of V_{OC} and J_{SC} are typically 0.8V and 18-20mA. The series resistance of the device influences the fill factor FF, the last ingredient of the overall efficiency η of a DSSC (eq. 1).

$$\eta = V_{OC} \times J_{SC} \times FF \tag{1}$$

Literature data on the most recent progress in DSSC development is assembled in table 1 [8–24]. To our knowledge, the highest η was reported to be 14.7%[23].

As one can conclude, an optimisation of DSSCs efficiency is a key issue to deal with before proceeding to up-scale production. In order to improve their performance, much consistent and labour work is needed. Each component of DSSCs must be re-examined and optimised. The two main components, examined in this thesis, are (i) photo-sensitiser and (ii) electrolyte. Along with semiconductor nanoparticles, they constitute a complex multi-interface system, where the processes and the factors influencing them are still not understood. Electrolyte molecules and additives co-adsorb on semiconductor's surface, with different impact for the electron injection[25]. Furthermore, solvent molecules can mediate the non-desired desorption of sensitiser[26]. An understanding of the dye's photophysics and its dependence on the electrolyte, as well as the role of electrolyte in the solvation of the dye before and after the excitation are of high importance for advancement in the design of these components of DSSCs.

The two main issues, linked with electrolyte in liquid DSSCs are: (i) slow regeneration of oxidised dye and (ii) short stability of the cell due to desorption of the dye as well as electrolyte leakage and volatility[27]. Thus, the criteria for the ideal electrolyte can be formulated as: (i) low viscosity and high conductivity, (ii) low volatility, (iii) high thermal and electrochemical stability, (iv) optical transparency, (v) low cost and (vi) ease of purification.

Ionic liquids are promising candidates for use in electrochemical devices and in DSSCs[28], boosting the stability of the latter devices to thousands of hours[29]. These organic salts are liquid around the room temperature and possess a number of peculiar properties: low vapour pressure, high electrochemical and thermal stability, high conductivity etc. The ease of chemical tunability of these systems paves to a high potential in material design. Among the drawbacks of ionic liquids one can mention their high viscosity and cost. To overcome these negative points, ionic liquids are usually mixed with conventional organic solvents (acetonitrile, γ-butyrolactone, propylene carbonate (PC)), water and other low-viscosity ILs. Liquid iodide salts, used in IL-based DSSCs, also have high viscosity and, when mixed with low-viscosity ILs at high concentrations lead to the reductive quenching of the sensitiser. As it

Table 1: Literature data on the DSSCs' characteristics of indoline and other dyes: open-circuit current (V_{OC}, in V), short-circuit current (J_{SC} , in mA/cm^2), fill factor *FF* and efficiency (η, in %). Some details about the constructed DSSC are also added: the use of anti-aggregation agents and semiconductor type. The I^-/I_3^- redox pair was used for all the lit. resources except for P3HT hybrid solar cell[13].

sensitizer	V_{OC}	J_{SC}	*FF*	η, %	ref.	
N719	0.695	15.1	0.51	6.86	[8]	quasi-solid state, TiO_2
	0.681	5.53	0.674	2.54	[9]	Zn_2SnO_4
D131	0.66	5.55	0.71	2.6	[10]	cholic acid
	0.62	6.95	0.714	3.08	[9]	Zn_2SnO_4
	0.613	11.16	0.739	5.06	[11]	TiO_2
	0.87	9.84	0.45	5.13	[12]	TiO_2
D131+black dye	0.696	22.59	70	11	[11]	TiO_2
D131 + N719	0.644	8.15	0.685	3.6	[9]	Zn_2SnO_4
D102	0.8	5.9	0.53	2.5	[13]	P3HT/TiO_2
	0.65	9	0.66	3.88	[10]	cholic acid
	0.68	3.88	0.68	1.79	[9]	Zn_2SnO_4
	0.674	9.71	0.742	4.86	[14]	TiO_2
	0.604	17.76	0.57	6.1	[15]	TiO_2
	0.76	24.24	0.53	9.8	[16]	TiO_2
	0.77	6.9	0.53	3.76	[12]	TiO_2
D149	0.685	12.4	0.52	5.66	[8]	quasi-solid state, TiO_2
	0.641	10.94	0.7	4.95	[17]	ZnO
	0.68	11.08	0.57	4.23	[10]	cholic acid
	0.63	4	0.45	-	[18]	CDCA, TiO_2
	0.6	0.8	0.6	-	[18]	CDCA, ZnO
	0.2	0.05	-	-	[18]	CDCA, Al_2O_3
	0.644	19.86	0.694	8.85	[24]	TiO_2, CDCA
	0.707	12.52	0.72	6.38	[14]	TiO_2
	0.693	18.5	0.624	8	[24]	CDCA, TiO_2
	0.653	19.96	0.694	9.03	[19]	TiO_2
	0.612	16.13	0.676	6.67	[19]	TiO_2
	0.78	6.24	0.44	3.45	[12]	TiO_2
	0.691	12.23	0.658	5.56	[20]	ZnO
	0.563	14.1	0.537	4.27	[21]	ZnO
D205	0.653	12.7	0.67	5.34	[17]	ZnO
	0.71	18.68	0.707	9.4	[24]	TiO_2, CDCA
	0.728	13.73	0.719	7.18	[14]	TiO_2
NKX-2700	0.69	15.9	0.75	8.2	[22]	DCA, TiO_2
black dye	0.68	11.2	0.55	5.37	[8]	quasi-solid state, TiO_2
	0.677	21.51	0.689	10.04	[11]	TiO_2
N3	0.83	9.18	0.49	5.25	[12]	TiO_2
ADEKA-1+LEG4	0.994	9.55	0.776	14.7	[23]	TiO_2

is described in literature[28], ILs' cations affect the kinetics of the regeneration of the dye, while their anions interact with the surface of semiconductor and change its energetics. Imidazolium ionic liquid $BmimBF_4$ and propylene carbonate are prototypical ionic liquid and molecular solvent pair, considered in this thesis as a model system to understand the influence of these unique media on the photophysics

of the organic dyes. Their chemical structures, as well as basic physical properties are presented in fig. 2. Density and molar conductivity of these mixtures are available[30]. Measurements of viscosity dependence on the mixture composition were performed in the group of Slobodan Gadžurić, University of Novi Sad (Serbia), and used in this thesis.

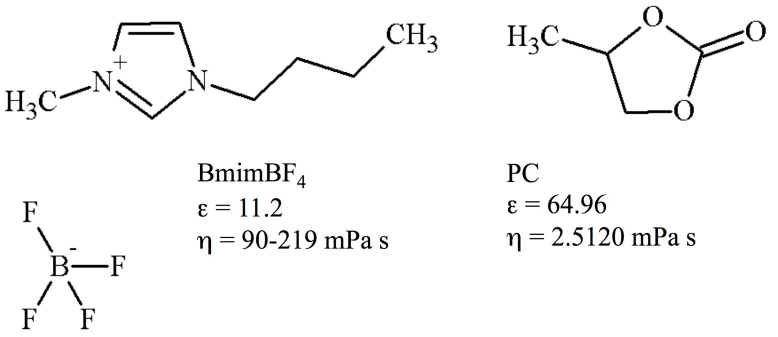

Figure 2: Structures of $BmimBF_4$ and PC. Dielectric constants of $BmimBF_4$ and PC were taken from references [31] and [32], respectively. Due to a large data scatter, the viscosity of ionic liquid, extreme values were taken from references [33] and [34]. The viscosity of PC was taken from [32].

The sensitiser is a key component of a DSSC. An ideal candidate molecule must [35]:

- absorb all light below a threshold wavelength of 920nm
- carry attachment groups to firmly graft it to the semiconductor
- inject the electron after the photo-excitation with a high quantum yield
- have the energy level of the excited state, matching the conduction band of the semiconductor
- have a sufficiently high redox potential to be regenerated by the redox couple
- be stable and sustain about 10^8 turnover cycles (an estimation of 20 years of exposure to natural light)

When compared to the originally used ruthenium complexes, organic photo-sensitisers have a number of advantages: (i) higher extinction coefficients, (ii) tunability of the structure to extend the spectral response, (iii) easier to synthesise and cheaper, (iv) less demanding to purify and (v) environmentally safer.

In order to improve the DSSCs efficiency, the processes that take place after the light harvesting must be clarified. The importance of combination of theoretical and experimental methods in the design of materials in development of DSSCs was outlined in literature[6]. For example, the photo-sensitizer properties, such as the energy of excited state and ground state electron levels, can be predicted using quantum chemistry calculations in order to pick out the most perspective structures and thus the extensive synthetic work can be avoided. Macroscopic quantities, such as short circuit current and IPCE (incident photon conversion efficiency) spectra are also possible to model using a computational procedure, reported in [36]. In line

with these reflections, both experimental and theoretical methods of research were applied during this thesis.

Thus, this thesis problematic is centred on the following question: How the solvent (conventional organic solvents, IL/MS mixtures) affects the spectroscopic and photodynamic properties of the DSSC photosensitizers?

Organization of the thesis

This thesis presents an investigation of the photo-physics of organic sensitisers for DSSCs in conventional organic solvents, ionic liquids and their mixtures by the means of steady-state and time-resolved electronic spectroscopy and molecular dynamics simulations. It is organised in the following way.

The solvatochromism study of indoline dyes D131, D102, D149 and D205 is presented in Chapter 1. Steady-state absorption and fluorescence data was used to distinguish the solvent-solute interactions and the way they affect the electronic spectra of organic photosensitisers. Chapter 2 is devoted to the time-resolved study of dyes by the means of time-correlated single photon counting and femtosecond UV-Vis transient absorption. Particular attention was paid to the possible deactivation pathways of indoline dyes. The importance of solvation dynamics in the photophysics of organic dyes was put forward.

Theoretical and experimental investigation of solvation dynamics in $BmimBF_4$/PC mixtures, using C153 fluorescent probe, is reported in Chapter 3. The time scales of the solvation response and the role of different mixture components in this process are discussed in terms of the structure changes in the solvation shell upon the excitation.

The summary of the key results of this thesis are summarised in Conclusion. The perspectives for future work were also discerned.

Appendices are devoted to the explanation of the principles of techniques used and experimental details of the time-resolved set-ups.

Bibliography

[1] A. Fakharuddin, R. Jose, T. M. Brown, F. Fabregat-Santiago, and J. Bisquert, "A perspective on the production of dye-sensitized solar modules," Energy Environ. Sci., vol. 7, pp. 3952–3981, 2014.

[2] A. Hinsch, J. M. Kroon, R. Kern, I. Uhlendorf, J. Holzbock, A. Meyer, and J. Ferber, "Long-term stability of dye-sensitised solar cells," Progress in Photovoltaics: Research and Applications, vol. 9, no. 6, pp. 425–438, 2017.

[3] N. Roslan, M. Ya'acob, M. Radzi, Y. Hashimoto, D. Jamaludin, and G. Chen, "Dye sensitized solar cell (dssc) greenhouse shading: New insights for solar radiation manipulation," Renewable and Sustainable Energy Reviews, vol. 92, pp. 171 – 186, 2018.

[4] B. O'Regan and M. Grätzel, "A low-cost, high efficiency solar cell based on dye-sensitized colloidal tio$_2$ films," Nature, vol. 353, pp. 737–740, 1991.

[5] H. Tsubomura, M. Matsumura, Y. Nomura, and T. Amamiya, "Dye sensitised zinc oxide: aqueous electrolyte: platinum photocell," Nature, vol. 261, pp. 402 EP –, Jun 1976.

[6] P. J. Holliman, C. Kershaw, A. Connell, E. W. Jones, R. Hobbs, R. Anthony, L. Furnell, J. McGettrick, D. Geatches, and S. Metz, "A perspective on using experiment and theory to identify design principles in dye-sensitized solar cells," Science and Technology of Advanced Materials, vol. 19, no. 1, pp. 599–612, 2018.

[7] L. L. Tobin, T. O.Reilly, D. Zerulla, and J. T. Sheridan, "Characterising dye-sensitised solar cells," Optik - International Journal for Light and Electron Optics, vol. 122, no. 14, pp. 1225 – 1230, 2011.

[8] M. Fakis, E. Stathatos, G. Tsigaridas, V. Giannetas, and P. Persephonis, "Femtosecond decay and electron transfer dynamics of the organic sensitizer d149 and photovoltaic performance in quasi-solid-state dye-sensitized solar cells," The Journal of Physical Chemistry C, vol. 115, no. 27, pp. 13429–13437, 2011.

[9] H. Lihua, J. Lilong, and W. Mingding, "Metal-free indoline dye sensitized solar cells based on nanocrystalline zn2sno4," Electrochemistry Communications, vol. 12, no. 2, pp. 319 – 322, 2010.

[10] T. Dentani, Y. Kubota, K. Funabiki, J. Jin, T. Yoshida, H. Minoura, H. Miura, and M. Matsui, "Novel thiophene-conjugated indoline dyes for zinc oxide solar cells," New J. Chem., vol. 33, pp. 93–101, 2009.

[11] R. Y. Ogura, S. Nakane, M. Morooka, M. Orihashi, Y. Suzuki, and K. Noda, "High-performance dye-sensitized solar cell with a multiple dye system," Applied Physics Letters, vol. 94, no. 7, p. 073308, 2009.

[12] R. Jose, A. Kumar, V. Thavasi, K. Fujihara, S. Uchida, and S. Ramakrishna, "Relationship between the molecular orbital structure of the dyes and photocurrent density in the dye-sensitized solar cells," Applied Physics Letters, vol. 93, no. 2, p. 023125, 2008.

[13] A. Abrusci, K. R. S. Santosh, M. Al-Hashimi, M. Heeney, A. Petrozza, and H. J. Snaith, "Influence of ion induced local coulomb field and polarity on charge generation and efficiency in poly(3-hexylthiophene)-based solid-state dye-sensitized solar cells," Advanced Functional Materials, vol. 21, no. 13, pp. 2571–2579, 2011.

[14] D. Kuang, S. Uchida, R. Humphry-Baker, S. M. Zakeeruddin, and M. Grätzel, "Organic dye-sensitized ionic liquid based solar cells: Remarkable enhancement in performance through molecular design of indoline sensitizers," Angewandte Chemie International Edition, vol. 47, no. 10, pp. 1923–1927, 2008.

[15] T. Horiuchi, H. Miura, and S. Uchida, "Highly-efficient metal-free organic dyes for dye-sensitized solar cells," Chem. Commun., pp. 3036–3037, 2003.

[16] X. Li, D. Zhang, Z. Sun, Y. Chen, and S. Huang, "Metal-free indoline-dye-sensitized tio2 nanotube solar cells," Microelectronics Journal, vol. 40, no. 1, pp. 108 – 114, 2009.

[17] H.-M. Cheng and W.-F. Hsieh, "High-efficiency metal-free organic-dye-sensitized solar cells with hierarchical zno photoelectrode," Energy Environ. Sci., vol. 3, pp. 442–447, 2010.

[18] J. Sobuś, J. Karolczak, D. Komar, J. A. Anta, and M. Ziółek, "Transient states and the role of excited state self-quenching of indoline dyes in complete dye-sensitized solar cells," Dyes and Pigments, vol. 113, pp. 692 – 701, 2015.

[19] S. Ito, S. Zakeeruddin, R. Humphry-Baker, P. Liska, R. Charvet, P. Comte, M. Nazeeruddin, P. Péchy, M. Takata, H. Miura, S. Uchida, and M. Grätzel, "High-efficiency organic-dye- sensitized solar cells controlled by nanocrystalline-tio2 electrode thickness," Advanced Materials, vol. 18, no. 9, pp. 1202–1205, 2008.

[20] T. Yoshida, J. Zhang, D. Komatsu, S. Sawatani, H. Minoura, T. Pauporté, D. Lincot, T. Oekermann, D. Schlettwein, H. Tada, D. Wöhrle, K. Funabiki, M. Matsui, H. Miura, and H. Yanagi, "Electrodeposition of inorganic/organic hybrid thin films," Advanced Functional Materials, vol. 19, no. 1, pp. 17–43, 2009.

[21] E. Hosono, Y. Mitsui, and H. Zhou, "Metal-free organic dye sensitized solar cell based on perpendicular zinc oxide nanosheet thick films with high conversion efficiency," Dalton Trans., pp. 5439–5441, 2008.

[22] Z.-S. Wang, Y. Cui, Y. Dan-oh, C. Kasada, A. Shinpo, and K. Hara, "Thiophene-functionalized coumarin dye for efficient dye-sensitized solar cells: Electron lifetime improved by coadsorption of deoxycholic acid," The Journal of Physical Chemistry C, vol. 111, no. 19, pp. 7224–7230, 2007.

[23] K. Kakiage, Y. Aoyama, T. Yano, K. Oya, J.-i. Fujisawa, and M. Hanaya, "Highly-efficient dye-sensitized solar cells with collaborative sensitization by silyl-anchor and carboxy-anchor dyes," Chem. Commun., vol. 51, pp. 15894–15897, 2015.

[24] S. Ito, H. Miura, S. Uchida, M. Takata, K. Sumioka, P. Liska, P. Comte, P. Pechy, and M. Grätzel, "High-conversion-efficiency organic dye-sensitized solar cells with a novel indoline dye," Chem. Commun., pp. 5194–5196, 2008.

[25] T. Le Bahers, F. Labat, T. Pauporté, P. P. Lainé, and I. Ciofini, "Theoretical procedure for optimizing dye-sensitized solar cells: From electronic structure to photovoltaic efficiency," Journal of the American Chemical Society, vol. 133, no. 20, pp. 8005–8013, 2011.

[26] F. De Angelis, S. Fantacci, and R. Gebauer, "Simulating dye-sensitized tio2 heterointerfaces in explicit solvent: Absorption spectra, energy levels, and dye desorption," The Journal of Physical Chemistry Letters, vol. 2, no. 7, pp. 813–817, 2011.

[27] F. Sauvage, "A review on current status of stability and knowledge on liquid electrolyte-based dye-sensitized solar cells," Advances in Chemistry, vol. 2014, 2014.

[28] F. Hao and H. Lin, "Recent molecular engineering of room temperature ionic liquid electrolytes for mesoscopic dye-sensitized solar cells," RSC Adv., vol. 3, pp. 23521–23532, 2013.

[29] K. Duckhyun, K. Chulwoo, C. Hyunbong, S. Kihyung, K. Moon-Sung, and K. Jaejung, "A new class of organic sensitizers with fused planar triphenylamine for nanocrystalline dye sensitized solar cells," Journal of Photochemistry and Photobiology A: Chemistry, vol. 219, no. 1, pp. 122 – 131, 2011.

[30] A. Stoppa, J. Hunger, and R. Buchner, "Conductivities of binary mixtures of ionic liquids with polar solvents," Journal of Chemical & Engineering Data, vol. 54, no. 2, pp. 472–479, 2009.

[31] H. Weingärtner, "The static dielectric constant of ionic liquids," Zeitschrift fur Physikalische Chemie, vol. 220, pp. 1395–1405, 2006.

[32] J. Barthel, R. Neueder, and H. Roch, "Density, relative permittivity, and viscosity of propylene carbonate + dimethoxyethane mixtures from 25c to 125c," Journal of Chemical & Engineering Data, vol. 45, no. 6, pp. 1007–1011, 2000.

[33] J. Jacquemin, P. Husson, A. A. H. Padua, and V. Majer, "Density and viscosity of several pure and water-saturated ionic liquids," Green Chem., vol. 8, pp. 172–180, 2006.

[34] J. G. Huddleston, A. E. Visser, W. M. Reichert, H. D. Willauer, G. A. Broker, and R. D. Rogers, "Characterization and comparison of hydrophilic and hydrophobic room temperature ionic liquids incorporating the imidazolium cation," Green Chem., vol. 3, pp. 156–164, 2001.

[35] M. Grätzel, "Dye-sensitized solar cells," Journal of Photochemistry and Photobiology C: Photochemistry Reviews, vol. 4, no. 2, pp. 145 – 153, 2003.

[36] T. Le Bahers, T. Pauporté, P. P. Lainé, F. Labat, C. Adamo, and I. Ciofini, "Modeling dye-sensitized solar cells: From theory to experiment," The Journal of Physical Chemistry Letters, vol. 4, no. 6, pp. 1044–1050, 2013.

Chapter 1

Solvatochromism of indoline dyes: experimental and theoretical study

The material presented in this chapter forms the basis of publication [1].

Nowadays, new organic photosensitizers are replacing the commonly used Ru-complexes in dyes sensitized solar cells. Even when they are linked to TiO_2 or ZnO_2 semiconductors, their spectroscopic behavior can be influenced once immersed in a solvent. Therefore it is crucial to understand how solvatochromic effects can influence the photophysical properties of the organic photosensitizer and to isolate which solvent parameters can be responsible for the dye absorption spectral shifts. Here indoline derivative photosensitizers D205, D149 and D102 have been studied by steady-state spectroscopy. Some qualitative trends on the spectral shifts of those compounds have been first isolated. Then multivariate regression analyses following both Kamlet-Taft and Catalan scales have been applied to the observed spectral shifts (absorption maxima, emission maxima and Stokes shifts). Solvents dipolarity and polarizability are definitely the preponderant parameters which rule the spectroscopic characteristics of this class of dyes, but some interesting link has been evidenced between HB acceptor ability solvents parameter and a blue shift of absorption spectra of the dyes. This could lead to an alteration of the overlap of the photosensitizer absorption spectrum and the solar light, leading to a decrease of the photoconversion efficiency of the solar cell. Our results point out to the importance of the choice of the electrolyte, particularly their HB acceptor ability parameter, on the properties of the photosensitizer.

1.1 Introduction

Indoline derivatives D205, D149, D131 and D102 (figure 1.1) are organic molecules used in DSSCs. Although the recent reports about their photophysical properties were published [2–4], the dependence of their properties on the nature of the solvent is still not clear. This point is extremely important, as in the DSSCs, the dye is anchored to the semiconductor surface, but the rest is immersed in the solvent. The photophysical properties, such as absorption and emission spectra position and shape, fluorescence quantum yield, excited state lifetime and its other evolution characteristics are strongly dependent on the dye's environment. The purpose of the present work is to distinguish the key features of the solvent dependence of the dyes' properties.

For the purpose of the best performance of DSSCs, the organic sensitiser must contain donor, acceptor and π-bridge moieties. The structure of indoline dyes D205, D149, D131 and D102 are shown in figure 1.1. The above mentioned donor moiety is shown on the left, it is represented by triphenylethylene and indoline cores. The differences between the molecules consist in the π-bridge and acceptor groups: –C≡N group for D131, rhodanine ring for D102 and two rhodanine rings for D149 and D205. The dyes have a similar anchor group: carboxyl –COOH. The octyl chain was introduced to D205 to make some distance between the semiconductor and the sensitiser in order to preclude the undesired electron recombination process.

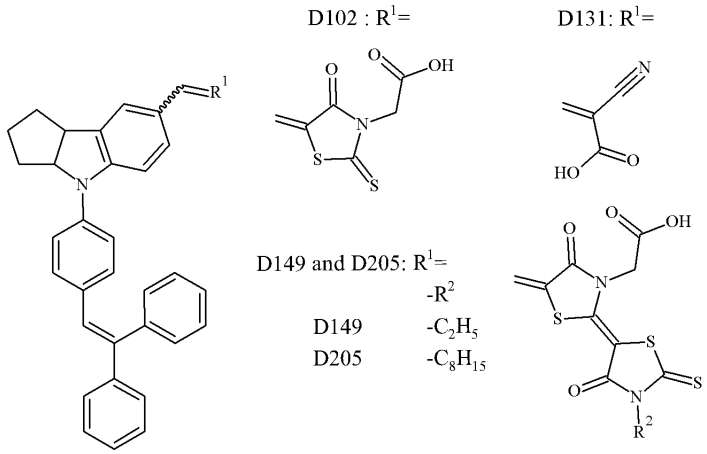

Figure 1.1: Chemical structures of D102, D131, D149 and D205 organic dyes.

These indoline dyes were first presented in 2003 by Mitsubishi Paper Mills Corporate Research Center in the article [5]. In this paper, D131 and D102 dyes were used to construct the DSSCs that exhibited an efficiency of 4.03% and 5.11%, respectively. Later, the D149 dye was synthesised by the same group [6] as well as its derivatives, including the one with three rhodanine rings. D149 boosted the performance to 6.51%. D205 sensitizer appeared in literature in 2008, with idea to substitute the ethyl chain by an octyl chain[7]. There, an important enhancement in the performance of DSSCs, sensitized with D205 was observed – 7.18%. The presence of an anti-aggregation reagent improved the D205/TiO_2 power conversion efficiency to the remarkable value of 9.40%[8].

This last decade, a number of studies on indoline dyes were published. The summary on the literature data about the steady-state spectral properties of D149 is

assembled in table 1.1 and for D131, D102 and for D205 in table 1.2. Fakis et al. performed steady-state and time-resolved measurements, as well as quantum calculations on D149 indoline dye[4]. Steady-state spectroscopy revealed non-monotonic shift of the absorption and the emission spectra with solvent polarity, also the Stokes shifts were found to be in linear dependence with polarity. The dipole moment was found to increase by 13.2 D upon the photo-excitation. A dual fluorescence, observed in steady-state and time-resolved spectra was ascribed to the $S_2 \rightarrow S_0$ emission and impurities. Time-resolved fluorescence decays of D149 were shown to be short and wavelength-dependent with solvation dynamics of organic solvents that is entangled in possible relaxation mechanisms of D149. In an earlier work, the same group published the fluorescence up-conversion measurements of D149 in toluene, acetonitrile (ACN), poly (methyl methacrylate) films and on Al_2O_3 and TiO_2 semiconductors[9]. Complex dynamics was evidenced, caused by the existence of aggregates, multiphasic electron injection mechanism, relaxation of hot species as well as fluorescence. The quasi-solid state DSSCs efficiency with D149 was measured to be promising 5.66%. Another solid-state hybrid solar cell was described in [10]. This DSSC is based on light-absorbing polymer poly(3-hexylthiophene), incorporating D102 indoline dye. The efficiency of the device was boosted by the addition of ionic liquid EmimTFSI and this fact was related by the authors to the increase of the charge-transfer character of the excited state of the dye. The highest efficiency of 2.5% was achieved for a EmimTFSI containing cell, while with the addition of LiTFSI a drop in open-circuit voltage was observed.

D149 and D205 [12, 18] were also investigated when adsorbed on ZnO, the alternative semiconductor that is used to construct DSSCs. In the latter publication, the importance of the semiconductor morphology was stressed. The secondary spherical ZnO nanoparticles were synthesised to cause the scattering of the light in the semiconductor layer with a possibility of the random laser effect and increase of the photon absorption. The optimised energy conversion efficiency of 4.95% for D149 and of 5.34% for D205 was achieved. In the former publication, only the D149 dye was used on ZnO. The broadening of the absorption spectrum of the absorbed dye was ascribed to the existence of aggregates. Femtosecond transient absorption measurements revealed an electron injection time constant of 150 fs, much shorter when compared to 170 ps excited state lifetime of the dye. The oxidised form of the dye was observed as a long-lived ground state bleach signature. Using this part of transient absorption signal in the measurements of the systems without the redox couple, the recombination time was calculated to be longer than 1 ns. This time constant corresponds to a process when the electron in the semiconductor returns to the oxidised dye. In the presence of Li^+ ions, the electron injection was shown to be much faster, probably due to the change in band position of ZnO. The improvement of the efficiency of DSSCs with addition of Li^+ was confirmed in the article [19]. In this work, the D149-sensitized nanocrystalline TiO_2 films absorption spectra were also red-shifted and widened compared to the D149 spectrum in ethanol solution. Further red-shift upon addition of lithium salt and the lowering of conduction band edge enhanced the light harvesting and electron injection efficiencies in the solar cell. The latter was demonstrated by the comparison of the absorption signal, ascribed to absorption of D149 cation, for D149/TiO_2/ACN(Li^+) and other systems: D149/TiO_2/ACN, D149/TiO_2/air, D149/TiO_2/ACN($Bmim^+$). Cation absorption was shown to be stronger when $LiClO_4$ was added to ACN.

Table 1.1: Gathered in literature data on the spectroscopic properties of D149 in organic solvents, polymer matrices and on the semiconductiors: maximum absorption and emission wavelengths (λ_{max}, in nm), Stokes shift ($\Delta\bar{\nu}$, in cm^{-1}). Quantum calculation results: a - PBE0/6-31+G(d), b - B3LYP/3-21G, c - PBE0/6-311+G(d,p), d - M05/6-31G(d)

Environment	λ_{max}^{abs}	λ_{max}^{em}	$\Delta\bar{\nu}$	ref.	Environment	λ_{max}^{abs}	ref.
C_6H_6	540	590	1570	[11]	1:1 ACN,t-BuOH	527	[12]
	532	571	1284	[4]		526	[6]
	529	597	-	c[4]	ZnO	513	[12]
	533			[9]		521	[13]
ACN	530	661	3740	[11]		505	[14]
	522	615	2897	[4]	TiO_2	518	[9]
	538	607	-	c[4]		541	[6]
	529	664	4050	[2]		516	[14]
	524			[9]	vacuum	505	b[15]
	528			d[16]	Al_2O_3	507	[14]
MeOH	528	670	4015	[11]			
	528	670	4260	[2]			
	561	640	0.42 eV	a[17]			
	527	644	0.27 eV	[17]			
PMMA	533	591	1840	[11]			
PS	540	605	1990	[11]			
$CHCl_3$	548	620	2119	[4]			
	534	601		c[4]			
	549	643	2780	[2]			
	550			[13]			
THF	526	601	2372	[4]			
	536	605		c[4]			
	531	621	2870	[2]			
	526			[7]			
DCM	544	625	2382	[4]			
	537	606		c[4]			
acetone	528	614	2652	[4]			
	538	607		c[4]			
	530	659	3860	[2]			
EtOH	531	664	4020	[2]			

As a semiconductor for DSSCs, ZnO exhibits much lower performance than TiO_2, independently from the morphology of the ZnO used[20]. The possible reasons for this detrimental behaviour were suggested to be: (i) the density of acceptor states, (ii) low dielectric constant that facilitate the long lifetime of dye cation-electron pairs and (iii) low refractive index that facilitates the self-quenching of singlet excited states of the dye. Different dyes that can be cografted with indoline derivatives help to get a panchromatic solar cell [21, 22]: the cosensitizers used are squarine dyes (SQ2) [22] and N719[21]. In the latter publication, with nanocrystalline Zn_2SnO_4, 3.08% efficiency was achieved for D131 dye[21], higher than that of D102 (1.79%) and N719 dye (2.54%). The coadsorption of D131 and N719 helped to increase

the efficiency up to 3.6%. The authors concluded that higher oxidation potential of D131 than that of D102 precludes fast charge recombination after the electron injection. The hole transport between the dye molecules in D131 and MP13 (4-((4-(bis(4-methoxyphenyl)amino)phenyl)ethynyl)benzoic acid) on TiO_2 based DSSCs is shown to be one of the factors that increase the rate of electron recombination[23]. Transient absorption measurements and Monte Carlo simulations of electron and hole diffusion were performed. Authors concluded that the hole lifetime is influenced by an incomplete coverage by the dye monolayer and TiO_2 surface inhomogeneity. The authors also suggest possible ways to decrease the rate of recombination: (i) addition of the non-conjugated chains in the structure of the dye, (ii) use of coadsorbents and (iii) limiting of the adsorbed dye concentration to 50%.

The modification of the chemical structure of D131, D102 and D149 by the extension of π-bridge, using thiophene rings, lead to the improvement of the efficiency of the constructed DSSCs[13]. Although the absorption spectra shifted to the red in all the cases, only D131 derivative resulted in a better efficiency of the cell. D149 showed the best results among the tested sensitisers, exhibiting the highest short-circuit current and conversion efficiency. The position of the carboxylate group in parent indoline molecule (with phenyl at the place of triphenylethylene, cf. fig 1.1) was varied in [24], and the compound with the carboxymethyl group at the inner rhodanine ring exhibited the best performance. Also, the increase of the donor core strength by addition of methoxy group to the phenyl shifted the absorption spectrum to the red (D149-type - 525nm, compound - 542nm) and showed the highest efficiency (4.53% in ZnO-based DSSC).

Another interesting study of Lohse et al [2] on the same dye D149 was performed by the means of steady-state, TCSPC and femtosecond transient absorption. The Stokes shift linear proportionality to polarity was confirmed. Again, the fluorescence lifetime was found to be inversely proportional to polarity. Interestingly, the transient absorption spectra didn't show any particular dynamics of D149 dye, apart the shift of the negative signal, ascribed to stimulated emission, due to the solvation. A considerable influence of hydrogen bonding on the D149 excited state dynamics was underlined.

Table 1.2: Gathered in literature data on the spectrsocpic properties of D131, D102 and D205 in organic solvents, polymer matrices and on semiconductiors: maximum absorption and emission wavelengths (λ_{max}, in nm), Stokes shift ($\Delta\bar{\nu}$, in cm^{-1}). Quantum calculation results: a - PBE0/6-31+G(d), b - B3LYP/3-21G.

Environment	λ_{max}^{abs}	λ_{max}^{em}	$\Delta\bar{\nu}$	ref.	λ_{max}^{abs}	λ_{max}^{em}	$\Delta\bar{\nu}$	ref.	λ_{max}^{abs}	λ_{max}^{em}	ref.
		D131				D102				D205	
C_6H_6											
ACN					530			[b][15]			
MeOH	491	598	0.66 eV	[a][17]	523	616	0.55 eV	[a][17]			
	422	543	0.46 eV	[17]	491	625	0.36 eV	[17]			
$CHCl_3$	463			[13]	514			[13]			
THF					531			[b][15]	532		[7]
					494			[7]			
1:1 ACN, t-BuOH					491			[25]			
ZnO	405			[13]	476			[13]			
TiO_2					540			[25]			
vacuum					488			[b][15]	506		[b][15]
Zn_2SnO_4	412			[21]	503			[21]			

A comprehensive quantum-chemical study of the D131, D102 and D149 dyes was published by Le Bahers et al. [17]. PBE0/6-31+G(d) level of theory was used to characterise the structure and the electronic states of dyes. Good quantitative and qualitative agreement between experimental and theoretical values has been achieved for absorption and fluorescence maxima. From a structural point of view, a sizeable loss in co-planarity of indoline and acceptor units was evidenced. A planarization of the triphenylethylene unit was observed in S_1 state. The hypothesis on the ultrafast twisting of the triphenylethylene donor unit and the conical intersection, linked to this process was put forward in [3]. The authors attribute the fast time component of 20-40 ps in the time-resolved measurements to the deactivation channel by the torsion of ethylene (cf. the donor unit in figure 1.1). The CASSCF/CASPT2 methodology was applied to describe the internal conversion process of the triphenylethylene unit. A longer fluorescence lifetime (in the order of nanoseconds) of the donor unit when embedded into a polymer matrix supports the authors' interpretation. The influence of D149 conformation on the absorption spectra was considered in the article of Fukunishi et al. [16], where 16 different structures were analysed by means of quantum calculations with B3LYP/6-31G(d) level of theory. The conformations are reported to have an influence on the position of the absorption bands, but the oscillator strengths were different for the conformations with 0° and 180° between rhodanine and indoline parts. Indeed, the latter conformation has higher oscillator strength for long-wavelength band and is thus beneficial for the efficiency of DSSC. The authors proposed to introduce the substituents of the type $–CH_3$, –OH and –Cl to fix the desired confirmation. The reversible photo-isomerization reaction of D149 dye within the exocyclic double bond between the rhodanine and indoline cores and the aggregation are the factors that lead to a short lifetime of the excited state and then to the decrease of the efficiency of the DSSCs [11]. NMR measurements confirmed the structure of the photo-isomer. D149 in polymer matrix (PMMA, PS) and upon dilution exhibited longer fluorescence decays. A particular feature of Baryshnikov et al quantum calculations [15] is that the excited state of the D102, D149 and D205 molecules has triplet nature. The calculated absorption wavelength are in semi-quantitative agreement with experiment. However, the tabulated non-zero oscillator strengths of these transitions obviously suggest that the calculations were made only for the singlet-singlet allowed transitions.

The aggregation of D149, D205 and perfluorinated D205 dyes was investigated using molecular dynamics simulations [26]. The aggregation of the sensitiser molecules is known to reduce the efficiency of the electron injection. Therefore, the anti-aggregating agents, like chenodeoxycholic acid (CDCA) are added to DSSCs. Indeed, the increase of the 5% efficiency of the thiophene-functionalised coumarin-based dye to 8.2% upon the addition of CDCA was reported [27]. The MD simulations of the systems CDCA, D149 and D149/CDCA by the clusters of 128 molecules were reoprted[26]. Authors showed that the conformational flexibility of D149 and its diffusion coefficient are enhanced in D149/CDCA system, due to the more disordered structure. The fast ageing of D149-based DSSCs with TiO_2 and ZnO as semiconductors was related to the rearrangement of the dye layer [14]. Authors suggest the formation of aggregates upon the immersion of the semiconductor with absorbed dye in the electrolyte. The singlet-singlet annihilation was proposed as the mechanism of the self-quenching process. The decay associated spectra (DAS) were reported for D149 in solution and in the cells with TiO_2, ZnO and Al_2O_3.

Interestingly, two of these time components were assigned to the locally excited and charge transfer states, both taking part in electron injection process. An elegant study of the D102 and D205 aggregates on TiO_2 anatase surface was published by Pastore and De Angelis [28]. The quantum calculations of the dyes on the cluster showed different preferred (having the lowest energy) mutual orientation of D102 and D149 dimers when anchored to the semiconductor surface, the former being oriented with more efficient π-π stacking, producing larger red shift of the absorption spectrum. The shifts, calculated for the favoured aggregation schemes are in almost quantitative agreement with the experimental values and are typical for the aggregation scheme of J-type.

In summary, the literature review shows that the indoline derivated dyes are perspective candidates for use in the DSSCs. Despite the large number of published articles on this point, the lack of understanding how the solvent properties affect the steady-state absorption and fluorescence spectra and the photodynamics of these dyes is still prevalent. Indeed, the non-monotonic shift of steady-state absorption spectra with polarity [4] must be clarified. In this Chapter, the study of the solvatochromism of the indoline derivated dyes is presented. Firstly, the experimental data on their steady-state spectra is shown, followed by its analysis using theoretical and empirical solvent scales. Then, the quantum calculations of the frontier orbitals and absorption energies are demonstrated. Finally, the solvent dependence of the quantum yields and the EEMs of the dyes are discussed.

1.2 Experimental study of the solvatochromism of indoline photosensitisers

As was mentioned in the introduction, in DSSCs, the sensitizer is immersed in the electrolyte – the mixture of the solvent, redox pair and other additives that optimise the DSSC performance. The influence of the solvent used in a dye bath soaking on the resulting DSSC efficiency was reported previously [29]. The most promising dye, presented in this article was later investigated using steady-state and time-resolved absorption and fluorescence techniques in the work of Ziolek et al. [30]. The authors showed that the nature of the solvent affects the equilibrium between neutral and anionic forms of the dye, which is important for its chemisorption on TiO_2. Additionally, solvent may induce a shift in absorption spectra and excited state energy level. This affects the match between the absorption spectrum of the dye and the solar spectrum, the over-potential value between the conductive band of a semiconductor and a dye [31]. Therefore the overall efficiency of DSSCs is greatly affected by the choice of the solvent. Strong solvent dependence of the properties of certain fluorophores (especially those with large dipole moment change upon the photo-excitation), e.g. BODIPY derivatives, was shown in works[32–34] and constitutes a basis of the development of chemosensors .

The current work was largely motivated by the understanding of the importance of the solvent's influence at a level of the dye. UV-Vis absorption and emission spectra of the dyes were recorded in various organic solvents and in ionic liquids. The absorption and emission spectra of D205 in 16 different organic solvents are shown in fig. 1.2. The colour gradient was chosen for different spectra, according to the band maximum position. Certainly, different mechanisms of solvent influence

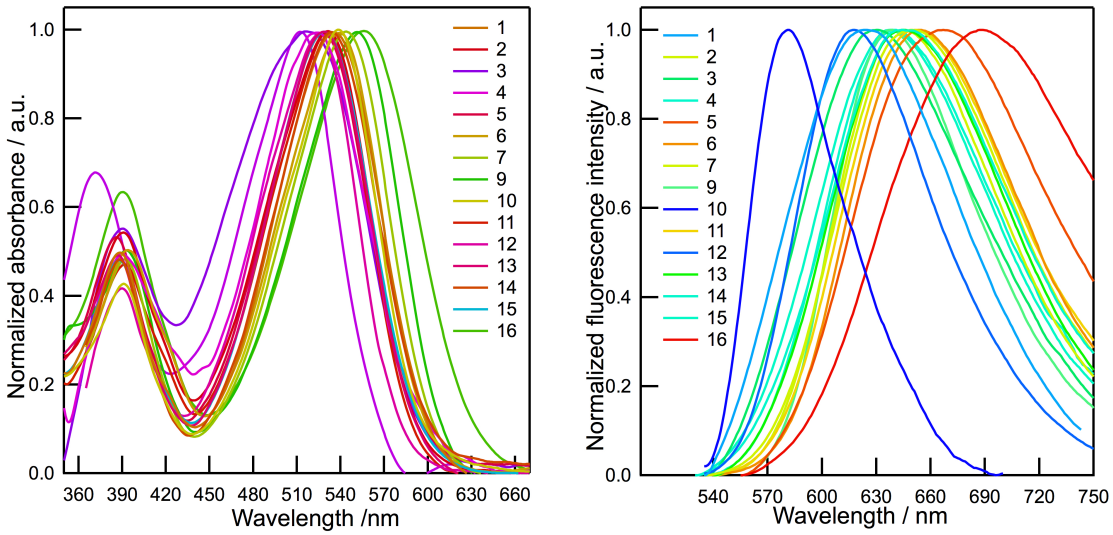

(a) (b)

Figure 1.2: Steady state absorption (a) and emission (b) spectra of D205 in 16 various solvents listed in table 1.3. Emission spectra were corrected for the wavelength dependent detector response.

on the chromophore differentiate spectral features of the latter, so that the given representation of the data permits to group the solvents with similar overall effect. The choice of the solvents was made in order to cover different properties of the solvents: acidity, basicity, polarity, polarisability, viscosity etc. Due to the low solubility of the indoline dyes, the work solutions were prepared by dilution of the saturated solutions of a given dye in a given solvent. In the steady-state experiments, the concentration of the dye was lower than 10^{-5} M.

The first comment to make on figure 1.2 is that the absorption and emission steady-state spectra of D205 are broad and featureless. Indeed, the two broad bands in absorption and the one in emission can be ascribed to $S_0 \rightarrow S_2$, $S_0 \rightarrow S_1$, $S_1 \rightarrow S_0$ electronic transitions, respectively. This assignment was based on the published data on the steady-state spectra of indoline dyes [4]. The energy difference between the two bands in absorption also is reasonably high to assign them to different electronic transitions, and not to the vibronic levels. Certainly, $S_0 \rightarrow S_2$ transition, due to its higher energy, is located in the shorter wavelength region. According to the Kasha's rule, in emission spectra, the band is assigned to $S_1 \rightarrow S_0$ transition. It says that whatever is the populated state after excitation, the emission is always arising from the lowest excited energy state. Indeed, the internal conversion from S_n to S_1 is far faster than the spontaneous emission process. In any case, the emission spectra were recorded after the excitation at the maximum of $S_0 \rightarrow S_1$ band. The near mirror image of the $S_0 \rightarrow S_1$ and $S_1 \rightarrow S_0$ bands is indeed observed, further corroborating this interpretation. Concerning the double fluorescence, it was claimed in the literature to be observed using ultrafast time-resolved techniques, like a fluorescence up-conversion [4]. However, the impurities in the samples and the high concentrations used for such a kind of experiment (associated with the formation of aggregates) can be possible reasons for those weak signals. In the present work, the samples were excited mainly at the $S_0 \rightarrow S_1$ band wavelengths range, thus the

double fluorescence possible effect can be safely ignored.

The dyes' absorption and emission spectra, measured in this work are in reasonable accordance with overall trends, found in literature. The dyes absorb light up to 630 nm (D205 has the most-red-shifted spectrum) and exhibit a large Stokes shift. The structure may be further improved in order to shift λ_{abs} to near-IR range.

At the first glance, the spectral band position for both absorption and emission follows solvent's polarity. While absorption spectra slightly change their characteristics, fluorescence maximum moves for about 110nm: from ca. 580nm in toluene to ca. 690nm in tri-fluoroethanol. This indicates that upon the photo-excitation the molecule changes its dipolar moment. The dipole moment in the excited state is much larger than in the fundamental state. This behaviour is inherent for the D-π-A structure of the D205, D149, D131 and D102 indoline dyes, and is supported by quantum calculations [4]. One must mention that the spectral features are very similar for all the studied dyes. The difference resides mainly in the maximum red shift for more elongated D102, D149 and D205 structures. The data on the spectral properties of D205, D149, D131 and D102 indoline dyes in various solvents are listed in tables 1.3 and 1.4.

Table 1.3: The spectroscopic properties of D205 in 16 organic solvents: maximum absorption and emission wavelengths (λ_{max}, in nm) and wavenumbers ($\bar{\nu}_{max}$, in cm^{-1}), Stokes shift ($\Delta\bar{\nu}$, in cm^{-1}) defined as the difference of maximum wavenumbers for absorption and emission, fluorescence quantum yield Φ_{fluo} (Nile Blue in methanol ($\Phi_{fluo} = 0.27$) was used as a standard [35]); solvent properties: dielectric constant ϵ and refractive index n, taken from [36]. The names of the solvents as well as their short names are listed this way: 1 pentanol (5-ol); 2 propylene carbonate (PC); 3 gamma-butyrolactone (g-Bl); 4 acetonitrile (ACN); 5 methanol (MeOH); 6 dimethylsulfoxide (DMSO); 7 dichloromethane (DCM); 8 cyclohexane (CX); 9 chloroform ($CHCl_3$); 10 toluene (TLN); 11 dimethylformamide (DMF); 12 tetrahydrofurane (THF); 13 ethanol (EtOH); 14 propanol (n-3ol); 15 butanol (n-4ol); 16 trifluoroethanol (TFE).

	Solvents	ϵ	n	λ^{abs}_{max}	λ^{em}_{max}	$\bar{\nu}^{abs}_{max}$	$\bar{\nu}^{em}_{max}$	$\Delta\bar{\nu}$	Φ_{fluo}
1	5-ol	15.13	1.4107	515	624	19,418	15,798	3620	0.146
2	PC	66.14	1.4189	532	650	18,797	15,175	3622	0.149
3	γ-Bl	39.00	1.4341	515	631	19,417.5	15,674	3744	0.141
4	ACN	36.64	1.3442	525	640	19,048	15,432	3616	0.123
5	MeOH	33.00	1.3288	524	671	19,084	14,815	4269	0.02
6	DMSO	47.24	1.4793	541	653	18,484	15,152	3332	0.15
7	DCM	8.93	1.4242	544	645	18,382	15,456	2926	0.14
8	CX	2.02	1.4235	524	545	19,084	18,349	735	0.01
9	$CHCl_3$	4.81	1.4459	550	638	18,182	15,576	2606	0.11
10	TLN	2.38	1.4941	538	581	18,588	17,211	1376	-
11	DMF	38.25	1.4305	531	652	18,832	15,106	3726	0.15
12	THF	7.52	1.405	528	618	18,939	16,077	2862.4	0.07
13	EtOH	25.30	1.3611	527	645	18,975	15,291	3684	0.03
14	n-3ol	20.80	1.385	534	644	18,727	15,244	3483	0.05
15	n-4ol	17.84	1.3988	530	637	18,868	15,552	3316	0.06
16	TFE	27.68	1.2907	557	691	17,953	14,306	3647	0.01

Table 1.4: The spectroscopic properties of D149, D102 and D131 in 12 organic solvents: maximum absorption and emission wavelengths (λ_{max}, in nm) and wavenumbers ($\bar{\nu}_{max}$, in cm^{-1})), Stokes shift ($\Delta\bar{\nu}$, in cm^{-1}) defined as the difference of maximum wavenumbers for absorption and emission, quantum yield Φ_{fluo}. The names of the solvents as well as their short names are listed in the same way as in table 1.3.

	Solvents	λ_{max}^{abs}	λ_{max}^{em}	$\Delta\bar{\nu}$	Φ_{fluo}	λ_{max}^{abs}	λ_{max}^{em}	$\Delta\bar{\nu}$	Φ_{fluo}	λ_{max}^{abs}	λ_{max}^{em}	$\Delta\bar{\nu}$	Φ_{fluo}
		D149				D102				D131			
1	5-ol	530	631	3169	0.094	488.5	610	4211	0.103	419	504	4373	0.0584
2	PC	538	649	3527	0.200	507	635	3976	0.134	415	515	4983	0.0717
3	g-Bl	538	645	3273	0.225	508	635	3937	0.141	418	529	5479	0.0543
4	ACN	526	640	3749	0.143	503	626	4182	0.150	457	611	5807	0.0304
5	MEOH	527	647	3684	0.005	497	617	4044	0.004	424	556	5923	0.0394
6	DMSO	542	651	3367	0.212	509	630	3972	0.233	430	558	5557	0.0686
7	DCM	540	629	2918	0.151	512	616	3531	0.106	467	602	5054	0.0688
8	CX	524	545	735	0.009	490	518	1103	0.004	453	528	3348	0.034
9	$CHCl_3$	552	627	2167	0.114	515	622	3644	0.163	470	600	4610	0.1097
10	TLN	539	582	1430	0.036	505	560	2008	0.031	462	535	3084	0.0362
11	DMF	532	652	3714	0.099	500	635	4375	0.054	418	521	5078	0.0732
12	THF	528	618	2913	0.094	501	597	3349	0.090	452	552	4313	0.0847

Along with polarity, the influence of hydrogen bonding (HB) donor ability of the solvent on the steady-state spectra is evident. Indeed, steady-state fluorescence of the solvents is considerably red shifted in alcohols, when compared to the aprotic solvents with similar and even higher dielectric constant (see tables 1.3 and 1.4). This means that the additional stabilization of the dye's excited state in the alcohols occurs, and this reduces of the energy level of the S_1 state. In the DSSCs, the efficiency of the electron injection from the dye in the S_1 state to the conduction band of the semiconductor is obviously dependent on the difference in energy between these two energy levels. Thus, the additional decrease of the the energy of the S_1 state due to the hydrogen bonding may be undesirable for the possible use of these dyes as sensitizers for the DSSCs. The marked spectral shift in the protic solvents may also suggest the possibility of difference in the excited state dynamics, offering other excited state relaxation pathways.

1.3 Theoretical and empirical dependence of the UV-Vis absorption and emission spectra on the solvent

Solvatochromism is the sensitivity of the UV-VIS absorption and fluorescence spectra to the polarity of the medium [37]. Inherently asymmetric molecules of organic indoline dyes are dipolar in nature, thus they are the subject to the dispersion and dipole-dipole interactions with the solvent molecules, the latter being the most important in polar solvents. The ground state of the molecule is stabilized by the solvent cage, preferentially oriented in order to minimize the total energy of the solvate. The change in the magnitude of the dipole moment is typical for the D-π-A systems upon the photo-excitation, giving the excited state with a greatly larger dipole moment. Thus, the solvent cage interaction with the dye is stronger in the excited state than in the ground state. With the polarity of the solvent, the relative difference between solute ground and excited states stabilization will become more and more appreciable, leaving less energy difference between the states. This decrease of the energy gap will induce an increase of the absorption wavelength, resulting in a red shift of the absorption band. The above explained effect is depicted in fig. 1.3a. For zwitterionic betaine Reichardt dye, the bathochromic shifts as large as 9730 cm^{-1} when going from nonpolar solvent diphenyl ether to polar solvent water were observed [37]. However, if the excited state is less stabilised with respect to the ground state, hypsochromic shift will be observed (cf. figure 1.3b). Thus, a complicated interplay of different factors that oppositely influence the energy levels of the ground and excited states will result in the particular characteristics of absorption spectrum.

As can be seen in figure 1.2, $S_0 \rightarrow S_1$ spectral band of D205 exhibits solvent dependence, while $S_0 \rightarrow S_2$ band doesn't show any significant shift. This may be rationalised as the electron density distributions in S_0 and S_2 states resulting in similar overall dipole moment of the molecule. Concerning the lowest transition, it is evident that the band shift is not monotonic with polarity. This is valid for all the indoline dyes, except for D131 dye (cf. fig. 1.4a). The D131 dye exhibits pronounced hypsochromic shift when polarity increases, while D149, D102 and D205 don't show significant correlation of the band position with polarity. The D131 absorption maximum blue shift means that the ground state is more stabilized by

polar solvents than the excited state (as in the case, described in fig. 1.3b). The sign of dipole moment change is still early to determine.

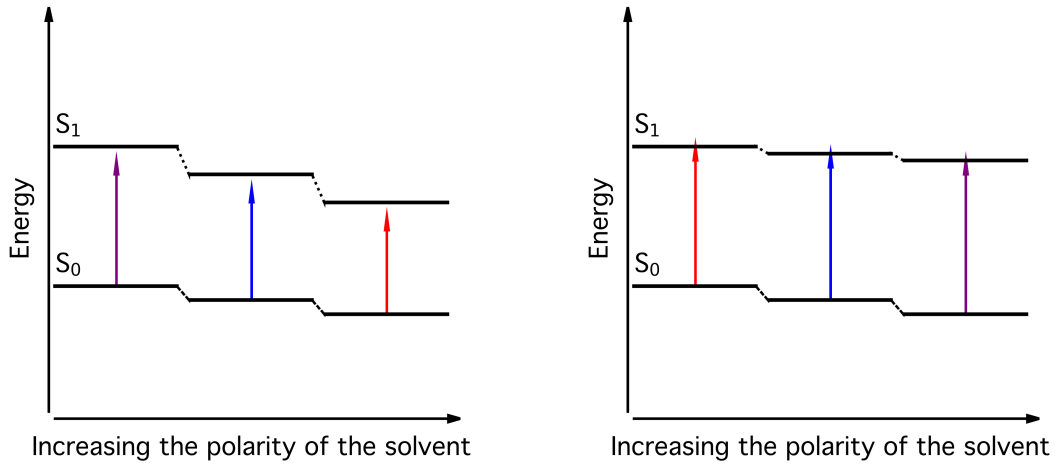

(a) (b)

Figure 1.3: Solvent polarity effect on the electronic levels relative energy, corresponding to (a) bathochromic and (b) hypsochromic shift of absorption spectrum.

Concerning the weak dependence of D149, D102 and D205, it can be explained by small dipole moment in the ground state and the mutual cancelling of solvent effect on the energy of ground and excited states. The small dipole moment in the ground state may be responsible for the weak effect of polarity on absorption spectra, as the randomly oriented solvent cage will have almost the same stabilising influence on both small and high dipole moments of ground and excited states.

Thus, steady-state fluorescence spectra were measured to acquire further information about the transitions in indoline derivatives. Emission spectra bathochromic shift must be more pronounced, as in the case of conventional organic solvents the solvent relaxation time is much shorter than the fluorescence lifetime of the first excited state. By the solvent relaxation we understand the reorganisation of the solvent cage around the excited chromophore in response to the fast perturbation caused by the quasi-instantenous change of the dipole moment of the dye upon the photo-excitation. As was shown in the works of Maroncelli[38], the solvation dynamics in common organic solvents occurs on the timescale of picoseconds, thus, the process is expected to be much faster than the typical nanosecond scale of spontaneous emission. Later in this work, it will be shown that it is not always the case for indoline dyes.

The emission maxima dependence on polarity are shown in figure 1.4b. One can see the important change in the correlation with polarity. Firstly, the D131 shift is still hypsochromic, but the slope is smaller. Secondly, D102, D149 and D205 show again very similar behaviour, the fluorescence of the first is blue-shifted. Thirdly, the D102, D149 and D205 show a very rapid increase of the fluorescence maximum wavelength in the solvents of weak polarity, reaching the plato, starting from the region, corresponding to the dielectric constant of 10. While these plots are not shown in energy scale, they already give a hint about the important and

fast (comparatively to the fluorescence lifetime) excited state evolution after the photo-excitation. Thus, before the molecule of the dye emits a photon, the energy of the excited stated decreases a lot due to solvation, and the fluorescence spectra show a bigger solvatochromic shift than the absorption spectra.

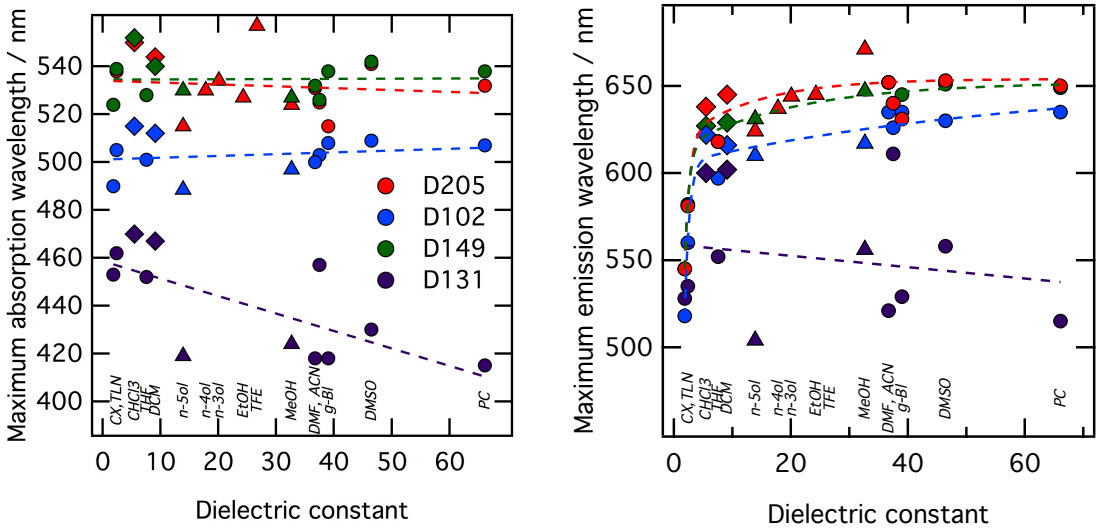

(a) (b)

Figure 1.4: Maximum absorption (a) and emission (b) wavelengths for $S_0 \rightarrow S_1$ transition for D205, D149, D102 and D131 indoline dyes in function of the dielectric constant of the solvent. The alcohols are shown as triangles, halogenated solvents as diamonds and aprotic solvents as circles. Regressions are shown as dashed lines, representing the general correlation with polarity of the solvent.

The difference between absorption and emission energy is called the Stokes shift. The theoretical dependence of Stokes shift on polarity of the solvent can be described by Lippert-Mataga equation 1.1. The derivation of this equation can be found in the book [39, see p.210]. This equation was derived for the fluorophore molecule in the solvent, modeled as a dielectric continuum, where only dipole-dipole and dispersion interactions are taken into account. Thus, the deviation from the Lippert plots means that specific solvent-solute interactions (like hydrogen bonding and electron pair acceptor/donor) or charge-transfer states may play a role.

$$\begin{aligned} \bar{\nu}_A - \bar{\nu}_F &= \frac{1}{4\pi\epsilon_0}\frac{2}{hc}\Delta f \frac{(\mu_E - \mu_G)^2}{a^3} + const, \\ \Delta f &= \left(\frac{\epsilon - 1}{2\epsilon + 1} - \frac{n^2 - 1}{2n^2 + 1}\right), \end{aligned} \tag{1.1}$$

where ϵ and n are the dielectric contant and the refractive index of the solvent, h is the Planck constant, c is the speed of light and a is the radius of the spherical cavity where the fluorophore resides.

When this theory is supported by the experiment, the change of the dipole moment of the dye upon the excitation can be estimated. The Lippert plots for D131, D102, D149 and D205 indoline dyes are shown in figure 1.5. As one can see,

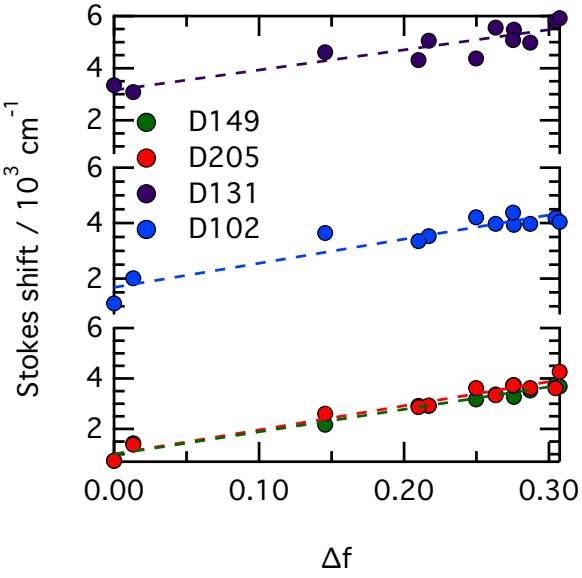

Figure 1.5: Lippert-Mataga plots for D102, D131, D149 and D205 organic dyes.

the plots show that the theory describes the systems under consideration reasonably well.

The positive slope of the Lippert-Mataga plots means that the excited state dipole moment magnitude is higher than the one of the ground state. Also, the linear regressions are almost parallel for all the dyes, so the ratio of change of the dipole moment to the cube of cavity radius must be similar.

The spherical cavity radii were calculated with Gaussian16 software [40] at M06HF/6-31G level of theory. The geometries were optimised and no negative frequencies were found. The volume keyword was used in order to calculate the volume inside a contour of 0.001 electrons/Bohr^3 density. The mean of 20 calculations was taken to calculate a radius, since a Monte-Carlo integration is used. Using the equation 1.1, we calculated the dipole moment changes for the D205, D149, D102 and D131 dyes (table 1.5). The dipole moment changes increase in the following order: D131<D102<D149<D205.

Table 1.5: Lippert plot slopes for D131, D102, D149 and D205 dyes, cavity radii calculated using Gaussian 16 programming package with M06HF/6-31G level of theory, calculated dipole moment changes using eq 1.1.

Dye	Slope	a, Å	$\Delta\mu$ / D	Dye	Slope	a, Å	$\Delta\mu$ / D
D131	7730.3	5.8705	12.46	D149	8934.3	6.456	15.45
D102	8723.2	6.1405	14.16	D205	9572.8	6.644	16.70

Along with the theoretically modelled solvent dependence, empirical solvent scales are frequently used. The two very successful ones proposed to understand the solvent role in dye solutions steady-state spectra are Catalan [41] and Kamlet-Taft [42] scales.

The Catalan scale is a general, multiparameter scale, designed to split the general dipolarity SP, polarisability SdP and specific acidity SA, basicity SB solvent scales. According to this approach, the solvent-dependent property can be modelled as

shown in eq. 1.2.

$$A = A_0 + b\mathrm{SA} + c\mathrm{SB} + d\mathrm{SP} + e\mathrm{SdP} \tag{1.2}$$

These characteristics are originally considered orthogonal to each other by the authors. The main improvement of this scale is the separation of the solvent effects in four distinct scales, evaluated by the analysis of steady-state spectroscopy data of judicially chosen probes. Thus, we tried to use Catalan scale to extract the information about the impact of different interactions on the steady-state spectra of indolines. The results of multivariate regression analysis are presented in table 1.6 . The analysis was performed for 12 solvents for n=1-12 (cf. table 1.3), using Igor pro programming package. The determination coefficients were also calculated and presented. The quality of fit can be examined using the coefficient of determination R^2, provided in the table.

As it can be seen, the Catalan solvent scale completely fails to explain the steady-state absorption and emission spectra of D131 and gives poor result for D205 absorption in organic solvents. Acceptable results were obtained for absorption of D102 and D149 and for emission of D102, D149 and D205. The determination coefficients are the best for the Stokes shift analysis (0.894, 0.95, 0.98 and 0.95). As the contributions of Catalan scale are normalized, the examination of the relative weight of the parameters of the fit can give an idea about the relative importance of the types of dye-solvent interactions.

Absorption spectra of D102, D149 and D205 are primarily affected by the polarisability of the solvent, which shifts the spectra to the red. Dipolarity, acidity and basicity of the solvent play a significant role, but to a much lesser extent. Only basicity component shifts the spectra to the blue. The situation about the fluorescence spectra is drastically different: the role of polarisability is smaller, while the dipolarity becomes a dominant factor, that also causes the red shift of the spectrum. Acidity of the solvent also shifts the spectrum to the red, and its contribution is slightly higher than for the absorption spectra. The effect of the basicity of the is less pronounced, turning even negative for D149.

The Stokes shift represents the relaxation energy of the excited state. It is important to understand that in ideal case, the parameters of the fit of the Stokes shift solvent dependence can be calculated in the same way as the Stokes shift itself: $p_\Delta = p_{abs} - p_{em}$. This is rather close to the result, shown in table 1.6. Thus, higher dipolarity of the solvent results in higher Stokes shift. This result is in a perfect accordance with Lippert-Mataga equation (cf. eq. 1.1), in case that in excited state the dipole moment is higher comparatively to the ground state. On the contrary of the dipolarity, the polarizability term is negative, hinting that the dispersion interaction is more significant in the ground state than in the excited state. The acidity and basicity contributions are also significant, but to less extent than the former two. For D131 dye, they seem to be less important than for the other dyes. As for D102 and D149, the basicity influence is higher than that of the acidity and stabilises more the excited state than the ground state. The same relative stabilisation is observed for D205. For D205, the acidity has the same stabilisation effect as basicity, but of higher magnitude. On the contrary, for D149 and D102 the sign of acidity contribution is negative, but the magnitude of the parameter is smaller than the uncertainty, like for D131. This suggests that the acidity influence must be similar on excited and ground states of D131, D102 and D149.

Table 1.6: Multivariate regression analysis of steady-state spectral data using Catalan solvent scale. All values are given in 10^3 cm^{-1}. The values of SA, SB, SP and SdP, used in the fit, are taken from [41].

	A_0	b_{SA}	c_{SB}	d_{SP}	e_{SdP}	R^2
			D131			
$\bar{\nu}_{abs}$	20±4	0.7±1.8	1.6±1.2	1.5±5.8	1.2±1.1	0.41
$\bar{\nu}_{em}$	15±5	0.3±2	1.4±1.3	3.7±7	-1.3±1.3	0.2
$\Delta\bar{\nu}$	4.7±1.5	0.3±0.6	0.2±0.4	-2.5±2	2.5±0.4	0.89
			D102			
$\bar{\nu}_{abs}$	22.22 ± 0.61	-0.24 ± 0.34	0.87 ± 0.20	-2.96 ± 0.84	-0.67 ± 0.15	0.89
$\bar{\nu}_{em}$	20.7±2.1	-0.6±1.2	0.06 ± 0.69	-2.8±2.9	-3.18 ± 0.52	0.88
$\Delta\bar{\nu}$	2.59±1.39	-0.21 ± 0.76	1.39 ± 0.48	-2 ± 1.9	2.50 ± 0.33	0.95
			D149			
$\bar{\nu}_{abs}$	22.07 ± 0.60	-0.85± 0.33	0.54 ± 0.20	-4.61 ± 0.83	-0.16 ± 0.15	0.86
$\bar{\nu}_{em}$	19.50 ±1	-0.74 ± 0.56	-0.37 ± 0.33	-2 ± 1	-2.76 ± 0.25	0.97
$\Delta\bar{\nu}$	3.01 ± 0.64	-0.29 ± 0.35	0.87 ± 0.21	-3.22 ± 0.87	2.67 ± 0.16	0.98
			D205			
$\bar{\nu}_{abs}$	21.5 ± 1.5	-0.55 ± 0.82	0.85 ± 0.48	-3.8 ±2.0	-0.17 ± 0.37	0.53
$\bar{\nu}_{em}$	19.5 ± 1.5	-1.72 ± 0.83	0.14 ± 0.49	-2±2	-2.79 ± 0.37	0.93
$\Delta\bar{\nu}$	2 ±1	1.17 ± 0.61	0.71 ± 0.46	-1.7 ± 1.3	2.62 ± 0.28	0.96

The influence of the solvent dipolarity, polarisability and basicity for all the four dyes is similar. It can be rationalised in the following way : (i) positive influence of the dipolarity of the solvent, representing the dipole-dipole interaction, confirms the higher dipole moment in the excited state than in the ground state; (ii) negative influence of the polarisability of the solvent, representing the dispersion interaction suggests a dominant role of donor moiety in this interaction, as the electron density on the electron rich phenyl rings is transferred to the acceptor moiety of the dye upon the excitation; (iii) positive influence of the basicity of the solvent, representing the hydrogen bonding interaction where the donor is the dye, is possibly due to the polarisation of O–H bond of carbonyl group upon the photoexcitation.

While the Catalan solvent scale was elaborated by one group, using a restricted number of selectively sensitive organic probes, Kamlet-Taft solvent scale is an example of the solvatochromic scale that is made by gathering values from different laboratories and scientific teams. The data on the solvents were taken from [43]. Originally 7-term equation, the mathematical form of the relation of the solute property A was reduced to the form, presented in eq. 1.3 [42].

$$A = A_0 + a\alpha + b\beta + s\pi^* \tag{1.3}$$

In this scale, α, β and π^* are the hydrogen bond donor ability, hydrogen bond acceptor ability and polarity/polarisability of the solvent, respectively. The adjustable parameters A_0, a, b, s represent the solute property in the gas phase and the sensitivity of this property to the corresponding solvent effect. Again, using multivariate regression analysis, Kamlet-Taft solvent scale was applied in order to discern the solvent effects on D131, D102, D149 and D205 steady-state UV-Vis absorption and emission spectra. The results are presented in table 1.7.

The dependence of steady-state absorption spectra of D131, D102, D149 and

Table 1.7: Multivariate regression analysis of steady-state spectral data using Kamlet-Taft solvent scale. All values are given in cm^{-1}. The values of α, β and π^*, used in the fit, are taken from [42].

	A_0	a_α	b_β	c_{π^*}	R^2
			D131		
$\bar{\nu}_{abs}$	21282±775	1.8 ± 5	18.3 ± 8.7	9.1 ± 11	0.41
$\bar{\nu}_{em}$	18308 ± 865	-7.9 ± 6	11 ± 9.9	-11.6 ± 12.3	0.23
$\Delta\bar{\nu}$	2975.2 ± 412	9.7 ± 3	7.4 ± 4.7	20.8 ± 5.8	0.76
			D102		
$\bar{\nu}_{abs}$	20321 ± 128	-0.70 ± 1.65	8.04 ± 2.05	-11.67 ± 2.05	0.84
$\bar{\nu}_{em}$	19100 ± 438	-12 ± 6	-0.83 ± 7.01	-37.8 ± 7.02	0.85
$\Delta\bar{\nu}$	1220 ± 401	11 ± 5	8.88 ± 6.42	26.20 ± 6.44	0.84
			D149		
$\bar{\nu}_{abs}$	18966 ± 222	-0.98 ± 2.86	5.53 ± 3.55	-7.26 ± 3.55	0.41
$\bar{\nu}_{em}$	18327 ± 270	-9 ± 3	-5.89 ± 4.33	-31.52 ± 4.34	0.93
$\Delta\bar{\nu}$	638 ± 373	8 ± 5	11 ± 6	24.57 ± 5.98	0.85
			D205		
$\bar{\nu}_{abs}$	18996 ± 293	-0.8 ± 3.8	9.4 ± 4.7	-8.02± 4.71	0.44
$\bar{\nu}_{em}$	18360 ± 326	-15 ± 4	-0.79 ± 5.22	-33.87 ± 5.23	0.89
$\Delta\bar{\nu}$	636 ± 381	14 ± 5	10 ± 6	25.85 ± 6.11	0.87

D205 is described by the Kamlet-Taft solvent scale less correctly, as it can be judged by the determination coefficient values in table 1.7. However, the determination coefficient is also the best for the Stokes shift values (0.76, 0.84, 0.85 and 0.87). Also, the fluorescence band positions of D102, D149 and D205 are described reasonably well. Importantly, this scale gives similar results as Catalan concerning the relative importance of the solvent effects on the spectra. Indeed, the polarity/polarisability of the solvent induces the bathochromic shift of the emission spectrum of the indoline dyes, just as both SP and SdP of Catalan scale. The acidity of the solvent plays more pronounced role than the basicity of the solvent.

Stokes shift values of all the four dyes increase with the solvent basicity, acidity and polarity/polarisability. This result is in accordance with the Catalan analysis, the polarisability being a component of π^* value. In contrast to the Catalan, where the basicity is more important than the acidity contribution, Kamlet-Taft parameters of fit suggest their similar effect for all dyes. The contamination of π^* contribution by the acidity of the solvent, suggested in literature, could explain this fact, as the acidity, partly taken into account by π^* , will make less contribution to the overall shift. The latter π^* contribution remains dominant on Stokes shift solvent dependence. Interestingly, its weight is nearly the same for D102, D149 and D205, but lower for D131. This must be linked to the change of the dipole moment upon the photo-excitation of the dye. The gas phase Stokes shift increases in the row D205 $\simeq$D149<D102<D131. The gas phase Stokes shifts are very different for Kamlet-Taft and Catalan multivariate regression analyses.

1.4 Quantum calculations on the indoline dyes

As a complementary method of research, quantum chemistry calculations were coupled with the spectroscopic study of the dyes in order to help the interpretation of the results. The nature of electronic transitions in the studied systems and the dependence of their energy on environment are important for understanding.

DFT functionals were chosen for calculations, as the ones showing the best time/performance ratio for aromatic molecules. Truhlar group functional M06HF with 6-31G basis set were chosen to calculate the geometry and visualise the frontier orbitals. Further, TD-DFT calculations of D149 were performed with B3LYP, PBE0, M062X, M06HF, M05, MN15 and wB97XD functionals with 6-31+G(d) basis set.

1.4.1 The frontier orbitals of indoline dyes

The change in the dipole moment of indoline dyes, strongly suggested by the solvatochromism analysis, is directly linked to the redistribution of the electron density localisation upon the photo-excitation. Thus, the molecular orbitals that are possibly taking part in the $S_0 \rightarrow S_1$ transition, i.e. highest occupied (HOMO), second highest occupied (HOMO-1), lowest unoccupied (LUMO) and the second lowest unoccupied (LUMO+1) orbitals are visualised and then presented in figure 1.6. Indeed, the electron density is located on triphenylethylene, indoline and one rhodanine ring moieties on HOMO and is transferred to rhodanine rings on LUMO. The character of HOMO-1 and LUMO+1 is less pronounced but similar to HOMO and LUMO. Hence, intramolecular charge transfer is expected in D205 dye. The octyl chain is not involved in the transition, which is normal due to its saturated nature. This octyl chain only results in some spacing between the semiconductor and the dye, reducing the probability of charge recombination. Importantly, the electron density, although flowing from donor to acceptor, doesn't go directly to the anchor group, –COOH. This may decrease the potential of D205 as a sensitiser for DSSCs.

The characteristics of D149 orbitals are similar to D205 ones due to their structural analogy (cf. fig. 1.7). Upon the photo-excitation, the electronic density flows from donor to acceptor moieties of the molecule.

D102 molecule has only one rhodanine ring, compared to D149 and D205 dyes. Because of that, its π-system is less extended and the absorption and emission spectra are shifted to the blue. The orbitals for this dye are shown in figure 1.8. Probably because of the presence of only one rhodanine ring, the acceptor moiety is weaker and the charge transfer character is less pronounced in LUMO+1. Also, –COOH group doesn't participate in the significant molecular orbitals.

D131 dye doesn't contain rhodanine rings, but this dye has a –C≡N group, which is a very strong acceptor. One can see the pronounced charge transfer between HOMO and LUMO orbitals (cf. fig. 1.9). As for the D102 dye, the LUMO+1 doesn't represent interest anymore for a dye → semiconductor electron transfer, as the electron density is located on tri-phenyl ethylene moiety.

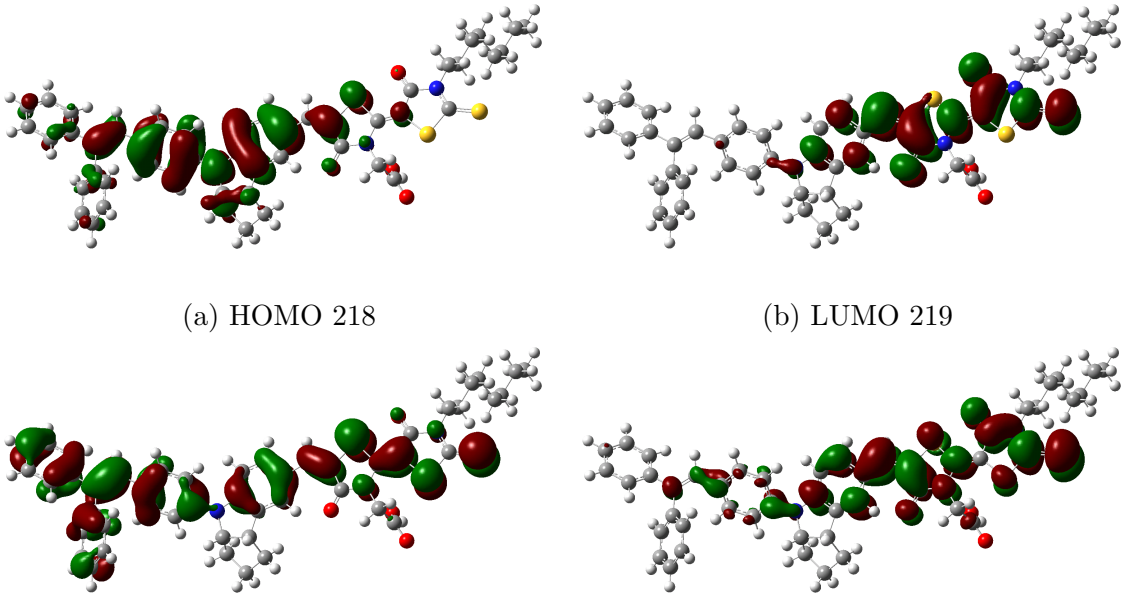

(a) HOMO 218 (b) LUMO 219

(c) HOMO-1 217 (d) LUMO+1 220

Figure 1.6: D205 orbitals, calculated with M06HF/6-31G level of theory. Isovalue=0.02 was used to visualise the isosurfaces of electron density.

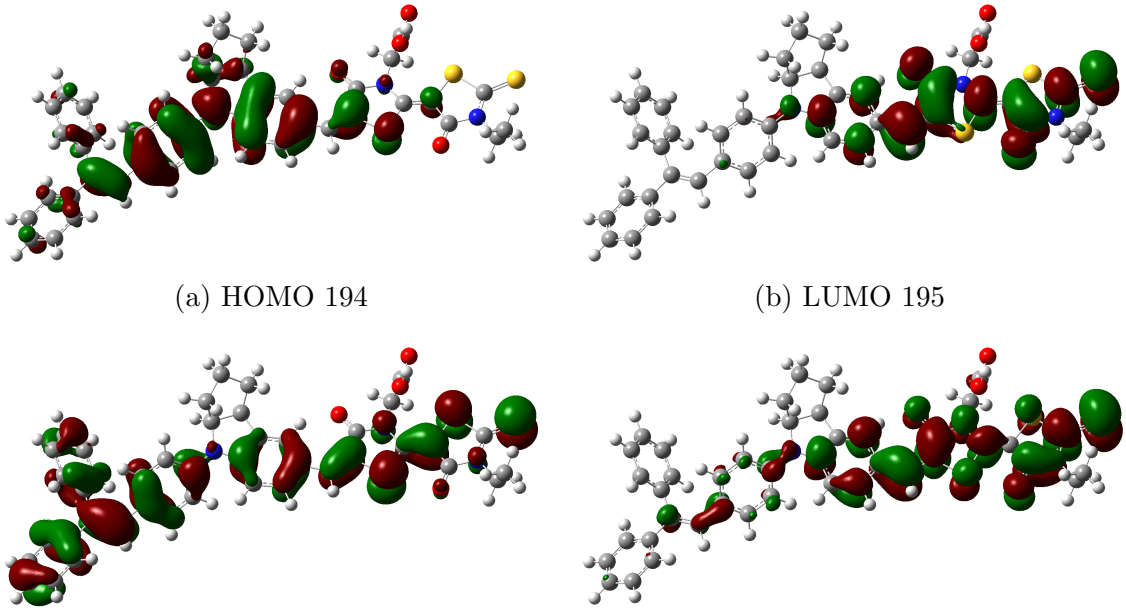

(a) HOMO 194 (b) LUMO 195

(c) HOMO-1 193 (d) LUMO+1 196

Figure 1.7: D149 orbitals, calculated with M06HF/6-31G level of theory. Isovalue=0.02 was used to visualise the isosurfaces of electron density.

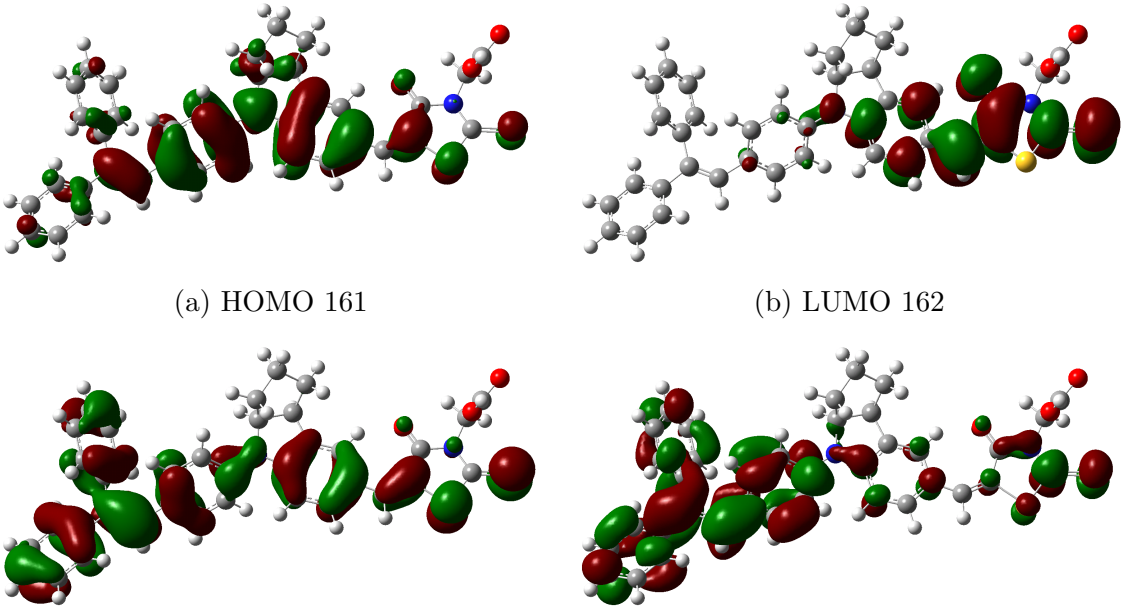

(a) HOMO 161 (b) LUMO 162

(c) HOMO-1 160 (d) LUMO+1 163

Figure 1.8: D102 orbitals, calculated with M06HF/6-31G level of theory. Isovalue=0.02 was used to visualise the isosurfaces of electron density.

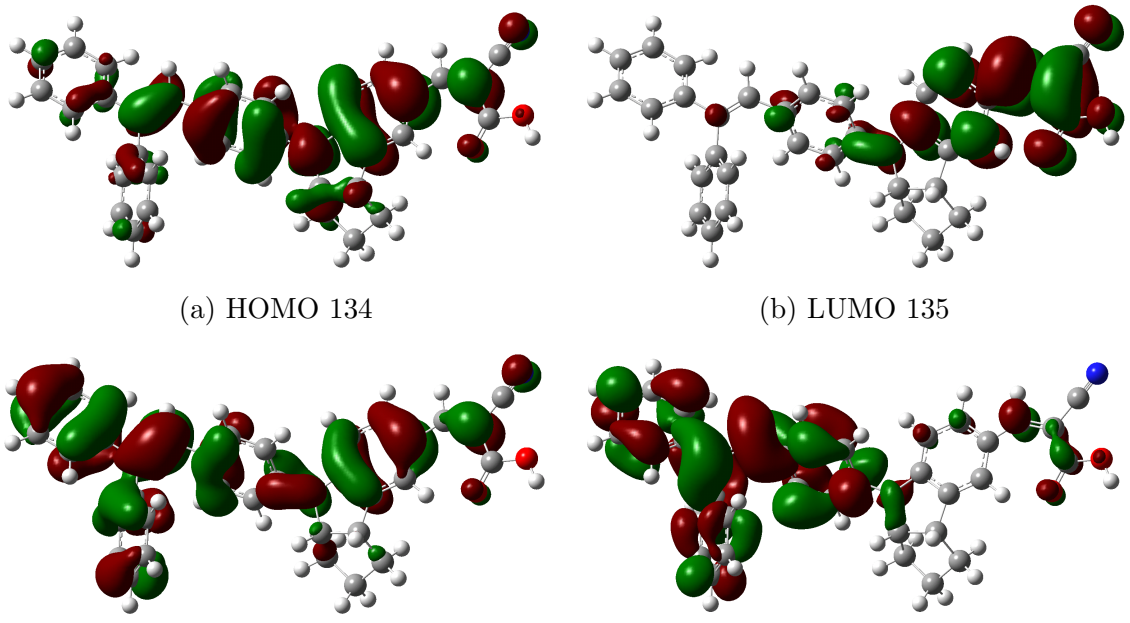

(a) HOMO 134 (b) LUMO 135

(c) HOMO-1 133 (d) LUMO+1 136

Figure 1.9: D131 orbitals, calculated with M06HF/6-31G level of theory. Isovalue=0.02 was used to visualise the isosurfaces of electron density.

1.4.2 Absorption spectra of D149 dye: the comparison of theory and experiment

Quantum calculations of the absorption spectra is a promising tool for the design of new dyes for solar cells, enabling to predict the way to tune the structure of the

aromatic compound in order to cover the maximum of the solar spectrum or its needed part (this may be important for the applications in the smart city design). However, the structures with a pronounced charge transfer upon excitation were shown problematic for the TDDFT method [44]. Therefore, the choice of appropriate functional and basis set are important to obtain helpful results. In this section, we will compare the results of B3LYP, PBE0, M062X, M06HF, M05, MN15 and wB97XD functionals with experimental data on D149 dye. The chosen solvents for the study were: cyclohexane, dimethyl sulfoxide, methanol, acetonitrile, tetrahydrofuran and 1-pentanol. As the experimental energies solvent dependence is weak, no significant shift in calculated energies is expected.

In order to use the computational resources rationally, we computed the geometry of the D149 with M06HF functional and 6-31+G(d) basis set, using PCM to account implicitly the solute-solvent interaction. Then, different functionals were used to calculate the vertical excitation energies, using the linear response correction methodology proposed by Guido and Caprasecca [45]. The results are shown in fig. 1.10.

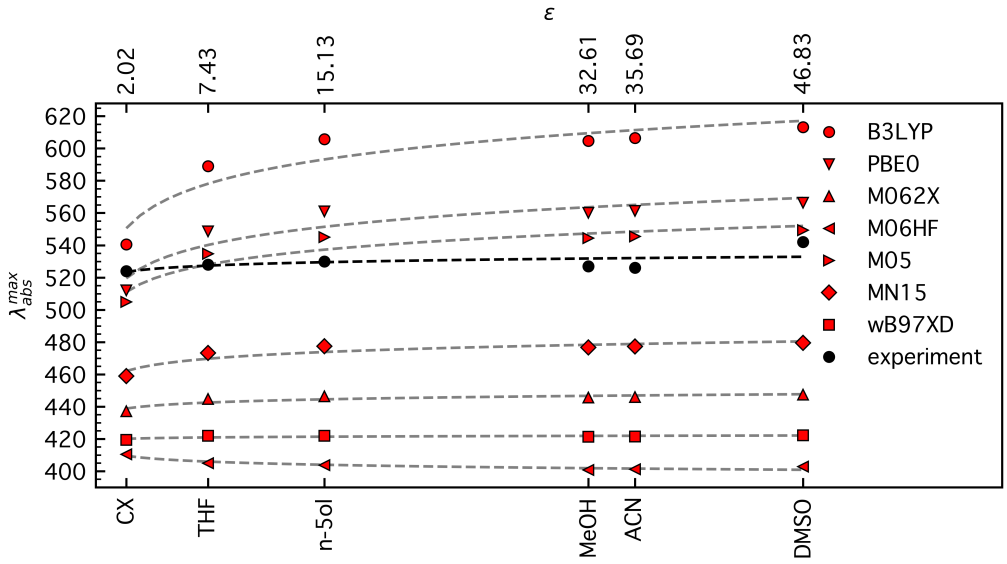

Figure 1.10: The excitation energies of D149 in cyclohexane, dimethyl sulfoxide, methanol, acetonitrile, tetrahydrofuran and 1-pentanol calculated with DFT functionals and 6-31+G(d) basis set. The experimental data on maximum of absorption of D149 is given for comparison.

An important comment to be made on the result. When different functionals are used for the theoretical description of D149, a shift by more than 200nm in calculated excitation energy is observed. This signature is completely different from what is observed for cyanine dyes: their transition energies are insensitive to the selection of a specific exchange-correlation functional[46]. The percentage of the exact exchange in these hybrid functionals is proportional to the calculated excitation energy of D149 in a given solvent. Thus, it is of crucial importance to be aware of this effect and to take it into account when choosing the theory for the computational design of new organic sensitisers for DSSCs.

Therefore, the best result was obtained when M05 functional was used. In

literature, this functional was also cited as the one giving excitation energies close to the experimental values [16].

1.5 Fluorescence quantum yield of indolines and its dependence on the solvent

The fluorescence quantum yield is the fraction of molecules in excited state that relax to the ground state, emitting a fluorescence photon[47]. It can be expressed using the rate constants of fluorescence and the rest of the processes that lead from excited to the ground state (eq. 1.4).

$$\Phi_{fluo} = \frac{k_r^S}{k_r^S + k_{nr}^S} \tag{1.4}$$

The fluorescence quantum yield is of great importance in the photophysics. It represents the relative weight of alternative de-excitation pathways, and its dependence on the solvent properties can hint about the character of these pathways. One elegant example is the study of the acridine fluorescence quantum yield in water micellar solutions [48]. As it is known, acridine doesn't fluoresce in aprotic organic solvents, while in protic solvents, water and acidic solutions it shows blue and green fluorescence, respectively. Thus, it was concluded that only the complexes of excited acridine can fluoresce, while the others cannot. This fact was used in the article to quantify the contact of acridine and water molecules in function of concentration of the surfactant. In the similar way, the study of the solvent dependence of indoline dyes Φ_{fluo} can help to understand their photophysics and propose the pathways of the de-excitation.

The quantum yields of D131, D102, D149 and D205 were measured using the reference method. With this method, the reference compound absorption and emission spectra must be measured in addition to those of the studied compound. The compilations of quantum yields of reference compounds are published (e.g. [35]). Importantly, the fluorescence spectra of the reference and the studied compounds must be in the same spectral window and the concentration of the samples must be low (OD<0.1) to avoid self-absorption effects. Finally, all the requirements being satisfied, the quantum yield of the studied compound was calculated using the equation 1.5.

$$\begin{aligned}\Phi_{sample}^{fluo}(\lambda_{exc}) = &\Phi_{ref}^{fluo}(\lambda_{exc}) \frac{\int_0^\infty I_{sample}^{fluo}(\lambda_{exc};\lambda_{fluo})\mathrm{d}\lambda_{fluo}}{\int_0^\infty I_{ref}^{fluo}(\lambda_{exc};\lambda_{fluo})\mathrm{d}\lambda_{fluo}} \\ &\frac{1-10^{-A_{ref}(\lambda_{exc})}}{1-10^{-A_{sample}(\lambda_{exc})}} \frac{n_{solv,sample}^2}{n_{solv,ref}^2}\end{aligned} \tag{1.5}$$

Nile Blue in methanol ($\Phi_{fluo} = 0.27$, for D102, D149 and D205) and C153 in ethanol ($\Phi_{fluo} = 0.38$, for D131) were used as standards [35]. The results are presented in tables 1.3 and 1.4. The dependence of fluorescence quantum yield on the solvent's dielectric constant is shown in figure 1.11. The following conclusions can be made from this figure: (i) Φ_{fluo} is linearly dependent on dielectric constant for aprotic solvents; (ii) Φ_{fluo} in halogenated solvents forms a stand-alone group (iii) Φ_{fluo} in

alcohols is much weaker than in the other solvents. The quantum yield is inversely proportional to the acidity of the solvent, distorting the apparent correlation to the dielectric constant (fig. 1.11). The relatively small quantum yield of the dyes also can be linked to the floppy structure of these compounds. Indeed, the parts of these large molecules are linked by single bonds, and this creates extensive conformational flexibility. Furthermore, the character of the double bond, connecting the indoline and the rhodanine moieties, may change upon the photoexcitatiion (cf. fig. 1.6a and fig. fig: LUMO219). Therefore, this bond may allow rotation about this bond-axis when the molecule is in its excited state.

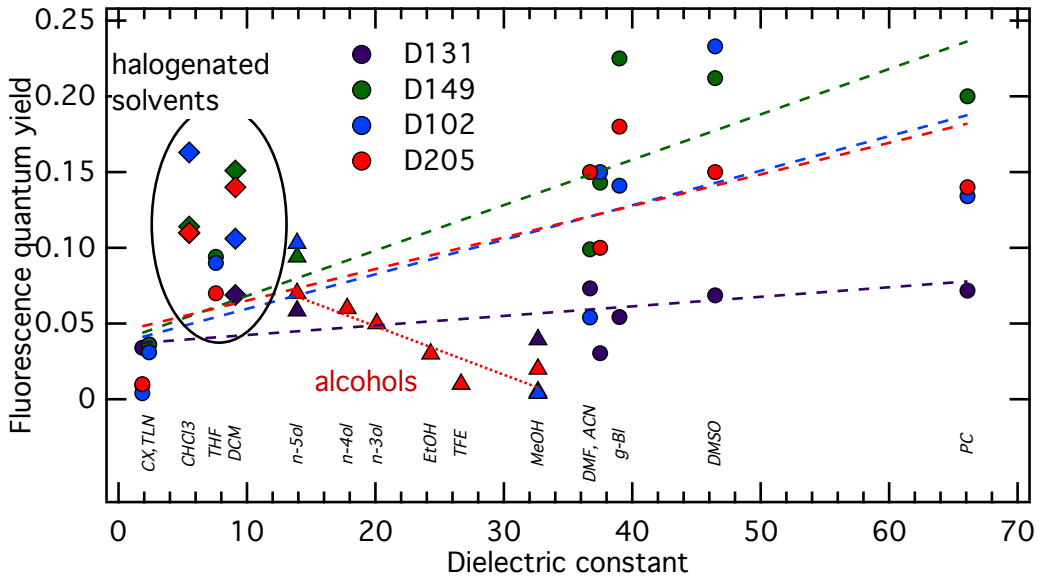

Figure 1.11: Fluorescence quantum yields of D102, D131, D149 and D205 organic dyes in function of dielectric constant of the solvent.

In order to figure out the dependence of quantum yield on the specific characteristics of the environment, the Catalan solvent scale, completed by the viscosity parameter was applied to the analysis. Theoretical quantum yields were modelled according to eq. 1.6. The results are given in table 1.8.

$$\Phi_{fluo} = \Phi_{fluo,0} + b * SdP + c * SP + d * SA + e * SB + f * \eta \qquad (1.6)$$

Table 1.8: Multivariate regression analysis of fluorescence quantum yield using the modified Catalan solvent scale.

	D131	D102	D149	D205
$\Phi_{fluo,0}$	0 ± 0.1	0 ± 0.06	0 ± 0.03	0 ± 0.02
b, SdP	0.015 ± 0.03	0.12 ± 0.08	0.19 ± 0.04	0.07 ± 0.04
c, SP	0.05 ± 0.13	0.04 ± 0.1	-0.01 ± 0.06	0.083 ± 0.06
d, SA	-0.04 ± 0.04	-0.17 ± 0.1	-0.22 ± 0.06	-0.16 ± 0.03
e, SB	0.02 ± 0.03	-0.06 ± 0.10	-0.1 ± 0.05	-0.046 ± 0.03
f, η	0.001 ± 0.008	0.03 ± 0.02	0.04 ± 0.01	0.027 ± 0.008
R^2	0.68	0.71	0.90	0.89

The determination coefficient R^2 values are lower for the D131 and D102 dyes than for the other two studied indolines. The results of this analysis confirm the observations, made from the graphic presentation of the dependence of Φ_{fluo} on the dielectric constant (fig. 1.11). Indeed, the increase in the dipolarity and in the polarisability of the solvent makes Φ_{fluo} of all the dyes higher, while the basicity and the acidity of the solvent weaken the fluorescence of D102, D149 and D205. Considering the correlation of Φ_{fluo} with the viscosity η, an influence of the dye's structure is clear: the parameter of fit f, η parallels the increase of the size of the molecule: D131<D102<D149<D205.

1.6 Excitation emission matrices of indoline dyes in protic and aprotic solvents of similar polarity

The excitation emission matrices (EEMs) of D131, D102, D149 and D205 dyes were recorded with the purpose to check if such complex molecules would obey the Kasha's rule. As it was mentioned above, the latter stipulates that the fluorescence occurs only from the lowest singlet excited state, as the internal conversion and the vibronic relaxation from S_n to S_1 state is quasi-instantaneous. This measurement is a very important step to take when doing the investigation of the photodynamics of new dyes.

The experimental results are presented in fig. 1.12 and in fig. 1.13 as colormaps. As one can see, no emission from S_2 state is observed at this sensitivity level and thus the Kasha's rule is fully respected. Also, the emission spectra overlap for all the excitation wavelength with non-negligible absorbance, and all the excitation spectra overlap for all the emission wavelengths with non-negligible emission, so the dye molecules under investigation are perfectly in the scope of these photochemistry laws.

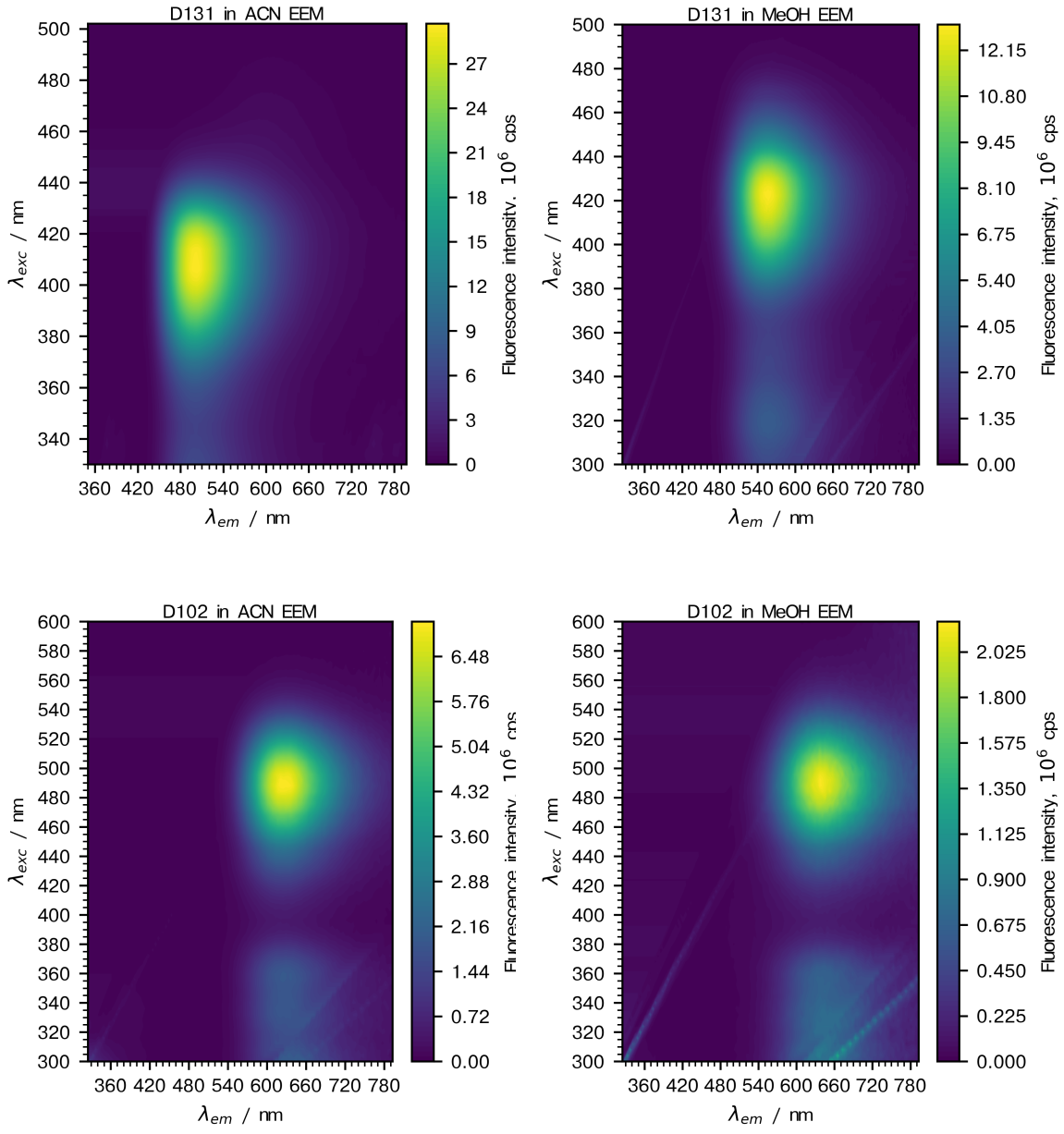

Figure 1.12: D131 and D102 EEM. The signal was corrected for the detector sensitivity and monochromator efficiency in excitation and emission.

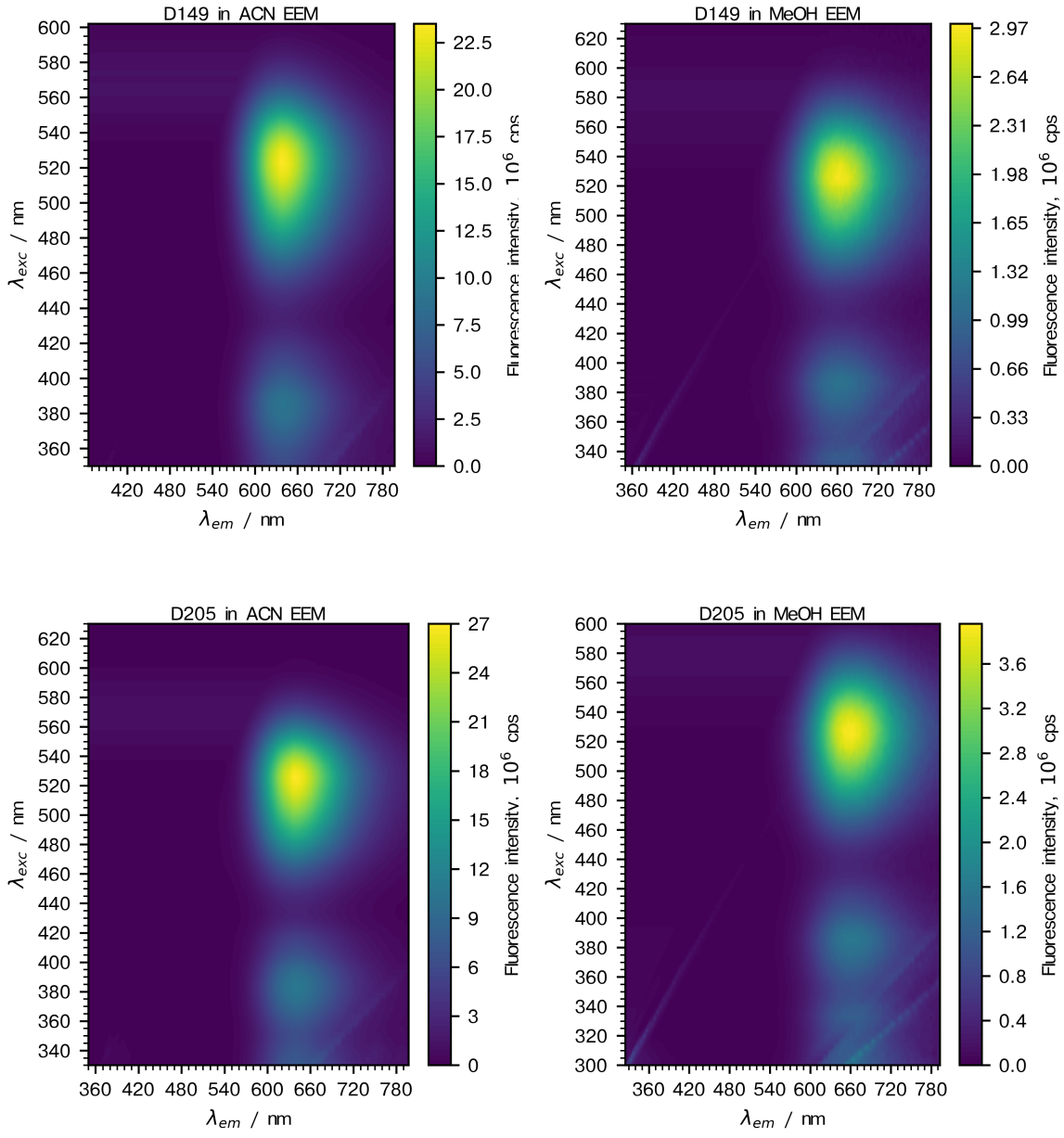

Figure 1.13: D149 and D205 EEM. The signal was corrected for the detector sensitivity and monochromator efficiency in excitation and emission.

Conclusions

In this chapter, the steady-state absorption and fluorescence spectroscopy measurements and quantum chemistry calculations were performed to investigate the solvent effect on the electronic transitions in D131, D102, D149 and D205 molecules.

Significant increase of dipole moment within the excitation was confirmed by Stokes shift dependence on solvent polarity and quantum calculations. Lippert-Mataga equation permitted the calculation of dipole moment change, 12.5D for D131, 14.1D for D102, 15.5D for D149 and 16.7D for D205. Within the excitation, electron density moves from donor tri-phenyl ethylene and indoline to acceptor rhodanine rings or cyanide group, in case of D131 dye. On the other hand, small dipole moment of these molecules in ground state was indicated by weak solvent dependence of the absorption spectra.

Detailed multivariate regression analysis of steady-state data applying Kamlet-Taft scale showed that polarity π^* and HB donor ability α of the solvent are the key properties that cause a red-shift of the emission spectra. Fluorescence quantum yield measurements confirm the importance of specific interactions (hydrogen bonding) on the photophysics of indoline dyes. Indeed, halogenated solvents and alcohols show distinct character of Φ_{fluo} dependence on the solvent's dielectric constant.

Along with Kamlet-Taft, Catalan solvent scale was also applied. A better description of experimental data is pointed by determination coefficients, closer to unity. Additionally, the separation of dipolarity and polarisability contributions is significant in the solvent effect interpretation for D102, D149 and D205 dyes: while the former was found to be insignificant for absorption band position but cause a red shift of emission band, the latter was found to be insignificant for emission but cause a red shift of absorption band. Thus, the dipolarity of the solvent is increasing the Stokes shift, but the polarisability has an opposite effect. The last observation was made for all indoline dyes studied in this work. Concerning the hydrogen bonding effect, Catalan multivariate regression analysis confirms the result achieved with Kamlet-Taft: HB donor ability and HB acceptor ability cause bathochromic and hypsochromic shifts of steady-state spectra, respectively. The HB donor and acceptor abilities of the solvent decrease the quantum yield of D102, D149 and D205, but have no effect on D131. Dipolarity and polarisability increase the Φ_{fluo} of all indoline dyes. Viscosity of the solvent has little effect on Φ_{fluo} of D131, but increases that of D102, D149 and D205. The summary of the solvent effects on D102, D149 and D205 absorption and emission spectra as well as Φ_{fluo} is depicted in fig. 1.14.

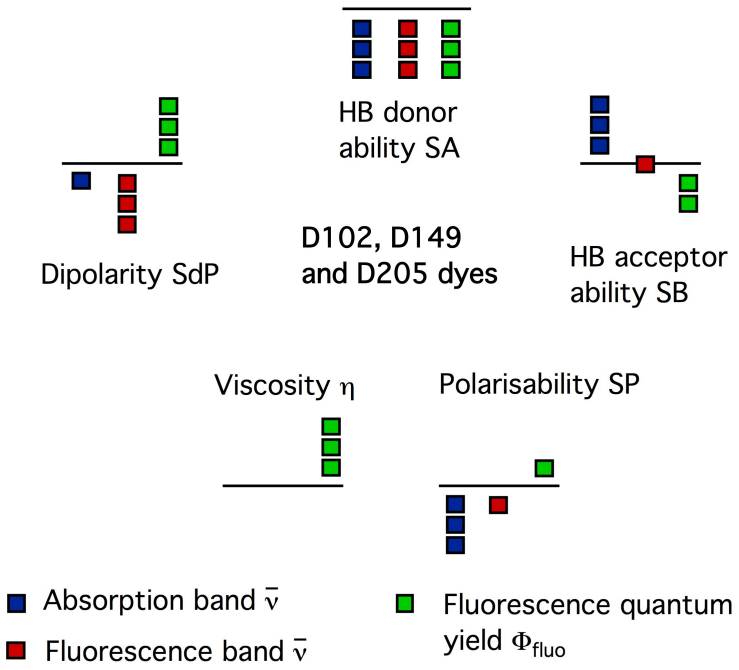

Figure 1.14: A summary of the solvent effects on the steady-state absorption, emission spectra and fluorescence quantum yield of D102, D149 and D205 dyes. The squares above and below the lbar correspond to the positive and negative effect of the solvent property, respectively. The number of the squares corresponds to the relative strength of the effect of the property of the solvent for a given dye. The colour code describes the absorption, emission mean wavenumbers and fluorescence quantum yield in red, blue and green, respectively.

Excitation energies and their solvent dependence were well modelled with M05/6-31+G(d) level of theory. More than 200nm of difference was found when using B3LYP and M06HF density functionals. On the contrary to the literature reports, no emission from S_2 state was observed with excitation emission matrices. Furthermore, the shape of emission spectra was found constant with excitation wavelength, so Kasha rule is perfectly valid for the molecules under study.

The two appealing points in the conclusions of this Chapter are: (i) HB donor ability causes a red shift of the absorption spectra of the indoline dyes, which is beneficial for their application in DSSCs and (ii) the strong dependence of Φ_{fluo} is likely to impact the fluorescence lifetimes. In order to get a more elaborated understanding of the processes, taking place after the photo-excitation of indoline dyes, time-resolved spectroscopy measurements were performed and presented in the following chapter.

Bibliography

[1] Y. Smortsova, H. Oher, F.-A. Miannay, R. Vanel, J. Dubois, O. Kalugin, and A. Idrissi, "Solvatochromic effects on a class of indoline derivatives organic photosensitizers: About the influence of hydrogen-bond acceptor and donor abilities parameters," Journal of Molecular Liquids, vol. 245, pp. 76 – 84, 2017. Recent Progresses on the Experimental & Theoretical-Computational Techniques for the Study of Liquids and Supercritical Fluids. From Simple to Complex Systems.

[2] P. W. Lohse, J. Kuhnt, S. I. Druzhinin, M. Scholz, M. Ekimova, T. Oekermann, T. Lenzer, and K. Oum, "Ultrafast photoinduced relaxation dynamics of the indoline dye d149 in organic solvents," Phys. Chem. Chem. Phys., vol. 13, pp. 19632–19640, 2011.

[3] A. M. El-Zohry, D. Roca-Sanjuán, and B. Zietz, "Ultrafast twisting of the indoline donor unit utilized in solar cell dyes: Experimental and theoretical studies," The Journal of Physical Chemistry C, vol. 119, no. 5, pp. 2249–2259, 2015.

[4] M. Fakis, P. Hrobárik, E. Stathatos, V. Giannetas, and P. Persephonis, "A time resolved fluorescence and quantum chemical study of the solar cell sensitizer d149," Dyes and Pigments, vol. 96, no. 1, pp. 304 – 312, 2013.

[5] T. Horiuchi, H. Miura, and S. Uchida, "Highly efficient metal-free organic dyes for dye-sensitized solar cells," Journal of Photochemistry and Photobiology A: Chemistry, vol. 164, no. 1, pp. 29 – 32, 2004. Proceedings of the Dye Solar Cell Osaka ICP-21 Pre-symposium. Dedicated to Professor Shozo Yanagida on the occasion of his retirement.

[6] T. Horiuchi, H. Miura, K. Sumioka, and S. Uchida, "High efficiency of dye-sensitized solar cells based on metal-free indoline dyes," Journal of the American Chemical Society, vol. 126, no. 39, pp. 12218–12219, 2004.

[7] D. Kuang, S. Uchida, R. Humphry-Baker, S. M. Zakeeruddin, and M. Grätzel, "Organic dye-sensitized ionic liquid based solar cells: Remarkable enhancement in performance through molecular design of indoline sensitizers," Angewandte Chemie International Edition, vol. 47, no. 10, pp. 1923–1927, 2008.

[8] S. Ito, H. Miura, S. Uchida, M. Takata, K. Sumioka, P. Liska, P. Comte, P. Pechy, and M. Grätzel, "High-conversion-efficiency organic dye-sensitized solar cells with a novel indoline dye," Chem. Commun., pp. 5194–5196, 2008.

[9] M. Fakis, E. Stathatos, G. Tsigaridas, V. Giannetas, and P. Persephonis, "Femtosecond decay and electron transfer dynamics of the organic sensitizer d149 and photovoltaic performance in quasi-solid-state dye-sensitized solar cells," The Journal of Physical Chemistry C, vol. 115, no. 27, pp. 13429–13437, 2011.

[10] A. Abrusci, K. R. S. Santosh, M. Al-Hashimi, M. Heeney, A. Petrozza, and H. J. Snaith, "Influence of ion induced local coulomb field and polarity on charge generation and efficiency in poly(3-hexylthiophene)-based solid-state dye-sensitized solar cells," Advanced Functional Materials, vol. 21, no. 13, pp. 2571–2579, 2011.

[11] A. El-Zohry, A. Orthaber, and B. Zietz, "Isomerization and aggregation of the solar cell dye d149," The Journal of Physical Chemistry C, vol. 116, no. 50, pp. 26144–26153, 2012.

[12] E. Rohwer, C. Richter, N. Heming, K. Strauch, C. Litwinski, T. Nyokong, D. Schlettwein, and H. Schwoerer, "Ultrafast photodynamics of the indoline dye d149 adsorbed to porous zno in dye-sensitized solar cells," ChemPhysChem, vol. 14, no. 1, pp. 132–139, 2013.

[13] T. Dentani, Y. Kubota, K. Funabiki, J. Jin, T. Yoshida, H. Minoura, H. Miura, and M. Matsui, "Novel thiophene-conjugated indoline dyes for zinc oxide solar cells," New J. Chem., vol. 33, pp. 93–101, 2009.

[14] J. Sobuś, J. Karolczak, D. Komar, J. A. Anta, and M. Ziółek, "Transient states and the role of excited state self-quenching of indoline dyes in complete dye-sensitized solar cells," Dyes and Pigments, vol. 113, pp. 692 – 701, 2015.

[15] G. V. Baryshnikov, B. F. Minaev, and V. A. Minaeva, "Quantum-chemical study of the structure and optical properties of sensitized dyes of an indoline-thiazolidine series," Optics and Spectroscopy, vol. 108, no. 1, pp. 16–22, 2010.

[16] H. Fukunishi, S. Nakamura, and S. Fujieda, "Influence of conformation on the absorption spectra of flexible organic dyes used in dye-sensitized solar cells," Computational and Theoretical Chemistry, vol. 1014, pp. 29 – 36, 2013.

[17] T. Le Bahers, T. Pauporte, G. Scalmani, C. Adamo, and I. Ciofini, "A td-dft investigation of ground and excited state properties in indoline dyes used for dye-sensitized solar cells," Phys. Chem. Chem. Phys., vol. 11, pp. 11276–11284, 2009.

[18] H.-M. Cheng and W.-F. Hsieh, "High-efficiency metal-free organic-dye-sensitized solar cells with hierarchical zno photoelectrode," Energy Environ. Sci., vol. 3, pp. 442–447, 2010.

[19] A. Namekawa and R. Katoh, "Improvement of light-harvesting and electron injection efficiencies by lithium ion in d149-sensitized nanocrystalline tio2 films," Chemical Physics Letters, vol. 634, pp. 37 – 41, 2015.

[20] J. Idígoras, J. Sobuś, M. Jancelewicz, E. Azaceta, R. Tena-Zaera, J. A. Anta, and M. Ziółek, "Effect of different photoanode nanostructures on the initial charge separation and electron injection process in dye sensitized solar cells: A photophysical study with indoline dyes," Materials Chemistry and Physics, vol. 170, pp. 218 – 228, 2016.

[21] H. Lihua, J. Lilong, and W. Mingding, "Metal-free indoline dye sensitized solar cells based on nanocrystalline zn2sno4," Electrochemistry Communications, vol. 12, no. 2, pp. 319 – 322, 2010.

[22] M. Rudolph, T. Yoshida, H. Miura, and D. Schlettwein, "Improvement of light harvesting by addition of a long-wavelength absorber in dye-sensitized solar cells based on zno and indoline dyes," The Journal of Physical Chemistry C, vol. 119, no. 3, pp. 1298–1311, 2015.

[23] D. Moia, A. Szumska, V. Vaissier, M. Planells, N. Robertson, B. C. O'Regan, J. Nelson, and P. R. F. Barnes, "Interdye hole transport accelerates recombination in dye sensitized mesoporous films," Journal of the American Chemical Society, vol. 138, no. 40, pp. 13197–13206, 2016.

[24] M. Matsui, A. Ito, M. Kotani, Y. Kubota, K. Funabiki, J. Jin, T. Yoshida, H. Minoura, and H. Miura, "The use of indoline dyes in a zinc oxide dye-sensitized solar cell," Dyes and Pigments, vol. 80, no. 2, pp. 233 – 238, 2009.

[25] T. Horiuchi, H. Miura, and S. Uchida, "Highly-efficient metal-free organic dyes for dye-sensitized solar cells," Chem. Commun., pp. 3036–3037, 2003.

[26] A. R. K. Selvaraj and S. Hayase, "Molecular dynamics simulations on the aggregation behavior of indole type organic dye molecules in dye-sensitized solar cells," Journal of Molecular Modeling, vol. 18, no. 5, pp. 2099–2104, 2012.

[27] Z.-S. Wang, Y. Cui, Y. Dan-oh, C. Kasada, A. Shinpo, and K. Hara, "Thiophene-functionalized coumarin dye for efficient dye-sensitized solar cells: Electron lifetime improved by coadsorption of deoxycholic acid," The Journal of Physical Chemistry C, vol. 111, no. 19, pp. 7224–7230, 2007.

[28] M. Pastore and F. De Angelis, "Aggregation of organic dyes on tio2 in dye-sensitized solar cells models: An ab initio investigation," ACS Nano, vol. 4, no. 1, pp. 556–562, 2010.

[29] H. Tian, X. Yang, R. Chen, R. Zhang, A. Hagfeldt, and L. Sun, "Effect of different dye baths and dye-structures on the performance of dye-sensitized solar cells based on triphenylamine dyes," The Journal of Physical Chemistry C, vol. 112, no. 29, pp. 11023–11033, 2008.

[30] M. Ziolek, X. Yang, L. Sun, and A. Douhal, "Interrogating the ultrafast dynamics of an efficient dye for sunlight conversion," Phys. Chem. Chem. Phys., vol. 12, pp. 8099–8108, 2010.

[31] R. Sánchez-de Armas, M. n. San Miguel, J. Oviedo, and J. F. Sanz, "Coumarin derivatives for dye sensitized solar cells: a td-dft study," Phys. Chem. Chem. Phys., vol. 14, pp. 225–233, 2012.

[32] W. Qin, M. Baruah, M. Sliwa, M. Van der Auweraer, W. M. De Borggraeve, D. Beljonne, B. Van Averbeke, and N. Boens, "Ratiometric, fluorescent bodipy dye with aza crown ether functionality: Synthesis, solvatochromism, and metal ion complex formation," The Journal of Physical Chemistry A, vol. 112, no. 27, pp. 6104–6114, 2008.

[33] M. Baruah, W. Qin, C. Flors, J. Hofkens, R. A. L. Vallée, D. Beljonne, M. Van der Auweraer, W. M. De Borggraeve, and N. Boens, "Solvent and ph dependent fluorescent properties of a dimethylaminostyryl borondipyrromethene dye in solution," The Journal of Physical Chemistry A, vol. 110, no. 18, pp. 5998–6009, 2006.

[34] A. Filarowski, M. Kluba, K. Cieslik-Boczula, A. Koll, A. Kochel, L. Pandey, W. M. De Borggraeve, M. Van der Auweraer, J. Catalan, and N. Boens, "Generalized solvent scales as a tool for investigating solvent dependence of spectroscopic and kinetic parameters. application to fluorescent bodipy dyes," Photochem. Photobiol. Sci., vol. 9, pp. 996–1008, 2010.

[35] A. M. Brouwer, "Standards for photoluminescence quantum yield measurements in solution (iupac technical report)," Pure Appl. Chem., vol. 83, no. 12, pp. 2213–2228, 2011.

[36] W. Haynes, ed., CRC Handbook of Chemistry and Physics. 6000 Broken Sound Parkway NW, Suite 300 Boca Raton, FL 33487-2742: CRC Press, 95 ed., 2015.

[37] C. Reichardt, Solvents and solvent effects in organic chemistry. VCH Verlagsgsellschaft mbH, 1988.

[38] M. L. Horng, J. A. Gardecki, A. Papazyan, and M. Maroncelli, "Subpicosecond measurements of polar solvation dynamics: Coumarin 153 revisited," The Journal of Physical Chemistry, vol. 99, no. 48, pp. 17311–17337, 1995.

[39] J. R. Lakowicz, Principles of Fluorescence Spectroscopy. Springer, 2006.

[40] M. J. Frisch, G. W. Trucks, H. B. Schlegel, G. E. Scuseria, M. A. Robb, J. R. Cheeseman, G. Scalmani, V. Barone, G. A. Petersson, H. Nakatsuji, X. Li, M. Caricato, A. V. Marenich, J. Bloino, B. G. Janesko, R. Gomperts, B. Mennucci, H. P. Hratchian, J. V. Ortiz, A. F. Izmaylov, J. L. Sonnenberg, D. Williams-Young, F. Ding, F. Lipparini, F. Egidi, J. Goings, B. Peng, A. Petrone, T. Henderson, D. Ranasinghe, V. G. Zakrzewski, J. Gao, N. Rega, G. Zheng, W. Liang, M. Hada, M. Ehara, K. Toyota, R. Fukuda, J. Hasegawa, M. Ishida, T. Nakajima, Y. Honda, O. Kitao, H. Nakai, T. Vreven, K. Throssell, J. A. Montgomery, Jr., J. E. Peralta, F. Ogliaro, M. J. Bearpark, J. J. Heyd, E. N. Brothers, K. N. Kudin, V. N. Staroverov, T. A. Keith, R. Kobayashi, J. Normand, K. Raghavachari, A. P. Rendell, J. C. Burant, S. S. Iyengar, J. Tomasi, M. Cossi, J. M. Millam, M. Klene, C. Adamo, R. Cammi, J. W. Ochterski, R. L. Martin, K. Morokuma, O. Farkas, J. B. Foresman, and D. J. Fox, "Gaussian16 Revision B.01," 2016. Gaussian Inc. Wallingford CT.

[41] J. Catalán, "Toward a generalized treatment of the solvent effect based on four empirical scales: Dipolarity (sdp, a new scale), polarizability (sp), acidity (sa), and basicity (sb) of the medium," The Journal of Physical Chemistry B, vol. 113, no. 17, pp. 5951–5960, 2009.

[42] M. J. Kamlet, J. L. M. Abboud, M. H. Abraham, and R. W. Taft, "Linear solvation energy relationships. 23. a comprehensive collection of the solvatochromic parameters, .pi.*, .alpha., and .beta., and some methods for simplifying the generalized solvatochromic equation," The Journal of Organic Chemistry, vol. 48, no. 17, pp. 2877–2887, 1983.

[43] Y. Marcus, "The properties of organic liquids that are relevant to their use as solvating solvents," Chem. Soc. Rev., vol. 22, pp. 409–416, 1993.

[44] H. Nitta and I. Kawata, "A close inspection of the charge-transfer excitation by tddft with various functionals: An application of orbital- and density-based analyses," Chemical Physics, vol. 405, pp. 93 – 99, 2012.

[45] C. Guido and S. Caprasecca, "How to perform corrected linear response calculations in g09," 03 2016.

[46] B. Le Guennic and D. Jacquemin, "Taking up the cyanine challenge with quantum tools," Accounts of Chemical Research, vol. 48, no. 3, pp. 530–537, 2015.

[47] B. Valeur, Molecular Fluorescence: Principles and Applications. Wiley, 2001.

[48] T. Wolff, "The solvent dependent fluorescence quantum yield of acridine as a probe for water in micelles and for the preferred location of acridine in micellar solutions," Berichte der Bunsengesellschaft für physikalische Chemie, vol. 85, no. 2, pp. 145–148, 1981.

Chapter 2

Time-resolved study of indoline dyes

In Chapter 1, a comprehensive analysis of the influence of the solvent on the spectroscopic properties of the indoline derivated dyes D131, D102, D149 and D205 was shown. In this Chapter, time-resolved spectroscopy was used to understand the photophysics of these dyes and its dependence on the solvent. Firstly, the results on the TCSPC measurements of the excited state lifetime of dyes in different solvents will be presented. The analysis was focused on the role of polarity, HB donor and acceptor abilities and viscosity of the solvent. Furthermore, the femtosecond UV-Vis transient absorption will help to investigate the excited state dynamics. The measurements in ionic liquid $BmimBF_4$, MeOH, DMSO and ACN give a global overview of the mechanism of the deactivation of the indoline derivated dyes. The roles of the solvation dynamics, the equilibrium between neutral and deprotonated forms of these dyes and their floppy structure are investigated.

2.1 Introduction

In the previous chapter, an important dependence of the spectral properties of dyes on the solvent was evidenced. Therefore, the photophysical characteristics, like the deactivation mechanism of dyes must be influenced by the solvent properties. In this chapter, the results of time-resolved study are shown, motivated by the high potential of indoline dyes as sensitizers for DSSCs. Time correlated single photon counting (TCSPC) and femtosecond UV-Vis transient absorption measurements were performed to elucidate this dependence.

Literature review, presented in the first chapter, confirms the dependence of the dye's fluorescence lifetime on its environment [1–4]. The hydrogen bonding ability of the solvent changes the relaxation constants a lot. Finally, a modification of the structure of dyes induces changes in their response to the photoexcitation.

2.2 Fluorescence lifetimes

Fluorescence intensity decays were recorded with TCSPC exciting at 420 nm for D131 and 520 nm for D102, D149 and D205. The emission wavelength was set close to the maximum emission, reported in Chapter 1 (cf. tables 1.3 and 1.4). Representative D205 fluorescence decays, as well as instrument response function are shown in fig. 2.1. Important dependence of D205 fluorescence lifetime on the solvent can be noted. Solutions of D205 in alcohols show the fastest decay, while D205 in dimethylsulfoxide has the longest lifetime. In general, the lifetime increases in a row MeOH <n-3ol <DCM <$CHCl_3$ <DMSO.

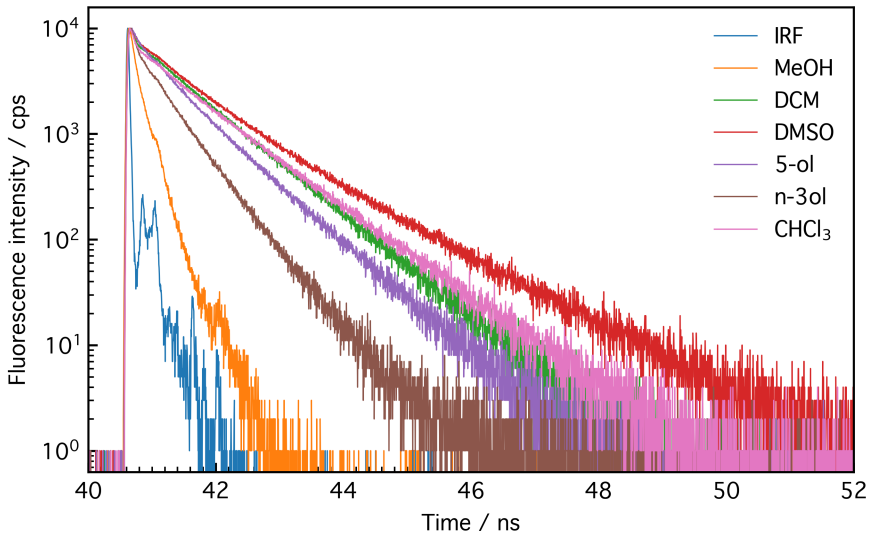

Figure 2.1: The fluorescence intensity decays of D205 in MeOH (λ_{em}=668 nm), DCM (642 nm), DMSO (657 nm), pentanol (642 nm), propanol (636 nm) and chloroform (637 nm). The instrument response function (IRF) at 522 nm (FWHM=40ps).

Fluorescence intensity decays and instrument response function were acquired and analysed using the iterative reconvolution algorithm. In this procedure, the theoretical model decay is convoluted with the IRF in iterative way, until an optimum

agreement with the observed data is reached. The sum of exponential decays was used as a model of the experimental data (cf. eq 2.1).

$$I(t) = \int_{-\infty}^{t} IRF(t') \sum_{i=1}^{n} C_i e^{-\frac{-t-t'}{\tau_i}} \mathrm{d}t' \tag{2.1}$$

The results of fluorescence lifetime measurements of D131, D102, D149 and D205 are presented in tables 2.2, 2.1, 2.3, 2.4. Because of the presence of rising time components (the ones with negative amplitude) in some of the D131 fluorescence decays, the preexponential factors were normalised to the sum of positive components in the following way:

$$A_i = \frac{C_i}{\sum_i C_i} \tag{2.2}$$

The negative amplitudes were also divided by the sum of positive components to have an idea about their contribution. The confidence intervals, given in tables, are automatically estimated from asymptotic standard errors by Fluofit software [5].

As it can be seen, the decays are described by the sum of two, three and four exponential terms. Multiple rate constants are possibly the result of the conformational distribution and the equilibrium between neutral (or acid) and anionic (or deprotonated, or base) forms of the dye, as there is only one fluorescent compound in solution. Therefore, for the further analysis, amplitude weighted average of the decay lifetimes was calculated according to the equation 2.3 and used.

$$\tau = \frac{\sum_i A_i \tau_i}{\sum_i A_i} \tag{2.3}$$

Table 2.1: The fitting parameters of the fluorescence decays of D131 using multiexponential functions: fluorescence lifetime components (τ_i, ps) and their relative contributions (A_i, normalized to the sum of positive components). The data are given for D131 in organic solvents: tetrahydrofurane (THF); dichloromethane (DCM); dimethylformamide (DMF); dimethylsulfoxide (DMSO); acetonitrile (ACN); pentanol (5-ol); butanol (n-4ol); propanol (n-3ol); ethanol (EtOH); methanol (MeOH); toluene (TLN); trifluoroethanol (TFE). Excitation and emission wavelengths were set to 420 nm and close to the maximum emission band position, respectively.

Solvent	A_1	τ_1	A_2	τ_2	A_3	τ_3	A_4	τ_4	χ^2
THF	0.050	2190±30	0.656	968±5	0.295	160±10	-1.202	12.2±0.8	1.002
DCM	0.018	1450±20	0.459	501±3	0.523	43±2	-1.083	24.4±0.5	1.081
DMF	0.254	1527±9	0.414	637±9	0.332	86±7	-	-	1.02
DMSO	0.407	523±2	0.180	320±7	0.413	53±2	-1.063	21.6±0.5	1.027
ACN	0.036	429±3	0.129	243±1	-0.762	9.59±0.07	0.835	5.46±0.06	0.997
5-ol	0.055	788±4	0.113	178±3	0.323	29.7±0.6	0.509	19.6±0.3	1.037
n-4ol	0.162	555±3	0.200	160±3	0.638	33.6±0.7	-1.057	19.2±0.3	1.02
n-3ol	0.003	2800±100	0.457	477±3	0.540	83±3	-1.159	14.8±0.6	0.973
EtOH	0.256	486±2	0.680	371±1	0.064	208±10	-1.092	20.7±0.3	0.978
MeOH	0.006	1032±20	0.259	325±2	0.735	320±0.4	-1.026	22.7±0.2	1.047
TLN	0.033	610±2	0.012	211±8	-0.269	5.67±0.09	0.955	2.02±0.03	1.065
TFE	0.001	4700±300	0.006	740±50	0.993	87.5±0.8	-1.154	16.3±0.5	1.054

Table 2.2: The fitting parameters of the fluorescence decays of D102 using multi-exponential functions: fluorescence lifetime components (τ_i, ps) and their relative contributions (A_i, normalized to the sum of positive components). The data are given for D102 in organic solvents: cyclohexane (CX); tetrahydrofurane (THF); dichloromethane (DCM); chloroform ($CHCl_3$); dimethylformamide (DMF); gamma-butyrolactone (g-Bl); dimethylsulfoxide (DMSO); acetonitrile (ACN); propylene carbonate (PC); pentanol (5-ol); methanol (MeOH); toluene (TLN). Excitation and emission wavelengths were set to 520 nm and close to the maximum emission band position, respectively.

Solvent	A_1	τ_1	A_2	τ_2	A_3	τ_3	χ^2
CX	0.026	228±10	0.974	88.8±0.5	-	-	1.047
THF	0.761	747±2	0.239	90±7	-	-	0.972
DCM	0.707	648±2	0.293	103±5	-	-	1.078
$CHCl_3$	0.481	731±2	0.127	141±7	0.391	33±2	1.015
DMF	0.731	683±3	0.269	140±8	-	-	1.038
g-Bl	0.080	1068±11	0.567	592±3	0.353	124±5	1.278
DMSO	0.492	769±2	0.245	326±6	0.263	79±4	1.041
ACN	0.081	671±7	0.531	348±2	0.388	88±3	1.056
PC	0.699	520±1	0.301	135±3	-	-	1.097
5-ol	0.405	535±2	0.595	197±2	-	-	1.025
MeOH	0.023	332±10	0.977	94±1	-	-	1.009
TLN	0.367	278±2	0.633	180±2	-	-	1.038

Table 2.3: The fitting parameters of the fluorescence decays of D149 using multi-exponential functions: fluorescence lifetime components (τ_i, ps) and their relative contributions (A_i, normalized to the sum of positive components). The data are given for D149 in organic solvents: cyclohexane (CX); tetrahydrofurane (THF); dichloromethane (DCM); chloroform ($CHCl_3$); dimethylformamide (DMF); gamma-butyrolactone (g-Bl); dimethylsulfoxide (DMSO); acetonitrile (ACN); propylene carbonate (PC); pentanol (5-ol); methanol (MeOH); toluene (TLN). Excitation and emission wavelengths were set to 520 nm and close to the maximum emission band position, respectively.

Solvent	A_1	τ_1	A_2	τ_2	A_3	τ_3	χ^2
CX	0.061	326±6	0.939	112±1		-	0.996
THF	0.334	938±5	0.260	509±9	0.406	92±4	0.974
DCM	0.515	693.2±1.9	0.157	279±8	0.328	51±3	1.168
$CHCl_3$	0.389	1017.2±3.5	0.164	463±11	0.447	76±3	1.296
DMF	0.724	473±2	0.276	180.3±6.4		-	1.042
g-Bl	0.389	987±3	0.251	676±7	0.360	138±5	1.038
DMSO	0.665	929±2	0.335	159±5		-	1.134
ACN	0.351	841±3	0.208	303±7	0.441	70±3	1.165
PC	0.673	717±2	0.327	148±4		-	1.099
5-ol	0.434	673±3	0.566	160±3	-0.309	37±4	0.987
MeOH	0.036	275±8	0.964	92.1±0.6		-	1.065
TLN	0.077	342±1	0.029	146±5	0.894	2.1±0.1	0.992

Table 2.4: The fitting parameters of the fluorescence decays of D205 using multi-exponential functions: fluorescence lifetime components (τ_i, ps) and their relative contributions (A_i, normalized to the sum of positive components). The data are given for D205 in 16 organic solvents: cyclohexane (CX); tetrahydrofurane (THF); dichloromethane (DCM); chloroform ($CHCl_3$); dimethylformamide (DMF); gamma-butyrolactone (g-Bl); dimethylsulfoxide (DMSO); acetonitrile (ACN); propylene carbonate (PC); pentanol (5-ol); butanol (n-4ol); propanol (n-3ol); ethanol (EtOH); methanol (MeOH); trifluoroethanol (TFE). Excitation and emission wavelengths were set to 520 nm and close to the maximum emission band position, respectively.

Solvent	A_1	τ_1	A_2	τ_2	A_3	τ_3	χ^2
CX	0.357	218±2	0.643	96±1	-	-	1.094
THF	0.461	590±3	0.201	263±8	0.338	63±4	0.971
DCM	0.581	848±4	0.419	114±6	-	-	1.058
$CHCl_3$	0.190	443±11	0.342	1008±4	0.468	69±3	0.912
DMF	0.407	958±4	0.209	478±11	0.384	79±5	0.969
g-Bl	0.076	1214±18	0.476	588±5	0.448	118±5	1.024
DMSO	0.245	1352±8	0.395	639±7	0.360	111±6	1.003
ACN	0.067	1059±16	0.474	496±4	0.459	82±4	1.087
PC	0.208	856±7	0.406	116±5	0.385	428±5	1.074
5-ol	0.497	791±3	0.503	208±4	-	-	1.003
n-4ol	0.552	672±3	0.448	159±3	-	-	1.044
n-3ol	0.420	527±3	0.580	126±3	-	-	1.019
EtOH	0.579	377±2	0.421	100±4	-	-	1.048
MeOH	0.024	370±9	0.976	111±1	-	-	1.049
TFE	0.018	771±24	0.378	449±2	0.604	67±2	1.168

The fluorescence lifetime obviously depends on the solvent viscosity η and dipolarity SdP. Higher viscosity of the environment assists to block the relaxation processes that result from the floppy structure of the fluorophore, like photoisomerisation. The dipolarity affects the energy of the electronic levels of the fluorophore and therefore the probability of radiative and non-radiative relaxation. The dependence on the dipolarity and viscosity of the solvent is presented in figure 2.2, where one can see the stork type plots. These plots reveal the difference in the interactions between the dye and the solvent for protic and aprotic solvents. Indeed, the regressions for the alcohols (shown in red) and the aprotic (blue) solvents are clearly distinct. These data confirm the suggestion about the particular photodynamics of the indoline dyes in the protic solvents.

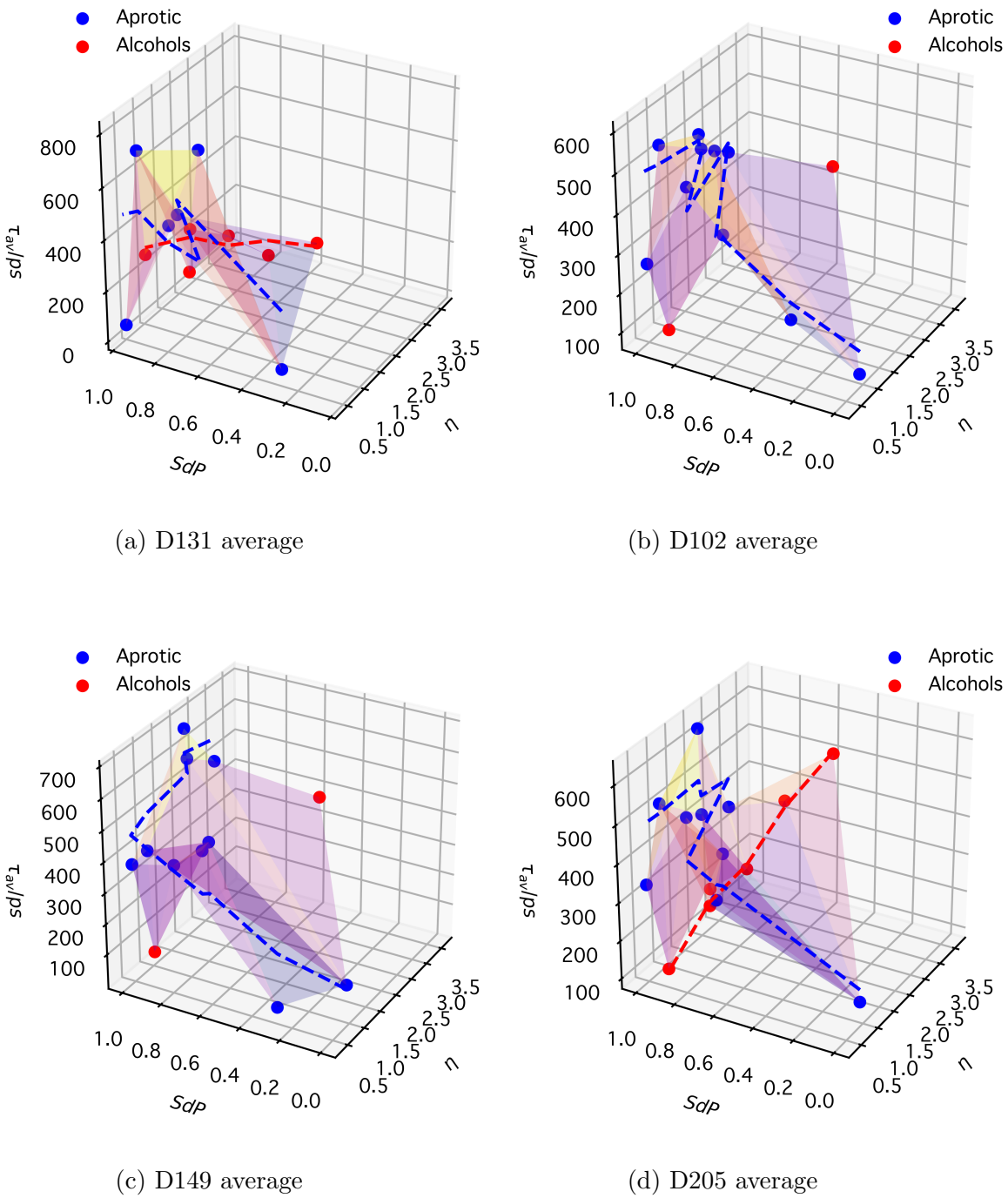

(a) D131 average

(b) D102 average

(c) D149 average

(d) D205 average

Figure 2.2: D131, D102, D149 and D205 weighted average fluorescence lifetimes, as function of the solvent dipolarity and viscosity. Solutions in alcohols are shown as blue points, and in aprotic solvents as red points. The values of viscosity of the solvents were taken from [6], for PC from [7], γ-Bl [8], TFE [9]. The values of SdP of the solvents were taken from [10]. Blue and red dashed lines correspond to multivariate regression of the type $\tau_{av} = a + b * SdP + c * \eta$ for aprotic solvents and alcohols, respectively.

In analogy with the dependence of quantum yield on the solvent properties, the Catalan solvent scale, completed by the viscosity parameter was applied to the analysis of average fluorescence lifetimes of the dyes. Empirical lifetimes were modelled according to eq. 2.4. The results are given in table 2.5.

$$\tau_{fluo} = \tau_{fluo,0} + b * SdP + c * SP + d * SA + e * SB + f * \eta \qquad (2.4)$$

Table 2.5: Multivariate regression analysis of average fluorescence lifetime using the modified Catalan solvent scale.

$\tau_{fluo,0}$	0 ± 1310	71 ± 98	40 ± 138	77 ± 88
b, SdP	120 ± 365	113 ± 139	447 ± 195	-90 ± 169
c, SP	251 ± 1730	253 ± 185	-1 ± 260	581 ± 226
d, SA	-26 ± 563	-651 ± 192	-644 ± 271	-257 ± 109
e, SB	573 ± 350	320 ± 169	12 ± 238	-74 ± 104
f, η	-186 ± 107	-12 ± 35	75 ± 49	55 ± 29
R^2	0.52	0.81	0.75	0.77

The determination coefficients and the estimated errors of fit parameters, shown in the table, show that the average lifetimes are not satisfactorily modelled by the modified Catalan solvent scale. The dye with cyanide functional group, D131, exhibits the worst result. As the indoline chromophore moiety is conjugated with -COOH group, spectroscopic behaviour of this molecule is the most sensitive to the equilibrium between neutral and deprotonated forms.

The other indoline derivatives, D102, D149 and D205 show better fit. For D102, D149 and D205, solvent hydrogen bond donor ability decreases the average lifetime. This behaviour is expected on the basis of examination of fig. 2.2.

As was mentioned in Chapter 1, the rate constants of radiative and non-radiative processes can be calculated from the quantum yield and the excited state lifetime of the molecule using the equation 1.4. The resulting values are reported in table 2.6.

Non-radiative relaxation rate constants of indoline dyes are strikingly one order higher than the radiative ones. Possible explanation of this is discussed in the next paragraph. For D102, D149 and D205, the highest k_{nr} are observed for methanol and cyclohexane. Clearly, the reason of large k_{nr} in MeOH is an additional mechanism of excited state deactivation, due to the hydrogen bonds formed by the solvent and the dye. The low solubility of the dye in cyclohexane, due to its low polarity, can cause the formation of aggregates. Excited state proton transfer (as suggested in the article [11]) and quenching by energy transfer[12] can be possible pathways of internal conversion for the neighbour dye molecules. The absorption spectra of D205 in cyclohexane (fig. 2.3) show a shoulder at around 640 nm. This band is possibly a J-aggregate band, as it has less energy than the monomer band. A carbocyanine dye exhibits a similar pattern upon aggregation [13].

Table 2.6: Rate constants of radiative and non-radiative relaxation of D205, D149, D102 and D131 in organic solvents. All values are given in 10^8 s^{-1}.

Solvent	D205		D149		D102		D131	
	k_r	k_{nr}	k_r	k_{nr}	k_r	k_{nr}	k_r	k_{nr}
CX	0.717	71.0	0.720	79.2	0.433	107.8		
THF	2.023	26.9						
DCM	2.590	15.9	3.616	20.3	2.170	18.3	1.424	19.3
$CHCl_3$	2.387	19.3	2.253	17.5	4.258	21.9		
DMF	2.884	16.3					1.077	13.6
g-Bl	3.316	20.2	3.728	12.8	3.034	18.5		
DMSO	2.405	13.6	3.158	11.7	4.867	16.0	2.348	31.9
ACN	3.576	25.5	3.673	22.0	5.485	31.1	5.905	188.4
PC	3.817	21.8	3.766	15.1	3.315	21.4		
5-ol	2.932	17.2			3.079	26.8	7.010	113.0
n-4ol	1.358	21.3						
n-3ol	1.697	32.2					1.245	35.6
EtOH	1.152	37.2					1.105	24.5
MeOH	1.706	83.6	0.507	100.9	0.402	100.0	1.211	29.5
TFE	0.446	44.2					1.242	103.1

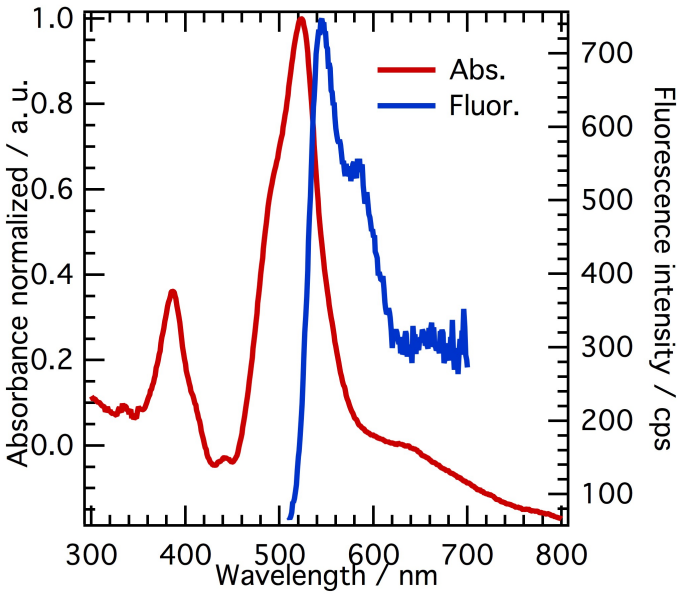

Figure 2.3: Absorption (red) and fluorescence (blue) spectra of D205 in cyclohexane. Fluorescence spectrum was recorded using excitation at 500 nm.

The floppy molecular structure of indoline molecules can explain their short excited state lifetimes. Considering figure 1.1, one can note two exocyclic double bonds that provide the possibility of excited state isomerisation and ultrafast relaxation. These double bonds are: 1) bond in the triphenylethylene moiety and 2) bond that links first rhodanine ring and indoline unit. The ultrafast twisting around the first bond was addressed in literature[4], and an additional mechanism for the radiationless decay through the ethenelike conical intersection was found. On the basis of these findings, the short excited-state lifetime component of 19-30 ps was attributed to this deactivation mechanism. An isomerization of D149 molecule, involving the second bond after the excitation to S_2 state was reported[12]. However, the possibility of the ultrafast relaxation of the excited state within the twisting around this bond was not considered previously, so the scan of potential energy surface (PES) was performed in order to test this hypothesis. Bond length and dihedral angle around the bond were chosen as the reaction coordinates, and PES rigid scans were performed for D149 molecule in ground and first excited states, using M05/6-31+G(d) level of theory. A cyclohexane environment was modelled using PCM.

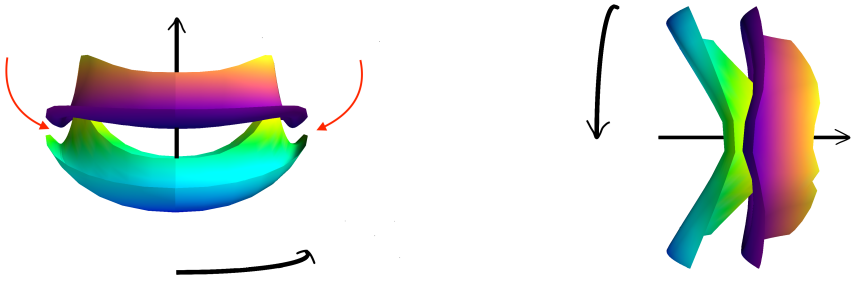

Figure 2.4: D149 potential energy surfaces in ground (jet colormap) and first excited (plasma colormap) states. Length (r) and dihedral angle (ϕ) around the double bond, that links rhodanine and indoline moieties are chosen as the reaction coordinates. PES are shown in cylindrical coordinates. The views along the +X and +Y axes are shown on the left and on the right, respectively. The linear arrow indicates the energy increase. The curved black arrow starts at 0° and ends at 90°. The red arrows indicate the regions of highly probable internal conversion.

In figure 2.4, resulting PES are shown in cylindrical coordinates: bond length stands r, dihedral angle stands for ϕ and energy E stands for Z. As one can see, in ground state, two isomers are energetically stable: one with dihedral angle close to 0° and another close to 180°. The corresponding minima on the PES of ground state are clearly seen and they are rather deep. In excited state, these minima become much more flat, and thus the twist around the double bond is facilitated. Two more local minima can be found in PES for the S_1, situated around 90° and 270°. For these geometries, energy difference between S_0 and S_1 is very small, and the ultrafast relaxation can be expected. Thus, the deactivation channel resulting from the twisting around the double bond, connecting donor and acceptor moieties, can't be neglected. We may suggest that the floppy character of the structure of these organic molecules is better to be avoided when designing the organic photosensitizers.

2.3 Transient absorption of indoline dyes

Measurements of fluorescence intensity decays, reported in the previous section, revealed complicated multi-exponential dynamics of the excited state, dependent on the solvent. However, this kind of study gives little about the scheme of the excited state evolution processes. Therefore, femtosecond transient absorption studies were performed.

For each dye, TA in three chosen solvents was performed: acetonitrile, methanol and dimethyl sulfoxide. Usually, the spectra are shown in three panels: till 1ps, till 30ps and till 1ns. All the spectra shown are the ones corrected for the GVD using the Sellmeier equation (see Appendix, eq. A.3).

2.3.1 Experimental spectra

According to the steady-state absorption spectrum of D131 dye, 410 nm excitation pulses were used to perform the measurements.

Spectra obtained for D131 in methanol are shown in fig. 2.5. As one can see, the excited state absorption covers all the spectral window, as was already observed by Lenzer [2]. The position of ground state bleach (GSB) was identified due to steady-state absorption and is slightly shifted to the red (432 nm when compared to steady-state absorption maximum 424 nm). This slight shift can be explained by that fact that all the bands overlap in this kind of difference spectra and the exact band position can be extracted only with proper data treatment. The stimulated emission (SE) band can be also identified using the steady-state fluorescence spectrum, shown in grey dash lines.

On the top panel, zero-time spectrum (the second in colour gradient) shows the nascent stimulated emission in the wavelength range 532 nm - 734 nm. Also, only one negative band is present at 472nm. After, this band splits in two for the longer times, forming ground state bleach and stimulated emission. On the first two upper panels, the bands shift can be observed. As it is shown in the lower panel, characterizing the dynamics succeeding the first 35 ps after the photo-excitation, all the excited state relaxation has finished. This is indicated by the curves crossing at the same wavelength-zero points: ≈395 nm, ≈460 nm and ≈670 nm. Solvation dynamics, geometry relaxation of this floppy molecule and shift of the equilibrium between neutral and deprotonated forms are the possible processes that cause the shift of stimulated emission and other bands in the TA spectra. To ascribe those possibilities, a multi-exponential global fit was performed to compare the decay associated spectra and steady-state spectra of the forms of the dye. This analysis will be described later in the chapter.

Spectra obtained for D131 in acetonitrile and in dimethylsulfoxide are shown in fig. 2.6 and fig. 2.7, respectively. The particular feature of all these three measurements is the considerable difference of the position of the stimulated emission band and the steady-state emission. In particular, acetonitrile solution the SE band is visible only till 2ps, while in DMSO it can't be easily resolved.

The TA spectra of D131 in DMSO reveal a particular interest from two points of view. First, the excited-state evolvement, that is finished after approximately 30 ps in acetonitrile and methanol, is clearly longer in DMSO. As DMSO has the highest viscosity among the three solvents used, we suggest that this excited state evolution

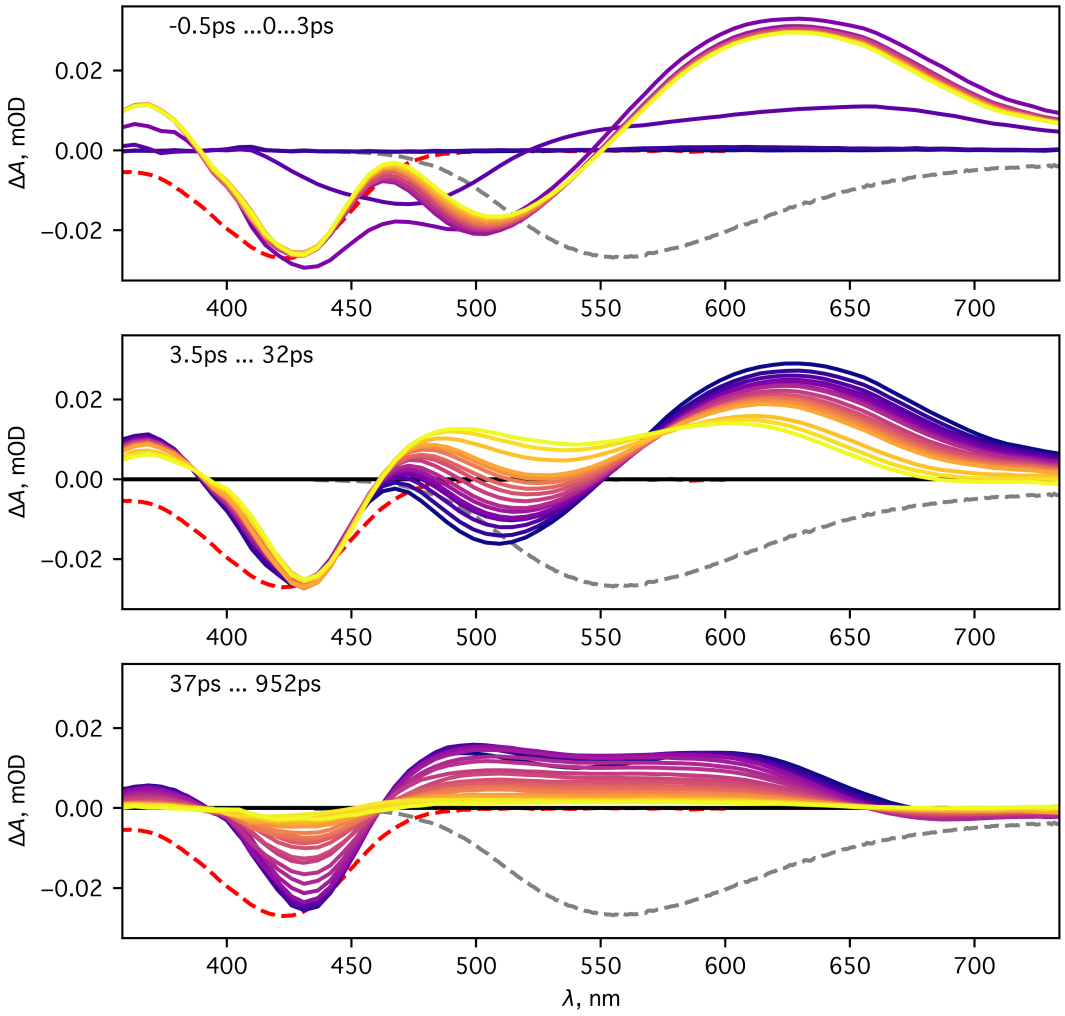

Figure 2.5: D131 transient absorption spectra in methanol. The colour gradient 'plasma', from East Bay to yellow colour, was chosen to represent the difference spectra in time ranges, indicated in text boxes in the panels. Red and grey dash lines show inverted and scaled steady-state absorption and emission spectra, respectively. Black lines on two lowest panels show the zero difference border.

can be correlated with the viscosity of the solvent. Second, the early times spectra of D131 in DMSO, shown on the top panel, exhibit sharp peaks that we assign to the Raman scattering of the solvent molecules. Importantly, this kind of signal can be observed only during the temporal and space overlap of pump and probe pulses. It is one of the options to get a measure of the cross-correlation function of pump and probe pulses that gives information about the time resolution of a transient absorption set-up. The application of this method, as well as the other options to measure the time resolution of the set-up is discussed in Appendix, subsection A.0.4. This time resolution depends on the pulse width of excitation and probe beams, excitation wavelength, sample absorbance, optics used etc. [14]. The knowledge of the time resolution is important to fit the kinetic data, using a convolution model, in order to get results with higher precision and accuracy.

According to the steady-state absorption spectrum of the D102 dye, 450 nm excitation pulses were used to perform the measurements. Spectra obtained for D102 in organic solvents are shown in fig. A.10, fig. A.11 and fig. A.12.

According to the steady-state absorption spectrum of D149 and D205 dyes, 488 nm excitation was used to record the difference absorption spectra. Spectra obtained for D149 in solvents are shown in fig. A.13, fig. A.14 and fig. A.15; for D205 – in fig. A.16, fig. A.17 and fig. A.18. Finally, spectra obtained for D205 in $BmimBF_4$ are shown in fig. 2.8. On the last figure, Raman scattering signals of $BmimBF_4$ can be noticed at 426 nm, 454 nm, 531 nm and 571 nm. They correspond to Stokes and anti-Stokes bands of the two energies: $\approx 1600 cm^{-1}$ and $\approx 2980 cm^{-1}$. These bands are present in Raman spectrum of $BmimBF_4$ and were assigned to symmetric and antisymmetric stretching modes in $Bmim^+$ cation[15].

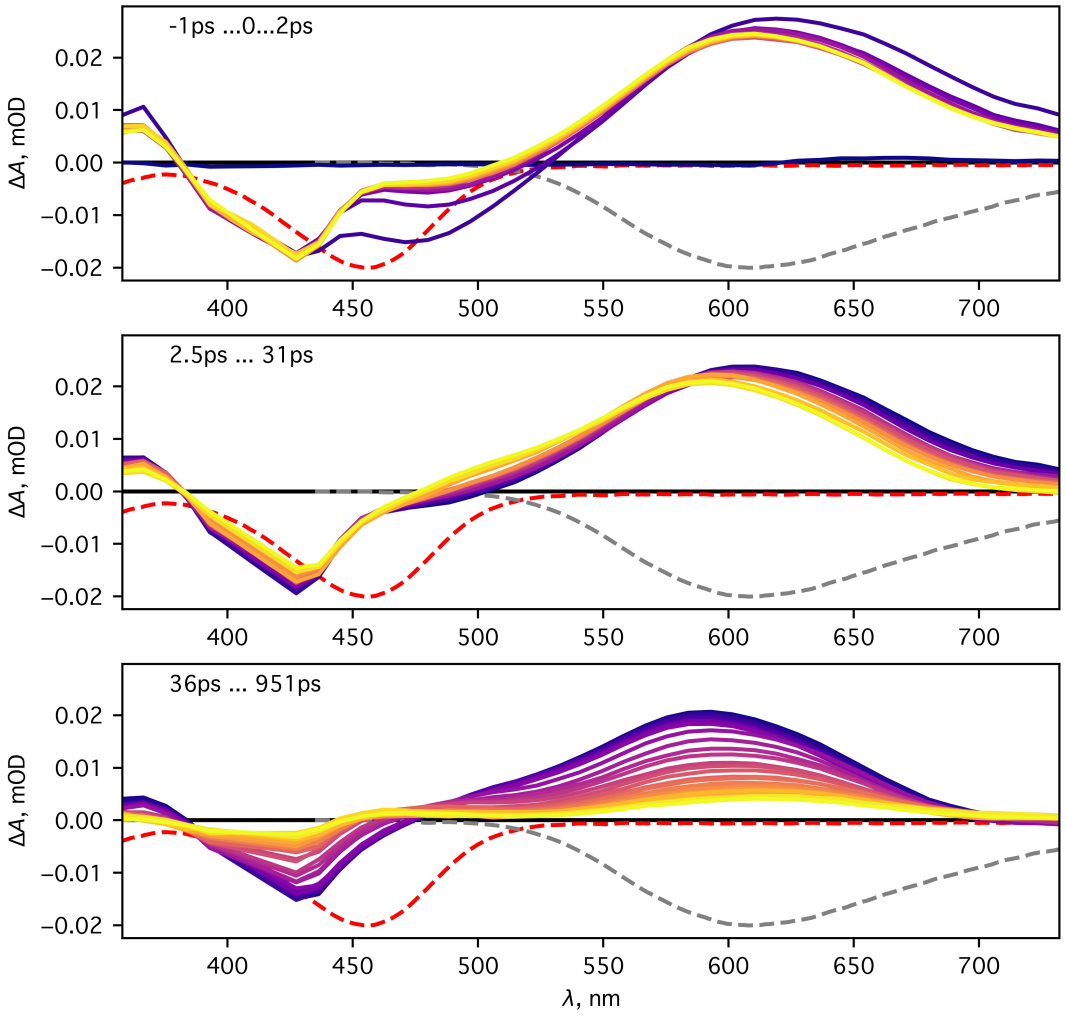

Figure 2.6: D131 transient absorption spectra in acetonitrile. The colour gradient 'plasma', from East Bay to yellow colour, was chosen to represent the difference spectra in time ranges, indicated in text boxes in the panels. Red and grey dash lines are used to show inverted and scaled steady-state absorption and emission spectra, respectively. Black lines on two lowest panels show the zero difference border.

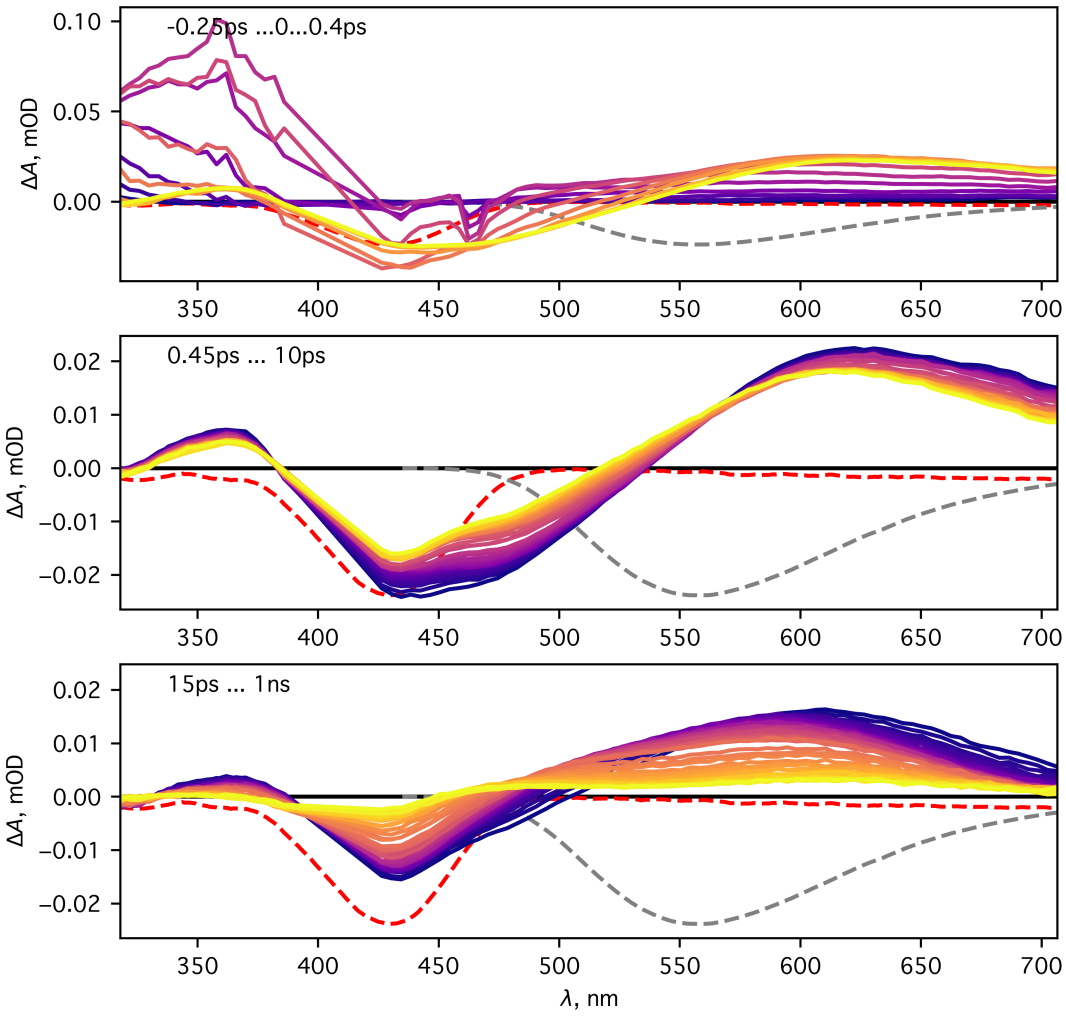

Figure 2.7: D131 transient absorption spectra in dimethylsulfoxide. The colour gradient 'plasma', from East Bay to yellow colour, was chosen to represent the difference spectra in time ranges, indicated in text boxes in the panels. Red and grey dash lines are used to show inverted and scaled steady-state absorption and emission spectra, respectively. Black lines on two lowest panels show the zero difference border.

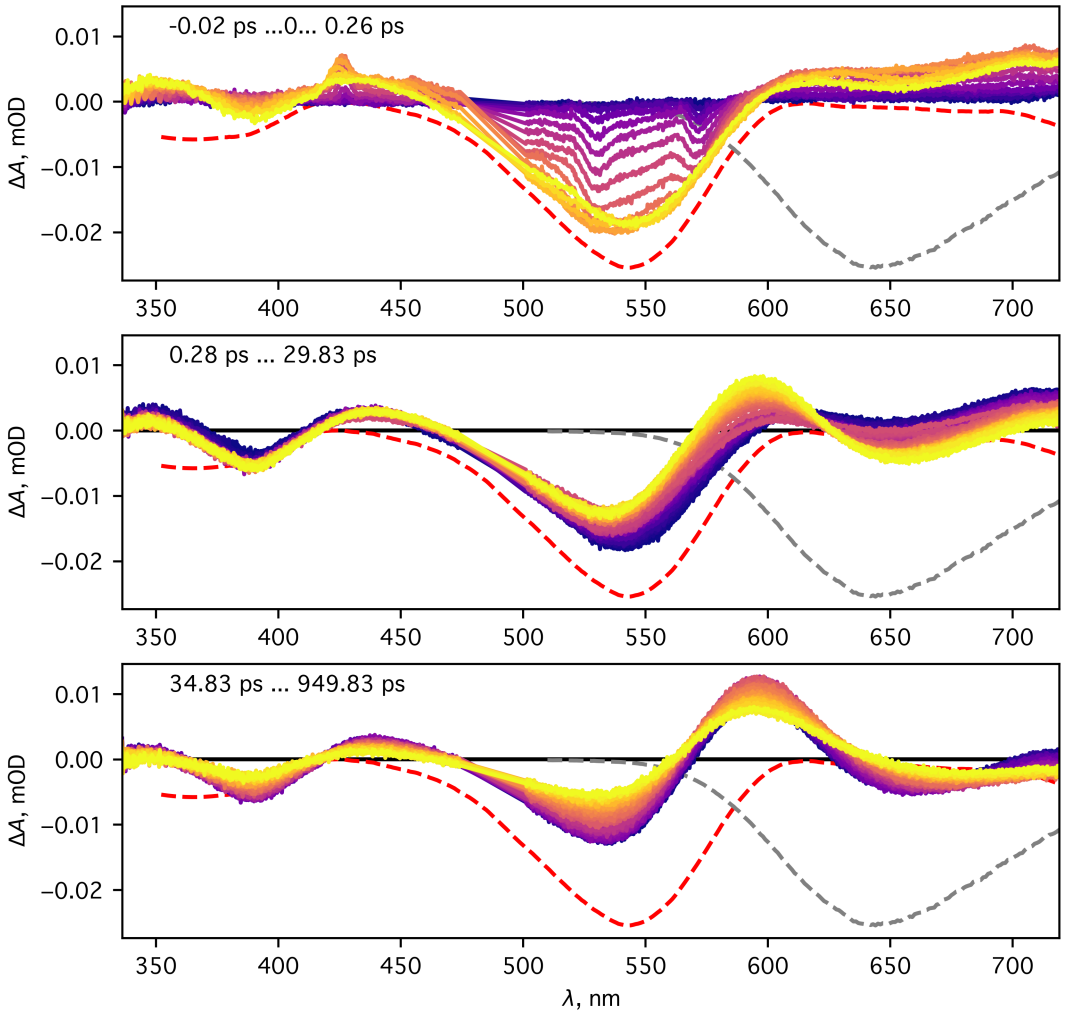

Figure 2.8: D205 transient absorption spectra in $BmimBF_4$. The colour gradient 'plasma', from East Bay to yellow colour, was chosen to represent the difference spectra in time ranges, indicated in text boxes in the panels. Red and grey dash lines are used to show inverted and scaled steady-state absorption and emission spectra, respectively. Black lines on two lowest panels show the zero difference border.

2.3.2 Global analysis

The recorded transient absorption spectra were treated according to an algorithm, using the home made software. Firstly, certainly the so-called 'pre-treatment 'was performed: the pump signal was removed from the spectra and then GVD correction was performed (cf. subsection A.0.3). Then, kinetics at nearly each 2 nm were extracted and modelled together by the convolution of the gaussian with a sum of exponential functions (see eq. 2.5) in order to obtain the best fit parameters: lifetimes τ_n, common for all the wavelengths, and $a_n(\lambda)$, representing the decay associated spectra, or component spectra.

$$\Delta OD_{exp}(t) = \int_0^\infty G(t') \sum^n a_n(\lambda) \exp(-\frac{(t - t_0 - t')}{\tau_n}) d(t') \tag{2.5}$$

During the fit, the overall chi-square (defined as in eq. 2.6) is minimised. In this definition, y is the calculated value, y_i is the measured value and σ_i is the estimated standard deviation of y_i. In its turn, the standard deviation is defined as in eq. 2.7.

$$\chi^2 = \sum_i (\frac{y - y_i}{\sigma_i})^2 \tag{2.6}$$

$$\sigma_i = \sqrt{\frac{1}{N} \sum (y_i - \bar{y})^2} \tag{2.7}$$

According to the experimental transient absorption spectra, no residual signal at long times was observed. Also, steady-state checks before and after the transient absorption experiment showed no difference in absorption spectra. Thus, the formation of triplet state or photoproducts can be excluded. Therefore, the scheme of the excited state evolution can be complicated only by the ultrafast deactivation processes. This information supports the use of global fit, or hard modelling of the experimental data.

The results of global fit are presented in table 2.7. The smallest number of exponentials that give satisfactory result was used to model the experimental data. The residuals were examined to judge the goodness of fit.

Table 2.7: The parameters of the global fit of TA spectra: lifetime components of D205, D149, D102 and D131 in solvents. Optimised full width half maximum of instrument response function is also given. Parameters, fixed during the fit, are marked by asterisk. The solvation times are taken from [16] for molecular solvents, and from [17] for ionic liquid $BmimBF_4$.

Solvent	FWHM / fs	τ_1 / ps	τ_2 / ps	τ_3 / ps	τ_4 / fs	τ_{solv} / ps
			D102			
MeOH	128.1 ±0.1	60.9 ± 0.4	8.05 ± 0.08	0.709 ±0.006	9.421 ±1e-3	0.03, 0.28, 3.2, 15.3
DMSO	122 ± 2	388 ± 4	5.90 ± 0.08	1.35 ± 0.02	8 ± 2	0.214, 2.29, 10.7
ACN	120.8 ± 0.4	271 ± 1	6.01 ± 0.08	0.314 ± 2e-3	10.6 ± 0.1	0.089, 0.63
			D205			
MeOH	190 ± 2	123.9 ± 0.3	7.30 ± 0.06	1.04 ± 0.01		0.03, 0.28, 3.2, 15.3
DMSO	154.3 ±0.9	331 ± 1	13.7 ± 0.1	1.43 ± 0.01	171 ± 3	0.214, 2.29, 10.7
ACN	104.8 ±0.6	315 ± 2	1.245 ± 0.009	0.079 ± 1e-3		0.089, 0.63
PC	107.4 ± 0.9	383 ± 3	5.325 ± 0.026	0.371 ± 2e-3	9.2 ± 0.2	0.03, 0.18, 2.03, 6.57
$BmimBF_4$	126.6 ± 0.9	1200*	88 ± 2	4.9 ± 0.1	136 ± 2	340
			D149			
MeOH	225 ±2	86.7 ± 0.8	7.44 ± 0.09	1.07 ± 0.01		0.03, 0.28, 3.2, 15.3
DMSO	140*	332 ± 3	6.51 ± 0.07	1.08 ± 0.01	153 ± 4	0.214, 2.29, 10.7
ACN	125 ± 1	227 ± 2	0.620 ± 0.007	0.041 ± 1e-3		0.089, 0.63
PeOH	103 ± 2	615 ± 29	44.0 ± 0.3	1.30 ± 0.01	12 ± 3	0.03, 0.67, 21.7, 151
			D131			
MeOH	120*	379 ± 3	17.7 ± 0.2	3.08 ± 0.04	338 ± 5	0.03, 0.28, 3.2, 15.3
DMSO	149.5 ± 0.1	371 ± 9	12.3 ± 0.2	0.487 ± 9e-3	10.655 ± 1e-3	0.214, 2.29, 10.7
ACN	120*	506 ± 25	113 ± 7	9.7 ± 0.1	920 ± 20	0.089, 0.63

As one can see, multiexponential functions were required to model the experimental data. To attribute the exponential components to different processes, additional information is needed. It can be useful to compare the lifetimes to the literature data on the solvation times in different solvents.

Also, decay associated spectra (DAS) and their comparison to the steady-state may be of great help.

D131 dye

D131 in MeOH DAS are shown in fig. 2.9. The following observations can be made: (i) DAS τ_4 is similar to the spectral features of the neutral form (NF) of D131 (literature data on the maximum wavelength is taken from [18]), (ii) a part, assigned to SE in DAS τ_2 and τ_3 is blue shifted with respect to the steady state fluorescence spectrum and (iii) DAS τ_1 is similar to the steady-state absorption and emission spectra (obtained in this work) and also to that of deprotonated form (DF) [18].

On the basis of these observations, the following hypothesis on the deactivation mechanism can be put forward. A summary of this hypothesis is depicted in fig. 2.10. The deprotonated form prevails in the solution of D131 in MeOH. The time components are attributed to $S_1 \rightarrow S_0$ transition and solvation dynamics. The $S_1 \rightarrow S_0$ transition of the protonated form occurs with the lifetime τ_4. Concerning the deprotonated form, two major processes can be put forward: the solvation shell relaxation with lifetimes τ_2 and τ_3 and the $S_1 \rightarrow S_0$ transition which occurs with a lifetime τ_1.

The values of τ_2 and τ_3 are similar to those found in the literature and are then attributed to the solvation dynamics. Indeed, the time constants of 17.7 ps and 3.08 ps compared to 15.3 ps and 3.2 ps solvation times in MeOH measured with C153 by Maroncelli group [16] are very close. In the DAS of τ_2 and τ_3, the GSB is almost absent. A large negative signal of the SE is blue-shifted when compared to steady-state fluorescence. The positive signals in the regions 530 nm - 734 nm and 590 nm - 734 nm in the DAS for τ_3 and for τ_2, respectively, are not attributed to ESA but to the bathochromic shift of the SE with these time constants.

A completely different picture is observed in the system D131 in acetonitrile. The DAS are reported in fig. 2.11. Part of spectrum around 400 nm was not considered in the analysis, as the shape of curves didn't permit the straightforward interpolation after correction for pump signal. In the same way, literature data from Dr. M. Ekimova thesis [18] is added to help the interpretation. The first comment to make on the data is that the steady state absorption and emission, as well as the component at 113ps (τ_2), correspond to the neutral form of the dye, making the major difference with the solution in methanol, for which the DF of the dye prevails in solution. Then, the spectral data on the deprotonated form of the dye corresponds to the DAS for τ_1 and for τ_3. While the τ_1 is most likely the lifetime of $S_1 \rightarrow S_0$ transition, τ_3 also represents a process that decreases the concentration of the S_1 deprotonated form in the system. It is probably the protonation of the dye in its excited state. In favour of this interpretation, one can note positive amplitudes in the spectral regions that correspond to the neutral form (440-460 nm, 600-750 nm). The second argument that supports this interpretation is the higher electronic density on the anchor group after the photo-excitation, as shown in chapter 1. This higher density must affect the equilibrium between the protonated and deprotonated forms in favour of the first one. Finally, the τ_4 component can be attributed to the solvation dynamics. Indeed,

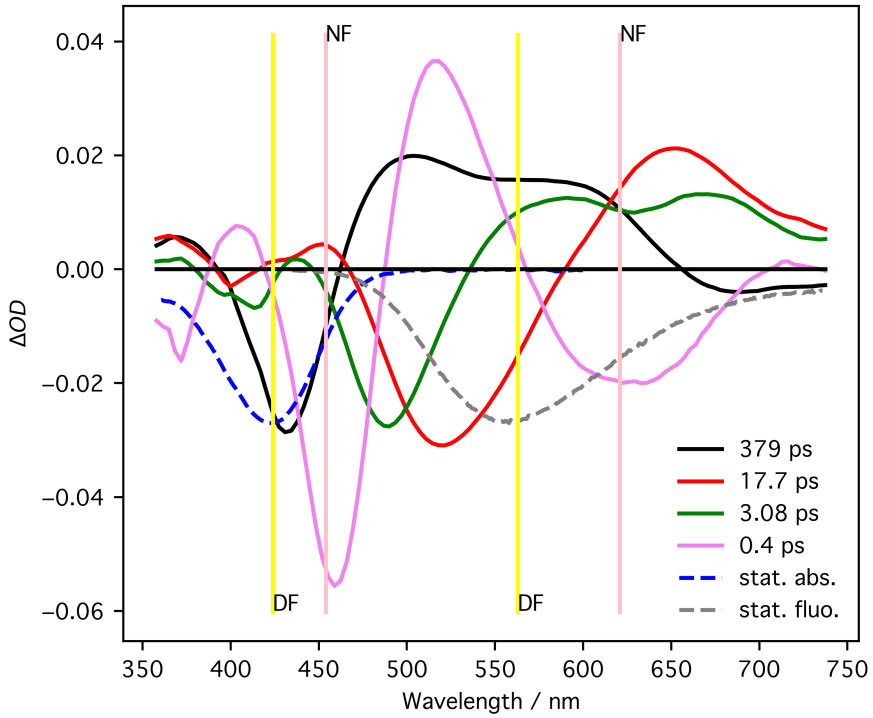

Figure 2.9: Decay associated spectra of D131 in MeOH (solid curves). The time components are presented as follows: τ_1=379 ps (black curve), τ_2=17.7 ps (red), τ_3 = 3.08 ps (green), and τ_4=0.4 ps (dark pink). Steady-state absorption and emission are shown as blue and grey dashed curves, respectively. The identifications of NF and DF were taken from the thesis of Dr. Maria Ekimova. The steady-state UV-Vis absorption and fluorescence spectra maxima of the NF and the DF of D131 in MeOH [18] are shown as yellow and pink vertical lines, respectively. The longer wavelength vertical line corresponds to the data on fluorescence.

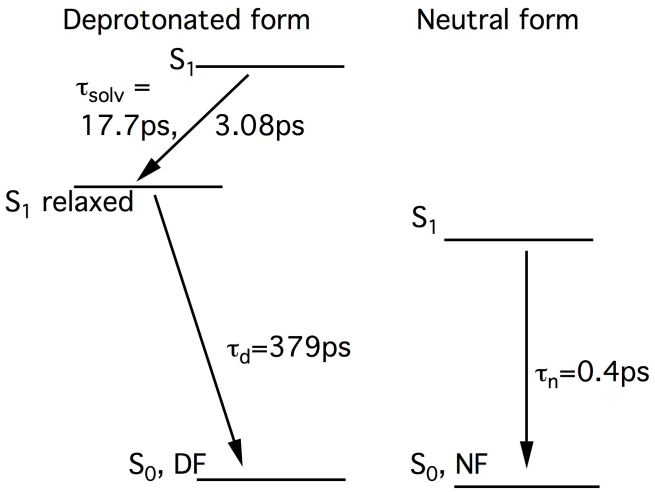

Figure 2.10: The hypothesis on the deactivation mechanism of the D131 dye in MeOH.

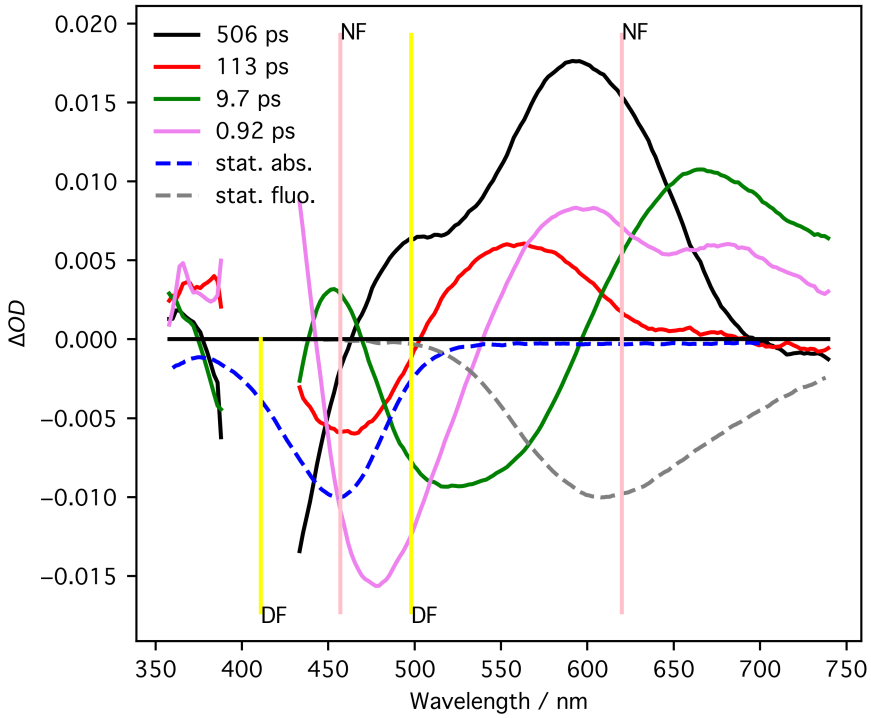

Figure 2.11: Decay associated spectra of D131 in ACN (solid curves). The time components are presented as follows: τ_1=506 ps (black curve), τ_2=113 ps (red), τ_3 = 9.7 ps (green), and τ_4=0.92 ps (dark pink). Steady-state absorption and emission are shown as blue and grey dashed curves, respectively. The steady-state UV-Vis absorption and fluorescence spectra maxima of the NF and the DF of D131 in ACN [18] are shown as yellow and pink vertical lines, respectively. The longer wavelength vertical line corresponds to the data on fluorescence.

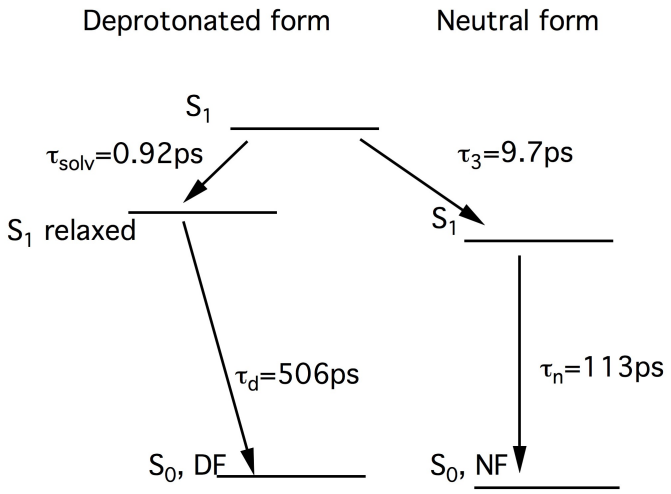

Figure 2.12: The hypothesis on the deactivation mechanism of the D131 dye in ACN.

a similar time order was found in literature, as shown in table 2.7. The deactivation mechanism hypothesis D131 in acetonitrile is illustrated in fig. 2.12.

Although methanol and acetonitrile solutions exhibit completely different behaviour, they have one interesting point in common. This point is, of course, interesting from the purely fundamental point of view. It is that the deprotonated form of the dye represents the longest lifetime of the excited state relaxation to the ground state. Future work may clarify this curious observation.

Acetonitrile and methanol are the two solvents, that are suitable to compare, as they have similar dielectric constant and viscosity, but different hydrogen bond donor ability. This last is, obviously, playing a dominant role in the fact that the neutral form of the dye prevails in acetonitrile and the deprotonated form prevails in methanol solution, with all the changes in the following dynamics. Much smaller lifetime of neutral form of the dye in methanol than in acetonitrile hints the possibility of the additional mechanism of deactivation due to the hydrogen bond network in methanol solution.

To get a more elaborated picture of the deactivation mechanism of the indoline dyes, the dye photophysics in the solvent with different polarity and viscosity must be examined. Thus, TA of D131 in DMSO measurements were performed, and the results are shown in table 2.7 and in fig. 2.13. Although the analysis of neutral and deprotonated forms was not found in literature, several interesting conclusions can be made.

Pump pulse and the solvent interaction results in appearance of coherent artefacts due to the Raman scattering. Because of this part of the signal, the fastest component must have been introduced. The DAS of the longest component τ_1 resembles the steady-state absorption to a large extent. It corresponds to the $S_1 \rightarrow S_0$ transition. This long component is the most probably the lifetime of the deprotonated form, as for the indoline dyes this form has longer lifetime than the neutral form. Finally,

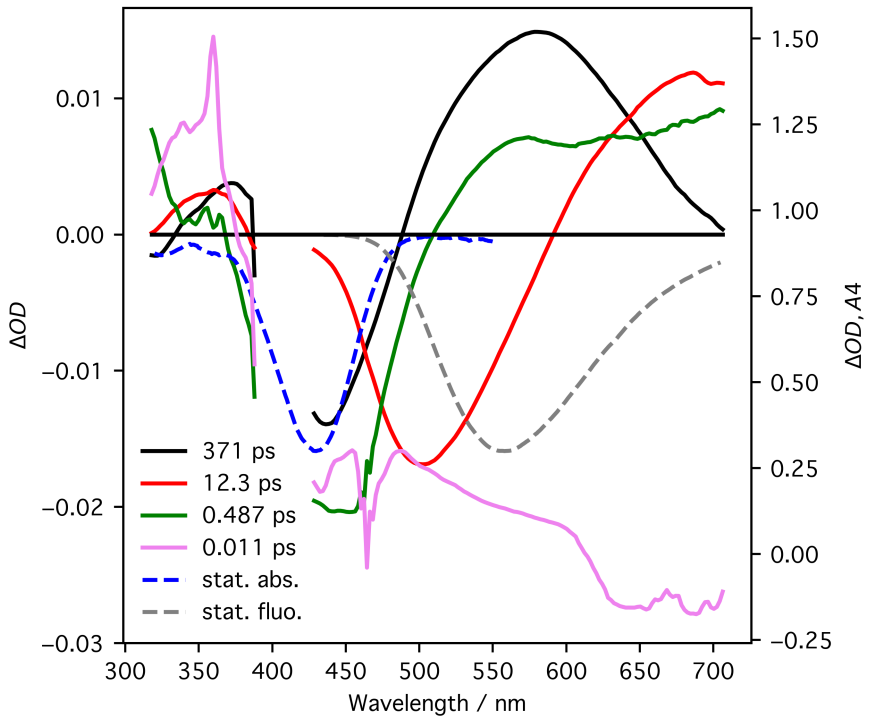

Figure 2.13: Decay associated spectra of D131 in DMSO (solid curves). The time components are presented as follows: τ_1=371 ps (black curve, left ordinate), τ_2=12.3 ps (red, left ordinate), τ_3 = 0.487 ps (green, left ordinate), and τ_4=0.011 ps (dark pink, right ordinate). Steady-state absorption and emission are shown as blue and grey dashed curves, respectively.

the characteristic shift of DAS τ_2 and τ_3 indicates that these time components may be attributed to the solvation dynamics. One can notice as well that the short component of the solvation dynamics τ_3 can be possibly mixed with the decay of the neutral form, as the DAS exhibits a broad negative signature, only slightly shifted to the red from the GSB of τ_1.

Dimethylsulfoxide is a solvent that has higher dielectric constant (also higher polarisability and dipolarity, cf. [19], but lower Lippert-Mataga polarity value) and viscosity than acetonitrile. If one compares the excited state lifetime of deprotonated form in acetonitrile and that in DMSO, one can see that the second is shorter. As the viscosity rarely has negative effect on the excited state lifetime [20], on can conclude that the lifetime of D131 is decreasing with the dielectric constant. This result is in contrast with the multivariate regression analysis of average fluorescence lifetime, discussed above in this chapter. However, the fluorescence intensity decays may give ambiguous results, as they don't give the information about the species present in the solution and may be wavelength dependent. At the same time, the neutral form lifetime is much shorter than that in acetonitrile and is of the time scale of that in methanol. This may hint that the HB acceptor ability of the solvent, high for DMSO (SB=0.647, [19]) and MeOH (SB=0.545, [19]), but low for acetonitrile (SB=0.286, [19]) play a dominant role in the deactivation process of the excited state of neutral form.

D102, D149 and D205 dyes

As it is mentioned in literature [18], D102 dye spectra are much less sensitive to the shift of protolitic equilibrium in the solution of the dye: while the spectral shift between neutral and anionic forms of D131 in methanol was found to be 1590 cm^{-1}, that of the D102 dye in the same solvent is only of 330cm^{-1}. This decrease in spectral sensitivity can be ascribed to the fact that the -COOH group of D102 is not conjugated with the chromophore core of the molecule, unlike the case of D131 (see fig. 1.1). Indeed, -COOH anchor is linked to the rhodanine acceptor moiety by -CH_2 group.

Apart from the gap between the anchor group and the chromophore, the rhodanine acceptor replaces the cyanide group in the structure of the D102 molecule. In general, rhodanine is considered as a strong electron density acceptor group. Its size is favourable for the extension of the conjugated system and shift of absorption in the region of interest.

The D149 and D205 molecules structures are designed similar to D102: anchor group is separated from the chromophore by saturated CH_2 group. Considering these two molecules helps to shed light on the effect of the second rhodanine ring and also that of octyl chain. As it was seen in chapter 1, bathochromic spectral shift, due to the larger conjugated chromophore, is observed.

The DAS of D102 in methanol are shown in fig. 2.14. Due to a small difference in the steady-state spectra of neutral and deprotonated forms, the TA spectra of different forms are difficult to be distinguished. This complicates the interpretation of the DAS. In spite of this, steady-state and the longest component can be clearly attributed to the deprotonated form, that obviously dominates in the solution. Two faster components, τ_2 and τ_3 have characteristic solvation dynamics profile: absence of ground state bleach, blue-shifted stimulated emission and positive amplitudes to the red. The fastest component (τ_4, shown in pink in fig. 2.14) exhibits Raman

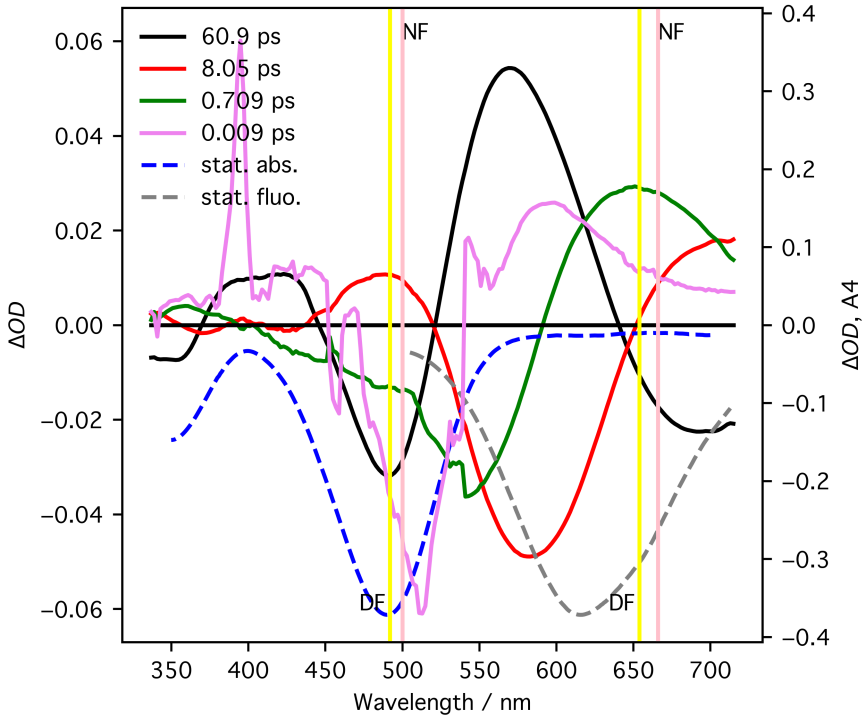

Figure 2.14: Decay associated spectra of D102 in MeOH (solid curves). The time components are presented as follows: τ_1=60.9 ps (black curve, left ordinate), τ_2=8.05 ps (red, left ordinate), τ_3 = 0.709 ps (green, left ordinate), and τ_4=0.009 ps (dark pink, right ordinate). Steady-state absorption and emission are shown as blue and grey dashed curves, respectively. Data from the thesis of Dr. Maria Ekimova is shown as vertical lines: steady-state spectra maxima of neutral and deprotonated forms of D102 in MeOH in pink and yellow, respectively.

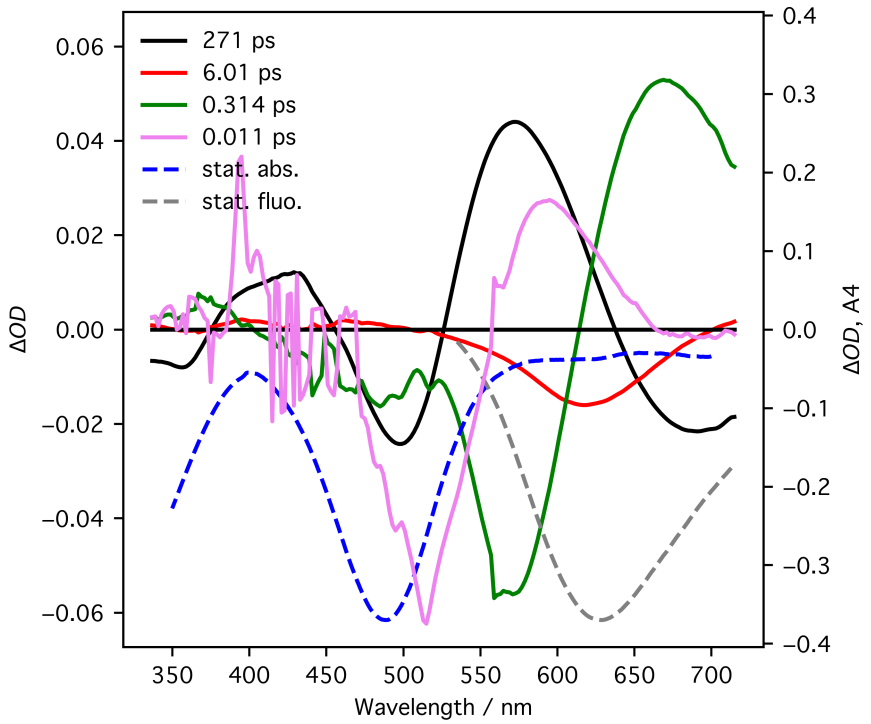

Figure 2.15: Decay associated spectra of D102 in ACN (solid curves). The time components are presented as follows: τ_1=271 ps (black curve, left ordinate), τ_2=6.01 ps (red, left ordinate), τ_3 = 0.314 ps (green, left ordinate), and τ_4=0.011 ps (dark pink, right ordinate). Steady-state absorption and emission are shown as blue and grey dashed curves, respectively.

features with wide Stokes contribution and positive amplitudes in the range 550 nm - 734 nm. Thus, we suggest that this time component represents not only the coherent artefacts, but also the part of solvation dynamics that is within the time resolution of the set-up.

The D102 DAS in acetonitrile and in dimethylsulfoxide are shown in fig. 2.15 and in fig. 2.16, respectively. On these graphs, the fastest component τ_4 (0.011 ps for ACN and 0.008 ps for DMSO) within the time resolution also exhibits clear Raman features. The longest component τ_1, 271 ps and 388 ps in ACN and DMSO, respectively, corresponds to the relaxation of excited state to the ground state.

The DAS of time components 0.011 ps and 0.314 ps in acetonitrile carry clear solvation dynamics features. Broad SE band of the component 6.01 ps in acetonitrile corresponds to additional excited state relaxation.

Considering D102 in DMSO DAS, the components 5.90 ps and 1.35 ps are attributed to the solvation dynamics due to their spectral shape. One should note that these constants are at least two times shorter than the ones reported by Maroncelli for C153, so other processes may be also entangled in the relaxation of the excited state.

D149 DAS in different solvents represent the best quality of experimental data that was acquired in this work. They are reported in fig. 2.17, fig. 2.18 and fig. 2.19. D149 in PeOH DAS is shown in fig. A.19.

D205 DAS are presented in fig. 2.20, fig. 2.21 and in fig. 2.22.

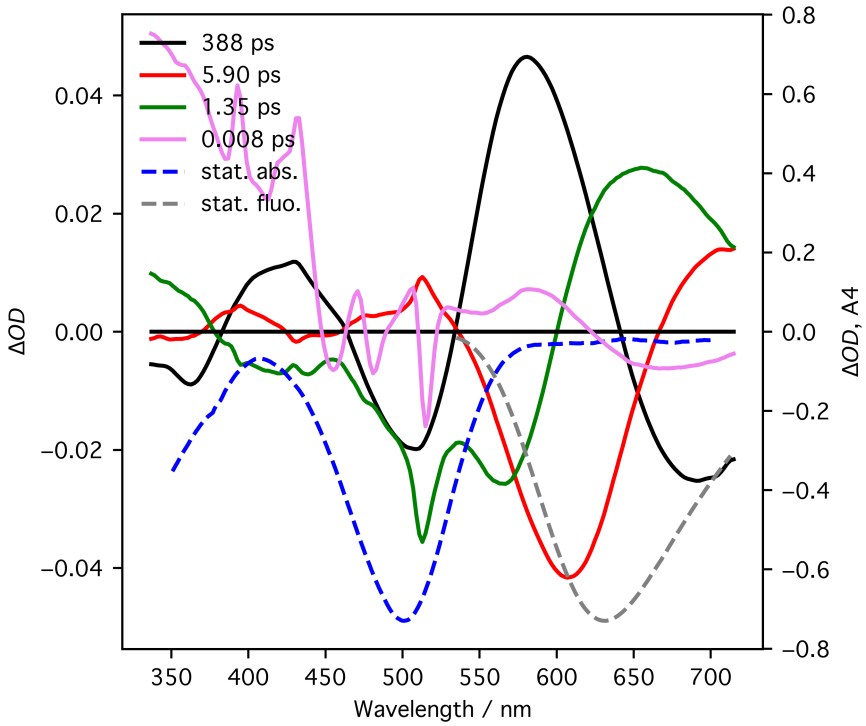

Figure 2.16: Decay associated spectra of D102 in DMSO (solid curves). The time components are presented as follows: τ_1=388 ps (black curve, left ordinate), τ_2=5.90 ps (red, left ordinate), τ_3 = 1.35 ps (green, left ordinate), and τ_4=0.008 ps (dark pink, right ordinate). Steady-state absorption and emission are shown as blue and grey dashed curves, respectively.

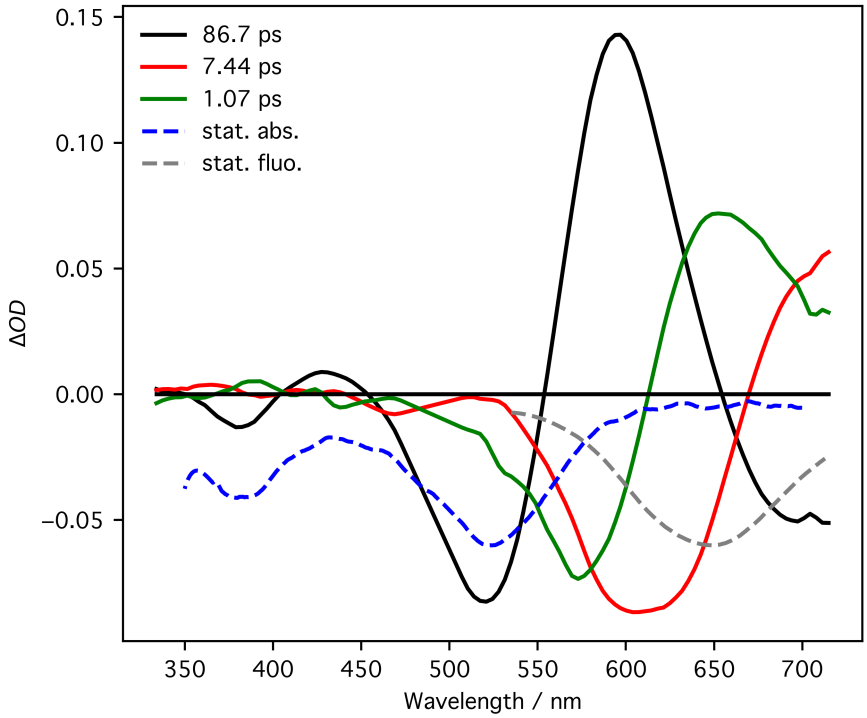

Figure 2.17: Decay associated spectra of D149 in MeOH (solid curves). The time components are presented as follows: τ_1=86.7 ps (black curve), τ_2=7.44 ps (red) and τ_3 = 1.07 ps (green). Steady-state absorption and emission are shown as blue and grey dashed curves, respectively.

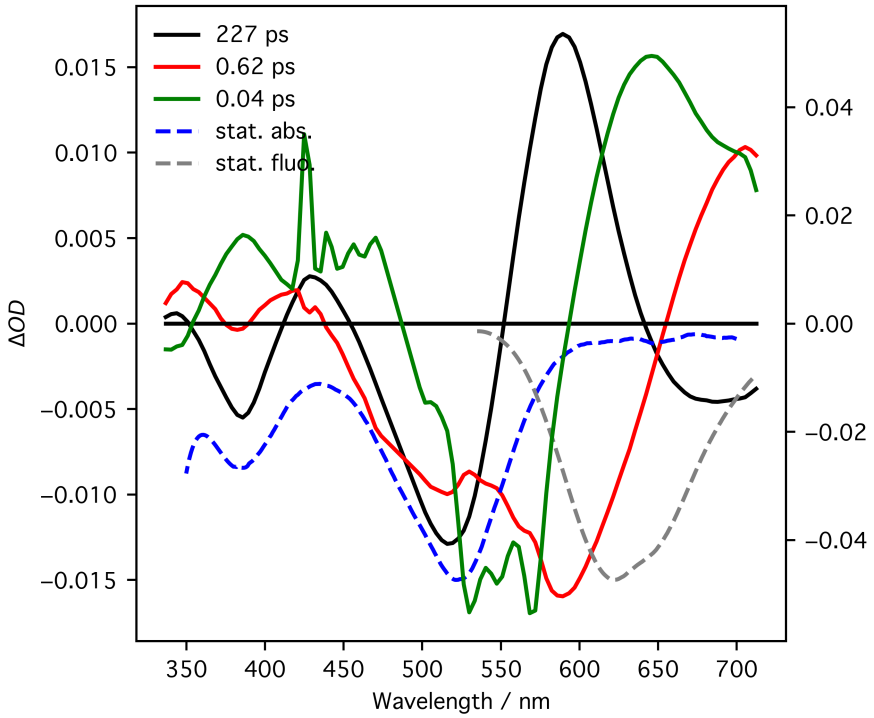

Figure 2.18: Decay associated spectra of D149 in ACN (solid curves). The time components are presented as follows: τ_1=227 ps (black curve, left ordinate), τ_2=0.62 ps (red, left ordinate) and τ_3 = 0.064 ps (green, right ordinate). Steady-state absorption and emission are shown as blue and grey dashed curves, respectively.

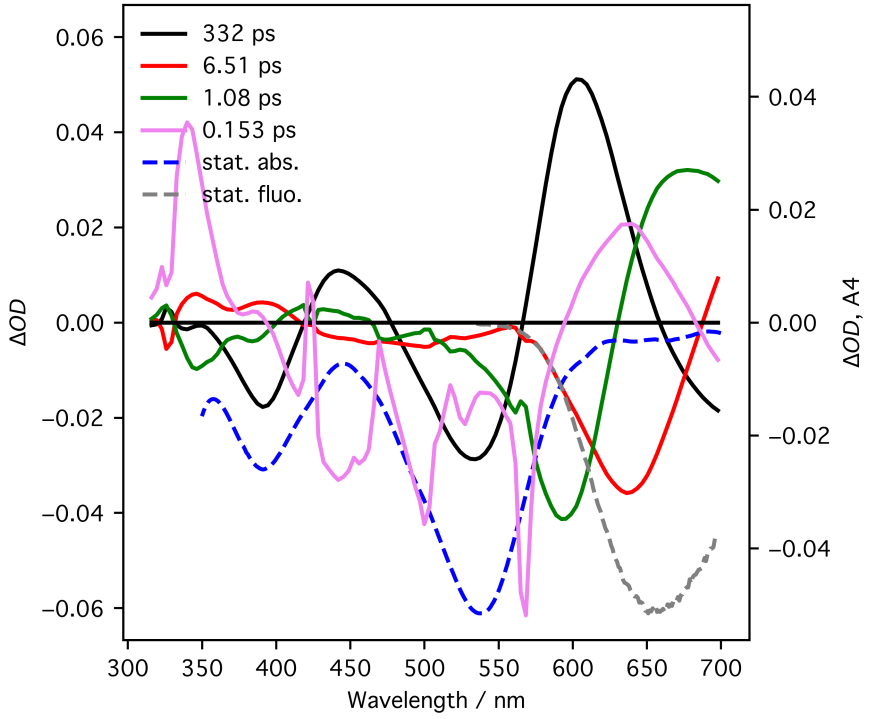

Figure 2.19: Decay associated spectra of D149 in DMSO (solid curves). The time components are presented as follows: τ_1=332 ps (black curve, left ordinate), τ_2=6.51 ps (red, left ordinate), τ_3= 1.08 ps (green, left ordinate) and τ_4= 0.153 ps (dark pink, right ordinate). Steady-state absorption and emission are shown as blue and grey dashed curves, respectively.

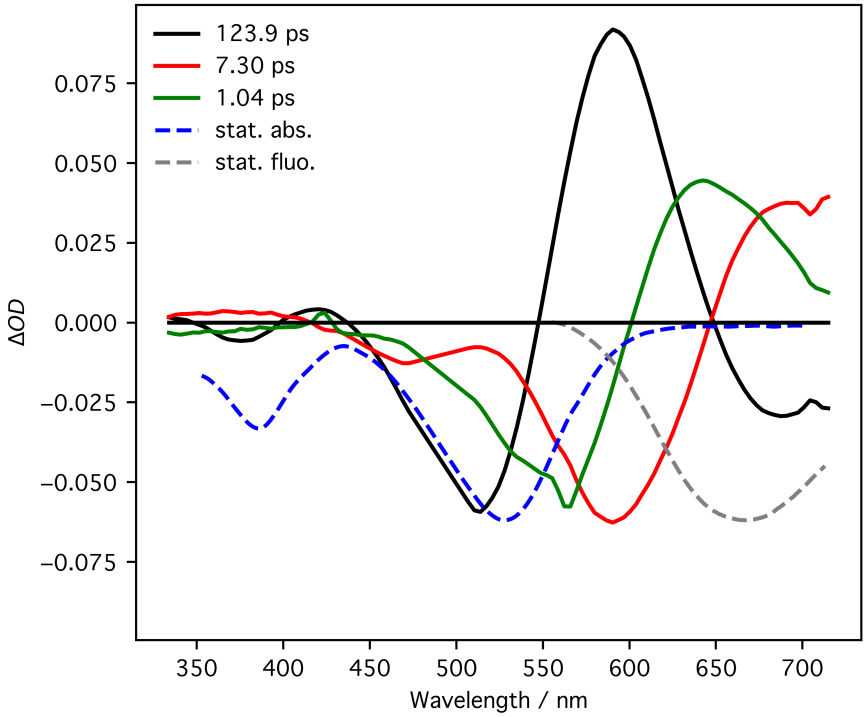

Figure 2.20: Decay associated spectra of D205 in MeOH (solid curves). The time components are presented as follows: τ_1=123.9 ps (black curve), τ_2=7.30 ps (red) and τ_3 = 1.04 ps (green). Steady-state absorption and emission are shown as blue and grey dashed curves, respectively.

D102, D149 and D205 photodynamics are very similar. The time constants are attributed for the same following processes: Raman scattering (the fastest component below the time resolution), solvation dynamics and S_1 to S_0 transition.

A summary of the comparison of the time constants, attributed to the solvation dynamics and those reported in literature for C153 [16], is presented in fig. 2.23. When one takes into account that the technique of measurement and the probe is different, a good accordance can be noted. Indeed, literature data were obtained using "golden probe"– the coumarin 153 molecule and fluorescence up-conversion set-up.

The times of relaxation from S_1 to S_0 in methanol, acetonitrile and dimethylsulfoxide are similar for D102, D149 and D205. As for lifetimes in methanol, they are particularly shorter than the lifetime of D131 and the lifetimes in DMSO and ACN. This hints an additional mechanism of excited state relaxation in protic solvents for D102, D149 and D205, probably introduced by its rhodanine rings and a more accessible twisting around the double bond that links acceptor and donor moieties of the molecule. The rotation around the double bond, that links donor and acceptor moieties is the one of the possible pathways of internal conversion and was considered in section 2.2. This motion may be hampered by the hydrogen bond, formed between the hydrogen atom of indoline and the oxygen or sulphur of the first rhodanine ring. In protic solvents, a solvent molecule may compete with indoline hydrogen for the electronegative atoms in the rhodanine ring. Thus, in absence of the stabilizing hydrogen bond, the twisting in a protic solvent becomes more effective.

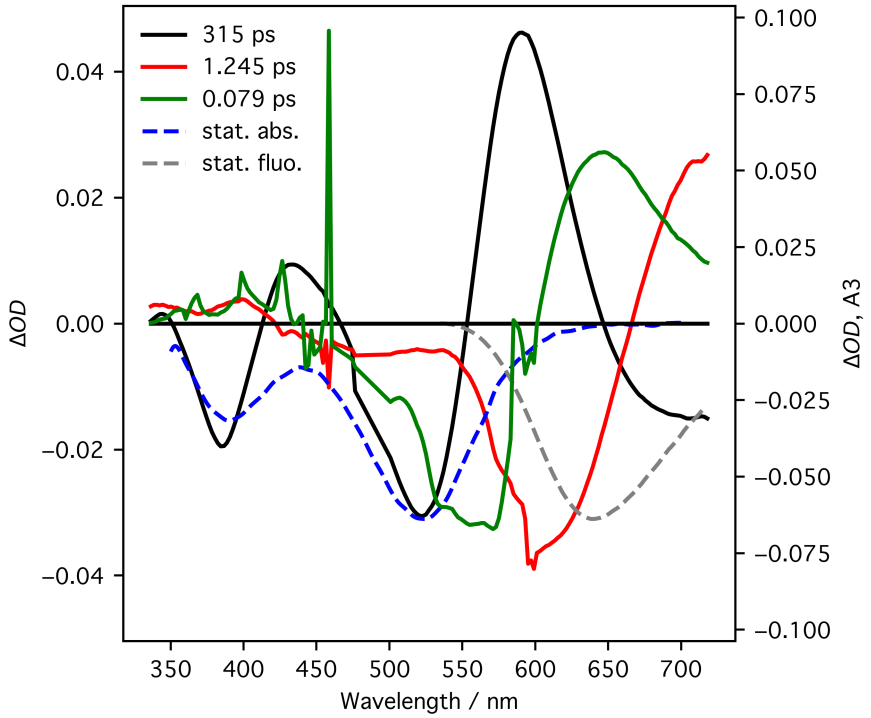

Figure 2.21: Decay associated spectra of D205 in ACN (solid curves). The time components are presented as follows: τ_1=315 ps (black curve, left ordinate), τ_2=1.245 ps (red, left ordinate) and τ_3 = 0.079 ps (green, right ordinate). Steady-state absorption and emission are shown as blue and grey dashed curves, respectively.

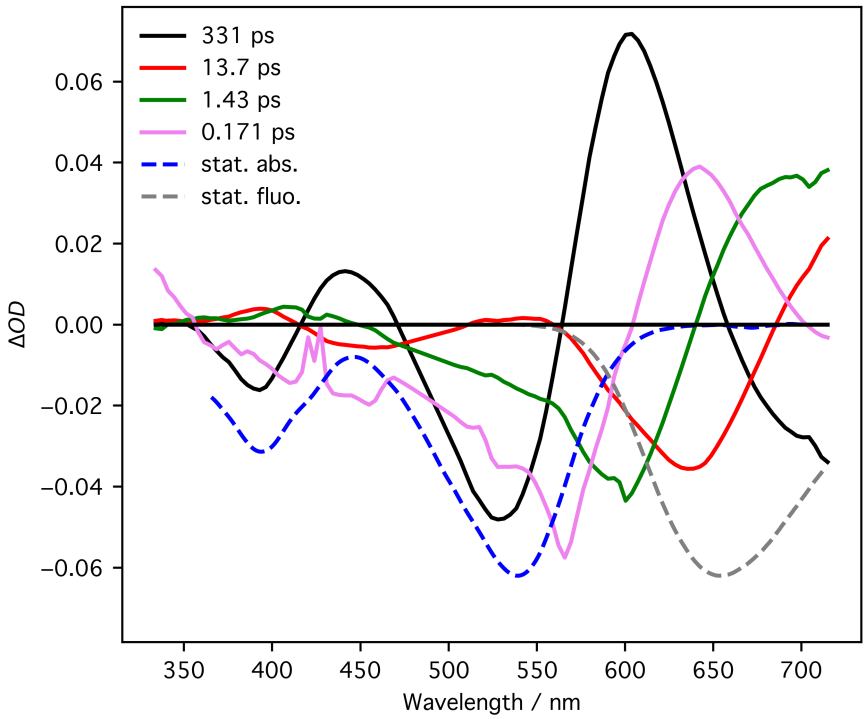

Figure 2.22: Decay associated spectra of D205 in DMSO (solid curves). The time components are presented as follows: τ_1=331 ps (black curve), τ_2=13.7 ps (red), τ_3= 1.43 ps (green) and τ_4= 0.171 ps (dark pink). Steady-state absorption and emission are shown as blue and grey dashed curves, respectively.

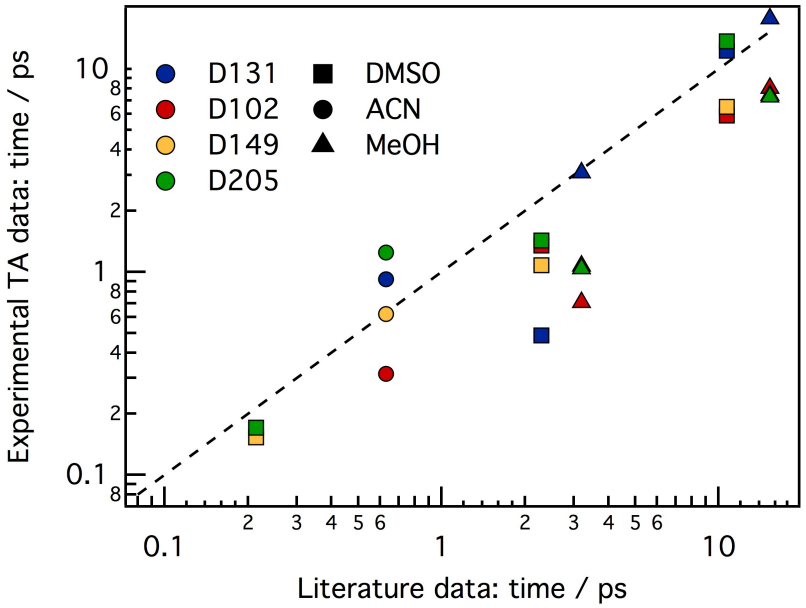

Figure 2.23: Comparison of solvation time constants, obtained for indoline dyes D131, D102, D149 and D205 with literature data, taken from [16] Colour code indicates the dye and the marker form indicates the solvent. Black dash line shows 1:1 correspondence.

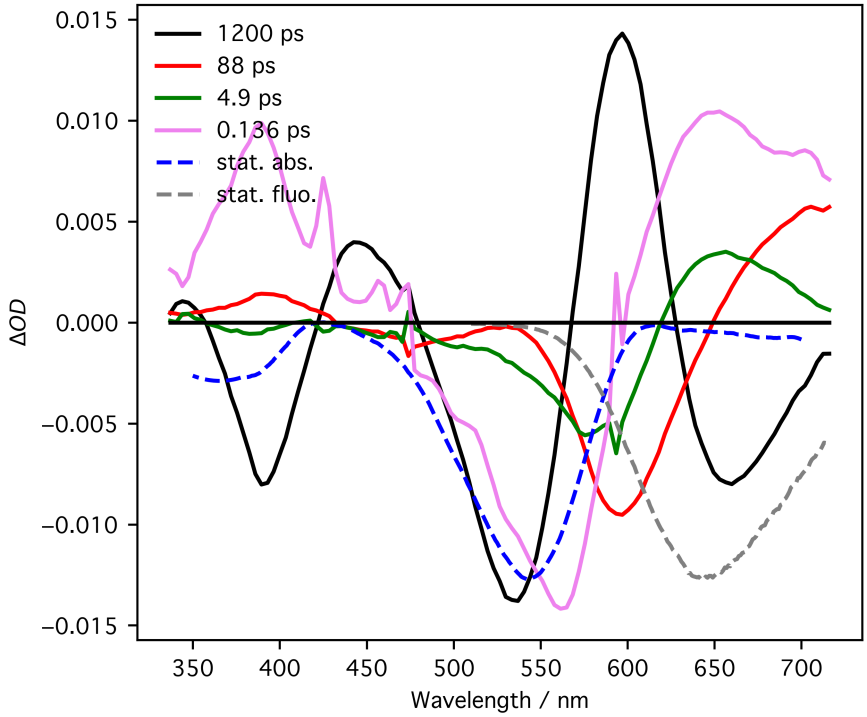

Figure 2.24: Decay associated spectra of D205 in $BmimBF_4$ (solid curves). The time components are presented as follows: τ_1=1200 ps (black curve), τ_2=88 ps (red), τ_3= 4.9 ps (green) and τ_4= 0.136 ps (dark pink). Steady-state absorption and emission are shown as blue and grey dashed curves, respectively.

Considering the lifetimes of D102, D149 and D205 in DMSO and ACN, they are all longer in DMSO than in ACN. The higher viscosity and polarity of DMSO can be a possible explanation.

D205 dye in ionic liquid $BmimBF_4$ and neat propylene carbonate

After the investigation of dyes' photophysics in conventional solvents, it was found that the main processes after the photo-excitation of dyes are the relaxation of the excited state to the ground state and the solvation dynamics.

As it was mentioned in the introduction, ionic liquids are good candidates for media in electrochemical devices, such as superconductors and dye sensitized solar cells[21]. Therefore, it is important to characterise the photophysics of indoline dyes in ionic liquids. The D205 dye, being the dye that exhibits the best performance in complete DSSC devices, was chosen to get an idea about the photophysics of indolines in ionic liquids. This decision is supported by the similarity of the photophysics of the D102, D149 and D205 dyes in conventional solvents.

Decay associated spectra of D205 in $BmimBF_4$ are presented in fig. 2.24.

The longest component, 1200 ps was fixed, being too long to fit the data in measured time window. This time constant was taken from the fit of the fluorescence decays (TCSPC), performed in this work. The spectrum of this component resembles to a large extent the steady state spectra of absorption and emission and clearly corresponds to the relaxation of excited state to the ground state. The three other components, 88ps, 4.9ps and 0.136ps have features, characteristic for solvation

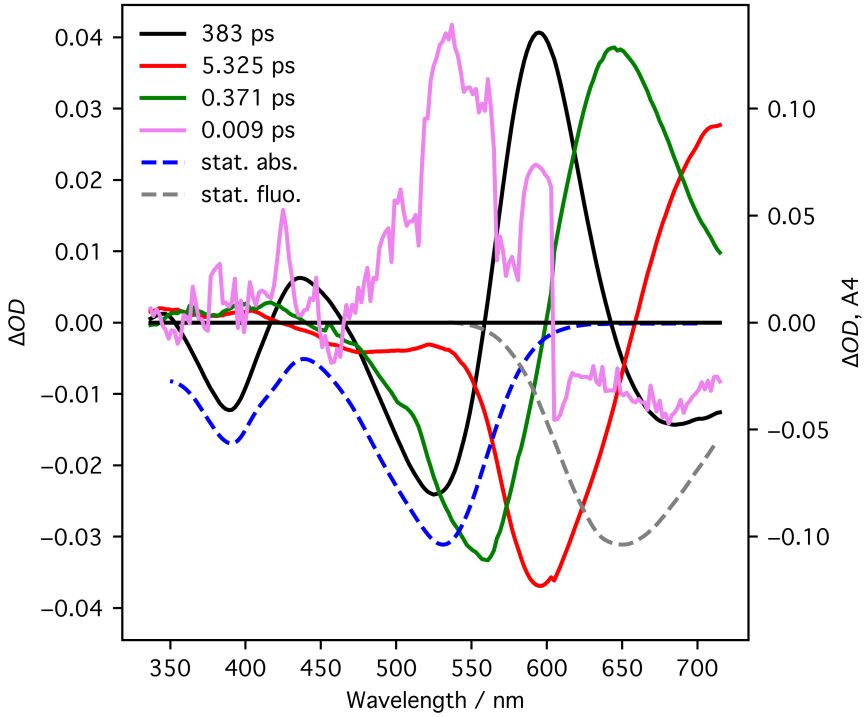

Figure 2.25: Decay associated spectra of D205 in PC (solid curves). The time components are presented as follows: τ_1=383 ps (black curve, left ordinate), τ_2=5.325 ps (red, left ordinate), τ_3= 0.371 ps (green, left ordinate) and τ_4= 0.009 ps (dark pink, right ordinate). Steady-state absorption and emission are shown as blue and grey dashed curves, respectively.

dynamics. The component of 0.136ps also carries the coherent artefacts due to the $BmimBF_4$. Therefore, the photophysics of the D205 dye in ionic liquid is very similar to its photophysics in organic solvents.

Ionic liquids (ILs) are often mixed with non-volatile conventional solvents (molecular solvents, MS), like propylene carbonate or γ-butyrolactone in order to reduce the viscosity and facilitate the charge transport. This is particularly important for DSSC efficiency. The transient absorption measurements were carried in the neat $BmimBF_4$ and in the neat propylene carbonate.

Decay associated spectra of D205 in the neat propylene carbonate are shown in fig. 2.25. In this figure, the longest component was attributed to S_1 to S_0 deactivation, components 0.371 ps and 5.325 ps are attributed to the solvation dynamics, and the component below the time resolution was added to model the Raman signal from propylene carbonate (PC).

In summary, the same processes as in conventional solvents are characteristic for D205 dye solutions in the ionic liquid $BmimBF_4$ and PC. These processes are S_1 to S_0 deactivation and solvation dynamics. In literature, the latter process was found to be not mono-exponential in conventional organic solvents, and demanding complex models in ionic liquids and their mixtures. In view of the complexity of this process and its high importance in photochemical reactions etc., different methods are needed to get its clear understanding (time-resolved measurements, molecular dynamics and quantum chemical simulations etc.). While the situation with the

conventional solvents is relatively understood, solvation dynamics in ionic liquids and their mixtures with molecular solvents is very little explored [22–25].

2.4 TCSPC measurements of the solvation dynamics of D205 in ionic liquids and IL/MS mixtures

In this section, time-resolved fluorescence measurements of D205 in the given media are presented. The ionic liquids BmimTFSI, $BmimBF_4$ and mixtures of $BmimBF_4$ with propylene carbonate were chosen due to a number of literature data available on these systems: density and conductivity [26], Raman and Infrared spectroscopy [15], NMR [27, 28], dielectric spectroscopy [29] and molecular dynamics simulations [30]. The molecular structures of $Bmim^+$ cation, $TFSI^-$ and BF_4^- anions and of propylene carbonate are presented in fig. 2.26.

According to the definition, solvation dynamics is accessed through the time evolution of the fluorescence emission spectrum in approximation that only process that contributes to the decrease of excited state energy is the solvation shell relaxation (eq. 2.8). Thus, emission spectra at different times after the excitation must be measured. When the measurements are made in kinetic mode, i.e. the decays and not the spectra are acquired, the spectra can be reconstructed, following the procedure, explained in the article of Maroncelli [16].

$$C(t) = \frac{\nu(t) - \nu(10.032ns)}{\nu(32ps) - \nu(10.032ns)} \tag{2.8}$$

In this work, fluorescence intensity decays were measured at 17 different emission wavelengths, covering the complete fluorescence spectrum. The decays were modelled with multiexponential functions, convoluted with IRF, in the same manner as it is explained in the beginning of Chapter 2. After, lifetime components and their amplitudes were used for time resolved spectra reconstruction.

The matrix that contains the intensities at different wavelengths in a row and at different times in a column, must be simply transposed to switch from the kinetic to spectral mode. However, the spectra, achieved in this way, are not corrected for detector sensitivity dependence on wavelength, nor for monochromator efficiency dependence. These may be possible reasons for distortion of the shape of time-resolved spectra. Therefore, the spectra were corrected using steady state spectra

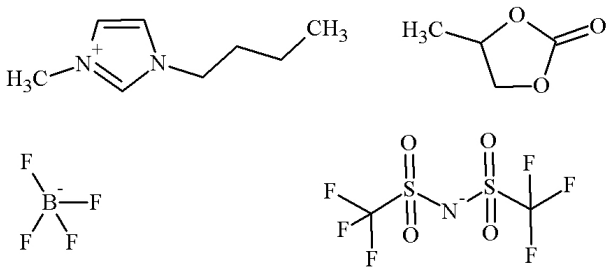

Figure 2.26: Chemical structures of $Bmim^+$ cation (top left), BF_4^- anion (bottom left), PC (top right) and $TFSI^-$ anion (bottom right).

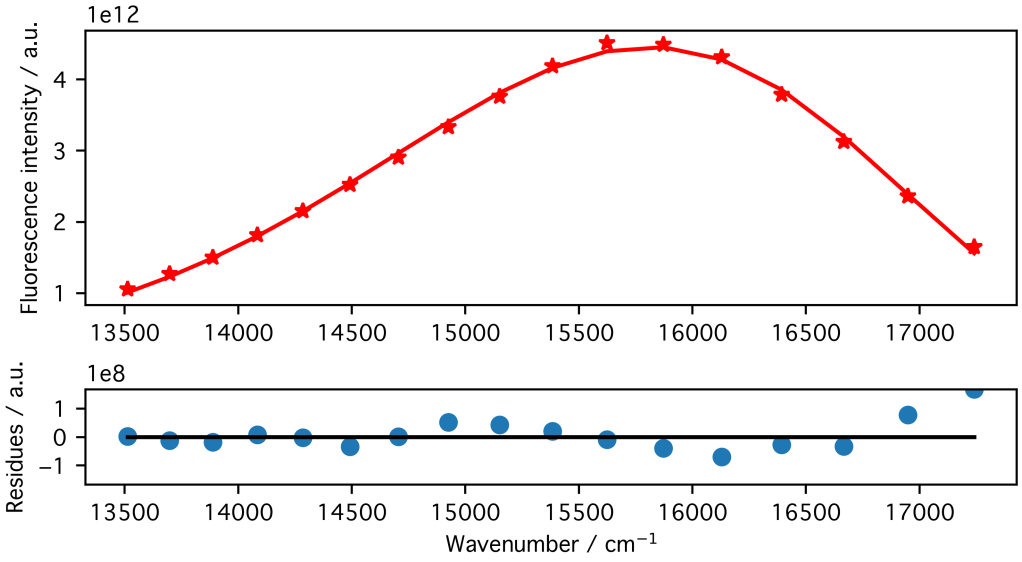

Figure 2.27: D205 in $BmimBF_4$ time-resolved fluorescence spectrum at 72 ps after the photo-excitation (points, top panel) and its lognormal fit (line, top panel), fit residuals (points, bottom panel).

shape, in the way that the integral under the decay is proportional to the intensity in steady-state spectrum $S(\lambda)$ at the same emission wavelength (eq. 2.9). The area under the kinetics, modelled as a sum of n exponentials, is simply the sum of amplitude and lifetimes products.

$$I_{corr}(t,\lambda) = \frac{S(\lambda)}{\sum_{i=1}^{n} A_i(\lambda)\tau_i(\lambda)} \sum_{i=1}^{n} A_i(\lambda)\exp(-\frac{t}{\tau_i(\lambda)}) \tag{2.9}$$

Using corrected amplitudes, time-wavelength matrix was constructed with time step of 4ps, starting from 32ps and up to 10ns. Such a time window was imposed by the time resolution of TCSPC set-up and the lifetime of indoline molecules. Each spectrum was converted in wavenumber scale, using a λ^2 factor and modelled with a simplified lognorm function (eq. 2.10) [31]. The quality of fit was evaluated visually, plotting experimental and theoretical data for randomly chosen time points as well as residuals dependence on wavenumber (see fig 2.27). Levenberg-Marquardt algorithm was used for the fit.

$$I(\nu) = I_0\exp(-\beta^2[\ln\frac{\nu - a}{b}]^2) \tag{2.10}$$

This form of lognormal function permits the calculation of maximum and mean wavenumbers, full width half maximum and asymmetry in a simple way (eq. 2.11, 2.12 , 2.13, 2.14).

$$\nu_{max} = a + b \tag{2.11}$$

$$\nu_{mean} = a + b\exp(\frac{3}{4\beta^2}) \tag{2.12}$$

$$FWHM = 2b\sinh(\frac{\sqrt{\ln 2}}{\beta}) \tag{2.13}$$

$$\rho = \exp(\sqrt{\ln 2}/\beta) \tag{2.14}$$

First moment wavenumber ν_{mean} time dependence was used to calculate the solvation response function (SRF). After the fit of TCSPC decays, all the data analysis was performed with python coded program, available upon request.

SRFs of D205 in BmimBF$_4$, BmimTFSI and mixtures are shown in fig. 2.28. On these figure, one can see that the solvation dynamics is largely finished after 1.5ns. As the data was plotted in semilogarithmic scale, a conclusion about the multi-exponential character of the solvation dynamics can be made. This result is in accordance with the observation, described in literature.

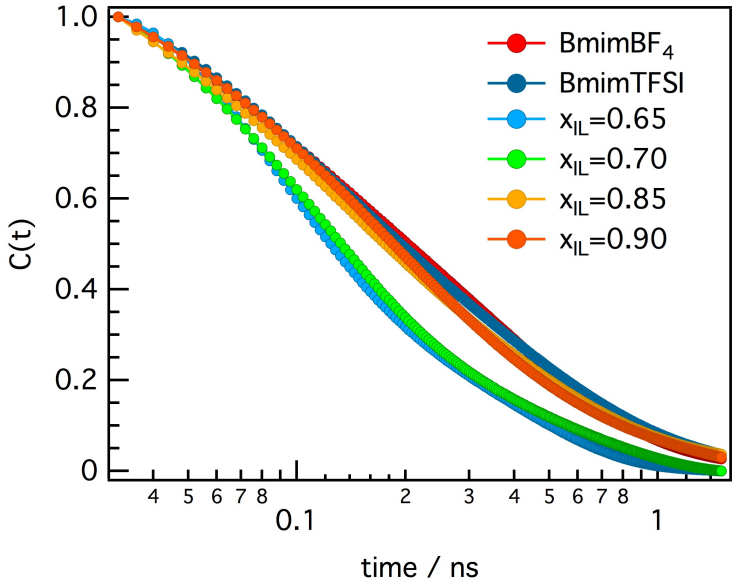

Figure 2.28: Solvation response functions of solutions of D205 in $BmimBF_4$, BmimTFSI and in mixtures of $BmimBF_4$/PC with ionic liquid molar fractions x_{IL}=0.90, 0.85, 0.70 and 0.65.

Importantly, the solvation response functions, that are calculated starting from 32 ps, can be modelled with a sum of exponentials, and these times obtained in such a way can be compared to the times, obtained with another methods, for example transient absorption. The best fit parameters are presented in table 2.8.

Solvation response obtained for D205 in $BmimBF_4$ was modelled with biexponential function, and the time constants of 384 ps and 69 ps were obtained. Long time component is certainly too long to be compared with transient absorption data, but the components of 69 ps and 88 ps (the time component in the DAS of D205 in this IL) are very similar.

Solvation response functions in BmimTFSI and mixtures were also modelled with biexponential functions. In BmimTFSI, the solvation times were found to be of the same order of magnitude as those of $BmimBF_4$, but slightly longer: 429 ps and 87

Table 2.8: The best fit parameters of D205 SRFs in ionic liquids and $BmimBF_4$/PC mixtures with x_{IL}=0.65, 0.70, 0.85 and 0.90: the time components of the solvation τ_1 and τ_2, the weight of the first time component % of τ_1 and average solvation time τ_{av}. The χ^2 parameter is also shown.

Solution	τ_1 / ps	τ_2 / ps	% of τ_1	τ_{av} / ns	χ^2
$BmimBF_4$	384	69	66	277	0.0031
BmimTFSI	429	87	56	279	0.0001
x_{IL}=0.65	305	71	37	158	0.0088
x_{IL}=0.70	506	96	27	206	0.0010
x_{IL}=0.85	384	84	54	246	0.0004
x_{IL}=0.90	438	127	44	263	0.0007

ps. in view of this similarity, dominant role of cation in the solvation dynamics of D205 can be anticipated.

Considering the fit of SRFs of D205 in mixtures, interesting results were obtained. Starting from the mixture with x_{IL}=0.70, the solvation time components are longer in mixtures than in the neat ionic liquid, on the contrary of expectations based on higher viscosity of the IL. However, the percentage of the longest solvation time component in IL is twice higher than that in the mixtures. Therefore, the weighted average solvation time parallels the viscosity of the solvent. Considering only the mixtures, the balance between the amplitudes of the solvation time components stays constant, but the time components themselves increase with the addition of the IL.

In summary, the solvation time components of D205 in $BmimBF_4$, obtained by TCSPC and transient absorption are in reasonable agreement. Also, due to the different time scales, not all the components can be compared. This results also from the multiregime solvation dynamics in ionic liquids and IL/MS mixtures.

-In order to understand the nature of these solvation time component, additional measurements, using a golden probe C153 were performed, covering 4 orders in a time range. Also, molecular dynamics simulations were made to get a mechanistic comprehension of the processes in ionic liquid and IL/MS mixtures.

Conclusions

Pursuing the same aim of understanding of the processes, taking place after the photo-excitation of the indoline dyes D131, D102, D149 and D205 in solutions, time-resolved electronic spectroscopy was applied. In this chapter, the results of these measurements are reported.

In agreement with the results from the first chapter, specific interactions were also found to have a large effect on the kinetics of excited state relaxation. Indeed, the excited state population decays in protic solvents (alcohols) are much shorter than in the aprotic solvents of similar polarity. Thus, we suggest that there is an additional mechanism of excited state relaxation through the hydrogen bonding. The indoline derivative with conjugated carbonyl group D131 showed clear difference in spectra of neutral and deprotonated forms. One can expect that the neutral species forms a hydrogen bonded complex with a HB donating solvent, and within the excitation, an ultrafast proton transfer occurs, and the dye returns simultaneously to the ground state. On the contrary, in aprotic solvents, the neutral form S_1 radiative relaxation to S_0 is significant.

Additionally, the deactivation channels through the ultrafast twisting around two exocyclic double bonds: one in the donor unit and one connecting the donor and acceptor moieties, are obviously responsible for the short lifetime of indoline derivated sensitizers.

Transient absorption spectroscopy confirms the equilibrium between the neutral and deprotonated forms of the molecule. While it is clearly seen from distinct spectral features of the different forms of the D131 molecule, conjugation break between the chromophore part of D102, D149 and D205 reduces the spectral difference between the forms. Using global analysis, lifetimes of neutral τ_n and deprotonated τ_d forms of D131 were obtained, the former being much faster than the latter in protic solvent methanol. In aprotic solvent acetonitrile, the lifetime of the neutral species is also faster than that of deprotonated ones, but longer than τ_n in methanol. In dimethyl

sulfoxide, τ_n is on the order τ_n in methanol, but the mechanism of the ultrafast deactivation is different. Most probably, high HB acceptor ability of DMSO plays a role.

Considering D102, D149 and D205 molecules, transient absorption treatment revealed that the main processes that take place after the photo-excitation are the solvation dynamics and $S_1 \rightarrow S_0$ deactivation. Solvation time constants, obtained from global analysis, are of the same order as the literature data on τ_{solv}, measured using coumarin 153 golden probe [16]. The difference between neutral and anionic species in spectral features and radiative constants is not visible in electronic spectra, as discussed above, but the general photophysics pattern is presumed to be maintained. The proposed photophysics scheme is shown in fig. 2.29.

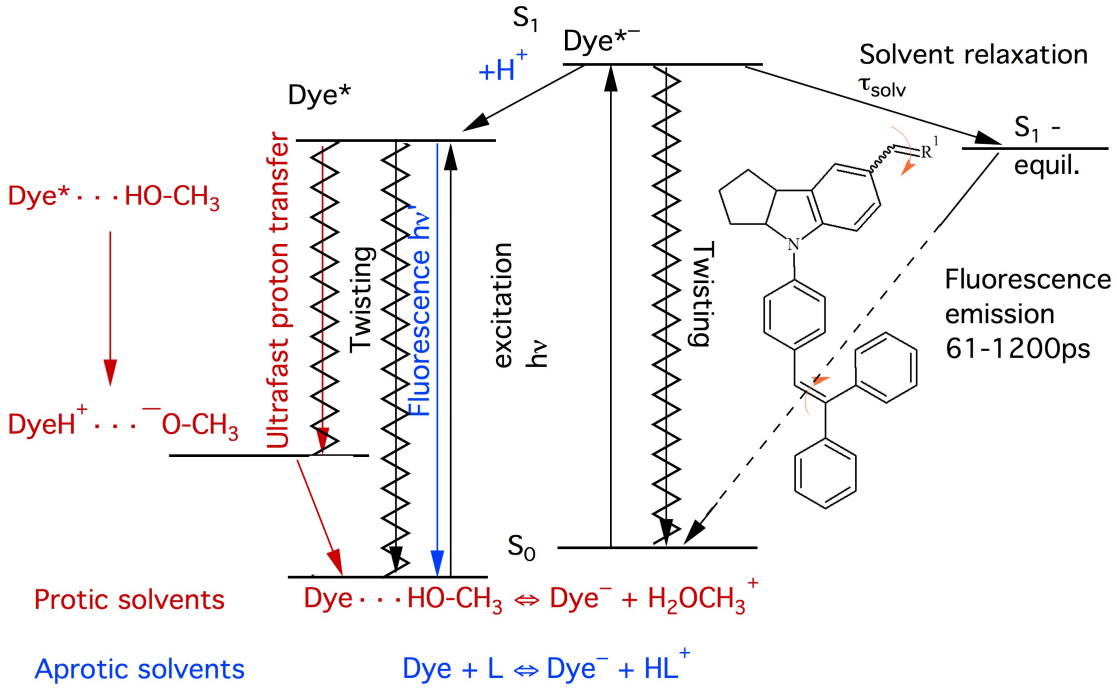

Figure 2.29: Indoline dyes D131, D102, D149 and D205 photophysics scheme, developed by the means of steady-state and time-resolved spectroscopies. The events in protic and aprotic solvents are given in red and blue, respectively. The events in black are the ones shared for both groups of solvents.

The photophysics of the most efficient among the studied dyes, D205, was also studied in ionic liquid $BmimBF_4$ and $BmimBF_4$/PC mixtures. Similarly to the solutions in organic solvents, solvation dynamics plays a major role in the excited state relaxation of D205 in ionic liquid, as shown by transient absorption results. Motivated by these findings, solvation response functions were reconstructed from measured fluorescence intensity decays and the similar time constant was obtained.

While the mechanism of the solvation dynamics in conventional organic solvents was addressed in literature, the situation with ionic liquids and especially IL/MS remains unclear. In order to elucidate the roles of mixture components, fluorescent probe C153 was used in time-resolved measurements and molecular dynamics simulations, reported in the following part of this thesis.

Bibliography

[1] M. Fakis, P. Hrobárik, E. Stathatos, V. Giannetas, and P. Persephonis, "A time resolved fluorescence and quantum chemical study of the solar cell sensitizer d149," Dyes and Pigments, vol. 96, no. 1, pp. 304 – 312, 2013.

[2] P. W. Lohse, J. Kuhnt, S. I. Druzhinin, M. Scholz, M. Ekimova, T. Oekermann, T. Lenzer, and K. Oum, "Ultrafast photoinduced relaxation dynamics of the indoline dye d149 in organic solvents," Phys. Chem. Chem. Phys., vol. 13, pp. 19632–19640, 2011.

[3] M. Fakis, E. Stathatos, G. Tsigaridas, V. Giannetas, and P. Persephonis, "Femtosecond decay and electron transfer dynamics of the organic sensitizer d149 and photovoltaic performance in quasi-solid-state dye-sensitized solar cells," The Journal of Physical Chemistry C, vol. 115, no. 27, pp. 13429–13437, 2011.

[4] A. M. El-Zohry, D. Roca-Sanjuán, and B. Zietz, "Ultrafast twisting of the indoline donor unit utilized in solar cell dyes: Experimental and theoretical studies," The Journal of Physical Chemistry C, vol. 119, no. 5, pp. 2249–2259, 2015.

[5] PicoQuant, FluoFit: User's Manual and Technical Data, Version 4.2.

[6] D. R. Lide, ed., CRC Handbook of Chemistry and Physics. Boca Baton, FL: CRC Press, 2005.

[7] J. Barthel, R. Neueder, and H. Roch, "Density, relative permittivity, and viscosity of propylene carbonate + dimethoxyethane mixtures from 25c to 125c," Journal of Chemical & Engineering Data, vol. 45, no. 6, pp. 1007–1011, 2000.

[8] S. Aparicio and R. Alcalde, "Characterization of two lactones in liquid phase: an experimental and computational approach," Phys. Chem. Chem. Phys., vol. 11, pp. 6455–6467, 2009.

[9] J. Salgado, T. Regueira, L. Lugo, J. Vijande, J. Fernández, and J. García, "Density and viscosity of three (2,2,2-trifluoroethanol+1-butyl-3-methylimidazolium) ionic liquid binary systems," The Journal of Chemical Thermodynamics, vol. 70, pp. 101 – 110, 2014.

[10] J. Catalán, "Toward a generalized treatment of the solvent effect based on four empirical scales: Dipolarity (sdp, a new scale), polarizability (sp), acidity (sa), and basicity (sb) of the medium," The Journal of Physical Chemistry B, vol. 113, no. 17, pp. 5951–5960, 2009.

[11] A. M. El-Zohry and B. Zietz, "Concentration and solvent effects on the excited state dynamics of the solar cell dye d149: The special role of protons," The Journal of Physical Chemistry C, vol. 117, no. 13, pp. 6544–6553, 2013.

[12] A. El-Zohry, A. Orthaber, and B. Zietz, "Isomerization and aggregation of the solar cell dye d149," The Journal of Physical Chemistry C, vol. 116, no. 50, pp. 26144–26153, 2012.

[13] J. Moll, S. Daehne, J. R. Durrant, and D. A. Wiersma, "Optical dynamics of excitons in j aggregates of a carbocyanine dye," The Journal of Chemical Physics, vol. 102, no. 16, pp. 6362–6370, 1995.

[14] N. Tkachenko, Optical Spectroscopy: Methods and instrumentations. Elsevier Science, 2006.

[15] N. E. Heimer, R. E. D. Sesto, Z. Meng, J. S. Wilkes, and W. R. Carper, "Vibrational spectra of imidazolium tetrafluoroborate ionic liquids," Journal of Molecular Liquids, vol. 124, no. 1, pp. 84 – 95, 2006.

[16] M. L. Horng, J. A. Gardecki, A. Papazyan, and M. Maroncelli, "Subpicosecond measurements of polar solvation dynamics: Coumarin 153 revisited," The Journal of Physical Chemistry, vol. 99, no. 48, pp. 17311–17337, 1995.

[17] S. Arzhantsev, H. Jin, G. A. Baker, and M. Maroncelli, "Measurements of the complete solvation response in ionic liquids," The Journal of Physical Chemistry B, vol. 111, no. 18, pp. 4978–4989, 2007.

[18] M. Ekimova, Time-resolved laser spectroscopy studies on dye molecules in ionic liquids. PhD thesis, Universitat Siegen, 2014.

[19] A. Filarowski, M. Kluba, K. Cieslik-Boczula, A. Koll, A. Kochel, L. Pandey, W. M. De Borggraeve, M. Van der Auweraer, J. Catalan, and N. Boens, "Generalized solvent scales as a tool for investigating solvent dependence of spectroscopic and kinetic parameters. application to fluorescent bodipy dyes," Photochem. Photobiol. Sci., vol. 9, pp. 996–1008, 2010.

[20] A. Vyšniauskas, M. Qurashi, N. Gallop, M. Balaz, H. L. Anderson, and M. K. Kuimova, "Unravelling the effect of temperature on viscosity-sensitive fluorescent molecular rotors," Chem. Sci., vol. 6, pp. 5773–5778, 2015.

[21] F. Hao and H. Lin, "Recent molecular engineering of room temperature ionic liquid electrolytes for mesoscopic dye-sensitized solar cells," RSC Adv., vol. 3, pp. 23521–23532, 2013.

[22] M. Liang, X.-X. Zhang, A. Kaintz, N. P. Ernsting, and M. Maroncelli, "Solvation dynamics in a prototypical ionic liquid + dipolar aprotic liquid mixture: 1-butyl-3-methylimidazolium tetrafluoroborate + acetonitrile," The Journal of Physical Chemistry B, vol. 118, no. 5, pp. 1340–1352, 2014.

[23] X.-X. Zhang, M. Liang, J. Hunger, R. Buchner, and M. Maroncelli, "Dielectric relaxation and solvation dynamics in a prototypical ionic liquid + dipolar protic liquid mixture: 1-butyl-3-methylimidazolium tetrafluoroborate + water," The Journal of Physical Chemistry B, vol. 117, no. 49, pp. 15356–15368, 2013.

[24] A. Stoppa, J. Hunger, G. Hefter, and R. Buchner, "Structure and dynamics of 1-n-alkyl-3-n-methylimidazolium tetrafluoroborate + acetonitrile mixtures," The Journal of Physical Chemistry B, vol. 116, no. 25, pp. 7509–7521, 2012.

[25] S. Daschakraborty and R. Biswas, "Composition dependent stokes shift dynamics in binary mixtures of 1-butyl-3-methylimidazolium tetrafluoroborate with water and acetonitrile: Quantitative comparison between theory and complete measurements," The Journal of Physical Chemistry B, vol. 118, no. 5, pp. 1327–1339, 2014.

[26] A. Stoppa, J. Hunger, and R. Buchner, "Conductivities of binary mixtures of ionic liquids with polar solvents," Journal of Chemical & Engineering Data, vol. 54, no. 2, pp. 472–479, 2009.

[27] P. D. Vu, A. J. Boydston, and C. W. Bielawski, "Ionic liquids via efficient, solvent-free anion metathesis," Green Chem., vol. 9, pp. 1158–1159, 2007.

[28] O. N. Kalugin, A. V. Riabchunova, I. V. Voroshylova, V. V. Chaban, B. A. Marekha, V. A. Koverga, and A. Idrissi, "Transport properties and ion aggregation in mixtures of room temperature ionic liquids with aprotic dipolar solvents," in Modern Problems of Molecular Physics (L. A. Bulavin and A. V. Chalyi, eds.), (Cham), pp. 67–109, Springer International Publishing, 2018.

[29] E. Thoms, P. Sippel, D. Reuter, M. Weiß, A. Loidl, and S. Krohns, "Dielectric study on mixtures of ionic liquids," Scientific Reports, vol. 7, no. 1, p. 7463, 2017.

[30] A. Mondal and S. Balasubramanian, "Quantitative prediction of physical properties of imidazolium based room temperature ionic liquids through determination of condensed phase site charges: A refined force field," The Journal of Physical Chemistry B, vol. 118, no. 12, pp. 3409–3422, 2014.

[31] T. Gustavsson, L. Cassara, V. Gulbinas, G. Gurzadyan, J.-C. Mialocq, S. Pommeret, M. Sorgius, and P. van der Meulen, "Femtosecond spectroscopic study of relaxation processes of three amino-substituted coumarin dyes in methanol and dimethyl sulfoxide," The Journal of Physical Chemistry A, vol. 102, no. 23, pp. 4229–4245, 1998.

Chapter 3

Fluorescent probe dependence of the solvation dynamics in ionic liquid $BmimBF_4$ and propylene carbonate mixtures

The material presented in this chapter forms the basis of publication

Smortsova, Y.; Miannay, F.-A.; Koverga, V.; Dubois, J.; Kalugin, O.; Idrissi, A. *Fluorescent probe dependence of the solvation dynamics in ionic liquid $BmimBF_4$ and propylene carbonate mixtures: a time-resolved fluorescence and quantum chemistry study.* J.Mol.Liq, submitted.

In this Chapter, the probe dependence of the solvation dynamics is investigated. Steady-state and time-resolved fluorescence measurements of solvation of C153, C102, 4-ANMP and PRODAN fluorescent probes in $BmimBF_4$ and $BmimBF_4$/PC mixtures with a molar fraction of ionic liquid equal to 0.65 and 0.85 are reported. Quantum chemical calculations were performed to complete the experimental data interpretation. All the four studied probes exhibit similar solvation dynamics, with their average solvation times following the trend 4-ANMP<C153 ≅ C102<PRODAN. A specific interactions hypothesis was put forward to explain the slight divergence of 4-ANMP and PRODAN spectra shift. The C153 molecule, showing a big change in dipole moment (8.7 D) upon the photoexcitation, little geometry relaxation upon the excitation due to its rigid structure, small change in dipole moment orientation and relatively small hydrogen bonding ability is thus proved to be the most adequate for use in the study of the solvation dynamics in various environments, including ionic liquids and ionic liquid/molecular solvent mixtures.

3.1 Introduction

A contribution of the solvation dynamics as one of the processes taking place in the solutions of chromophores after the photo-excitation is of great importance. This phenomenon was scrupulously studied in conventional organic solvents[1–3], ionic liquids (ILs)[4–7] and ionic liquid/molecular solvent (IL/MS) mixtures[8–10] by the means of picosecond and femtosecond time-resolved fluorescence spectroscopy, Kerr-gated emission measurements[11], dielectric spectroscopy, three-pulse photon echo peak shift (3PEPS)[12] and molecular dynamics simulations[13–15]. The information on the solvent response to the electric field perturbation is pertinent for the study of the reactions in solutions as well as photophysics of organic dyes after the photo-excitation. In this regard, ILs are the media of a particular interest. Because of their peculiar properties as high conductivity, thermal stability and extremely low vapour pressure, ILs are considered as "green solvents"and are good candidates for use in the supercapacitors [16], dye-sensitized solar cells (DSSCs)[17] and other electrochemical devices[18]. However, the high viscosity of the majority of the ionic liquids may hamper the charge transport, therefore ILs are often mixed with organic molecular solvents, like propylene carbonate, γ-butyrolactone and acetonitrile, thus increasing the conductivity of these systems[19]. The literature review concerning the solvation dynamics in such mixtures reveals a multi-regime response, similar to the one in neat ionic liquids that (i) extends up to several nanoseconds, (ii) strongly depends on the IL molar fraction (x_{IL}) and (iii) correlates with the microviscosity[8–10]. Gaussian, sum of exponentials, and stretched exponential mathematical forms were proposed to fit different components of the solvation response. The fastest Gaussian component was suggested to be due to the inertial motion of the solvent molecules/ions, while the structural reorganisation of IL was proposed as the origin of the longer multi-exponential component of the solvation response in regard of its strong correlation with viscosity. The molecular dynamics simulations[14, 15] addressed the role of translational and rotational motions in the solvation dynamics and revealed the major importance of the former ones, alike in the conventional solvents. Also, the decomposition to cation and anion as well as sole and pair (collective) components of the solvation dynamics was reported[15, 20], and the idea about the domination of the anion translation in the solvation dynamics was put forward[14].

In time-resolved fluorescence measurements, a fluorescent probe is used to monitor the shift of its fluorescence spectrum in time, and the solvation response functions (SRFs), achieved in this way, are then compared to the predictions of dielectric continuum theory and molecular dynamics. These functions are presumed to be independent of the used fluorescent probe, and the verification of this assumption has been the subject of a number of studies, involving a specific interactions importance analysis[21–23], search for molecularity (i.e. probe dependence of the solvation dynamics[24]) in ILs[25–27] and solute size and character of charge redistribution influence by molecular dynamics simulations[13]. In the early work of Karmakar et al. on the solvation dynamics of C153 and PRODAN in two ILs, $EmimBF_4$ and $BmimBF_4$[26], it was shown that solvation responses of the probes were biexponential. Minor difference between the two ILs was observed. The fast time component of the solvation responses was associated with the motion of the anions while the longest one with the motion of both cations and anions. The results were not dependent on the used probes. This was confirmed two years later by Maroncelli et al.: [25].

Interestingly, it was reported that rotational correlation times seemed to follow the hydrodynamic predictions as in conventional solvents meaning in few words that the biggest structure has the longest rotational correlation time. Although, recently the same group showed that the hydrodynamic predictions are not valid for the rotational correlation times of 4-AP compared to the ones of C153[27]. Futhermore, using a semi-molecular theory [28], Biswas et al. evidenced no significant probe dependence of the SRFs. To summarise the main results of literature on the probe dependence of the solvation dynamics processes in ILs, both theoreticians and experimentalists are according on the fact that the SRFs of the different probes are similar. These solvation responses are sometimes bi-exponential or nonexponential and the rotational correlation times do not follow the hydrodynamic predictions. It is worth noticing that there is a lack of proposed hypothesis on the interaction probe-ILs components that could explain these observations on solvation and rotational dynamics. Considering the choice of the solvation probes in literature, various derivatives of coumarin (e.g. C153 as the most popular molecule)[5, 6, 9, 22, 23], anilines[21], aminophthalimides[21, 23, 24, 27, 29], as well as PRODAN[26], DCS (4-dimethylamino-4'-cyanostilbene)[30] and ionic probes ([25]) were employed. The main result of these works is that the complexity of the solvation dynamics processes is affected by the large number of factors and in particular by specific solute-solvent interactions, resulting in up to two-fold differences in the solvation times and observed shift magnitudes.

Indeed, the Coumarin 153 was used in the seminal works of Maroncelli et al. to uncover the time scales of the solvation dynamics in conventional organic solvents, supporting the dielectric response theory predictions [1, 2, 5, 21]. This probe possesses a number of advantages with respect to the other probes: (i) its rigid structure prevents large geometry distortions and thus diminishes the possibility of non-radiative relaxation pathways, resulting in relatively high quantum yield and long lifetime of several nanoseconds; (ii) its large dipole moment change upon the photo-excitation causes large solvatochromic shift of fluorescence spectra with solvent polarity and facilitates the time-resolved measurements due to larger observed shift; (iii) a relatively low ability for the specific interactions like hydrogen bonding makes coumarin a neutral probe; (iv) an absorption spectrum centred around 400 nm and emission spectra situated around 520 nm facilitate the use of this probe in time-resolved fluorescence measurements. Another coumarin derivative, C102, possesses similar properties, but smaller change in dipole moment because of the absence of perfluorinated methyl group in its structure.

Unlike C153, the photophysics of PRODAN fluorescent probe, widely exploited for its extreme sensitivity to the environment [31–33], is still questioned. An emission from two excited states, close in energy in conventional solvents, was suggested[34, 35]. Along with the increase in dipole moment upon the excitation, the twisted excited state geometry makes it difficult to interpret the excited state dynamics. Mennucci et al.[36], performed quantum chemistry calculations, showing that the excited state involved in the emission is planar and that the dipole moment almost doubles within the excitation. The calculated twisted conformation was however attributed to an artefact of TD-B3LYP computational method. The shoulder on the blue edge steady-state emission of PRODAN in water solutions was interpreted as a signature of the aggregation of probe molecules[37]. In addition to the hydrogen bonding effect on the spectroscopic properties of this probe, specific interactions like π-π stacking

were found to take place in water solutions containing fulvic acids [38], suggesting a particular importance of this type of interaction.

The aminophthalimide derivatives are hydrogen bonding (HB) sensitive fluorescent probes. Indeed, large shift in fluorescence spectra and shorter fluorescence lifetimes were observed in alcohols[39]. The 4-ANMP, 3-AP and 4-AP hydrogen bonding behaviour was explored by the means of rotation coherence spectroscopy and infrared-optical double resonance spectroscopy of jet cooled water complexes[40, 41]. Interestingly, the cluster of 3-AP with a single water molecule shows strong hydrogen bonding with C=O group, but not with NH_2. While, the water dimer cluster of 4-ANMP and 4-AP bridge the NH_2 and the -C=O adjacent group. The 4-ANMP showed larger shift upon water complexation in fluorescence excitation spectra than 4-AP. The same group studied 4-ANMP by the emission following two-photon absorption technique and showed the emission from the upper states (S_n) [42]. The authors showed that the quantum efficiency of the one of such S_n-S_0 bands depends on the energy gap with respect to the S_1 state and, hence, the solvent relaxation. Peculiar nanosecond solvation dynamics of 4-AP and 4-ANMP was observed in mixtures of nonpolar and polar solvent, like toluene-ethanol, toluene-acetonitrile [43] and even 2-propanol-modified supercritical CO_2 [44]. A solvation shell reconstruction with preferential solvation by polar solvent molecules in the excited state was proposed as an explanation of this unusual behaviour. In these systems, translational motion plays an important role in the solvation dynamics, and the mixtures of IL/MS are very much alike in this way, although to our knowledge, no preferential solvation effects were observed.

Albeit the vast number of studies, the origin of the different behaviour of these probes is still not clear and needs further investigation. Also, the solvation dynamics probe dependence in IL/MS mixtures was not explored yet. The present study considers the solvation dynamics of the probes C153, C102, 4-ANMP and PRODAN (fig.3.1) in the $BmimBF_4$ IL and its mixtures with propylene carbonate ($x_{IL} = 0.65$ and 0.85). For this aim, steady-state electronic spectroscopy and time-resolved fluorescence experiments were performed as well as complementary quantum chemistry calculations of probes dipole moments and geometries optimisation in ground and excited states.

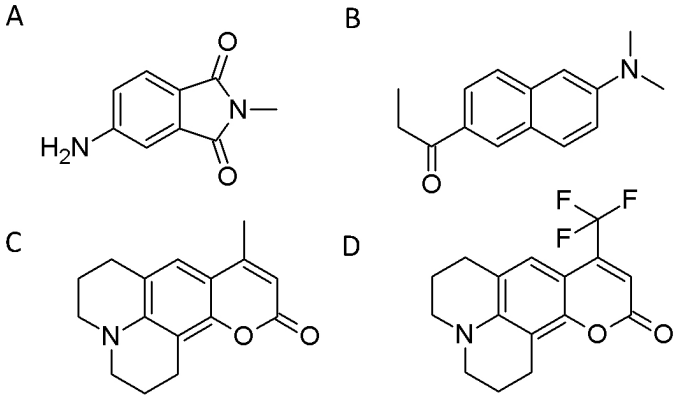

Figure 3.1: Fluorescent probes chemical structure: (A) - 4-ANMP, (B)- PRODAN, (C) - C102, (D) - C153.

The plan of this chapter is the following: first, we will detail the experimental

procedures and present the systems studied, as well as the data treatment performed. Second, the steady-state and time-resolved absorption and fluorescence spectroscopy results will be presented and discussed. Then, the quantum chemistry calculations, supporting the experimental work, will be introduced. The hydrogen bonding possibilities analysis and the possible explanations of solvation response molecularity will be discussed in the last section, before the conclusions of the work.

3.2 Steady-state absorption and fluorescence

The steady-state fluorescence spectra of 4-ANMP, PRODAN, C153 and C102 in $BmimBF_4$ IL and $BmimBF_4$/PC mixtures with x_{IL} = 0.65 and 0.85 are presented in fig.3.2.

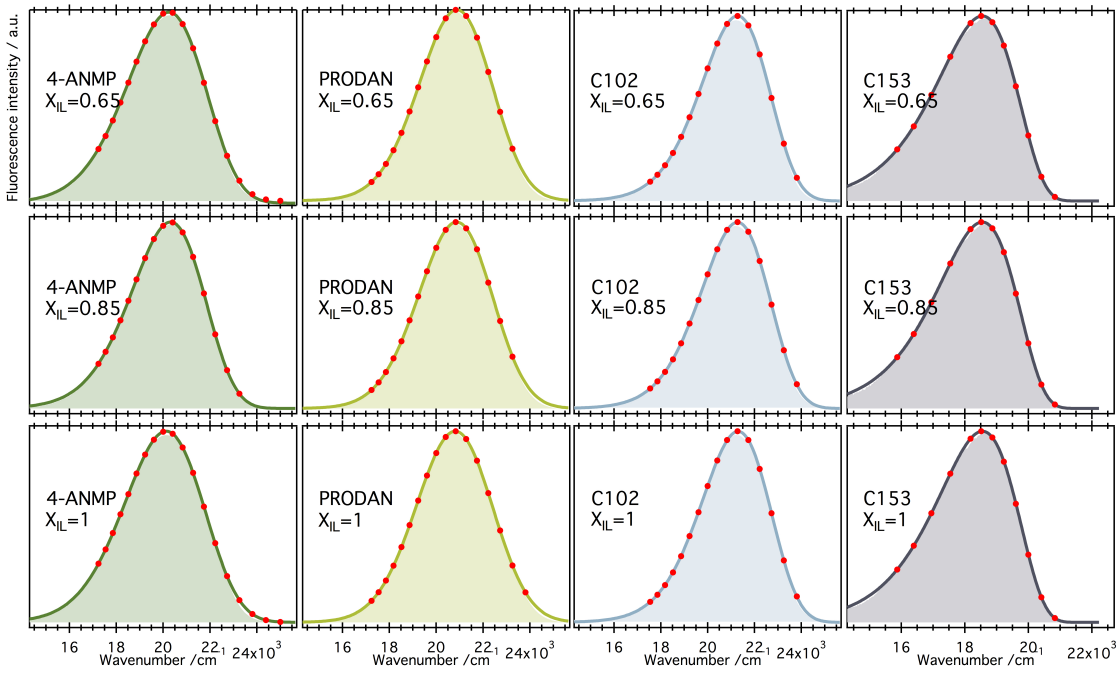

Figure 3.2: Steady-state fluorescence emission spectra of 4-ANMP, PRODAN, C102 and C153 fluorescent probes in $BmimBF_4$ IL and $BmimBF_4$/PC mixtures with x_{IL} = 0.65 and 0.85. Filled areas under the spectra represent the experimental spectra, solid lines are lognormal fit results and points show the wavenumbers chosen for TCSPC decays measurements.

As one can see from the graph, the fluorescence spectra are broad and structureless. The shape of these spectra is similar to those of the same probes in polar solvents. No significant shift of fluorescence and absorption spectra was observed in this range of x_{IL}.

The results of absorption and emission spectra analysis with lognormal distribution are presented in table 3.1. The fit parameters of the fluorescence spectra are more reliable than the ones concerning the absorption spectra. This is due to the fact that the absorption bands of the dyes are located in the blue region, on the edge of the visible and UV light, very close to the intense absorption bands of IL and PC in UV. Thus, the deconvolution of the probes' absorption spectra is complicated. Also, the absorbance of our samples was kept very low (less or equal to 0.1), so

the variations in the absorption spectra parameters for different mixtures must be taken with caution. However, the values of the peak wavenumber for absorption and fluorescence are in a good agreement with the reported ones in [5, 26], that are also presented in table 3.1.

Although all the probes show significant solvatochromism in conventional organic solvents[2, 36, 39, 45], no shift is observed for the fluorescence spectra in the different mixtures. Two possibilities may be explain this behaviour: (i) the preferential solvation by IL, giving essentially the same microenvironment of the probe in all the three systems; (ii) the same 'effective'polarity and energy of interactions that yields similar steady-state absorption results. According to our former time-resolved fluorescence anisotropy measurements in the similar IL/PC mixtures[9], the rotational correlation time of C153 is very different in this x_{IL} range, suggesting a large difference in its microenvironment. Thus, the steady-state results can be rationalized by the similar polarity and the interaction energy between the dye and mixture components.

To understand the energetics of solvation, it is interesting to compare the steady-state spectra of the probes in IL and in IL/MS mixtures with the results in conventional solvents. A comprehensive solvatochromism analysis of C153 was performed by Gustavsson et. al., the FWHM and the spectra centroid data for C153 in 18 different solvents being published[22]. In our systems, the absorption spectra mean wavenumber of C153 ($23.49{\cdot}10^3$ cm^{-1}) is close to the one in formamide and ethyleneglycol ($23.83{\cdot}10^3$ cm^{-1} and $23.88{\cdot}10^3$ cm^{-1}, respectively). As it is reported in table 3.1, the FWHM is in the same range as that obtained in organic conventional solvents. Our fluorescence spectra mean wavenumber of C153 is very close to the one in ethanol ($17.83{\cdot}10^3$ cm^{-1}), the peak wavenumber is also very close to ethanol ($18.53{\cdot}10^3$ cm^{-1})[23], the FWHM being unusually narrow (see table 3.1). The Stokes shift of C153 is close to the values in diethyl ether, THF and ethyl acetate. Our PRODAN fluorescence peaks are close to the acetonitrile value ($21.3{\cdot}10^3$ cm^{-1}) [35] in consistency with the E_T^N (empirical normalized parameters of solvent polarity) of acetonitrile (0.46) and the one of the IL estimated by Karmakar and Samantha [26] (0.50). The large emission red shift of 4-ANMP in protic solvents was reported in literature[39]; in the present work, the fluorescence band of 4-ANMP in IL is red-shifted in comparison to the acetonitrile (488nm and 470 nm, respectively), following the Reichardt polarity scale trend for aprotic solvents. Thus, given the particular hydrogen bonding sensitivity of 4-ANMP, we made a conclusion that the hydrogen bonding between 4-ANMP (as an acceptor) and IL doesn't play a significant role. However, one should note that the dipolar solvents, possessing high basicity don't cause a large shift in the fluorescence of 4-ANMP, although the hydrogen bonding between the NH_2 group of 4-ANMP and solvent molecules is anticipated. Thus, we cannot exclude the hydrogen bonding formation between the 4-ANMP amino group (as a donor) and IL anion.

The $FWHM$ of 4-ANMP fluorescence spectrum is the largest among the probes studied. The excitation spectra of 4-ANMP in $BmimBF_4$, recorded at different emission wavelengths (fig.3.3) are identical in shape to the absorption spectra, indicating the presence of only one species in the ground state in the solution and the absence of heterogeneity in the IL. Thus, one can conclude that the energy of solvation in IL must be close to the one in polar organic solvents, like formamide, ethylene glycol and THF. This corroborates the results known from literature when comparing Kamlet-Taft dipolarity/polarizability parameters for ILs with conventional

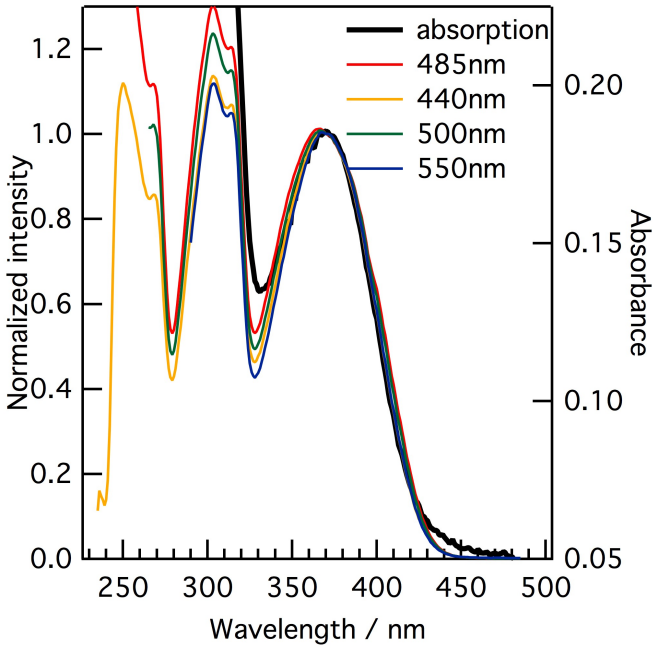

Figure 3.3: 4-ANMP in $BmimBF_4$ absorption (bold black curve) and excitation spectra at 485nm, 440nm, 500nm and 550nm emission wavelengths.

organic solvents (0.96 vs 0.83 for the IL and PC, respectively) [46, 47].

In summary, taking into account only the steady-state data, all the fluorescent probes give similar information on the media studied: (i) a similar polarity of ILs and its mixtures with PC; (ii) the energetics of solvation in IL and IL/PC mixtures is close to the solvation in polar organic solvents.

Table 3.1: Peak (ν_{peak}) and mean (ν_{mean}) wavenumbers, full width half maxima ($FWHM$) (in 10^3 cm^{-1}) of measured absorption and fluorescence spectra of C153, C102, 4-ANMP and PRODAN fluorescent probes in $BmimBF_4$ and $BmimBF_4$/PC mixtures.

System	Absorption			Fluorescence				
	ν_{peak}	ν_{mean}	$FWHM$	ν_{peak}	ν_{mean}	$FWHM$	$\Delta\nu$	$\Delta\nu^c_{obs}$
				C153				
$BmimBF_4$	23.28, 23.49[a]	23.49	3.82	18.55, 18.66[a], 18.62[b]	17.87	3.05	5.63	0.75
x_{IL}=0.85	23.39	23.66	3.74	18.55	17.87	3.04	5.79	0.59
x_{IL}=0.65	23.4	23.61	3.8	18.55	17.86	3.06	5.76	0.63
				C102				
$BmimBF_4$	25.66	25.95	4.01	21.3	20.92	3.48	5.03	1.13
x_{IL}=0.85	25.83	26.28	3.76	21.27	20.91	3.47	5.37	1.05
x_{IL}=0.65	25.76	25.84	3.76	21.28	20.91	3.47	4.94	0.86
				4-ANMP				
$BmimBF_4$	26.8	26.81	5.1	20.13	19.81	4.03	7	1.02
x_{IL}=0.85	26.9	26.9	4.41	20.32	19.91	3.72	7	0.77
x_{IL}=0.65	26.78	26.79	4.25	20.24	19.88	3.92	6.91	0.77
				PRODAN				
$BmimBF_4$	27.77	27.78	5.04	20.81	20.70, 21.05[b]	3.83	7.08	1.45
x_{IL}=0.85	27.9	27.9	5.1	20.87	20.71	3.7	7.19	1.51
x_{IL}=0.65	27.4	27.41	4.3	20.88	20.71	3.68	6.7	1.4

[a] - from ref [5], [b] - from ref [26], [c] - values of the observed spectral shift in time-resolved fluorescence experiments

3.3 Time-resolved fluorescence spectra

Solvation dynamics was calculated from the time-resolved emission spectra, reconstructed according to the procedure reported in the data treatment section. Intensity normalized TRES and time-resolved area normalized emission spectra (TRANES) are reported in appendix (figs. B.1 to B.3 and figs. B.4 to B.6, respectively). The latter representation of TRES was proposed by Periasamy [48, 49]. In our case, no isoemissive points were found in TRANES. As was stressed by the authors, the presence of the isoemissive point doesn't mean itself that two fluorescent species exist in the sample and a solid chemical foundation is needed to claim this fact. The absence of isoemissive points in mixture with $x_{IL} = 0.85$ and 0.65 and in neat IL can be rationalized by the possibility of the solvation dynamics occurring at the same time scale. We performed additional measurements of the time-resolved fluorescence anisotropy for 4-ANMP at different emission wavelengths and observed no dependence of neither the limiting anisotropy nor the rotational correlation time, thus rejecting the hypotheses about the heterogeneity of the IL and its mixtures and dual emission of the probe.

The measured SRFs are shown in fig.3.4. As it can be observed, they roughly overlap for the different fluorescent probes. The best overlap between the various probes' responses was achieved for the neat IL solution. We suppose that the mixtures preparation could also induce slight discrepancies for the different fluorescent probes.

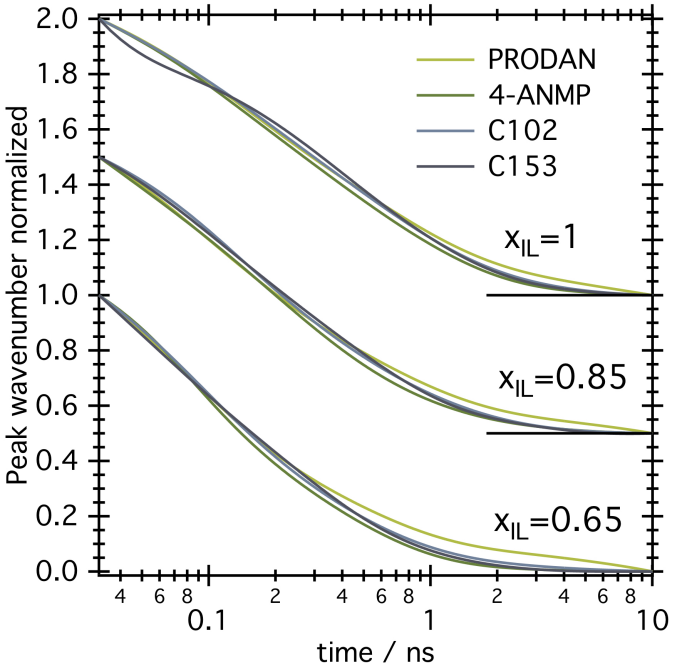

Figure 3.4: SRFs (eq.2.8) of C153, C102, 4-ANMP and PRODAN fluorescent probes in $BmimBF_4$ and $BmimBF_4$/PC mixtures.

To understand the fraction of the solvation response observed in the time scale of our experiment of 32ps-10ns, we rely on the estimation of Gustavsson et al.[22], that introduced the value of $4.85{\cdot}10^3$ cm^{-1} Stokes shift due to purely intramolecular contribution of C153. The total (from steady-state) and time-resolved observed shift are given in table 3.1. Thus, we can presume that in our TCSPC experiment,

we observe about $(100\% \cdot \frac{0.75}{5.64-4.85} = 95\%)95\%$ of the total shift. The large length-scale collective motions that emerge on the picosecond time scales, dominated by translational motion may lead to these slow relaxation dynamics [15]. A glass type solvation dynamics with characteristic deformation and reformation of the cage of neighbours was put forward by Arzhantsev et al. in the study of the solvation in various ILs [11]. Thus, the structure of the first solvation shell seems to play an important role at such longer times and one should expect very similar solvation response from different fluorescence probes.

The SRFs (eq.2.8) were analysed with multiexponential and stretched exponential models to estimate the time components and the average solvation times (eq.3.1 and3.2). The results are presented in tables3.2 and3.3.

$$C(t) = \sum_{i=1}^{n} B_i \exp(-\frac{t}{\tau_{si}}); \sum_{i=1}^{n} B_i = 1 \tag{3.1}$$

$$C(t) = \exp(-(\frac{t}{\tau_s})^{\beta}) \tag{3.2}$$

Although the SRFs of the different probes are fairly close, the solvation times do show significant difference. Indeed, the average solvation times are rather close for C153 and C102, being insignificantly longer for C102 molecule. The solvation times characteristics of 4-ANMP are faster than the ones of the former two probes, but still conserving the trend. As observed during our time-resolved measurements, the typical fluorescence decay of the 4-ANMP is almost 6 times longer than the ones of the other probes (fig.3.5), decreasing the resolution of the short time components on the initial stage of TRES reconstruction. The PRODAN solvation times are about 1.2-1.8 times longer than the other three. The long tail in PRODAN solvation response doesn't vanish completely at 10 ns, therefore the obtained long time components of the fit should be considered with caution. All the probes exhibit an increase of the average solvation time upon addition of the IL. Interestingly, the probes solvation times follow the trend PRODAN>C102 $\cong$ C153>4-ANMP. A similar trend in integral solvation times (PRODAN=C102>C153) was found by Ito et al.[25] in their investigation of solvation dynamics in $BmimPF_6$ IL. Mandal and Samanta[50] performed measurements in $BmimBF_4$ and in other ILs, but no pattern of the solvation time variation was identified. The 4-ANMP probe solvation dynamics in n-alcohols was investigated by Laitinen et al. [29]. Compared to the data on C153 in the article of Maroncelli and Fleming[1], the solvation time measured with 4-ANMP in n-butanol is much faster (132 ps vs 510 ps measured with C153). Specific interactions like hydrogen bonding were underlined in the article of Vauthey group [23]. Indeed, the solvation dynamics of C102 in ethanol was found to be slower than the one of C153. Also, the solvation of 4-AP was found 60% slower than for coumarin family. The hydrogen bonding ability analysis of the probes will be discussed later in this article.

Considering the bi-exponential fit results, for all the probes the first (longer) component has smaller amplitude (being the smallest for PRODAN) than that of the faster one. The latter amplitude is decreasing upon the addition of the IL. Actually, the neat IL solutions show almost half of the solvation response presented by its slow component.

The longer time component values are similar for 4-ANMP, C102 and C153 (table 3.2). It is about 1.6-1.7 times greater for PRODAN, but a smaller amplitude abates

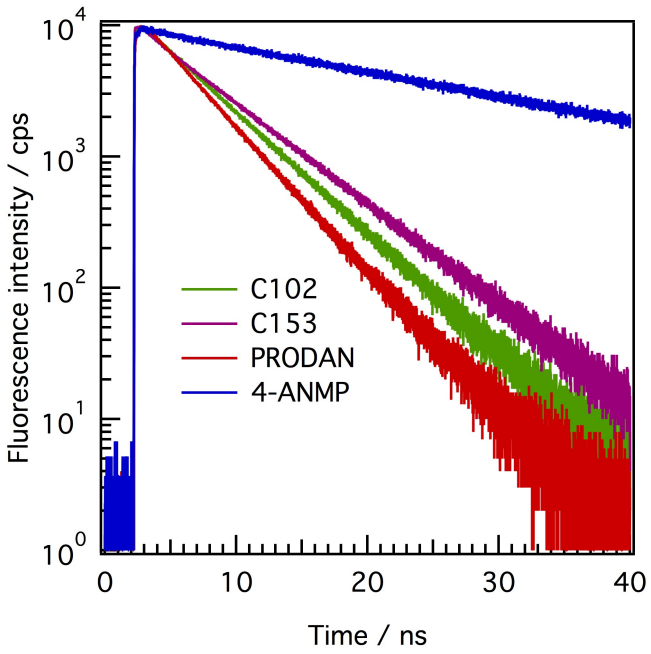

Figure 3.5: Fluorescence decays of C102 (green), C153 (purple), PRODAN (red) and 4-ANMP (blue) in neat $BmimBF_4$, recorded at their respective maximum emission wavelengths. It has to be noticed that 4-ANMP has the longest decay (6 times longer than the decays of the other studied probes).

Table 3.2: Amplitudes B_i, solvation times τ_{si} of components and weighted average solvation time $< \tau_{solv} >$ of the bi-exponential fit, parameters of the stretched exponential fit τ_s and β of measured solvation dynamics decays of C153, C102, 4-ANMP and PRODAN fluorescent probes in $BmimBF_4$ and $BmimBF_4$/PC mixtures.

System	B_1, %	τ_{s1} / ns	τ_{s2} / ns	$< \tau_{solv} >$ / ns	τ_s / ns	β
			C153			
$BmimBF_4$	43.38	1.2263	0.2916	0.6672	0.5415	0.71
x_{IL}=0.85	35.14	1.0115	0.1869	0.5048	0.3891	0.71
x_{IL}=0.65	35.04	0.6289	0.1205	0.3365	0.2695	0.75
			C102			
$BmimBF_4$	42.44	1.2503	0.2208	0.677	0.5311	0.68
x_{IL}=0.85	33.49	1.0401	0.1629	0.5079	0.3832	0.68
x_{IL}=0.65	26.1	0.8317	0.1265	0.3581	0.2668	0.68
			4-ANMP			
$BmimBF_4$	46.11	1.001	0.1696	0.5914	0.4785	0.7
x_{IL}=0.85	27.23	1.0831	0.1867	0.4569	0.3421	0.69
x_{IL}=0.65	34.36	0.5184	0.0878	0.3004	0.2445	0.77
			PRODAN			
$BmimBF_4$	32.14	1.9327	0.2729	0.8005	0.5497	0.58
x_{IL}=0.85	26.71	1.694	0.1973	0.6099	0.3867	0.53
x_{IL}=0.65	17.77	2.5242	0.1816	0.6087	0.2779	0.47

its effect on the average solvation time. The second time component is similar for C153, C102 and PRODAN and shorter for 4-ANMP. Except for 4-ANMP and for

PRODAN in x_{IL}=0.65 mixture, the longer time component amplitudes and both time components increase with the increase of x_{IL}.

The solvation times of C153 in IL in the present work are almost two times faster than the values reported by Karmakar and Samanta[26], the equality of amplitudes of the two time components being conserved. Also, their weight of the long component is close to our experiment with PRODAN, time components being again faster than the reported ones.

A tri-exponential fit of SRFs was also performed. The results are shown in table 3.3. The χ^2 values for three exponential fit are 3 to 102 times smaller than the ones for bi-exponential fit (fig.3.6). The components of the solvation functions of C153 and PRODAN in neat IL are compared on fig3.7. Again, as the solvation dynamics of PRODAN is longer than the maximum time window used in our experiment (10ns), its longest solvation time was estimated to be equal to 3.76 ns. This value is estimated because the longest component of PRODAN's solvation is unreliable due to the time window of the reconstructed spectra fit. The second and the third time components of the PRODAN solvation dynamics are comparable in magnitude with the three other probes. A similar average solvation times for both coumarins has to be noticed. The times of solvation components are similar for 4-ANMP, but the amplitude of the second (the fastest) component is higher than for the coumarins, resulting in a faster average solvation time. This second time component is mixture composition independent for the coumarins, but increases for 4-ANMP and PRODAN with x_{IL}. Furthermore the amplitude of this second time component is increasing upon the dilution of the IL.

The average solvation time of fluorescent probes shows the same trends as for the bi-exponential fit. Also, all the four probes show the same trend in average solvation time within the solvent. The average solvation time obtained with the three-exponential fit differs slightly from the one achieved from the bi-exponential fit: the highest difference was observed for PRODAN probe. This can be explained by an enhancement of the quality of three-exponential fit for PRODAN and 4-ANMP probes (fig.3.6).

One more interesting way to fit the solvation response in ILs was used by Maroncelli research group [5, 11]. It is the analysis with stretched exponential model (eq.3.2). Although this model provides the worst description of our experimental data (see chi-square values in figure 3.6), we report the information achieved in table 3.2. As it can be noticed, the times obtained are very close for C153, C102 and PRODAN, while 4-ANMP exhibits faster dynamics, following the result of other model functions. The shape of the solvation response is similar for C153, C102 and 4-ANMP (β=0.68-0.75) and is in agreement with literature expectations for TCSPC and other lower time resolution methods[11]. PRODAN shows smaller stretching coefficient (0.58-0.47), decreasing with dilution of IL.

The extrapolation of emission spectral features to infinite time (10.032 ns) can also give interesting information. The peak wavenumber of C153 TRES at 10ns in neat $BmimBF_4$ is close to the one reported in literature (18.51 and $18.41 \cdot 10^3$ cm^{-1} [27]), representing the "fully-relaxed"emission of C153. The relaxed FWHM and mean wavenumber are compared to steady-state values in fig.3.8. Firstly, all the points lay below the diagonal, what is rationalized with the spectrum bathochromic shift with time and the comparable time scales of excited state depopulation and solvation dynamics in IL and its mixtures. This result corroborates with long time

Table 3.3: Amplitudes B_i, solvation times τ_{si} of components and weighted average solvation time $< \tau_{solv} >$ of the tri-exponential fit of measured solvation dynamics decays of C153, C102, 4-ANMP and PRODAN fluorescent probes in $BmimBF_4$ and $BmimBF_4$/PC mixtures.

System	B_1, %	B_2, %	τ_{s1} / ns	τ_{s2} / ns	τ_{s3} / ns	$< \tau_{solv} >$ / ns
			C153			
$BmimBF_4$	20.82	31.81	1.6163	0.0313	0.4281	0.7059
x_{IL}=0.85	17.34	36.35	1.3705	0.0658	0.3568	0.5224
x_{IL}=0.65	14.37	41.38	0.9122	0.042	0.2415	0.3527
			C102			
$BmimBF_4$	19.16	35.21	1.9221	0.0971	0.5268	0.7288
x_{IL}=0.85	14.08	50.64	1.6684	0.1112	0.4831	0.5425
x_{IL}=0.65	6.03	57.41	2.2825	0.0808	0.4012	0.4188
			4-ANMP			
$BmimBF_4$	13.01	41.13	1.8851	0.1052	0.5937	0.639
x_{IL}=0.85	11.64	42.18	1.8026	0.0911	0.3808	0.4953
x_{IL}=0.65	3.63	58.55	1.5858	0.0714	0.3815	0.3243
			PRODAN			
$BmimBF_4$	17.16	38.31	2.983	0.0951	0.5424	0.9103
x_{IL}=0.85	11.83	49.97	3.3719	0.0853	0.4963	0.764
x_{IL}=0.65	10.35	55.02	3.7568	0.0672	0.365	0.7194

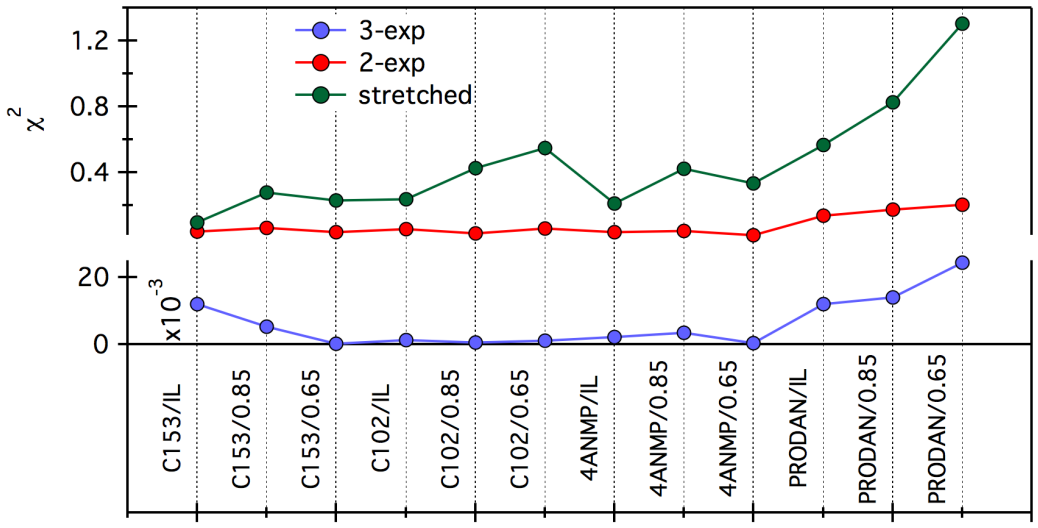

Figure 3.6: χ^2 values of bi- and three-exponential fit of solvation responses of C153, C102, 4-ANMP and PRODAN fluorescent probes in $BmimBF_4$ and $BmimBF_4$/PC mixtures.

spectra of DCS, red-shifted with respect to steady-state fluorescence, as reported by Ito et al. [25]. Secondly, the 4-ANMP mean wavenumber values almost coincide with the steady-state values. This can be explained from the point of view that the lifetime of 4-ANMP is much longer than the fluorescence lifetime of the C102, C153 and PRODAN. Thus, the ratio fluorescence lifetime/solvation time is much higher and the emission comes mainly from the "relaxed"excited state. Thirdly, a particular

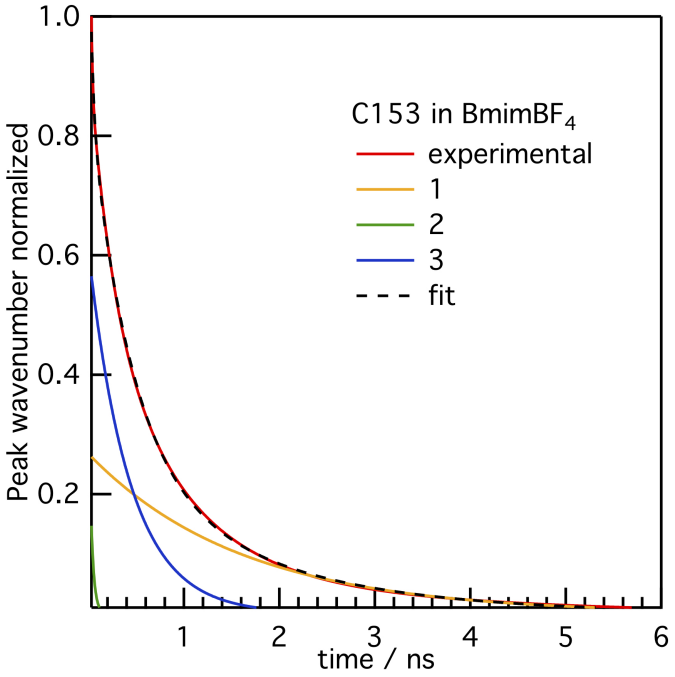

Figure 3.7: Solvation function components from tri-exponential fit of C153 (solid line) and PRODAN (dashed line) in $BmimBF_4$. Red curves represent the experimental function. Orange, blue and green are the 1^{st} , 2^{nd}, 3^{rd} components, respectively.

attention must be paid to scattered and displaced points of FWHM of PRODAN. This is possibly related to the longer solvation time of this probe.

An interesting point to discuss is the intrinsic lifetime of the fluorescent probe in the solvent. It is dependent on both the chemical structure of the probe itself and the properties of the solvent: its polarity, specific interactions ability, etc. However, the measurements of intrinsic lifetime are complicated with the entangled solvation dynamics process. These complications are usually not discussed in the literature, for the reason that the lifetime is usually much longer than the solvation dynamics in conventional organic solvents. This is not the case when viscous solvents are considered as in our work. In these media, the solvation dynamics may occur at a comparable time scale as the fluorescence of the probe. Thus, disentangling of these two processes may be problematic.

Similar to the solvation dynamics determination, the intrinsic lifetime of the probe in a given solvent may be evaluated from the time-resolved emission spectra. In fact, the area under the time-resolved emission spectrum is proportional to the excited state population. Thus, calculating the area of the TRES at each time step and analysing the time evolution with an exponential function, one can extract the intrinsic lifetime of the fluorescent probe. Two thousand points were generated within the spectral window defined by the lognorm fit parameters (eq.2.10) $(2\nu_{mean} - a; a)$. The time behaviour of these areas is represented in fig.3.9. As one can see, C153, C102 and PRODAN probes show quasi-mono-exponential decay of the excited state population with time. Although an emission from two distinct excited states and a bi-exponential decay were suggested for PRODAN in literature [35], apparently such effects are not observed in the present work. Novaira et al. [34] put forward the idea about locally excited (LE) and intramolecular charge transfer (ICT) dual emission

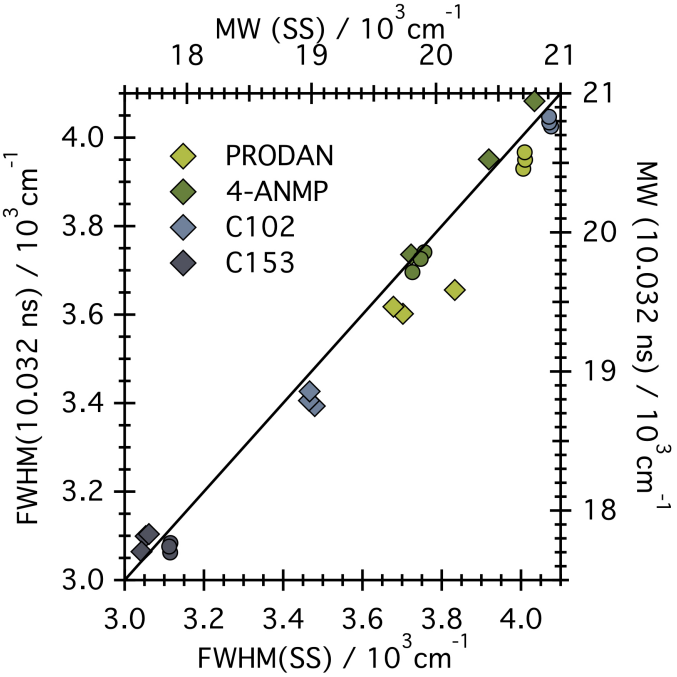

Figure 3.8: $FWHM$ (left-bottom, diamonds) and mean wavenumber (right-top axis, circles) of time-resolved emission spectra and steady-state emission spectra of C153, C102, 4-ANMP and PRODAN fluorescent probes in $BmimBF_4$ and $BmimBF_4$/PC mixtures. The colour code differences the probes and is explained on the graph. The solid line describes the diagonal, or 1:1 values.

of PRODAN in reverse micelles as a unique environment. However, like in the present work, they didn't observe dual fluorescence in n-heptane, benzene and water. Contrarily to the other probes, 4-ANMP's intrinsic fluorescence exhibits a multi-exponential decay. This decay can suggest multiple different excited state-solvent configurations for 4-ANMP - IL/PC mixtures. Also, the excited state population decays appear to be very close for the mixtures and neat IL, confirming the result of steady-state spectroscopy about a very similar solvation effect of the neat IL and its mixtures with propylene carbonate.

A similar analysis was performed by Kumpulainen et al. [23]. Multi-exponential fit was required to describe the areas decay and the fastest components seemed to correlate with solvation dynamics. Unfortunately, the lifetimes of the fluorescent probes considered in this study are too close or longer than the time-window of the calculated spectra, thus making unreliable the exponential analysis of the curves, discussed below. The access to the time steps longer than 10ns is complicated because of the fluorescence lifetime restriction: the fluctuations are too strong to be fitted by the lognormal function.

The time-resolved fluorescence anisotropy decays were measured for the C153, PRODAN and 4-ANMP probes in neat IL and for 4-ANMP and C153 in x_{IL}=0.65 mixture at the maximum emission wavelength. The results are presented in the supporting information (fig.3.10), and indicate strong retardation of PRODAN and 4-ANMP's reorientations in the studied systems. The span in correlation rotational times is much larger than what could be expected from the probe size differences, suggesting strong specific interactions of PRODAN and 4-ANMP with

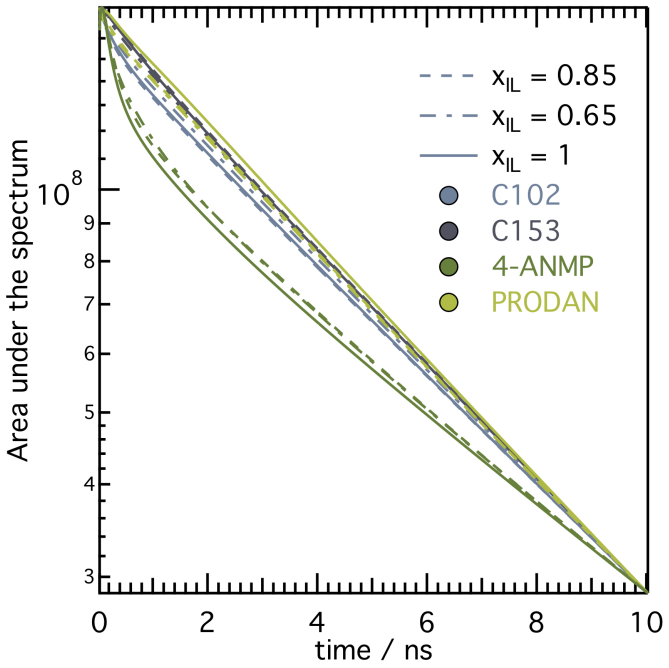

Figure 3.9: Reconstruction of the intrinsic excited state population decays of the probes using the area under the TRES of C153, C102, 4-ANMP and PRODAN fluorescent probes in $BmimBF_4$ and $BmimBF_4$/PC mixtures, corresponding to the intrinsic lifetimes of the probes. Logarithmic scale was chosen in order to respect the exponential character of the theoretical dependence.

the constituents of the IL. The nature of these kinds of interactions and the possible arrangements are discussed in the following sections of this paper.

To summarize, the time-resolved fluorescence experiments reveal that: (i) the solvation response in IL $BmimBF_4$ and its mixtures with propylene carbonate for high x_{IL} is fairly similar for all the fluorescent probes used. But it has to be noticed that while coumarins C153 and C102 exhibit indistinguishable solvation dynamics, almost two-fold variations are observed for 4-ANMP and PRODAN, representing the fastest and the slowest solvation response, respectively; (ii) when the solvation dynamics and fluorescence lifetime are of comparable order, the emission can occur from the unrelaxed excited states and the resulting steady-state emission spectra are blue-shifted when compared to the completely relaxed TRES (10.032ns); (iii) while C102, C153 and PRODAN show almost linear excited state population decay, 4-ANMP shows multiexponential behaviour for the reasons that are not still clear; (iv) time-resolved fluorescence anisotropy reveals retardation of PRODAN and 4-ANMP reorientation when compared to C153, strongly suggesting the presence of specific interactions of PRODAN and 4-ANMP with IL constituents.

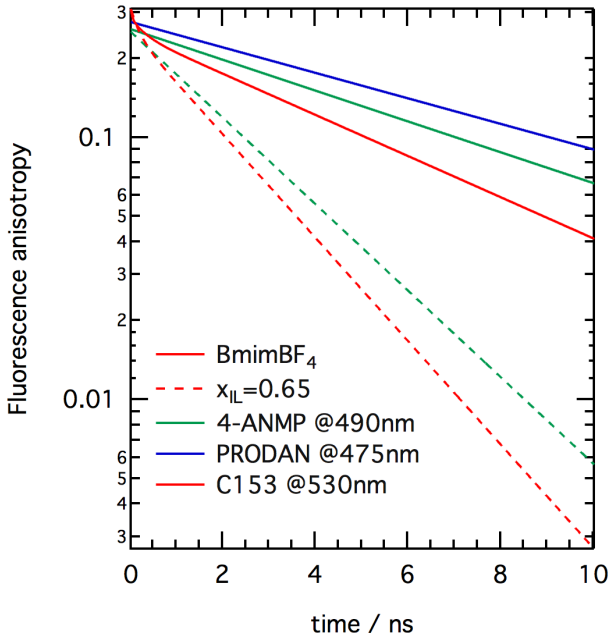

Figure 3.10: Time-resolved fluorescence anisotropy of 4-ANMP, C153 and PRODAN probes in $BmimBF_4$ and 4-ANMP and C153 in $BmimBF_4$/PC mixture with x_{IL}=0.65. Fluorescence decays with HV, HH, VV and VH polarisations were recorded at maximum emission wavelength for each sample, as indicated in the legend. G-factor was calculated using HH/HV integration and was fixed during the VH and VV decays global fit.

3.4 Quantum chemical calculations

In order to interpret the experimental results and to gather more information on the various probes studied in this work, we performed quantum chemical calculations. The results of quantum chemical calculations of ground and excited state dipole moments as well as their change; calculated absorption wavelength and the molecular orbital contributions to S_0-S_1 transition are shown in table 3.4.

This table deserves a few comments to be made. Firstly, the dipole moment in the excited state was calculated without the excited state geometry optimisation, thus neglecting all the intramolecular relaxation after the photo-excitation. This is reasonable for relatively rigid structures, as C102 and C153 but questionable for PRODAN and 4-ANMP molecules that obviously exhibit a sizeable excited state structure equilibration. However, this kind of information is quite meaningful for the characterisation of the molecule right after the absorption of photon. Secondly, the PCM may not be valid for the solvation in ILs calculations, although in literature [51], the authors claim good agreement with experimental data. When comparing the experimental maxima of absorption, a good agreement was achieved for 4-ANMP probe, while a non-negligible blue-shift of theoretical absorption is observed for C153, C102 and PRODAN. This can be rationalized with the fact that the solvation in ILs can not be approximated as a dipole in dielectric continuum, stressing the importance of the molecularity of solvation in such systems.

The calculated dipole moment change is increasing in the row 4-ANMP<C102 <C153<PRODAN, following the same trend as the Stokes shift (table 3.1, $\Delta\nu$).

Table 3.4: Ground (μ_G) and excited state (μ_E) dipole moments, their vector difference ($\Delta\mu$), change in direction α° and absorption maximum and molecular orbitals contributions extracted from quantum chemistry calculations of 4-ANMP, C153, C102 and PRODAN probes in $BmimBF_4$ IL using PCM. Excited state relaxed geometry dipole moments and experimental absorption maxima are given in parenthesis.

Probe	μ_G / D	μ_E D	$\Delta\mu$ / D	$\lambda_{abs,calc}$ / nm	1^{st} exc state	α°
4-ANMP	6.2622	12.1439 (13.3853)	5.9712	370.86 (373)	44 → 47 0.10722 46 → 47 0.68439	6.77
C153	10.1859	18.7898	8.7198	397.19 (426)	80 → 81 0.69603	5.38
C102	10.6328	17.5199	7.7839	363.74 (385)	68 → 69 0.69465	15.27
PRODAN	8.3484	16.6996 (17.3593)	8.9376	348.48 (360)	61 → 62 0.66861 61 → 63 0.18389	15.54

The 4-ANMP fluorescent probe doesn't fall into this generalization, underlining the importance of the specific interactions and possible substantial geometry relaxation after the photo-excitation. In the extensive study of Chapman et al.[21], the solvatochromism characteristics of 11 probes were reported, including the probes used in the present work. The reported magnitude of the change in the probe polarity ΔS is following the same trend as for our calculated dipole moment change, PRODAN>C153>C102>4-ANMP.

The increase in dipole moment change when comparing C102 and C153 obviously comes from the fact that the perfluorinated methyl group strengthens the acceptor moiety of the C153 molecule (indeed, the electron density flows from julolidine part to CF_3 and lactone parts, fig.3.11). The relatively small dipole moments of 4-ANMP are probably due to the decrease of electron withdrawing efficiency of N-methyl substituted phthalimide unit in addition to weaker donor character of lone amino group comparatively to substituted amine in C102 and C153. The N,N-dimethyl substitution in PRODAN and the moderate ketone electron withdrawing group result in highest dipole moment change for PRODAN probe.

The solvent-probe interaction in ILs is logically strongly dependent on the interaction with partial charges of the probe molecules, as a consequence of the presence of the free charges in the system. This may also generate differences in solvation dynamics for probes with various $\vec{\mu}_G$ and $\vec{\mu}_E$ orientations in IL solutions. Therefore it is interesting to consider the angle between ground and excited state dipole moments of the probes. This quantity increases in the row C153<4-ANMP<C102<PRODAN. One can preclude that substantial change in dipole moment orientation for PRODAN and C102 can cause the difference in reorientational and translational motions contribution in the solvation dynamics, increasing the relevance of the former one. We suggest that only the solvation dynamics of the probes with similar dipole moments angle can be compared. These differences may be at the origin of the empirical correction of the solvation dynamics by the anisotropy decays in literature [23, 24, 27].

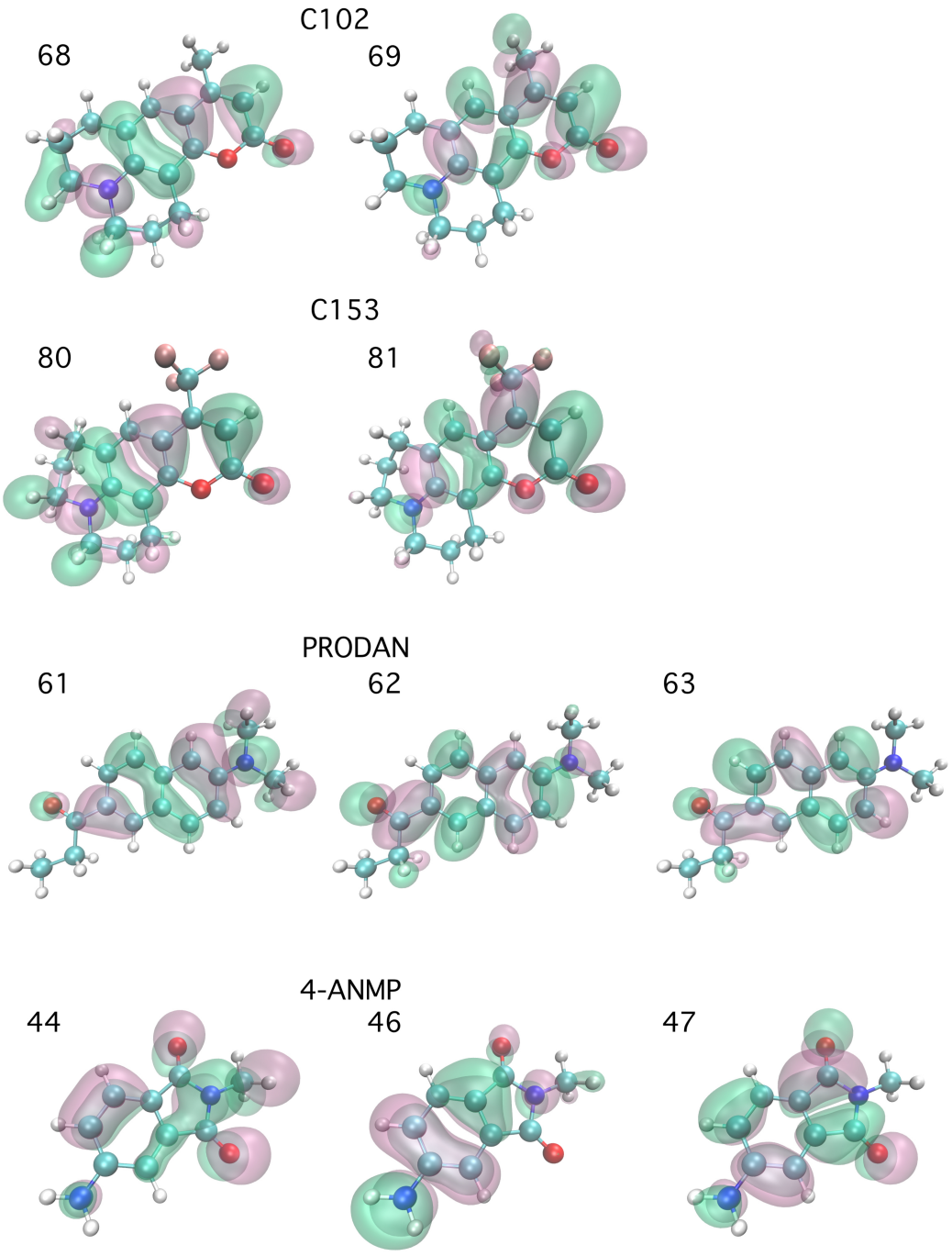

Figure 3.11: Molecular orbitals of C102 (HOMO is 68), C153 (HOMO is 80), PRODAN (HOMO is 61) and 4-ANMP (HOMO is 46), involved in S_0-S_1 transitions listed in table 3.4. The population analysis was performed using M06-2X/6-311G(d) level of theory. 0.02 isovalue was set for the surfaces presentation. Negative surfaces are in mauve, and positive in green.

We believe that the fluorescence anisotropy decays also contain information about the solvation dynamics, and such a correction can partly subtract some components. Also, the approach of empiric power law dependence didn't help to explain the molecularity of solvation response in ethanol, as shown by Vauthey et al. [23].

In order to understand how the electronic density is delocalized after the photoexcitation in the probes structures, the molecular orbitals involved in S_0-S_1 transition are shown in fig.3.11 and listed in table 3.4. It can be clearly seen, that the intramolecular charge transfer occurs in all studied structures and this fact is in accordance with a large dipole moment change upon an excitation to S_1 state. As it can be noticed from fig.3.11, the electron density is delocalized from the julolidine core of C153/C102 or amino/ substituted amino-groups of 4-ANMP and PRODAN to the electron withdrawing lactone moiety of C153 and C102, phthalimide core of 4-ANMP or propionyl group of PRODAN. One more interesting observation can be made: the dipole moment change depends not only on the strength of the donor and acceptor groups, but also on their geometric separation. Thus, PRODAN, having naphthalene ring as a π-bridge, exhibits higher dipole moment change than 4-ANMP that has only one benzene ring but strong electron-withdrawing phthalimide group. This analysis proves that all the probes possess an efficient transfer of the electron density and engender an important force field perturbation upon the photo-excitation.

In order to get insight in the effect of geometry relaxation of the probe after the photo-excitation we then optimized the excited state geometries of 4-ANMP and PRODAN, C102 and C153. Our results confirm the marginal geometry changes in the case of C102 and C153 (the relaxed excited state and ground state geometries are shown in fig.3.13). The resulting structures of 4-ANMP and PRODAN are shown in fig. 3.12 where they were overlaid over the benzene (for 4-ANMP)/naphthalene (for PRODAN) ring. These calculations are helpful to estimate the degree of change in equilibrium geometry upon the excitation (although the qualitative characterisation is poor at this level of theory). As one can see from fig.3.12 panels, the structures in the ground (green) and excited (blue) states differ significantly, especially in the moieties containing nitrogen. Interestingly, the aliphatic chain of PRODAN and ketone group almost coincide. Also, the aromatic naphthalene and benzene groups change only marginally. Furthermore, amino and substituted amino group, being out-of-plane in ground state, is coplanar to the aromatic rings in excited state. This result is in line with both Yang and Zhang theoretical work on 4-ANMP [52], and Wetzler semiempirical calculations on the same probe [43]. It can be rationalized by the possibility of delocalisation of free electron pair of nitrogen to the electron acceptor moiety. Thus, the lone electron pair that made amino group actually out of plane, is partly delocalised, allowing the amino group to return to sterically preferable position.

Examining the bonds lengths, angles and dihedral angles, the major differences were found for bonds in pyrroline ring (Δl=0.062 angstrom), angles CCN, CNH (ΔA=3.447° and 3.660° max) and dihedral angle CCNH in 4-ANMP (19.772° max). As for PRODAN, the major change in bond lengths is 0.05 for the atoms of benzene ring close to amino group, also angles CNC (2.681° max) and dihedral CCNC (7.501° change). The biggest changes in bonds, angles and dihedral angles are shown in fig.3.14 as green sticks, dashes and dihedrals, respectively. As the dipole moment depends on the geometry, we calculated the dipole moment in excited state with relaxed geometry (table 3.4, value in parenthesis). The dipole moment in relaxed geometry is greater than the one with ground-state geometry.

Thus, given the possibility of the intramolecular relaxation in PRODAN and 4-ANMP and the large change of dipole moment direction of C102 and PRODAN upon the excitation, C153 is proven beneficial for solvation dynamics measurement

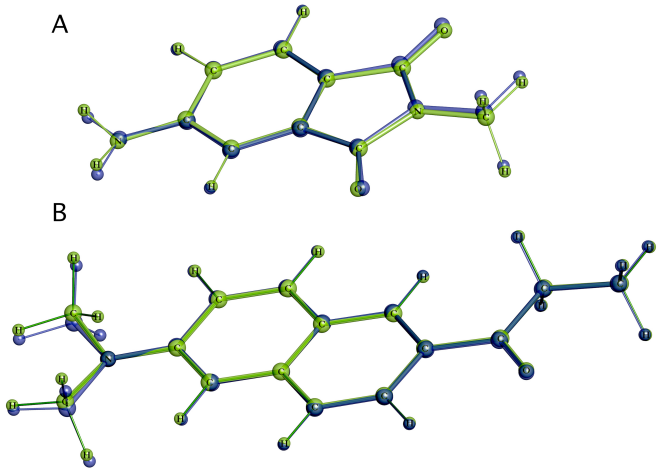

Figure 3.12: 4-ANMP (A) and PRODAN (B) overlaid geometries in ground (green) and excited (blue) state. A set is aligned over nitrogen and benzene group, B set is aligned over nitrogen and naphthalene group.

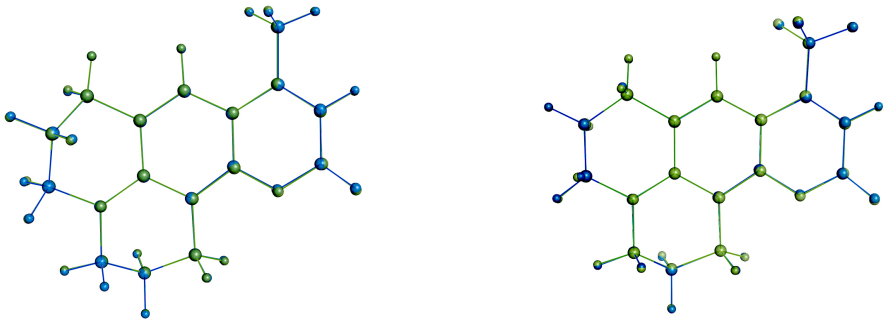

Figure 3.13: Overlaid C102 (left) and C153 (right) ground (blue) and S_1 excited state (green) optimized geometries.

with expectation of differences in solvation dynamics measured for all these probes.

These quantum chemistry calculations helped to explain the Stokes shifts differences allowing the access to dipole moments. The calculations also evidenced the electron density delocalisation upon excitation as well as the geometries changes for the S_0-S_1 transition.

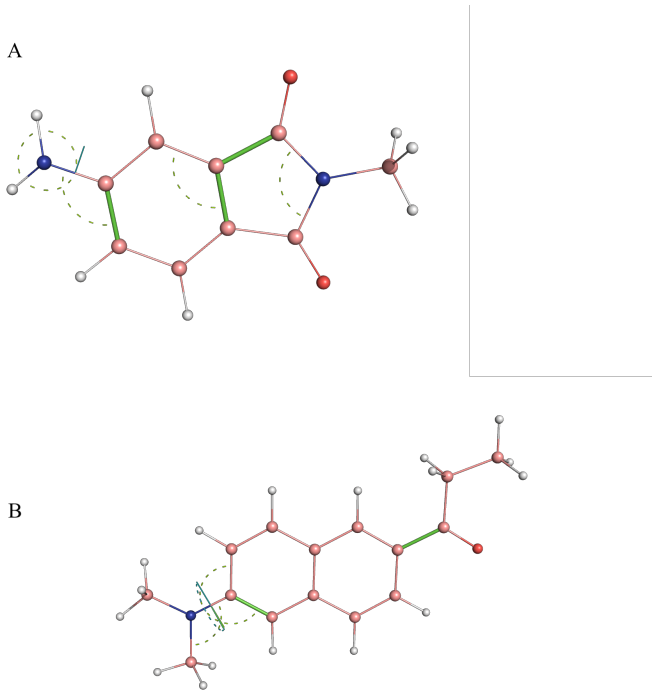

Figure 3.14: Ground state structures of 4-ANMP (A) and PRODAN(B), respectively. Green sticks, and dashes show the biggest changes in bond lengths, angles and dihedral angles.

3.5 Specific interactions: hydrogen bonding and π-stacking

Although some works ([21]) reported the insensitivity of the solvation dynamics of 4-ANMP, PRODAN, C102 and C153 probes to the hydrogen bonding, we consider important to analyse the hydrogen bonding donor/acceptor character of the probes' functional groups and ILs constituents under the study. Here we present an analysis of the hydrogen bonding relative strength in ground and excited states similar to the one made by Gustavsson et al. [22], who also performed the study of the solvation dynamics probe dependence in DMSO and methanol.

The C102 and C153 probes present similar hydrogen bonding ability characteristics. For both probes, H-bond established with julolidine nitrogen H-bond acceptor weakens upon the excitation and the H-bond with carbonyl oxygen (also acceptor) strengthens upon the excitation. For C153, the strengthening of hydrogen bonding involving perfluorinated methyl group is also expected. As the evidence of hydrogen bond with C=O group of C153 in MeOH, the red shift of carbonyl stretching mode of C153 was reported by Krolicki et al. [53]. A similar situation can be observed for PRODAN, where the hydrogen bonding weakens with dimethyl-amino group and strengthens for carbonyl acceptor group. Due to the presence of NH_2 group, 4-ANMP molecule, different behaviour is awaited. Apart from the similar (i) hydrogen bond strengthening with C=O and (ii) NH_2 group H-bond with nitrogen atom weakening, strengthening of H-donor NH_2 ability is expected. The first stabilisation has been put forward due to the downshift of donor OH resonance in 4-AP and 4-ANMP water clusters upon the excitation to S_1 state by Topp M. [40]. Also, the absence of imide

NH in 4-ANMP that weakens the hydrogen bonding in the excited state along with the strengthening of the carbonyl hydrogen bond was suggested by the authors to be the reason of particular sensitivity of 4-ANMP to the hydrogen bonding. Indeed, a much greater shift of 4-ANMP water complex fluorescence excitation resonance than the one of 4-AP was observed[41]. Regarding the solvents, one can see the following picture: propylene carbonate has H-acceptor C=O group, along with anion H-bond acceptor character. Differently, imidazolium cation possesses H-bond donor character.

Concerning the π-interaction possibility, little is known for coumarin derivatives and 4-ANMP fluorescent probes. In contrast, PRODAN quenching by fulvic acids was observed to be in evident correlation with aromaticity of the quencher molecule [38]. Regarding the structure, one can see that unlike C153, C102 and 4-ANMP fluorescent probes, PRODAN has an extended aromatic core - naphthalene ring, that may engender the enhanced π-interaction between PRODAN and aromatic imidazolium cation. This stacking must drastically influence on the solvation shell reorganization timescales as well as the reorientation of PRODAN due to Brownian motion, retarding considerably these two processes.

In regard of the steady-state, time-resolved experiments and quantum calculations, we put forward the following hypothesis of the observed probe dependence in neat IL and its mixtures with molecular solvent. As the emission spectra of 4-ANMP are particularly sensitive to the hydrogen bonding through C=O groups and the drastic shift is not observed, we conclude that this type of interaction is rather weak in $BmimBF_4$ and $BmimBF_4$/PC mixtures. However, the hydrogen bonding with anion through NH_2 group is still possible, providing an additional mechanism of the solvation dynamics by the strengthening of the hydrogen bond and resulting in faster spectral shift, observed in the present work. On the other hand, naphthalene ring, being a distinct feature of PRODAN among the probes studied, provides a possibility for the above-mentioned π-interaction with aromatic imidazolium cation. Because of the big size of the imidazolium cation, the solvation dynamics is awaited to be slower than for the other probes. Our time-resolved fluorescence anisotropy measurements of 4-ANMP, C153 and PRODAN in neat IL support this hypothesis, as the average rotational times follow the trend C153 (3.8 ns)>4-ANMP (7.38ns)<PRODAN(8.9ns) (see fig.3.10). The longer anisotropy decays of 4-ANMP and PRODAN can be therefore attributed to hydrogen bonding interactions and π-interactions with aromatic imidazolium cation, respectively.

Conclusions

The aim of this work was to verify if the SRFs in IL/MS mixtures were independent on the chosen probe and if not, to isolate which probe was the most adequate to accurately reveal the solvation dynamic processes. In this work, the probe dependence of solvation dynamics in $BmimBF_4$ and $BmimBF_4$/propylene carbonate mixtures were studied using C153, C102, PRODAN and 4-ANMP probes. Time-resolved fluorescence TCSPC (kinetic mode TRES as well as fluorescence anisotropy) and steady-state absorption and fluorescence measurements were performed. Quantum chemistry calculations of dipole moments in ground and excited state, comparison of equilibrium S_0 and S_1 geometries were performed to help the interpretation of the experimental results.

In this chapter, we evidenced a lot of phenomena:

1. The major factors that are responsible for solvation dynamics and other photophysical properties difference of ILs and IL/molecular solvent mixtures are: (i) the differences in dipole moment in ground state, μ_G , in excited state, μ_E , and the change of the dipole moment upon the excitation $\Delta\mu$ as the consequence of the existence of free charges in ILs; (ii) the angle between the ground and excited state dipole moments α° of the probes that leads to change in a balance in translational/rotational motions roles in the solvation dynamics; (iii) the geometry relaxation upon the excitation, the time scale of which is clearly solvent-dependent but the magnitude and time is not still understood; (iv) the specific interactions between probe molecule and IL, like hydrogen bonding and π-stacking; (v) the preferential solvation by a molecular solvent or IL constituents in mixtures that directly affects the composition of the solvation shell and its reorganisation after the perturbation.

2. The Stokes shift of the different probes follows the trend of the dipole moment change, except 4-ANMP which shows a high Stokes shift, possibly due to its small size.

3. For all the probes, the average solvation times are increasing with x_{IL}. An intuitive conclusion is that whatever is the considered probe, the addition of IL is inducing a slow-down of the solvation and rotational dynamics.

4. All the solvation probes show similar non-exponential solvation dynamics that can be modelled with bi- or tri-exponential functions. All the probes show the similar trend of the average and of the component of the solvation time on the mixture composition. The solvation responses of C102 and C153 were identical in our experiment. The 4-ANMP molecule showed the fastest solvation response.

5. Although 4-ANMP possesses both H-bond donor and acceptor properties, making this molecule able for hydrogen bonding interactions with H-bonding donor cation and H-bonding acceptor anion and propylene carbonate, only the latter two interactions seem to be consistent with our experiment results. The hydrogen bonding character of the rest of the fluorescent probes C153, C102 and PRODAN are relatively similar. Specific π-interaction of PRODAN with imidazolium cation is proposed to be the rationalization of slow solvation dynamics that this probe exhibits in IL and IL/molecular solvent mixtures. Our time-resolved fluorescence anisotropy measurements support the hypothesis of the relative importance of the anion and the cation in the probe-dependent solvation dynamics.

The C153 molecule, showing big change in dipole moment (8.7 D), little geometry relaxation upon the excitation due to its rigid structure, small change in dipole moment orientation and relatively small hydrogen bonding ability is thus proved the most adequate probe for use in the study of the solvation dynamics in various environments, including ILs and ionic IL/MS mixtures.

Bibliography

[1] M. Maroncelli and G. R. Fleming, "Picosecond solvation dynamics of coumarin 153: The importance of molecular aspects of solvation," The Journal of Chemical Physics, vol. 86, no. 11, pp. 6221–6239, 1987.

[2] E. W. Castner, M. Maroncelli, and G. R. Fleming, "Subpicosecond resolution studies of solvation dynamics in polar aprotic and alcohol solvents," The Journal of Chemical Physics, vol. 86, no. 3, pp. 1090–1097, 1987.

[3] M. Maroncelli and G. R. Fleming, "Comparison of time-resolved fluorescence stokes shift measurements to a molecular theory of solvation dynamics," The Journal of Chemical Physics, vol. 89, no. 2, pp. 875–881, 1988.

[4] Y. Nagasawa and H. Miyasaka, "Ultrafast solvation dynamics and charge transfer reactions in room temperature ionic liquids," Phys. Chem. Chem. Phys., vol. 16, pp. 13008–13026, 2014.

[5] H. Jin, G. A. Baker, S. Arzhantsev, J. Dong, and M. Maroncelli, "Solvation and rotational dynamics of coumarin 153 in ionic liquids: Comparisons to conventional solvents," The Journal of Physical Chemistry B, vol. 111, no. 25, pp. 7291–7302, 2007.

[6] R. Karmakar and A. Samanta, "Solvation dynamics of coumarin-153 in a room-temperature ionic liquid," The Journal of Physical Chemistry A, vol. 106, no. 18, pp. 4447–4452, 2002.

[7] A. Samanta, "Dynamic stokes shift and excitation wavelength dependent fluorescence of dipolar molecules in room temperature ionic liquids," The Journal of Physical Chemistry B, vol. 110, no. 28, pp. 13704–13716, 2006.

[8] M. Liang, X.-X. Zhang, A. Kaintz, N. P. Ernsting, and M. Maroncelli, "Solvation dynamics in a prototypical ionic liquid + dipolar aprotic liquid mixture: 1-butyl-3-methylimidazolium tetrafluoroborate + acetonitrile," The Journal of Physical Chemistry B, vol. 118, no. 5, pp. 1340–1352, 2014.

[9] Y. Smortsova, F.-A. Miannay, H. Oher, B. Marekha, J. Dubois, M. Sliwa, O. Kalugin, and A. Idrissi, "Solvation dynamics and rotation of coumarin 153 in a new ionic liquid/molecular solvent mixture model: [bmim][tfsi]/propylene carbonate," Journal of Molecular Liquids, vol. 226, pp. 48 – 55, 2017. Molecular Liquids Meet Ionic Liquids: From Fundamentals to Applications with Particular Attention to Ionic Liquids.

[10] X.-X. Zhang, M. Liang, J. Hunger, R. Buchner, and M. Maroncelli, "Dielectric relaxation and solvation dynamics in a prototypical ionic liquid + dipolar protic liquid mixture: 1-butyl-3-methylimidazolium tetrafluoroborate + water," The Journal of Physical Chemistry B, vol. 117, no. 49, pp. 15356–15368, 2013.

[11] S. Arzhantsev, H. Jin, G. A. Baker, and M. Maroncelli, "Measurements of the complete solvation response in ionic liquids," The Journal of Physical Chemistry B, vol. 111, no. 18, pp. 4978–4989, 2007.

[12] M. Muramatsu, Y. Nagasawa, and H. Miyasaka, "Ultrafast solvation dynamics in room temperature ionic liquids observed by three-pulse photon echo peak shift measurements," The Journal of Physical Chemistry A, vol. 115, no. 16, pp. 3886–3894, 2011.

[13] B. M. Ladanyi and M. Maroncelli, "Mechanisms of solvation dynamics of polyatomic solutes in polar and nondipolar solvents: A simulation study," The Journal of Chemical Physics, vol. 109, no. 8, pp. 3204–3221, 1998.

[14] Z. L. Terranova and S. A. Corcelli, "On the mechanism of solvation dynamics in imidazolium-based ionic liquids," The Journal of Physical Chemistry B, vol. 117, no. 49, pp. 15659–15666, 2013.

[15] M. N. Kobrak, "A comparative study of solvation dynamics in room-temperature ionic liquids," The Journal of Chemical Physics, vol. 127, no. 18, p. 184507, 2007.

[16] A. Eftekhari, "Supercapacitors utilising ionic liquids," Energy Storage Materials, vol. 9, pp. 47 – 69, 2017.

[17] S. Denizalti, A. K. Ali, C. Ela, M. Ekmekci, and S. Erten-Ela, "Dye-sensitized solar cells using ionic liquids as redox mediator," Chemical Physics Letters, vol. 691, pp. 373 – 378, 2018.

[18] M. Neto, R. Leones, F. Sentanin, J. S. S. Esperanca, M. J. Medeiros, A. Pawlicka, and M. M. Silva, "Electrochemical applications of electrolytes based on ionic liquids," ECS Transactions, vol. 45, no. 29, pp. 235–244, 2013.

[19] O. N. Kalugin, A. V. Riabchunova, I. V. Voroshylova, V. V. Chaban, B. A. Marekha, V. A. Koverga, and A. Idrissi, "Transport properties and ion aggregation in mixtures of room temperature ionic liquids with aprotic dipolar solvents," in Modern Problems of Molecular Physics (L. A. Bulavin and A. V. Chalyi, eds.), (Cham), pp. 67–109, Springer International Publishing, 2018.

[20] M. N. Kobrak, "Characterization of the solvation dynamics of an ionic liquid via molecular dynamics simulation," The Journal of Chemical Physics, vol. 125, no. 6, p. 064502, 2006.

[21] C. F. Chapman, R. S. Fee, and M. Maroncelli, "Measurements of the solute dependence of solvation dynamics in 1-propanol: The role of specific hydrogen-bonding interactions," The Journal of Physical Chemistry, vol. 99, no. 13, pp. 4811–4819, 1995.

[22] T. Gustavsson, L. Cassara, V. Gulbinas, G. Gurzadyan, J.-C. Mialocq, S. Pommeret, M. Sorgius, and P. van der Meulen, "Femtosecond spectroscopic study of relaxation processes of three amino-substituted coumarin dyes in methanol and dimethyl sulfoxide," The Journal of Physical Chemistry A, vol. 102, no. 23, pp. 4229–4245, 1998.

[23] T. Kumpulainen, A. Rosspeintner, and E. Vauthey, "Probe dependence on polar solvation dynamics from fs broadband fluorescence," Phys. Chem. Chem. Phys., vol. 19, pp. 8815–8825, 2017.

[24] M. Sajadi, M. Weinberger, H.-A. Wagenknecht, and N. P. Ernsting, "Polar solvation dynamics in water and methanol: search for molecularity," Phys. Chem. Chem. Phys., vol. 13, pp. 17768–17774, 2011.

[25] N. Ito, S. Arzhantsev, and M. Maroncelli, "The probe dependence of solvation dynamics and rotation in the ionic liquid 1-butyl-3-methyl-imidazolium hexafluorophosphate," Chemical Physics Letters, vol. 396, no. 1, pp. 83 – 91, 2004.

[26] R. Karmakar and A. Samanta, "Steady-state and time-resolved fluorescence behavior of c153 and prodan in room-temperature ionic liquids," The Journal of Physical Chemistry A, vol. 106, no. 28, pp. 6670–6675, 2002.

[27] X.-X. Zhang, J. Breffke, N. P. Ernsting, and M. Maroncelli, "Observations of probe dependence of the solvation dynamics in ionic liquids," Phys. Chem. Chem. Phys., vol. 17, pp. 12949–12956, 2015.

[28] S. Daschakraborty, T. Pal, and R. Biswas, "Stokes shift dynamics of ionic liquids: Solute probe dependence, and effects of self-motion, dielectric relaxation frequency window, and collective intermolecular solvent modes," The Journal of Chemical Physics, vol. 139, no. 16, p. 164503, 2013.

[29] E. Laitinen, K. Salonen, and T. Harju, "Solvation dynamics study of 4-amino-n-methyl-phthalimide in n-alcohol solutions," The Journal of Chemical Physics, vol. 104, no. 16, pp. 6138–6148, 1996.

[30] S. Arzhantsev, H. Jin, N. Ito, and M. Maroncelli, "Observing the complete solvation response of dcs in imidazolium ionic liquids, from the femtosecond to nanosecond regimes," Chemical Physics Letters, vol. 417, no. 4, pp. 524 – 529, 2006.

[31] U. Narang, J. D. Jordan, F. V. Bright, and P. N. Prasad, "Probing the cybotactic region of prodan in tetramethylorthosilicate-derived sol-gels," The Journal of Physical Chemistry, vol. 98, no. 33, pp. 8101–8107, 1994.

[32] F. M. Agazzi, J. Rodriguez, R. D. Falcone, J. J. Silber, and N. M. Correa, "Prodan dual emission feature to monitor bhdc interfacial properties changes with the external organic solvent composition," Langmuir, vol. 29, no. 11, pp. 3556–3566, 2013.

[33] T. A. Betts, J. Zagrobelny, and F. V. Bright, "Investigation of solute-fluid interactions in supercritical cf3h: A multifrequency phase and modulation fluorescence study," The Journal of Supercritical Fluids, vol. 5, no. 1, pp. 48 – 54, 1992. Proceedings of the 2nd International Symposium on Supercritical Fluids.

[34] M. Novaira, M. A. Biasutti, J. J. Silber, and N. M. Correa, "New insights on the photophysical behavior of prodan in anionic and cationic reverse micelles: From which state or states does it emit?," The Journal of Physical Chemistry B, vol. 111, no. 4, pp. 748–759, 2007.

[35] C. C. Vequi-Suplicy, K. Coutinho, and M. T. Lamy, "New insights on the fluorescent emission spectra of prodan and laurdan," Journal of Fluorescence, vol. 25, pp. 621–629, May 2015.

[36] B. Mennucci, M. Caricato, F. Ingrosso, C. Cappelli, R. Cammi, J. Tomasi, G. Scalmani, and M. J. Frisch, "How the environment controls absorption and fluorescence spectra of prodan: A quantum-mechanical study in homogeneous and heterogeneous media," The Journal of Physical Chemistry B, vol. 112, no. 2, pp. 414–423, 2008.

[37] S. Sun, M. P. Heitz, S. A. Perez, L. A. Colón, S. Bruckenstein, and F. V. Bright, "6-propionyl-2-(n,n-dimethylamino)naphthalene (prodan) revisited," Applied Spectroscopy, vol. 51, no. 9, pp. 1316–1322, 1997.

[38] P. Gadad, H. Lei, and M. A. Nanny, "Characterization of noncovalent interactions between 6-propionyl-2-dimethylaminonaphthalene (prodan) and dissolved fulvic and humic acids," Water Research, vol. 41, no. 19, pp. 4488 – 4496, 2007.

[39] S. Aich, C. Raha, and S. Basu, "Characterization of the triplet charge-transfer state of 4-amino-n-methylphthalimide in aprotic and protic media by laser flash photolysis," J. Chem. Soc., Faraday Trans., vol. 93, pp. 2991–2996, 1997.

[40] Y. Chen and M. R. Topp, "Infrared-optical double-resonance measurements of hydrogen-bonding interactions in clusters involving aminophthalimides," Chemical Physics, vol. 283, no. 1, pp. 249 – 268, 2002.

[41] B. A. Pryor, P. M. Palmer, P. M. Andrews, M. B. Berger, T. Troxler, and M. R. Topp, "Spectroscopy of jet-cooled polar complexes of aminophthalimides," Chemical Physics Letters, vol. 271, no. 1, pp. 19 – 26, 1997.

[42] T. G. Kim, M. F. Wolford, and M. R. Topp, "Ultrashort-lived excited states of aminophthalimides in fluid solution," Photochem. Photobiol. Sci., vol. 2, pp. 576–584, 2003.

[43] D. E. Wetzler, C. Chesta, R. Fernández-Prini, and P. F. Aramendía, "Dynamic solvation of aminophthalimides in solvent mixtures," The Journal of Physical Chemistry A, vol. 106, no. 11, pp. 2390–2400, 2002.

[44] T. A. Betts and F. V. Bright, "Reversible excited-state transient solvation in binary supercritical fluids revealed by multifrequency phase and modulation fluorescence," Appl. Spectrosc., vol. 44, pp. 1203–1209, Jul 1990.

[45] J.-Y. Choi, E.-J. Park, S.-H. Chang, and T.-J. Kang, "Solvent effects on the solvatochromism of 7-aminocoumarin derivatives in neat and binary solvent mixtures: Correlation of the electronic transition energies with the solvent polarity parameters," Bulletin of the Korean Chemical Society, vol. 30, pp. 1452–1458, 2009.

[46] S. Spange, R. Lungwitz, and A. Schade, "Correlation of molecular structure and polarity of ionic liquids," Journal of Molecular Liquids, vol. 192, pp. 137 – 143, 2014. Fundamental Aspects of Ionic Liquid Science.

[47] Y. Marcus, "The properties of organic liquids that are relevant to their use as solvating solvents," Chem. Soc. Rev., vol. 22, pp. 409–416, 1993.

[48] A. S. R. Koti, M. M. G. Krishna, and N. Periasamy, "Time-resolved area-normalized emission spectroscopy (tranes): A novel method for confirming emission from two excited states," The Journal of Physical Chemistry A, vol. 105, no. 10, pp. 1767–1771, 2001.

[49] N. Periasamy and A. Koti, "Time resolved fluorescence spectroscopy: Tres and tranes," Proc Indian Natn Sci Acad, vol. 69A, no. 1, pp. 41–48, 2003.

[50] P. K. Mandal and A. Samanta, "Fluorescence studies in a pyrrolidinium ionic liquid: Polarity of the medium and solvation dynamics," The Journal of Physical Chemistry B, vol. 109, no. 31, pp. 15172–15177, 2005.

[51] A. Eilmes and P. Kubisiak, "Explicit solvent modeling of solvatochromic probes in ionic liquids: Implications of solvation shell structure," The Journal of Physical Chemistry B, vol. 119, no. 41, pp. 13185–13197, 2015.

[52] D. Yang and Y. Zhang, "Modulation of the 4-aminophthalimide spectral properties by hydrogen bonds in water," Spectrochimica Acta Part A: Molecular and Biomolecular Spectroscopy, vol. 131, pp. 214 – 224, 2014.

[53] R. Królicki, W. Jarzeba, M. Mostafavi, and I. Lampre, "Preferential solvation of coumarin 153the role of hydrogen bonding," The Journal of Physical Chemistry A, vol. 106, no. 9, pp. 1708–1713, 2002.

Chapter 4

Solvation dynamics in ionic liquid and IL/MS mixtures

The molecular rearrangements occurring in electrolyte models for DSSCs after photo-excitation are of great interest. In this Chapter, the solvation in IL/MS mixtures is investigated. The steady-state and time-resolved measurements of the solvation of C153 in BmimBF_4/PC are presented. The TCSPC and fluorescence up-conversion techniques were used to obtain the experimental SRFs. The MD simulations were performed to help the interpretation of the experimental data. Good accordance between the measured and the calculated SRFs was achieved. The analysis of the structure of the solvation shell of C153 in ground and excited states was made. The importance of the hydrogen bonding in the solvation dynamics was underlined.

4.1 Introduction

As it was demonstrated in Chapter 2, solvation dynamics plays an important role in the photophysics of indoline dyes. Indeed, at least one time constant, resulting from global analysis of transient absorption spectra, was assigned to the solvation dynamics. Thus, an understanding of the solvation dynamics (the solvent molecules rearrangement around the probe) is of major interest for the organic photosensitizers, as the molecule in DSSCs is immersed in the solution, although it is anchored to the semiconductor. During the solvation dynamics, the excited state energy decreases and probably causes the decrease of the efficiency of the electron injection, linked to the overpotential dye-semiconductor conductive band in a straightforward way[1].

The solvation response is a fundamental characteristics of the solvent, important not only for photosensitizing organic dyes, but also for photochemical reactions[2] and symmetry breaking[3]. While the solvation dynamics in conventional solvents is more or less clear, the situation with ionic liquids and their mixtures, introduced in the previous chapter, is far from being understood[4].

Here, we present steady-state and time-resolved data for the probe coumarin 153 in ionic liquid $BmimBF_4$, propylene carbonate PC and their mixtures. Also, molecular dynamics simulations of these systems are discussed, in particular the results of the simulations of solvation response functions and the structure in equilibrium as well as its evolution during the solvation dynamics.

4.1.1 Solvation dynamics process

For a number of fluorophores, a big change of the electric dipole moment occurs upon the photo-excitation. This is perfectly the case of the indoline dyes. As we know, the movements of electrons are much faster than the movements of atoms. Thus, we can say that just after the photoexcitation, the dipole moment of the molecule has changed considerably, but the position of the solvent molecules didn't.

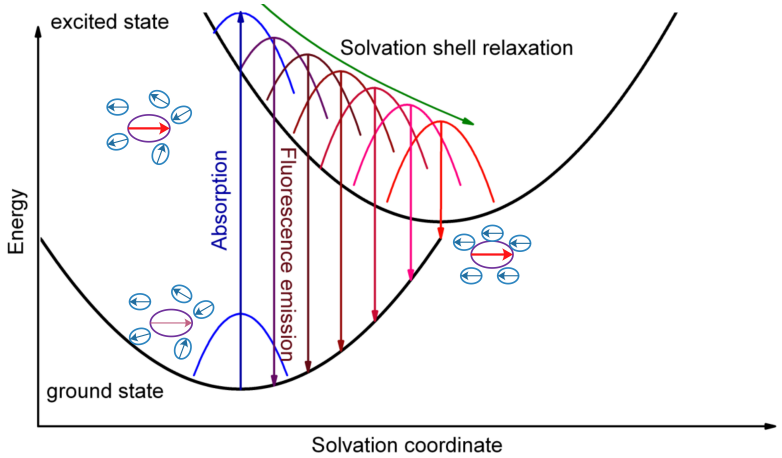

Figure 4.1: Solvation dynamics: the decrease of the free energy of the excited state due to the solvent molecules reorganizationx.

A sudden change in dipole moment of the dye corresponds to the sudden change in the electric field, acting on the environment of the probe. Thus, the solvent molecules are in statistic equilibrium with the ground state, but not with the excited

state. After the photoexcitation, the solvent molecules rearrange their orientations and positions in order to correspond to the statistic equilibrium with the new, excited state force field. This process is not instantaneous, as the photoexcitation, and is called the solvation dynamics. It can cover multiple time scales, like it is the case in ionic liquids and their mixtures. In hydrogen bond donor solvents, e.g. methanol, the solvent molecules reorientation and diffusion are not the only possible mechanisms of the solvation response. Rupture and re-formation of hydrogen bonds between a probe and solvent molecules take place along with inertial movements, rotational and translational diffusion [5].

Let's come back to our fluorophore. The energy of excited state obviously depends on the interactions of the probe with the environment. Thus, while the solvation shell rearranges in order to gain its equilibrium structure, the energy of the excited state decreases, and one can call this process a 'relaxation of the excited state'. In our approach, the electronic structure of the molecules stays the same, but its free energy decreases. Schematically, this process is shown in fig. 4.1.

Importantly, solvation dynamics is inherent to a solvent, and its characteristic time, in theory, doesn't depend on the probe. Thus, choosing a probe with absence of other processes (e.g. photochemical reactions), taking place after the excitation, one can measure the solvation time and use it for other molecules in the same solvent. The probe dependence of the solvation dynamics in ionic liquids and their mixtures is addressed in the Chapter 3. In literature, a variety of different fluorescent probes were used, but coumarin 153 (C153) is the one worth mentioning. Its rigid structure and simple two electronic state model for $S_0 \rightarrow S_1$ transition[6] make C153 the 'golden'probe to study the solvation dynamics. In general, solvent relaxation process was found to be probe dependent[7–14], and the origin of this dependency was assigned to solvent-probe specific interactions[7, 12, 13] or rotational motion of the probe [8, 10].

In order to measure the solvation dynamics, time-resolved emission spectra must be recorded. The normalized time evolution of the mean (or maximum) wavenumber (or frequency) is the solvation response function (eq. 4.1). Another method consists in a single emission transient measurement, collected at a special linear emission wavelength[15]. However, the accuracy of the solvation times achieved in this way is of the order of 30-40%[16]. Thus, spectral reconstruction method was used in this work.

$$C(t) = \frac{\nu(t) - \nu(10.032ns)}{\nu(0) - \nu(10.032ns)} \tag{4.1}$$

Due to the exponential character of the SRF and limited time resolution of used set-ups, the estimation of the position of t=0 emission spectrum is a subject of high uncertainty. In regard of this, Fee and Maroncelli have proposed a method of t=0 emission spectrum calculation[17]. Furthermore, the authors have reported a working approximation to calculate a mean wavenumber of emission spectrum at t=0, using the steady-state spectra in a given polar and non-polar solvent (eq. 4.2). This approximation was claimed to give the results within the error of $\pm 200 \mathrm{cm}^{-1}$.

$$\nu(t=0) \approx \nu(abs) - [\nu_{np}(abs) - \nu_{np}(em)] \tag{4.2}$$

In this work, the initial wavenumbers were the ones of the spectra at the half-rise of fluorescence intensity decays. These values already give an understanding of

the fraction of missed part of the solvation response, being the maximum of the information that we can expect from the part of SRF that is not actually measured.

Finally, the solvation response function can be modelled with a number of different functions and their combinations: gaussian, exponential and stretched exponential. In this work, multiple exponential functions are used. Integral solvation times (or weighted average solvation times) are also obtained.

4.1.2 Literature review

The solvation dynamics was studied in water[10, 18], common organic solvents [19, 20, 10, 12, 13, 21, 18], solid salts[22], ionic liquids[9, 11, 23–31], IL/MS mixtures[32–34], mixtures of conventional solvents[35, 14], micelles[36] and even in protein environments[37]. For these studies, the following fluorescent probes were used: coumarin 343 [10, 18, 14], 7-(dimethylamino)coumarin-4- acetic acid (DMACA) [10], coumarin 480 [14], 4-dicyano-methylene-2-methyl-6-(p-dimethylaminostyryl)-4H-pyran (DCM) [10], 3-aminophthalimide (3AP) [10], 4-aminophthalimide (4AP) [10, 13, 11, 35], N-methyl-6-oxyquinolinium betaine (MQ) [10], 4-AP-Ri (2'-deoxyribose) [10], 4-amino-N-methyl-phthalimide (4-ANMP) [20, 13, 35], 7-amino- 4-trifluoromethyl-coumarin (C151) [12], 7-diethylamino-4- trifluoromethyl coumarin (C35) [12], aniline [13], dimethylaniline (DMA) [13], 1-amino naphthalene (1-AN) [13], 2-aminoanthracene (2-AA) [13], 1-aminopyrene (1-APY) [13], coumarin 1 [13], coumarin 120 [13], coumarin 152 [13], coumarin 339 [13], coumarin 102 [13, 22, 11], (dimethylamino)-benzonitrile (DMABN) [13], indole [13], 1-methylindole (1-MI) [13], PRODAN [13, 9, 11], N,N-dimethyl-6-(N-(4-methylphenyl)amino)-2-naphthalenesulfonamide (TNSDMA) [22], 4-dimethylamino-4'-cyano-stilbene (DCS) [11], 9-phenyl-10-methyl-acridunium hexafluorophosfate (PAc PF_6) [11], 9,9'-bianthryl (BA) [24], 4-(9-anthryl)-N,N-dimethyl-aniline (ADMA) [24], oxazine 4 (Ox4) [25] and coumarin 153 [10, 19, 13, 21, 22, 9, 11, 23, 24, 26, 28, 29, 32, 14, 36]. The literature data on the solvation response in ionic liquid $BmimBF_4$, considered in this Chapter, are assembled in table 4.1.

The complete solvation response in imidazolium, pyrrolidinium and other ionic liquids was accessed by the means of broadband fluorescence upconversion and TCSPC techniques and reported in [38]. The SRFs were confirmed to be bimodal, as supposed in the early work, where only TCSPC technique was used [39]. A fast subpicosecond component was assigned to the solvent inertial motions and the later one to the diffusive, structural reorganization of the solvent. The latter, non-inertial component was found to follow the single correlation with viscosity for imidazolium, pyrrolidnium and tetralkylammonium ionic liquids [40]. In these systems, rotational correlation times of C153 were reported to behave much like in conventional solvents, and the non-exponential character of the anisotropy decays was attributed to non-Markovian friction effects due to the high viscosity of the ionic liquids. Similar conclusion about the bi-exponential character of the solvation response in imidazolium and pyrrolidinium ionic liquids was made by Arzhantsev et al[41]. The authors presented Kerr-gated emission and TCSPC measurements, using trans-Dimethylamino-4'-cyanistilbene molecule as the probe. They also stated that the dielectric continuum models, when applied to ILs, result in the SRFs that are 3-5 times faster than experimental ones. Finally, the comparison between DCS and C153 probes didn't suggest any probe dependence of SRF in ILs.

In the publication [42], it was illustrated that the integral solvation time in ionic liquids is correlated to the conductivity of the solvent via the relation of the form $\langle\tau_{solv}\rangle \propto \sigma^{-p}$, in support to the predictions of a simple dielectric continuum theory. Although this model provides a good representation of a dispersive nature of the SRF in ILs, the calculated times are a factor of 2-4 faster [38]. Another proposition to help the interpretation of the solvation dynamics, an extended Debye-Huckel dielectric continuum model was presented and applied to calculate the solvation dynamics in ionic fluids and the results were shown comparable to the SRFs from molecular dynamics simulations [43, 44]. Inversely, in the other work, the time-resolved studies of molecular solvation were proposed to use in order to obtain the dielectric dispersion of the microscopic environment [45].

On the basis of similar initial fast response of imidazoles and imidazolium ionic liquids, Headley et al. support the hypothesis that this part of SRF is governed by imidazolium cation [46]. However, this initial fast response was also observed in tribythylphosphine and in phosphonium ionic liquids, reported later by the same group [47]. In this article, the solvation response in phosphonium ionic liquids and their micelles in water was studied. Contrarily to Maroncelli works, the presence of a fast component of the solvation response that is finished in 100 ps is claimed.The difference in SRF construction was explained to be at the origin of the discrepancy of the results. Thus, we suggest that the initial part of the response is due to the fast inertial motions of the solvent, and it is a part of the solvation response that is present in all liquids. Muramatsu et al. [25] performed three-pulse photon echo peak shift measurements of oxazine 4 perchlorate in imidazolium and phosphonium ionic liquids. On the basis of correlations of solvation time components with both square root of mass of anion and the inertial factor, they made a conclusion that the ultrafast part of the solvation in these systems comes from anion's inertial motion, and further response is more global, including the motion of cation.

A very limited number of studies of solvation dynamics in the IL/MS mixtures is available in literature [48, 49]. All the data available was achieved with C153 fluorescent probe, and the results only for mixtures of $BmimBF_4$ with acetonitrile and water were reported. As a general outcome, the solvation energetics was found to change little with the ionic liquid molar fraction. Thus, no conclusion about the preferential solvation could be drawn. The dynamics is shown to be clearly bi-exponential in all cases, and the slower time component decreased with addition of molecular solvent in parallel with viscosity. Applied to mixtures, dielectric continuum and semimolecular (Biswas and co-workers [33]) theories didn't give satisfactory predictions of the solvation response. From the literature data on the solvation dynamics, no abrupt change in mixtures structure within the composition change was evident, as most of the measured properties undergo simple continuous evolution as a function of composition. Later, a new, improved version of the semimolecular theory was published[34], with almost quantitative agreement with experimental data. The model reproduced the composition dependence of the solvation time components, dynamic Stokes shifts and viscosity dependence of slow times for mixtures of $BmimBF_4$ with water and acetonitrile.

Solvation dynamics has also been the subject of theoretical studies by MD simulations. Thus, works considering conventional solvents and ionic liquids [26] were published. A comprehensive investigation on the collective/single molecule, rotational/translational features of solvent relaxation in CO_2 and acetonitrile and

Table 4.1: Best fit parameters of C153 solvation response functions in $BmimBF_4$ ionic liquid from literature.

Solute method	equation+ params						
C153	$a_1 exp(-t/\tau_1) + a_2 exp(-t/\tau_2)$						
[23]	a_1	a_2	τ_1	τ_2	$<\tau>$		
TCSPC	0.5	0.5	278ps	3.98ns	2.13 ns		
Oxazine 4	$\sum_i a_i exp(-t/\tau_i)$						
[25]	a_1	a_2	a_3	τ_1	τ_2	τ_3	
3PEPS	5.7 fs	1.7 fs	1.2 fs	110 fs	1.1 ps	21ps	
C153	$a_1 exp(-t/\tau_1) + a_2 exp(-t/\tau_2)^\beta$						
[26]	a_1	a_2	τ_1	τ_2	β		
MD	0.4	0.6	0.245 ps	1259.2 ps	0.31		
C153	$\sum_i f_i exp(-t/\tau_i)$						
[48]	f_1	f_2	f_3	τ_1	τ_2	τ_3	
FLUPS TCSPC	0.409	0.288	0.303	0.33 ps	49 ps	743 ps	
C153	$f_G exp(-1/2\omega_G^2 t^2) + (1-f_G)\sum_i a_i exp(-t/\tau_i)$						
[49]	f_G	ω_G	a_1	a_2	τ_1	τ_2	τ_3
FLUPS TCSPC	0.31	7.0ps^{-1}	0.19	0.4	1.8 ps	64 ps	790 ps
DCS	$f_1 exp(-t/\tau_1) + (1-f_1) exp[-(t/\tau_2)^\beta]$						
[41]	f_1	τ_1	τ_2	β			
KGE TCSPC	0.19	0.32 ps	0.13 ns	0.41			
C153	$f_G exp(-1/2\omega_G^2 t^2) + (1-f_G) exp[-(t/\tau_2)^\beta]$						
[8]	f_G	ω_G	τ	β			
FLUPS TCSPC	0.34	7.0ps^{-1}	0.17 ns	0.48			
4AP	$f_G exp(-1/2\omega_G^2 t^2) + (1-f_G) exp[-(t/\tau_2)^\beta]$						
[8]	f_G	ω_G	τ	β			
FLUPS TCSPC	0.26	5.3ps^{-1}	0.22 ns	0.47			
PRODAN	$\sum_i a_i exp(-t/\tau_i)$						
[9]	a_1	a_2	τ_1	τ_2			
TCSPC	0.62	0.38	280ps	3330ps			

their dependence on the character of perturbation is available[50]. Importantly, the collective part of SRF was shown to be significant in dipolar ACN. Concerning the ionic liquids, the most general understanding was achieved from [51]. In this study, both equilibrium and non-equilibrium simulations of SRF were performed,

using coarse-grained model of ionic liquid ILM2, three site model for acetonitrile and a list of different solutes: C153, diatomic solute, three inert gases and three single site solutes, having volume and energy parameters roughly similar to benzene, naphthalene and anthracene. Among the key findings of the article, one can list: 1) The bimodal character of the SRF is reproduced by simulations, although the subpicosecond component is largely overestimated; 2) The translational motions play a dominant role in the solvation dynamics in the IL and 3) The subpicosecond component is majorly represented by the inertial translation of the anion. The mechanism of the solvation dynamics in pyrrolidinium ionic liquids with bromide and more bulky bis(trifluoromethylsulfonyl)imide anions was modelled with more realistic full-atom force fields [52]. Steele analysis of the role of translational and rovibrational motions in the solvent relaxation process, decomposition to the cation and anion contributions as well as to single-ion and ion-pair components resulted in the following hypothesis. The most rapid response comes from the rovibrational components, then ionic translation dominates the subpicosecond timescale and finally, slow collective translational motions of ions finish the game. Concerning imidazolium ionic liquids, a study of C153 in $EmimBF_4$ is available[53]. Among the key findings of this article, preferential solvation of C153 by $Emim^+$ cation is important to be mentioned. The solvation dynamics was calculated with 5.015 μs production run, using linear response theory. Anion translational motion in and out of the solvation shell of C153 is proposed as the particular molecular motion, especially relevant to solvation dynamics.

4.2 Experimental measurements

4.2.1 Steady-state measurements of C153 in $BmimBF_4$/PC mixtures

The probe C153 is known to exhibit solvatochromism in the solvents of different polarity[19]. The subject of polarity of imidazolium ILs was considered in the articles [54–56], reporting investigations using different solvatochromic dyes. As a common conclusion, imidazolium ionic liquids are positioned in the middle to upper half of the polarity scale, at the same level as lower alcohols, such as methanol, and acetonitrile. Furthermore, the hydrogen bond donor ability similar to that of alcohols and low nucleophilicity were suggested[55].

Steady state absorption and fluorescence spectra of C153 were recorded in $BmimBF_4$ and propylene carbonate mixtures with different ionic liquid molar fractions. In figure 4.2a, normalised spectra are shown (top panel), as well as the dependence of peak wavenumber of absorption and emission spectra on mixture composition. Peak wavenumbers are also listed in table 4.2.

Broad and featureless bands of C153 are characteristic for its solutions in polar solvents. In this wavenumber region, only a single transition between S_0 and S_1 ground and excited stated contribute. The positions of these bands, interpreted in terms of peak or mean wavenumbers, must serve as a measure of the polarity of mixtures. On the basis of an analysis of the solvatochromic behaviour of C153 in conventional organic solvents[19], a slight red shift of spectra with increase of ionic liquid molar fraction obviously parallels the increase in polarity of mixtures. As an estimation of the polarity of neat mixture components, one can take a Reichardt normalised

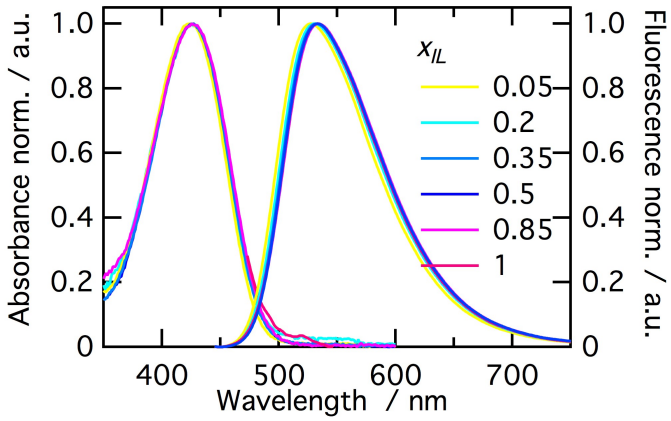

(a) Steady-state absorption and fluorescence spectra of C153 dye in $BmimBF_4$/PC mixtures.

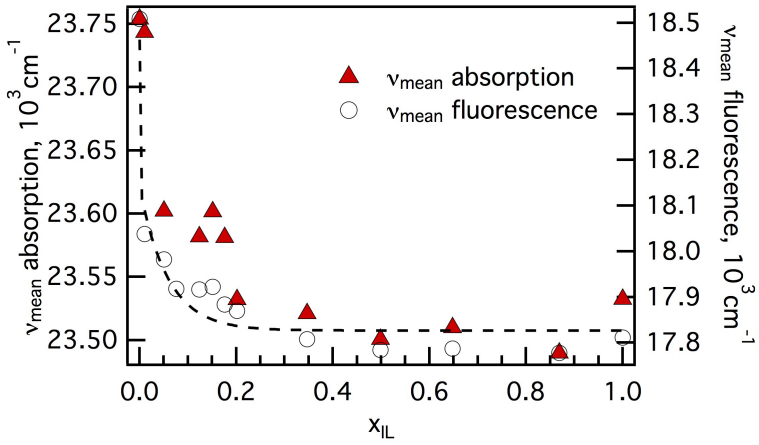

(b) Dependency of mean wavenumber of absorption and emission spectra of C153 on the ionic liquid molar fraction. Dashed line is the double exponential fit: $\nu^{em}_{mean} = 17827 + 323\exp(-x_{IL}/3e-4) + 313\exp(-x_{IL}/0.059)$

Figure 4.2: C153 in $BmimBF_4$/PC mixtures: steady-state spectra analysis

polarity parameter E_T^N. This estimation gives an idea about the microscopic polarity of the environment of the fluorescent probe. As probes, negatively solvatochromic pyridinium N-phenolate betaine dyes were used[57]. Reichardt polarity scale ranges from 0.000 for tetramethylsilane to 1.000 for water, as extreme nonpolar and polar reference solvents. E_T^N values were measured to be 0.472 for propylene carbonate and 0.673 for $BmimBF_4$ (N-(4-oxidophenyl)pyridinium dye was used, literature data [55]). Thus, the Reichardt polarity estimations corroborate with the results of C153 steady-state measurements: the polarity of $BmimBF_4$ is slightly higher than that of propylene carbonate. This effect is more prominent in emission than in absorption spectra (the difference in emission peak wavenumbers is higher than the one in absorption peaks, see fig. 4.2b). Stronger interaction between coumarin in excited state with its environment can be an explanation, possibly due to a higher dipole moment of C153 in excited state. Kamlet-Taft polarity/polarisability π^* parameter values for propylene carbonate (0.83[58]) and $BmimBF_4$(1.047[59]) are also in accordance with C153 steady-state results. Using exponential regression, shown as a dashed line in fig. 4.2b, one can make estimations of E_T^N and π^* parameters of the mixtures. An

Table 4.2: Maximum and mean wavenumbers, full width half maximum of absorption and fluorescence bands, Stokes shifts $\Delta\nu$ of C153 in $BmimBF_4$/PC mixtures. π^* and E_T^N are the calculated values, obtained using the exponential regression, shown in fig. 4.2. All values are given in 10^3 cm^{-1}.

x_{IL}	ν_{peak}^{abs}	ν_{mean}^{abs}	$fwhm_{abs}$	ν_{peak}^{em}	ν_{mean}^{em}	$fwhm_{em}$	$\Delta\nu$	π^*	E_T^N
0	23.76	23.75	3.48	19.08	18.51	2.98	5.25	0.830	0.472
0.0101	23.75	23.74	3.65	18.69	18.04	3.45	5.71	0.957	0.590
0.0504	23.61	23.60	4.29	18.63	17.98	3.43	5.62	1.002	0.631
0.0758				18.58	17.92	3.48		1.018	0.646
0.1238	23.59	23.58	4.37	18.57	17.92	3.43	5.67	1.034	0.661
0.1515	23.61	23.60	4.45	18.58	17.92	3.38	5.68	1.039	0.666
0.1764	23.59	23.58	4.50	18.54	17.88	3.43	5.70	1.042	0.668
0.2017	23.54	23.53	4.28	18.52	17.87	3.43	5.66	1.044	0.670
0.3468	23.53	23.52	4.56	18.46	17.81	3.42	5.71	1.047	0.673
0.4985	23.51	23.50	4.64	18.44	17.78	3.41	5.72	1.047	0.673
0.6479	23.52	23.51	4.86	18.44	17.79	3.36	5.72	1.047	0.673
0.8689	23.50	23.49	4.87	18.41	17.78	3.41	5.71	1.047	0.673
1	23.54	23.53	4.24	18.44	17.81	3.39	5.72	1.047	0.673

assumption about linear dependence between π^* (E_T^N) and the mean wavenumber of fluorescence band was made. The results are included in table 4.2.

The dependency of peak wavenumber on the mixture composition is not linear. A rapid change when a small amount of ionic liquid is added to propylene carbonate leads to the conclusion that C153 is preferentially solvated by the ionic liquid. Similar observations were made in the study of $BmimBF_4$/water mixtures [48]. Zhang et al. suggest the preferential solvation of coumarin by water from the dependency of peak wavenumber on the volume fraction of ionic liquid. However, the authors beware to assume that local compositions in ionic solutions can be inferred from that kind of plot.

Deviations of mixture polarity from linearity can be another explanation of C153 fluorescence maxima fast decrease at small x_{IL}. Non-ideal mixing of $BmimBF_4$ with molecular solvents, such as water and ethanol was reported[60]. However, the plateau of the values of the mean wavenumber of UV-Vis absorption and emission spectra above 0.2 favours the hypothesis about the preferential solvation. In view of this preferential solvation, the calculated E_T^N and $\pi*$ values for mixtures must be used with caution and the fact that these values were obtained with C153 probe must be taken into account.

4.2.2 TCSPC and up-conversion measurements

Time-resolved emission spectroscopy was used to follow the solvation dynamics in mixtures of ionic liquid with a molecular solvent. A literature review revealed a complex and non-exponential dynamics in ILs and mixtures that extend over different time scales: from femtoseconds to nanoseconds. In order to cover these times, at least two time-resolved fluorescence techniques must be used. In this work, fluorescence up-conversion and TCSPC measurements were performed on C153 solutions in mixtures of $BmimBF_4$/PC. The schemes of both setups are given in the

Appendix.

Fluorescence up-conversion time-resolved spectra were recorded for neat components (C153 solutions in propylene carbonate and $BmimBF_4$) and several compositions of mixtures. A typical result, emission spectra at different times after the photoexcitation of C153 in propylene carbonate, is shown in figure 4.3. C153 emission exhibits a bathochromic shift with time in parallel with solvent relaxation. The spectra were measured in time window from 1ps to 100ps. After the averaging of two measurements, spectra were corrected for the baseline and converted to wavenumber scale by multiplication by λ^2 factor. The obtained spectra were directly fit to a simplified lognormal distribution function, used in steady-state analysis. Data treatment was performed using python script, available upon request. Emission spectra of C153 in ethanol were recorded for delay times after 100ps and compared to a steady-state emission spectrum of the same solution (fig. E.2). The dependency of detector sensitivity on wavelength was found to be negligible.

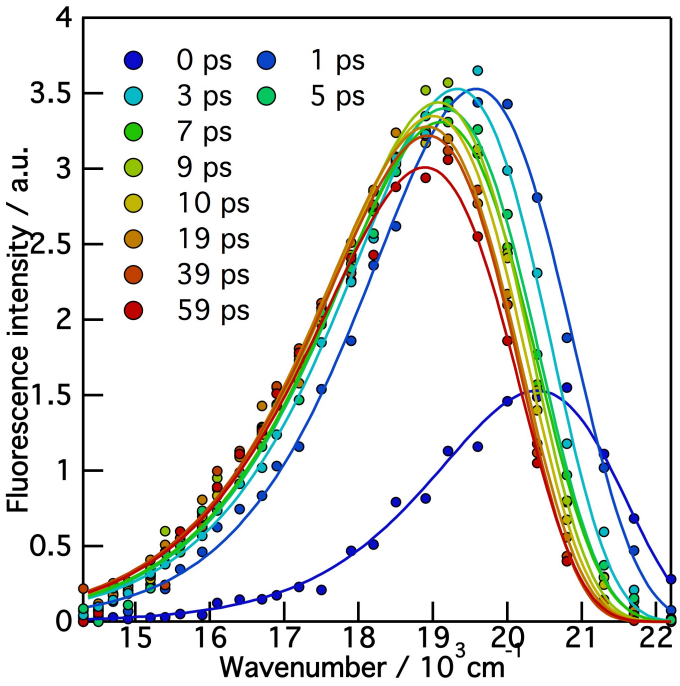

Figure 4.3: Time resolved emission spectra of C153 in propylene carbonate, measured with fluorescence up-conversion spectroscopy

The simplified lognormal distribution function (eq. 2.10) is a good estimation of shape of emission spectra of C153. Mean wavenumbers ν_{mean}, maximum wavenumbers ν_{max}, asymmetry ρ, and full width half maxima $FWHM$ were calculated and stored. An example of the dependency of parameters on time is shown in fig. 4.4. One can note a substantial decrease of mean and peak wavenumber values with time due to the relaxation of the solvation shell within first 20 ps. While the asymmetry changes negligibly, an increase in $FWHM$ at short times and further narrowing of emission spectra with time is observed. An initial increase in $FWHM$ is attributed to bad definition in this time interval, dominated by the instrument response function. Consequent decrease of spectral width is rather weak (about $100cm^{-1}$) and is negligible within the spectral resolution of our measurements. However, this slight decrease was already observed in literature at the same time scales for C153 in

propylene carbonate and is attributed to vibrational relaxation of C153 and changes in the distribution of solvent environments[61].

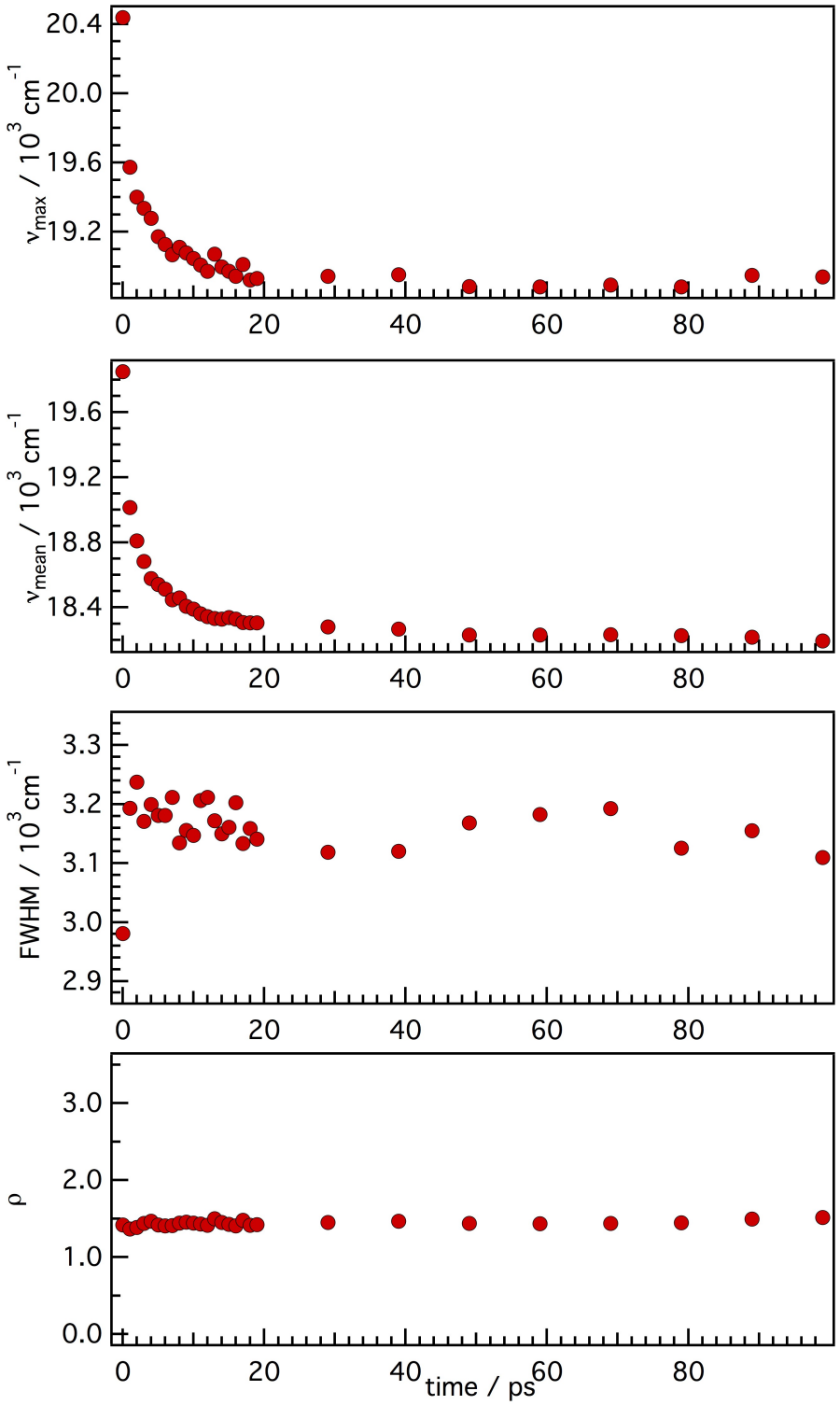

Figure 4.4: Evolution of mean ν_{mean} and peak ν_{max} wavenumbers, spectral full width half maximum ($FWHM$) and asymmetry ρ of time resolved emission spectra of C153 in propylene carbonate, measured with up-conversion fluorescence spectroscopy

TCSPC measurements were performed in kinetic mode: fluorescence intensity

decays were recorded at different emission wavelengths. The resulting decays were fit to multi-exponential functions using the same iterative reconvolution procedure, as described in Chapter 2. Fit parameters, as well as steady-state emission spectra, were used to reconstruct the time-resolved emission spectra, subsequently fit to the same simplified lognorm, as up-conversion results. Analogically, python script was used for reconstruction and fit, and it is available upon request.

Mean wavenumbers from up-conversion and TCSPC measurements were merged, overlapping in the time window of 32 ps - 100 ps, and the solvation response functions (SRFs) were calculated. In fig. 4.5, one can see the SRFs of C153 in neat PC, $BmimBF_4$, as well as their mixtures. The following observations can be made: (i) The solvation dynamics in the studied systems is clearly multi-exponential; (ii) About 35% of the solvation response occurs at the subpicosecond time scale; (iii) The solvation times become longer upon the addition of ionic liquid in parallel with viscosity.

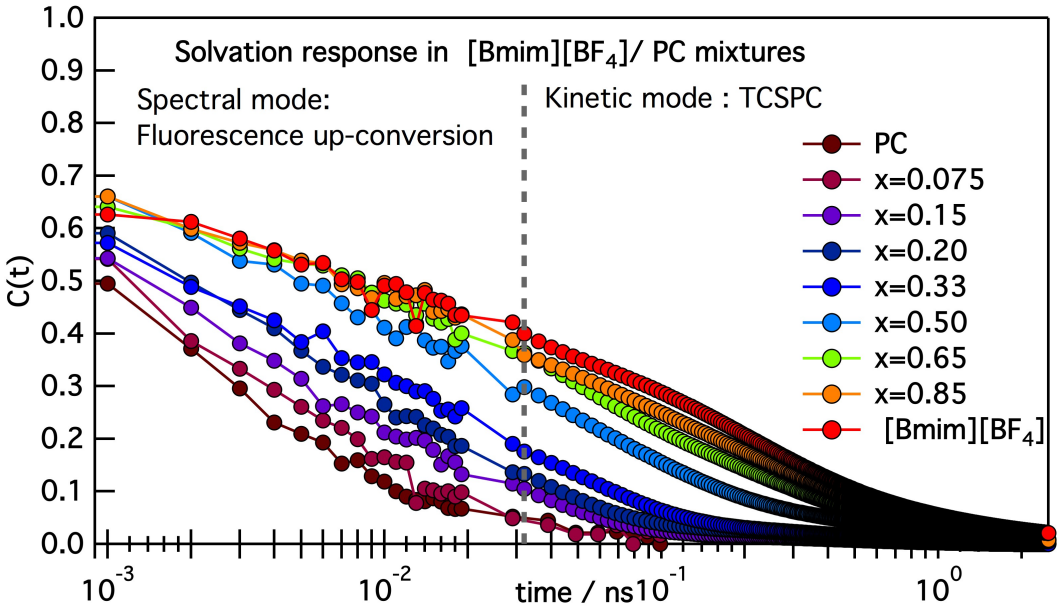

Figure 4.5: Solvation response functions, obtained with C153 for $BmimBF_4$/PC mixtures. Mean wavenumbers were merged from up-conversion and TCSPC experiments before the calculation of SRFs.

In order to get a quantitative information about the solvation dynamics, SRFs were fitted to n-exponential functions. The quality of fit was estimated with χ^2 parameter. The number of exponentials was chosen to get the best improvement of fit (ca. fig. C.1). The best fit parameters are listed in table 4.3.

Table 4.3: Top: best fit parameters of C153 solvation response functions to multiexponential functions: zero $y_0 \cdot 10^3$, amplitudes A_i, time components τ_i, ps and χ^2 values of the fit. Bottom: best fit parameters of C153 fluorescence anisotropy decays to multiexponential functions: amplitudes β_i, time components ϕ_i, ns and χ^2_{red} values of the fit.

x_{IL}	y_0	A_1	τ_1	A_2	τ_2	A_3	τ_3	A_4	τ_4	χ^2
0	15±5	0.170±0.030	16.0±4.00	0.470±0.030	2.6±0.3	-	-	-	-	0.0020
0.07	21±6	0.400±0.030	9.50±0.80	0.600±0.260	0.7±0.3	-	-	-	-	0.0046
0.15	16±1	0.268±0.007	29.0±1.00	0.370±0.010	2.9±0.2	-	-	-	-	0.0021
0.2	22.2±0.6	0.292±0.006	33.3±0.80	0.350±0.007	4±0.2	-	-	-	-	0.0024
0.33	18.8±0.6	0.230±0.010	63.0±2.00	0.241±0.010	12.4±1	0.23±0.02	1.2±0.2	-	-	0.0022
0.5	37±2	0.220±0.020	140±10.0	0.230±0.010	33±3	0.241±0.009	3.2±0.2	-	-	0.0039
0.65	24.7±0.9	0.234±0.004	278±7.00	0.243±0.004	47±2	0.165±0.004	5.1±0.3	-	-	0.0024
0.85	23.2±1	0.298±0.002	302±5.00	0.234±0.003	31±1	0.175±0.009	2.2±0.2	-	-	0.0034
1	11.7±0.9	0.111±0.004	1008±50.0	0.283±0.004	201±6	0.117±0.005	28±2	0.158±0.006	3.6±0.3	0.0067

x_{IL}	r_0	β_1	ϕ_1	β_2	ϕ_2	β_3	ϕ_3	ϕ_{av}	χ^2_{red}
0	0.23±0.02	0.23±0.02	0.14±0.01	-	-	-	-	0.14	1.099
0.0217	0.3±0.02	0.3±0.02	0.16±0.01	-	-	-	-	0.16	1.024
0.0546	0.32±0.02	0.32±0.02	0.18±0.01	-	-	-	-	0.18	1.035
0.0755	0.4±0.05	0.23±0.01	0.3±0.02	0.18±0.04	0.05±0.01	-	-	0.19	1.072
0.1017	0.31±0.03	0.25±0.01	0.27±0.02	0.06±0.02	0.12±0.05	-	-	0.24	1.023
0.1269	0.3±0.01	0.3±0.01	0.27±0.02	-	-	-	-	0.27	1.058
0.1493	0.31±0.05	0.27±0.01	0.29±0.02	0.04±0.04	0.05±0.06	-	-	0.26	1.079
0.1724	0.3±0.03	0.15±0.01	0.45±0.04	0.15±0.02	0.19±0.03	-	-	0.33	1.079
0.1992	0.3±0.02	0.175±0.009	0.5±0.04	0.13±0.02	0.18±0.03	-	-	0.36	1.043
0.3305	0.32±0.03	0.238±0.009	0.74±0.04	0.08±0.02	0.14±0.05	-	-	0.59	1.056
0.4985	0.33±0.03	0.251±0.007	1.36±0.05	0.08±0.02	0.15±0.06	-	-	1.08	1.04
0.6484	0.32±0.02	0.256±0.005	2.2±0.07	0.06±0.02	0.19±0.07	-	-	1.80	1.069
0.846	0.33±0.03	0.266±0.005	3.8±0.1	0.07±0.03	0.14±0.07	-	-	3.07	1.035
1	0.37±0.1	0.251±0.004	5.5±0.2	0.04±0.02	0.3±0.1	0.08±0.08	0.03±0.03	3.81	1.046

While SRFs in systems with low content of IL are well described with two exponential functions, higher concentration requests the introduction of the third and the fourth exponential terms. High viscosity of these systems, as well as ionic nature of their components are possible reasons of this complex dynamics. Weighted average solvation times were calculated, their dependency on viscosity of mixture is presented in fig. 4.6. Modelled by power law function, the best fit parameters are similar for mixtures with protic and aprotic polar solvents (propylene carbonate, water, acetonitrile). This would lead to the conclusion about the dominant role of ionic liquid in the dynamics of solvation. This is highly possible in regard of the preferential solvation of C153 by ionic liquid. Molecular dynamics simulations are needed to get insight to a structure of the solvation shell of C153 in mixtures of $BmimBF_4$ with propylene carbonate.

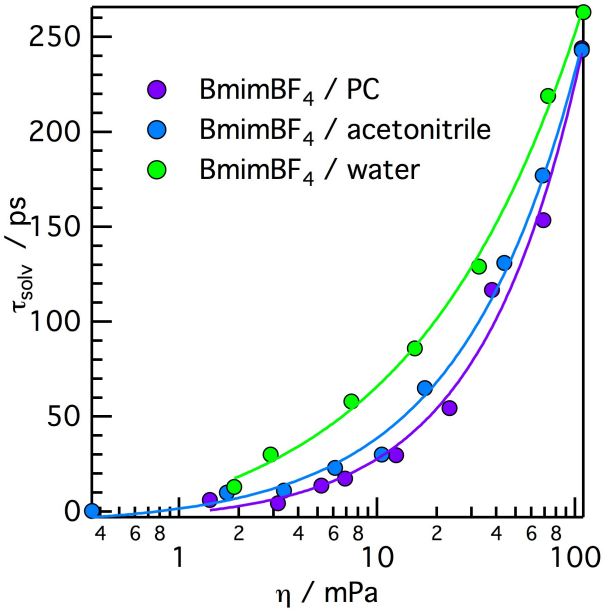

Figure 4.6: Average solvation times for C153 in mixtures of $BmimBF_4$ with propylene carbonate, water[48] and acetonitrile[49]. Solid lines are fits to functions: (i) PC $\tau_{solv} = -6+5\eta^{0.84}$, (ii) water $\tau_{solv} = -20+27\eta^{0.50}$, (iii) acetonitrile $\tau_{solv} = -7+9\eta^{0.72}$.

On the other hand, the dynamics in mixtures was studied by the means of fluorescence anisotropy measurements. The rotation of the probe, addressed in this way, is the characteristics of the microfluidity of its environment. Fluorescence anisotropy decays, measured with TCSPC, are shown in fig. 4.7. The rotation can be described as a free anisotropic rotation. Rotational correlation times are listed in table 4.3.

Weighted average rotational correlation times increase in parallel with viscosity (fig. 4.8). The dependency of $< \tau_{rot} >$ on viscosity is not linear. The monomial character of this dependency was already observed in the literature for mixtures of $BmimBF_4$ with acetonitrile. In analogy with solvation response, this complex dynamics is attributed to a high viscosity of these systems and ionic nature of its constituents.

According to the hydrodynamic theory, the rotational correlation times can be calculated, using the viscosity values. The ratio between the observed and calculated times is called a coupling constant. The result is presented in figure 4.9.

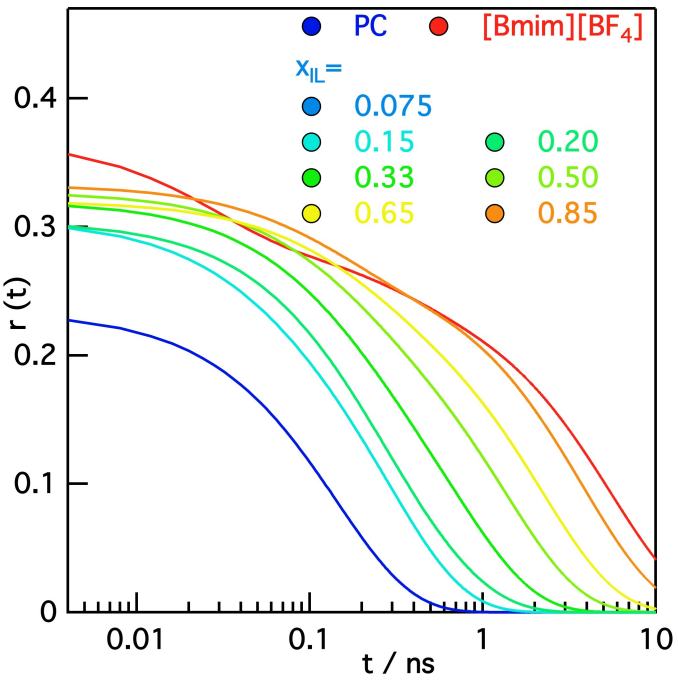

Figure 4.7: Fluorescence anisotropy decays of C153 in $BmimBF_4$/PC mixtures. Emission wavelength monochromator was set to 530nm.

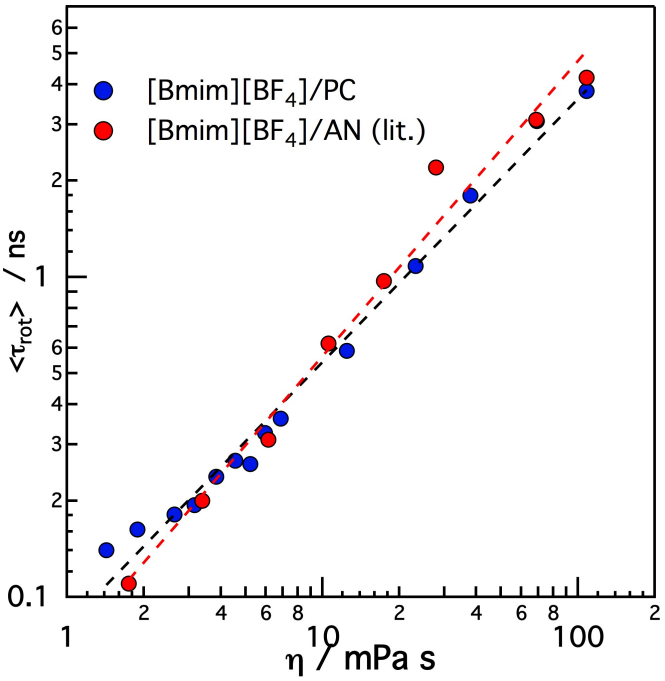

Figure 4.8: Log-log plot of average rotational correlation time of C153 in $BmimBF_4$/PC mixtures as a function of the mixture viscosity. Literature data for C153 in $BmimBF_4$ in acetonitrile was taken from [49].

One can note, that the calculated time constants are much higher than the observed ones. This can be rationalised in terms of different friction that is felt by ions and neutral C153 in solutions. Indeed, the ratios of observed to Stokes-Einstein

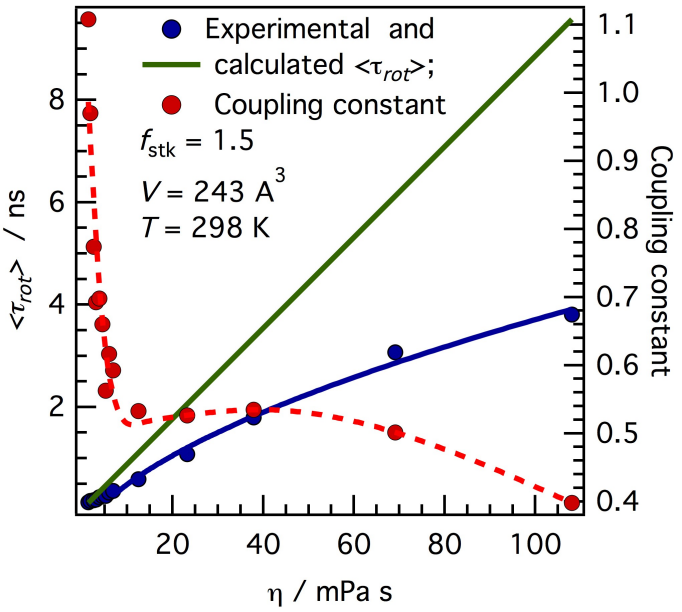

Figure 4.9: Experimental (dark blue) and calculated (green) rotational correlation times of C153 in $BmimBF_4$/PC mixtures as a function of mixture viscosity. Red circles are coupling constants.

friction coefficients for neutral solutes were found to be less than unity and largely dependent on ratio of solute/solute sizes [62]. The non-validity of Stokes-Einstein-Debye relations in neat ionic liquids and their mixtures was also stated in the work [63], and the dynamical heterogeneities were supposed to be related to this behaviour.

Also, interesting behaviour of coupling constant can be observed: almost linear decrease up to viscosities that correspond to around 0.20 ionic liquid molar fraction, constant for higher molar fractions and even lower value for the neat ionic liquid. We suggest that this is the direct evidence of different regimes in ionic liquid/MS mixtures: similar to normal electrolyte solution up to $x_{IL} = 0.20$ and, for higher molar fractions, an expanded ionic liquid, analogically to what was proposed in literature for imidazolium tetrafluoroborate mixtures with acetonitrile on the basis of measurements of dielectric spectra [64].

In summary, the measurements of the solvation dynamics and time-resolved fluorescence anisotropy in $BmimBF_4$/PC mixtures were performed. They reveal complex multi-exponential character of the dynamics in these systems. In order to elucidate the mechanism of these processes, MD simulations were conducted and presented in the following section.

4.3 Molecular dynamics simulations

Molecular dynamics simulations of C153 in neat $BmimBF_4$, neat propylene carbonate and their mixtures were performed using DLPOLY 4.07 software package[65]. Initial cubic configurations were constructed using Packmol program[66] with a distance tolerance of $2\mathring{A}$. The atoms of C153 were restrained to be in the central

region (20*20*20$\mathring{A}$) of the box. For the simulation of C153 in neat components, one C153 molecule and 863 molecules of PC or 863 ion pairs $BmimBF_4$ were used. For the simulations of C153 in $BmimBF_4$/PC mixtures, the sum of the number of PC molecules and ion pairs $BmimBF_4$ was kept to be 863, and the ratio was calculated to correspond the ionic liquid molar fractions, used in experimental measurements. The chosen systems are listed in table 4.4.

Table 4.4: Simulated systems: 1 C153 + N(PC) + N($BmimBF_4$ and the corresponding compositions (x_{IL}). Experimental density of the systems is also given, calculated using a polynomial fit to literature data[67] $d(x_{IL}) = 1200.4 + 49x_{IL} - 133x_{IL}^2 + 145x_{IL}^3 - 60x_{IL}^4$.

x_{IL}	N(PC)	N($BmimBF_4$)	d / kg m^{-3}
0	863	0	1200.40
0.02	845	18	1201.37
0.075	798	65	1203.40
0.15	734	129	1205.21
0.2	691	172	1205.94
0.33	578	285	1206.59
0.5	432	431	1206.03
0.65	303	560	1205.17
0.85	133	730	1203.73
1	0	863	1201.40

Force field parameters were taken from literature resources. The ionic liquid $BmimBF_4$ force field parameters were taken from the article of Mondal and Balasubramanian [68]. Cation was modelled flexible, except C-H bond lengths that were constrained as in original work. BF_4^- anion was kept rigid. Propylene carbonate force field was developed in the group of Prof. Idrissi. The molecule was modelled completely flexible. The force field of C153 was taken from the article [69]. The aromatic structure and the methylenic groups on the nonaromatic rings have been kept rigid, while stretching, bending, and torsion have been considered otherwise. The equilibrium geometry of C153 in ground state and charges in both ground and S_1 states were recalculated using Gaussian software[70] and M062X/6-311+G(d,p) level of theory.

The parameters for Lennard-Jones intermolecular potentials were mixed in accordance to Lorentz-Berthelot rule (eq. 4.3). Newtonian equations of motion were integrated with time step of 0.5fs for all systems containing propylene carbonate, and 2fs for a system of 1 C153 + 863 ionic pairs $BmimBF_4$. Cutoff radius was 12$\mathring{A}$, ewald precision, shake and quaternion tolerance were set to 1.0e-05. All simulations were performed at 293K and 1atm.

$$\epsilon_{ij} = \sqrt{\epsilon_i \epsilon_j}; \sigma_{ij} = \frac{\sigma_i + \sigma_j}{2} \tag{4.3}$$

The scheme of simulation was the following. Initial configurations were equilibrated in NPT ensemble for 5ns with C153 ground state charge distribution. During the equilibration, total energy and temperature of the system stabilises. After the equilibration, NVT run of 1ns was made to transfer into an NVT ensemble. Further, 10ns productive run was made to get structural properties in the system. The same

configuration was used to start the calculation of the solvation dynamics and also a 5ns equilibration with excited state charge distribution on atoms of coumarin. After a 5ns equilibration, 10ns productive run was made to get a structural properties with C153 in excited state. Schematically, the algorithm of simulation is shown in fig. 4.10. Production run trajectories were analysed using TRAVIS software package [71]. The structure of C153 solvation shell was analysed in terms of radial and angle distribution functions (RDFs, ADFs). Distance conditions were imposed for RDFs to investigate the strength of hydrogen bonding. RDFs were constructed in range 0-3.2nm and 300 bins are made, that corresponds to the resolution of 10.67pm. To get representative results, 50000 structure configurations were analysed (each hundredth of time steps of 2fs in 10ns).

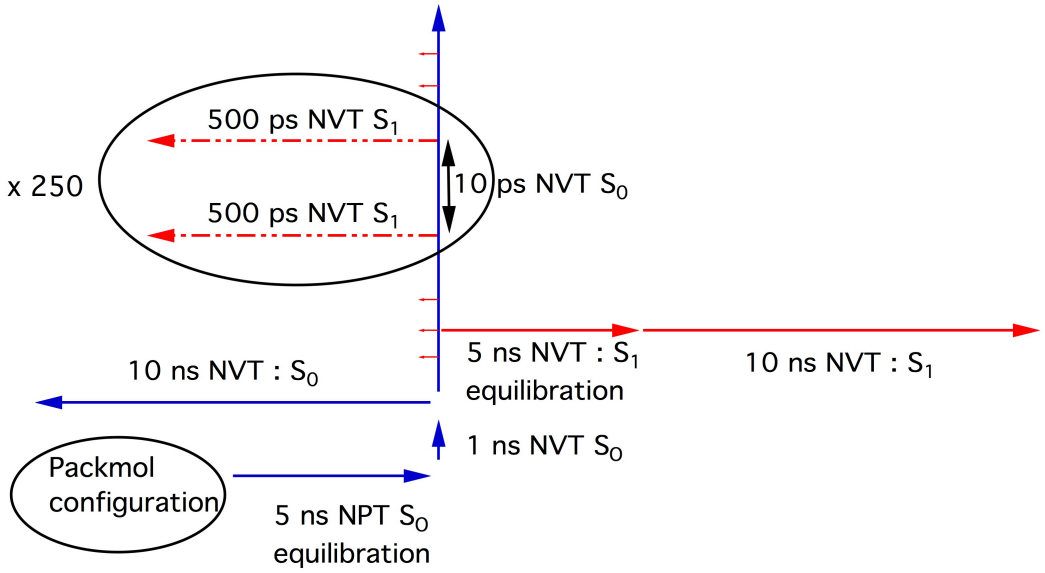

Figure 4.10: The scheme of molecular dynamics simulations of C153 in $BmimBF_4$/PC mixtures, and C153 in $BmimBF_4$ and C153 in PC.

4.3.1 Solvation response functions by nonequilibrium approach

The photoexcitation of a fluorescent probe is a quasi instanteneous process when compared to the time scale of the movements of nuclei. This process can be approximated as a change in charge distribution on the atoms of fluorescent probe and its equilibrium geometry. The latter factor can be safely simplified for probes with relatively rigid structure, like C153. Therefore, the force field perturbation is determined by a different charge distribution.

In MD simulations, the solvation dynamics can be modelled using two main approaches: (i) linear response theory and (ii) nonequilibrium simulations. The latter approach was used in this work. Its essence is illustrated in fig. 4.11. During the simulation of a system with charge distribution on C153 atoms that corresponds to its ground state (S_0), system configurations are saved each 10ps passed. These 'ground state' configurations are used as the starting ones in the simulation of 500ps with charge distribution on C153 atoms that corresponds to its first excited state

(S_1). Therefore, the solvation shell is let to relax freely in response to the electric field perturbation.

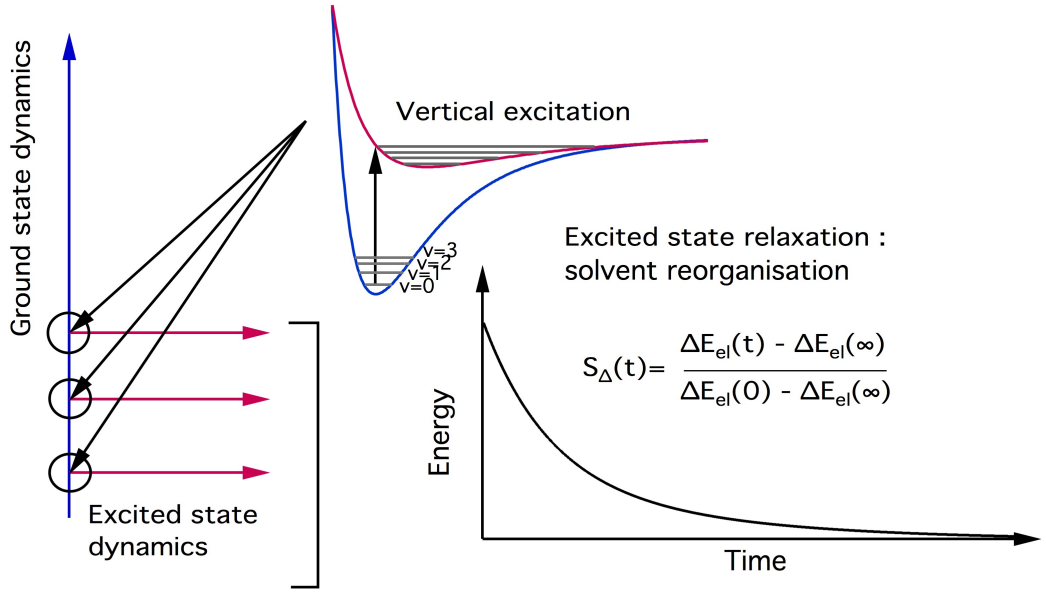

Figure 4.11: Illustration of the solvation dynamics modelling algorithm.

This relaxation was followed though the decay of the difference energy of coulombic interaction between the solvent components and coumarin atoms (eq. 4.4). This energy is calculated with a difference of partial charges on C153 in excited and ground states Δq_γ, taking a sum over each j of N solvent molecules, each C153 atom γ and each solvent atom η. When needed, the distance between each two sites $r_{\gamma,j\eta}$ was corrected for periodic boundary conditions. Python script was used to treat the trajectories, the program is available upon request.

$$\Delta E = \sum_{j=1}^{N_{\text{solv}}} \sum_{\gamma \epsilon \text{sol}} \sum_{\eta \epsilon \text{solv}} \frac{\Delta q_\gamma q_{j\eta}}{4\pi\epsilon_0 r_{\gamma,j\eta}} \tag{4.4}$$

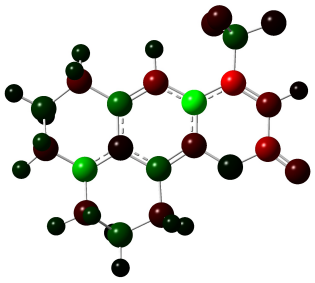

Figure 4.12: C153 molecule partial charges change within the excitation Δq. Δq is defined as $q_{S_1} - q_{S_0}$ and ranges from -0.194 to +0.194, from light red to light green, respectively. The image was generated using GaussView 6.0.16 software [72].

The distribution of the difference charges Δq are shown in fig. 4.12. C153 atoms are coloured in light green to light red corresponding to degrees of charge change from

the highest to the lowest. As one can note, julolidine moiety of C153 is coloured in light and dark green degrees, while the lactone part is light and dark red. Therefore, the julolidine and lactone parts are electron density donor and acceptor parts of C153. Upon the photoexcitation the electron density flows from the julolidine to lactone side with concomitant increase of electric dipole moment value.

The relaxation of a solvation shell depends on its initial structure. Therefore, a number of different initial configurations must be used to get a meaningful coulombic energy decays that can be compared with the experimental solvation response. In this work, 500 initial configurations were used and the resulting coulombic energy decays were averaged.

The result is presented in fig. 4.13. MD simulations are in excellent agreement with experimental data for neat components and a mixture with $x_{IL} = 0.20$. Thus, the force fields and the scheme of modelling of solvation dynamics seems to capture the experimental behaviour of these systems.

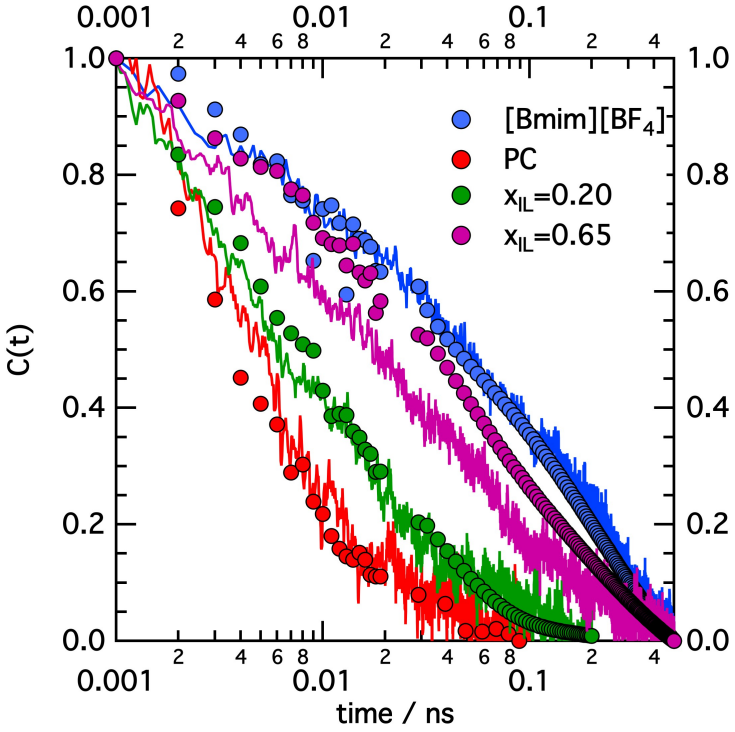

Figure 4.13: Calculated (solid lines) and experimental (filled circles) solvation response functions for C153 in $BmimBF_4$/PC mixtures and neat components. The functions are normalised from 1ps, for the reason of the experimental time resolution.

MD simulations permit a calculation of partial contribution of each type of interaction in the overall solvation response: C153-cation, C153-anion and C153-PC. This is straightforward, as the energy under consideration is the sum of the energies of coulombic interactions. Thus, the partition of SRFs into cation, anion and PC contribution can be accessed. The result is shown in fig. 4.14. The results are intriguing: in neat ionic liquid, about 70% of the subpicosecond solvation response is due to anion. As the $E_{C153-cation}$ is constant after 5 ps, the anion is completely responsible for the slower, diffusive part of the solvation response. This suggests a key role of anion translation in the solvation dynamics. In the mixture, a

different partition is observed: the subpicosecond solvation is dominated by propylene carbonate (about 60%). Cation and anion have very similar parallel decays that suggests a certain collectivity of this response. $E_{C153-PC}$ exhibits a slight increase after ≈70ps, partly compensating the effect of ionic liquid.

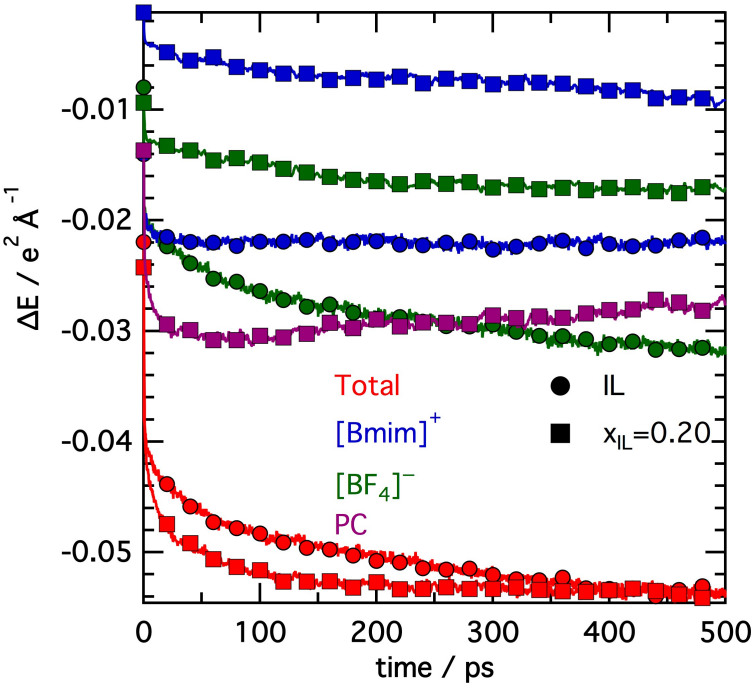

Figure 4.14: Calculated contributions of cation (blue), anion (green) and PC (magenta) to coulombic energy decays for C153 in $BmimBF_4$/PC mixture with $x_{IL} = 0.20$ (filled squares) and neat $BmimBF_4$ (filled circles). Total energy decays are shown in red. The markers are shown for each 50^{th} calculated point.

These results indicate a complex interplay between the interactions of molecular solvent and IL cation and anion with C153. The most important part of the C153 interactions with the solvent is the interaction with its solvation shell. Therefore, the rearrangement of the nearest neighbours around the probe is the basis of the solvation dynamics. Thus, the analysis of the structure of the solvation shell of C153 in ground and excited states is an important step in the understanding of the mechanism of this process. The analysis of the structure evolution during the non-equilibrium simulation can give additional information about the time-dependent character of this mechanism.

4.3.2 Structure of the solvation shell of C153 in ground and excited states

The numbering of atoms in C153, $Bmim^+$, PC as well as BF_4^- is shown in fig 4.15. The numbering of hydrogens is made in the way that a number of hydrogen is the same as the number of carbon atom to which it is linked.

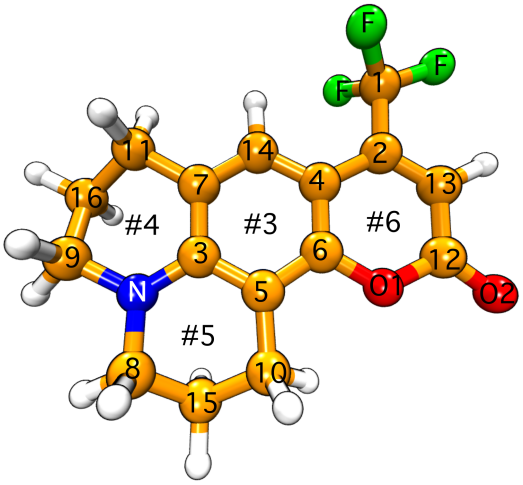

(a) C153 molecule.

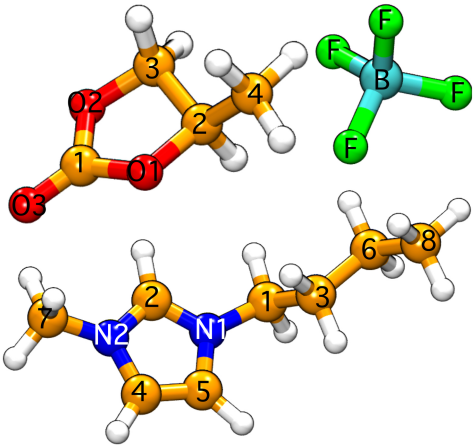

(b) Top: PC molecule and BF_4^-. Bottom: $Bmim^+$ cation.

Figure 4.15: The numbering that is used in structure analysis. The carbon and oxygen atoms are referenced afterwards as C_n and O_m. The hydrogens are referenced according to the carbon atoms to which they are linked: Hn. The references of the type #k correspond to the number of the geometrical centre of the ring number k in C153.

Neat ionic liquid

In this section, the results on the structure of the solvation shell of C153 in neat ionic liquid are discussed.

As it was mentioned above, the analysis of the structure was held using RDFs and ADFs. The former function shows the density of probability of finding a pair of sites a and b at a distance r. This function is normalised to the average density of the site in the system, so at the limit of this function at large distances equals to 1. To calculate this histogram, eq. 4.5 is used, where $\overrightarrow{r}_i(t)$ and $\overrightarrow{r}_j(t)$ denote the position of the sites a and b at the time moment t; and δ is the Kronecker symbol: it takes values of 1 in the interval [-w, w) (w is the bin width) and otherwise 0.

$$g_{ab}(r) = \frac{V}{N_a N_b} \sum_{i=1}^{N_a} \sum_{j=i+1}^{N_b} \langle \delta(r - |\overrightarrow{r}_i(t) - \overrightarrow{r}_j(t)|) \rangle_t \tag{4.5}$$

In a similar way, angular distribution functions, or ADFs, are defined as a density of probability to find a two vectors at a given angle between them (see the definition in ref. [71]). In this work, the ADFs were calculated only for the first nearest neighbour, which makes sense for the first solvation shell of C153.

Firstly, the RDFs were calculated between a centre of the ring of C153 (look fig. 4.15 for numbering) and: 1) boron atom of anion, 2) the centre of the ring of cation. The result is shown in fig. 4.16. Ground and excited state simulations are compared on the same figure. Except RDFs between C153 S_1 rings #6 and #5 and anion, RDFs don't show well-pronounced peaks. In the ground state, RDFs with anion have maximum intensity of 1.394 (#3) and even less with cation (1.2219, #4). Thus, the solvation shell of C153 doesn't have any marked and distinct character and resembles to a large extent to the structure in the bulk. Therefore, C153 is not

expected to alter a lot the structure of bulk ionic liquid.

In terms of CoR (C153)-A distances (CoR of cation and B of anion for A), RDFs show that the anion distances (distance at maximum intensity) to n^{th} ring of C153 can be classed as: #5 (0.517 nm) <#4 (0.539 nm) <#6 (0.549 nm) <#3 (592 nm). As for the cation, the shortest distance is between CoR #5 of C153 and CoR of cation (0.379 nm).

When comparing the RDFs for ground and excited state, a remarkable change in intensity of RDFs between #6-B and #5-B is observed. The distance of the former peak decreases by 0.043 nm, while the position of the latter peak doesn't change. It is worth noting that these peaks are rather wide ($FWHM$ of about 0.2 nm) and this gives non-zero density probability at shorter distances for C153 S_1 than for C153 S_0. The examination of the behaviour of the RDFs CoR#4 of C153 - B of anion and the RDFs CoR#3 of C153 - CoR of cation at short distances (their rising part) indicates less repulsive interaction in the excited state.

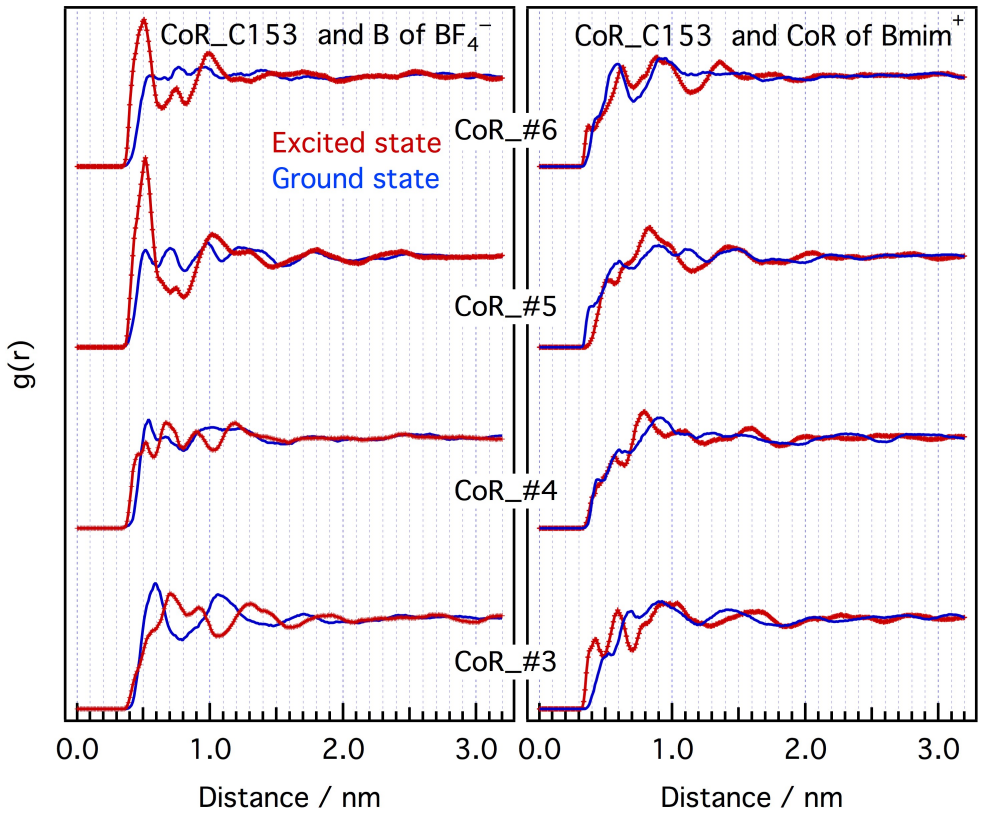

Figure 4.16: Radial distribution functions between the centres of the rings of C153 and: 1) left panel: boron atom of BF_4^- anion 2) right panel: centre of the ring of $Bmim^+$ cation. The results of simulations of C153 with ground and excited state charges are shown in dark blue and dark red colours, respectively. The analysis of 10ns trajectories was made. The RDFs were plot with offset of 2 each.

Hydrogen bonding interactions play a great role in a structure of ILs and IL/MS mixtures. Furthermore, on the basis of solvatochromic measurements in $BmimBF_4$, this IL was attributed to a class of moderately associative solvents[60].

The analysis of radial distribution functions between the most electronegative atoms O_1, O_2 and F of C153 and hydrogens of $Bmim^+$ cation has shown that the

most important contribution is made by H2 and H5 atoms of cation and O_2 atom of coumarin (fig.4.17). When comparing the results for ground and excited state, presented in fig.4.17, too, one can see higher density of probability at short distances (0.208 nm for H2 and 0.230 nm for H5) in excited state. Maximum intensity distance is shifted to the shorter distances by 0.02 nm for RDF H5-O_2.

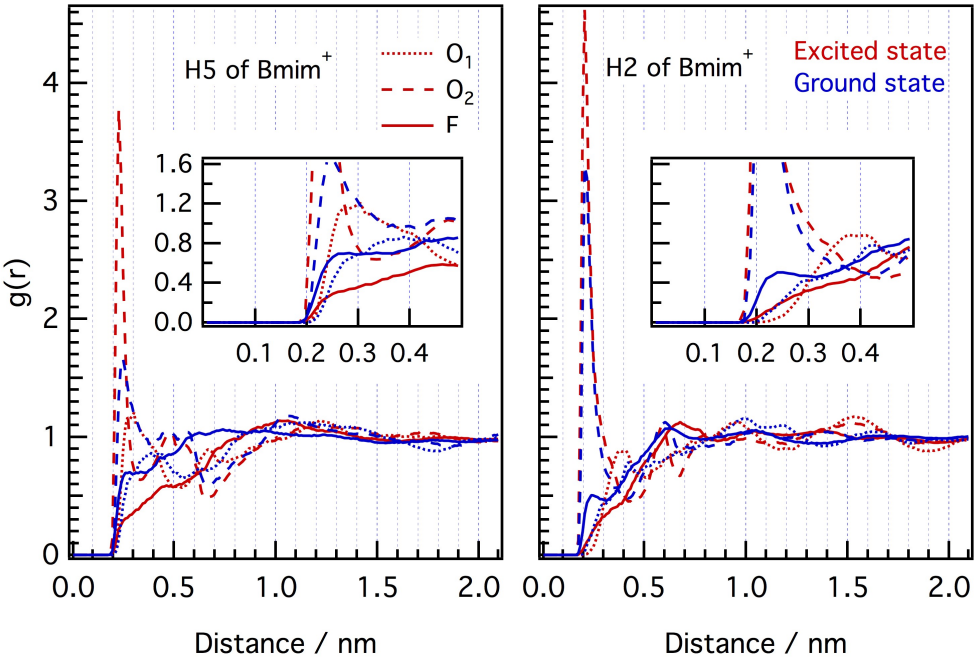

Figure 4.17: Radial distribution functions between O_1 (dotted lines), O_2 (dashed lines) and F (solid lines) atoms of C153 and: 1) left panel: H5 atom of $Bmim^+$ and 2) right panel: H2 atom of $Bmim^+$. The results of simulations of C153 with ground and excited state charges are shown in dark blue and dark red colours, respectively. The analysis of 10ns trajectories was made.

On the other hand, hydrogen bonding between anion and hydrogen atoms of C153 was considered. RDFs were calculated between fluorine atoms of anion and Hi of C153 and shown in fig. 4.18. In general, the intensity of these RDFs is not high: 1.16 for C153 S_0 (H16-F) and 1.62 for C153 S_1 (H9-F). They are characterized by two peaks distanced by about 0.19 nm. Thus, while the first peak is situated in the range 0.243 nm - 0.275 nm, the second is in the range 0.440 nm - 0.461 nm (for C153 S_0). As for C153 S_1, the distances of maxima are somewhat shorter: 0.243 nm - 0.269 nm and 0.435 nm - 0.456 nm. The distances of the first peak on RDFs vary in the following order for ground and excited states, respectively: H14 <H9=H13 <H11=H10 <H8=H16 <H15 and H9 <H14=H15 <H11-H8 <H16=H10. This ordering is not well defined, due to the small change in the position of the maximum. In spite of this, one can suggest a presence of weak hydrogen bonding between C153 and ionic liquid.

In order to consider the strength of hydrogen bonding between C153 and ionic liquid in more detail, the donor directionality is examined. This concept[73] says that H-bonds tend to become increasingly linear with their increasing strength. For this, an analysis, similar to the one described in [74], was performed. In this approach, the geometry of hydrogen bonding C-H$\cdots$A is retrieved in terms of C-A and H-A

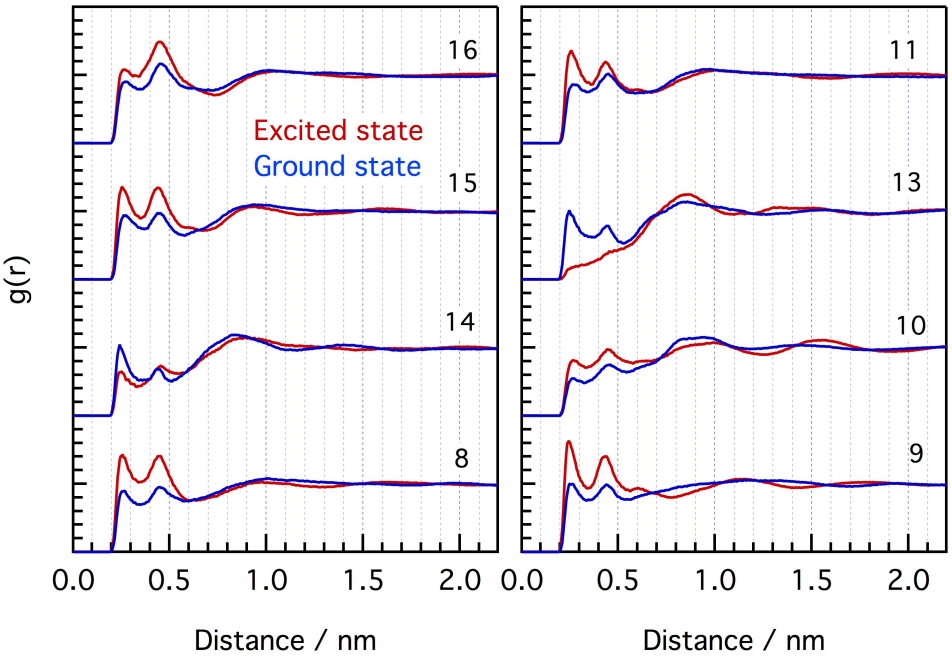

Figure 4.18: Radial distribution functions between Hi atoms of C153 and fluorine atoms of BF_4^-. The results of simulations of C153 with ground and excited state charges are shown in dark blue and dark red colours, respectively. The analysis of 10ns trajectories was made. The RDFs were plot with offset of 2 each.

distances. For this, RDFs with distance condition were resolved in terms of the first neighbour atom A. Average positions $< r_{C/H\cdots A} >$ were calculated and used to estimate the angles ∠C-H$\cdots$A . The result is plotted in fig. 4.19. In case of strong hydrogen bond, the geometry is linear, and the distance C-A is close to the sum of the distances C-H and H-A. This corresponds to an angle ∠C-H$\cdots$A = 180°. Bent hydrogen bonds are weaker than the linear ones. The orientation with an angle ∠C-H$\cdots$A = 90° corresponds to the weakest hydrogen bonding.

The hydrogen bonding between C153 and the anion can be characterised as bent for approximately 120-130°, while ≈115-120° is observed for cation. This is valid for the hydrogen bonding that falls into a region of weak hydrogen bonding, defined with distance conditions: up to 0.30 nm for H-A distance and up to 0.40 nm for C-A [75].

Let's consider the ground state simulation first. As one can see it in fig. 4.19 (blue cirles), weak hydrogen bonding is present between all hydrogens of C153 and fluorine atoms of anion. As for cation, weak hydrogen bonding is present only between H2 of cation and O_2 of C153. This indicates a stronger solvation of C153 by anion through this type of specific interaction. On the basis of H-A distances for C153 and anion, the hydrogen bonding strength can be classified as: H9 >H16≈ H8≈ H11 ≈ H15 >H13 >H14>H10. Thus, hydrogen bonding with anion is located preferentially in the vicinity of julolidine moiety of C153, in particular next to the nitrogen atom.

In excited state, hydrogen bonding strength variation increases, as can be concluded from shorter H-A (hydrogen - acceptor atom) distances (fig. 4.19, red circles). However, the angle ∠C-H$\cdots$A remains equal to ≈120-130° for anion and to ≈115-120° for cation. The order of the hydrogen bonding strength doesn't change, as well: H9

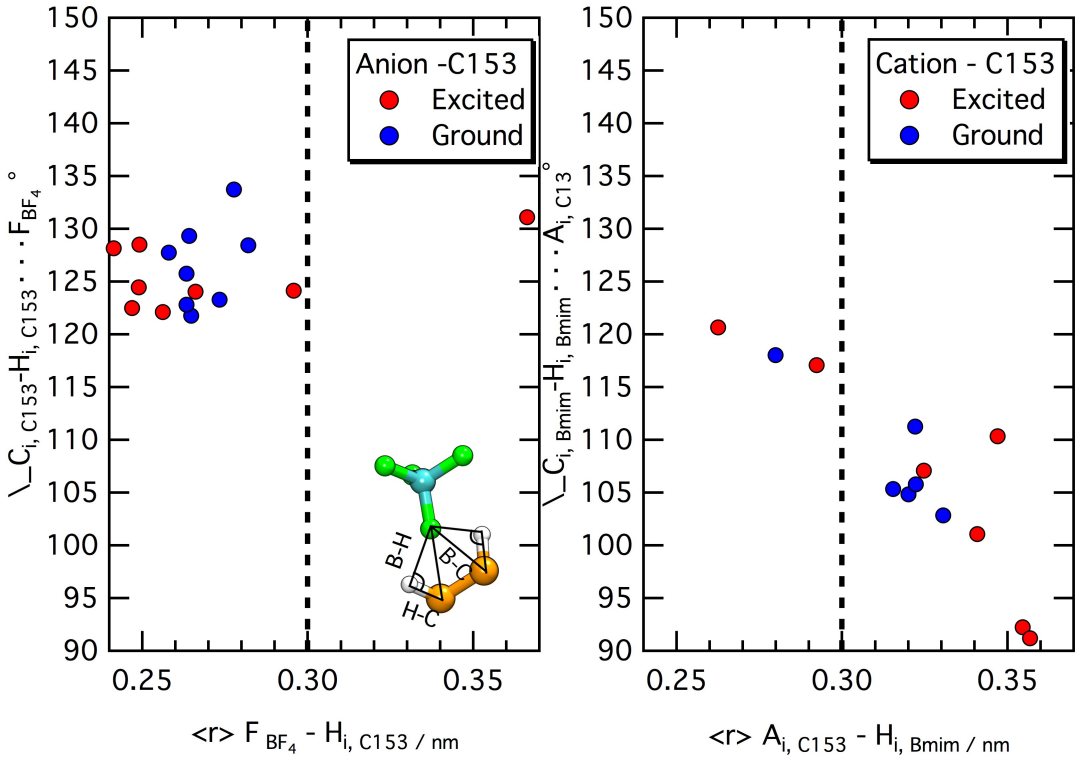

Figure 4.19: Left panel: ∠C-H· · ·A of the HB between the first nearest neighbour fluorine atom of anion and i^{th} carbon atom of C153 C_i as function of mean distance of the first nearest neighbour RDF between fluorine atom of anion and hydrogen atom, linked to the C_i. Right panel: ∠C-H· · ·A of the HB between the first nearest neighbour O_1, O_2 and F atoms of C153 and the i^{th} carbon atom of cation C_i as function of mean distance of the first nearest neighbour RDF between O_1, O_2 and F atoms of C153 and hydrogen atom, linked to the C_i.

>H8 ≈ H15 ≈ H11 >H16 >H10 >H14 >H13. In this list, the first six hydrogen bonds are stronger than in ground state, while the other three are weaker. Thus, one can suggest a certain 'migration' of hydrogen bonding strength between C153 and anion upon the excitation. The hydrogen bonding between C153 and cation changes as well, but these changes are not very strong. In excited state, a hydrogen bonding between H5 atom of $Bmim^+$ can be considered.

The changes in hydrogen bonding strength are obviously due to the change in partial charge distribution on C153 atoms (see fig. 4.12).

Combined distribution functions were used to get the information about the relative orientation of cation and coumarin. These functions were constructed from angle distribution function (ADF) and radial distribution function. Two types of ADFs were used: (i) α_n - the angle between a normal vector to the plane of n^{th} ring of C153 and a distance vector between the centre of the n^{th} ring of C153 and the centre of the ring of cation and (ii) β_n - the angle between a normal vector of the plane of the n^{th} ring of C153 and a normal vector of the plane of the ring of cation. Graphical representation of the two angles is shown in fig. 4.20. RDFs were constructed between the centres of the cation's ring and the centres of the n^{th} ring of C153. A distance condition was applied for these calculations: only the first

neighbour was taken into account. Thus, the angle α_n provides the information about the above/below/shifted position of the cation imidazolium ring with respect to the nth ring of C153. On the other hand, the angle β_n says if the rings of C153 and the ring of cation are parallel or perpendicular.

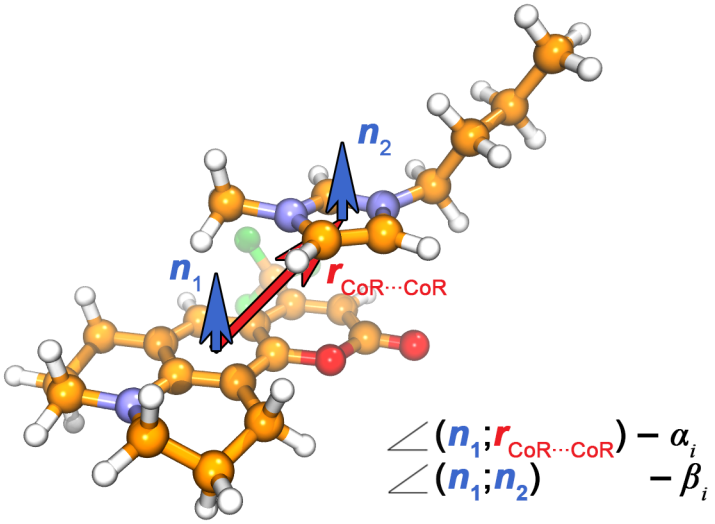

Figure 4.20: The vectors used for a definition of combined distribution functions between C153 and Bmim$^+$.

Combined distribution functions for ground and excited state are presented in fig. 4.21 and in fig. 4.22. For the sake of clarity, the colour - intensity correspondence was kept the same for both graphs.

In ground state, the position of cation's imidazolium ring relatively to C153 rings can be characterised as slightly shifted above and below with preference for the former. This is valid for C153 rings #3, #4 and #6, while the orientation within #5 is diffuse. It should be noted that the distance between the ring centres of C153 and that of imidazolium vary in range 0.3-0.63 nm. The ring #6 of C153 is the closest to Bmim$^+$ ring centre. Considering the lower panel of fig. 4.21, one can state parallel and antiparallel orientation of coumarin rings #6, #3 , #4 and imidazolium ring of cation. The strongest orientation is observed for the ring #6 of C153. We suggest that it is correlated with the stabilisation of this arrangement by the hydrogen bonding between imidazolium ring hydrogens and O_2 atom of C153, discussed above.

In excited state, the relative orientation of C153 rings and Bmim$^+$ is more strongly correlated (fig. 4.22). Contrarily to the ground state, the preference to the below position of imidazolium ring is pronounced. Parallel and anti-parallel orientations are preserved. The strongest correlation is observed for C153 rings #3 and #6. For these rings, the CoR-CoR distances are shorter than in the ground state. Stronger correlations in orientations of C153 rings and Bmim$^+$ parallel the stronger hydrogen bonding between cation and C153. Thus, after the excitation, the cation-C153 interactions become stronger.

Finally, the relative direction of C153 ring #6 and the imidazolium ring was examined. For this, combined distribution functions were again used. On the

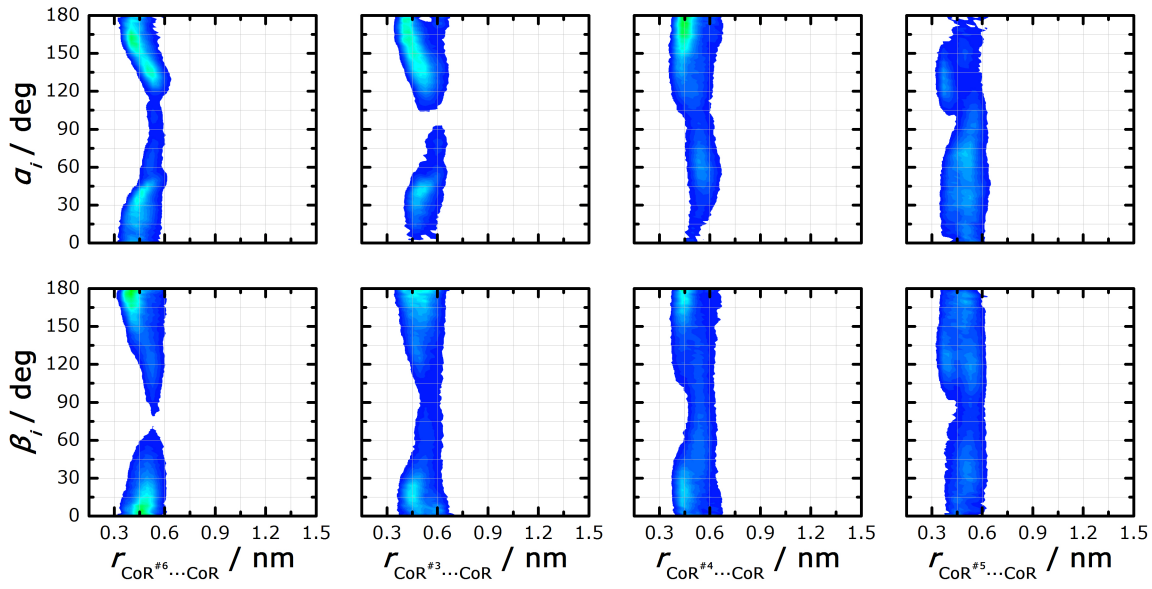

Figure 4.21: Contour plot of combined distribution functions between CoR of C153 in ground state and CoR of $Bmim^+$. The analysis of 10ns trajectory was made. The colour change from blue to red corresponds to the change in intensity from its minimum to its maximum. Minimum and maximum values are the same between the panels.

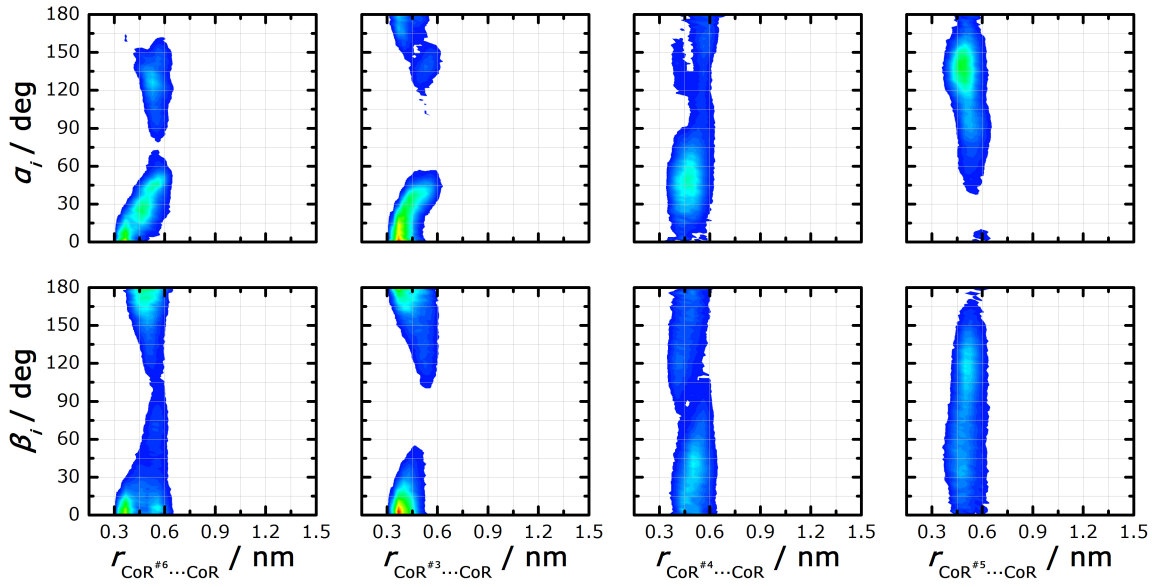

Figure 4.22: Combined distribution functions between CoR of C153 in excited state and CoR of $Bmim^+$. The analysis of 10ns trajectory was made. The colour bar min and max are same as for ground state graph (fig. 4.21)

one hand, radial distribution functions, analogical to CDFs, described above, were constructed. These are RDFs between the centres of the ring #6 of C153 and that of the imidazolium ring. On the other hand, ADFs were constructed for the angle γ between two vectors: O_1-C_2 (within C153) and CoR-C_2 (within $Bmim^+$). The result is shown in fig. 4.23.

The relative direction of C153 and $Bmim^+$ changes within the excitation. H2

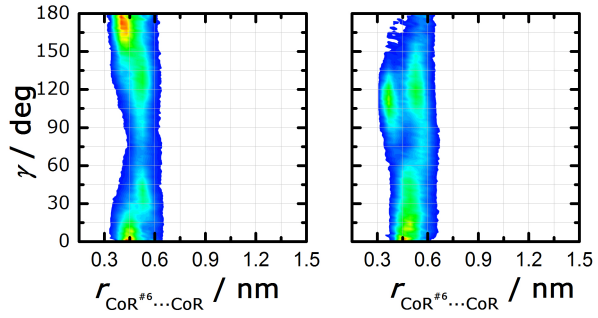

Figure 4.23: Combined distribution functions between CoR of C153 in and CoR of $Bmim^+$. The results of simulations with charge distributions on C153 atoms corresponding to ground and excited state are shown on the left and on the right, respectively. The analysis of 10ns trajectory was made. The colour bar min and max are the same for ground and excited state graphs.

of $Bmim^+$ points to CF_3/O_1 atoms of C153 S_0, that corresponds to $\angle\gamma = 0°$ and $\angle\gamma = 180°$, respectively. Upon the excitation, the preferential orientation is different: $\angle\gamma = 0°$ and $\angle\gamma = 120°$. The latter value can be interpreted as H2 of $Bmim^+$ and O_2 of C153 that become closer. This is in obvious correlation with the strengthening of hydrogen bonds between C153 and $Bmim^+$, discussed above.

Thus, the translation of anion and the reorientation of the cation is expected have an effect on the solvation dynamics in neat $BmimBF_4$. Let's connect this result with the result of SRFs partition in different interactions (fig. 4.14). As it was mentioned, the interactions between C153 and cation and anion are significant on the subpicosecond scale, while the latter dynamics is dominated by the interaction with the anion. Therefore, inertial translation of anion and reorientation of cation are principal changes in the solvation shell in subpicosecond scale, while the further solvation is totally defined by diffusive anion translation.

As discussed above, the hypothesis about the key role of anion in the solvation dynamics in neat ionic liquid was put forward. The analysis of the structure of the solvation shell has suggested the strengthening of hydrogen bonding between anion and the hydrogens of the julolidine moiety of C153 upon the excitation. In order to follow this translation in time, it is convenient to use RDFs.

RDFs were constructed between the N atom of C153 and the F atom of anion, calculated from non-equilibrium trajectories (fig. 4.24). Distance condition was applied: only the first nearest neighbour BF_4^- was taken into account. RDFs were averaged for 2 ps for each time point. An average over 500 trajectories was performed as well in order to get a representative result. As one can see in fig. 4.24, the translation of anion is clearly non-exponential in time: the ultrafast change in maximum intensity distance is followed by an almost linear part. This is in good accordance with what was shown for the decays of coulombic energy interaction between C153 and anion. Thus, it corroborates the conclusion about the key role of anion translation in solvation dynamics of neat $BmimBF_4$: the anion decreases the energy of C153 S_1 by approaching to its julolidine moiety.

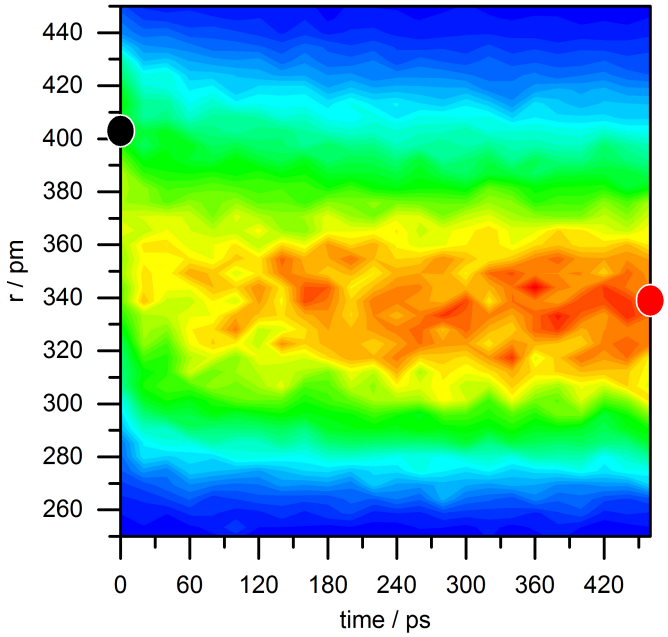

Figure 4.24: RDFs between N of C153 and F of anion, calculated from non-equilibrium trajectories. Only the nearest neighbour was taken into account. RDFs were averaged for 2 ps for each time point. An average over 500 trajectories was performed as well. Black and red cirles represent the mean distances of the equilibrium RDFs for C153 S_0 and S_1, respectively.

C153 in propylene carbonate

Like in the system C153 and IL, the solvation shell of C153 in PC is not well-defined. As the first step in the analysis of the solvation shell of C153 in PC, the RDFs were calculated between the centres of the rings of C153 and the centre of the ring of PC. They are shown in fig. 4.25. The strong similarity between these RDFs can be noticed. The peaks are smeared out, and a shoulder at short distances emerges. As for C153 S_0, the first peak is situated at the distance of 0.56-0.57 nm. Considering C153 S_1, PC molecules are situated next to the lactone ring of C153 (ring #6) and the julolidine rings (rings #4 and #5).

Furthermore, the analysis of the RDFs between the most electronegative atoms of propylene carbonate (O_1, O_2 and O_3) and the hydrogen atoms of C153. These RDFs were resolved in terms of the first peak intensity (g_{max}) and its position (r_{max}), they are presented in fig. 4.26. In such a way, the most important interactions can be discerned. As one can see, the RDFs between the O_3 atom of PC and the H8 and the H9 atoms of C153 have the shortest distance and the highest intensity peaks. Upon the excitation, the first peak in these RDFs become closer to the origin and more intense, as shown in fig. 4.27a.

The most important interactions among the electronegative atoms of C153 and hydrogens of PC are the ones between O_2 atom of C153 and H2 and H3 of the PC. Upon the excitation, the first peaks on RDFs become more intense and shift to the short distances (see fig. 4.27b).

The examination of the hydrogen bonding interactions was carried out in a similar way to one that was performed for the system of C153 in IL. The RDFs between the most electronegative atoms of C153 and PC and the carbons and hydrogens of

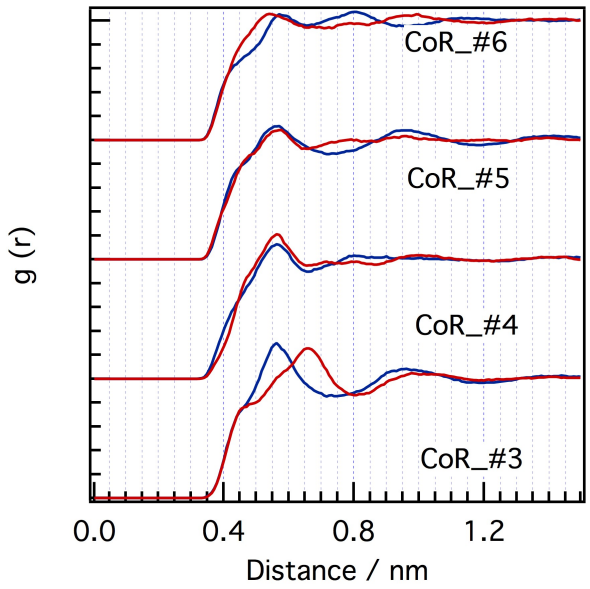

Figure 4.25: RDFs between the n^{th} CoR of C153 and CoR of PC. The results for ground and excited state are presented as dark blue and red lines, respectively. The curves are plotted with the offset of 1.

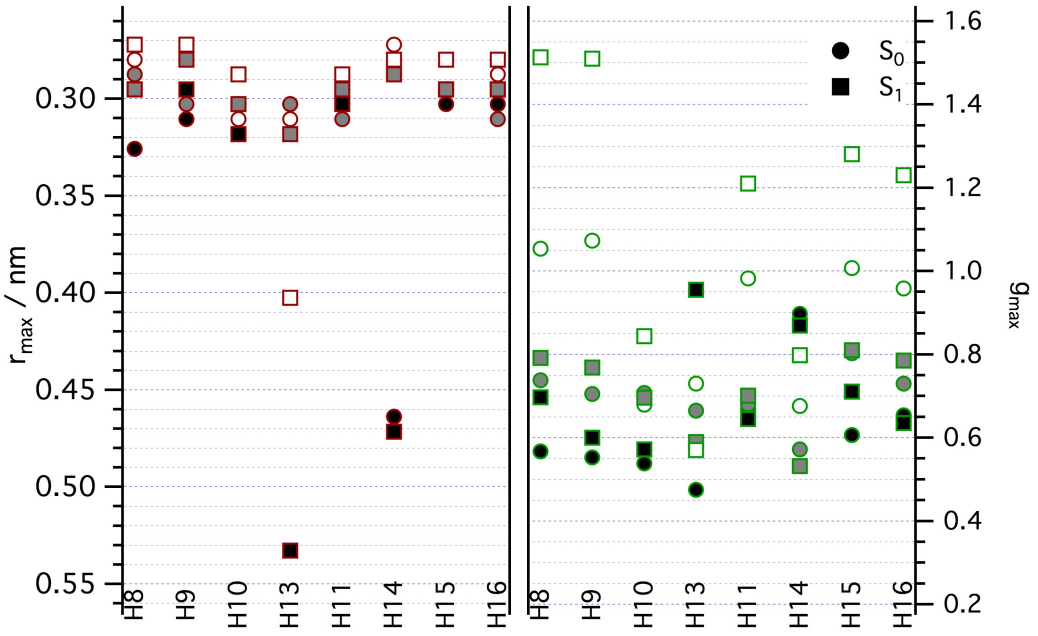

Figure 4.26: The position (left) and intensity (right) of the first peak of the RDFs for O1 (full black symb.), O2 (full grey symb.), O3 (hollow symb.) atoms of PC and Hi of C153. Analysis of C153 S_0 and C153 S_1 trajectories is shown as squares and circles, respectively.

PC and C153, respectively, were calculated with the first nearest neighbour distance condition. The mean distances were taken, the angle ∠C-H···A was calculated using the cosine law and plotted in fig. 4.28.

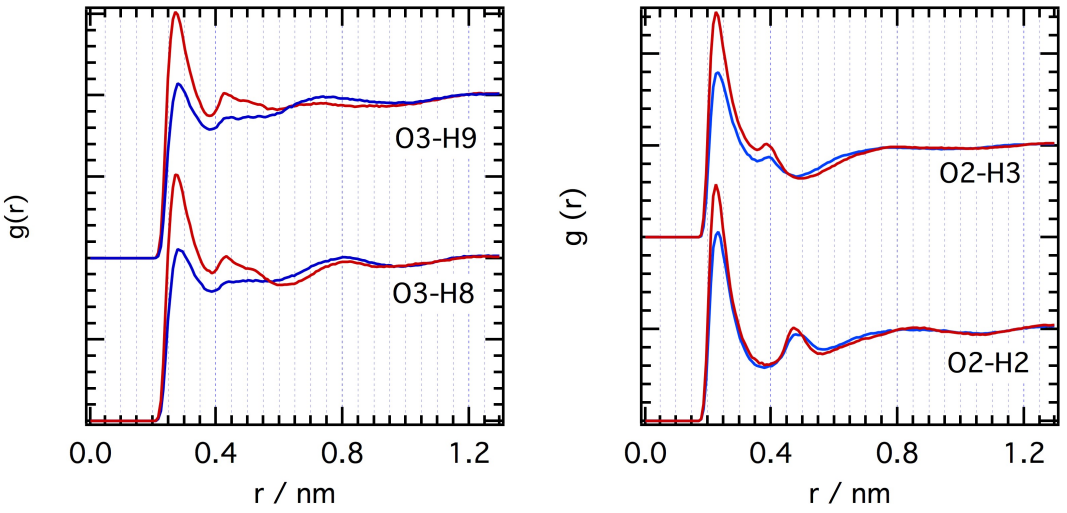

(a) (b)

Figure 4.27: Left: RDFs between O_3 atom of PC and H8 and H9 atoms of C153. Analysis of C153 S_0 and C153 S_1 trajectories is shown as blue and red lines, respectively. The curves are plotted with offset of 1. Right: RDFs between O_2 atom of C153 and H2 and H3 atoms of PC. Analysis of C153 S_0 and C153 S_1 trajectories is shown as blue and red lines, respectively. The curves are plotted with offset of 2.

When considering the HBs between the O_1, O_2 and O_3 atoms of PC and the hydrogens of C153, the left panel of fig. 4.28 must be inspected. Only the HBs with participation of O_3 and the hydrogens of the julolidine rings of C153 can be assigned to the weak hydrogen bonding. These HBs are bent for approximately 125-130degree. Upon the excitation, the bending of these bonds doesn't change, but the mean distance decreases, suggesting a stronger hydrogen bonding.

On the other hand, the right panel of fig. 4.28 illustrates the HBs between O_1, O_2 and F atoms of C153 and hydrogens of PC. These HBs fall into the range of the weak hydrogen bonding. This is valid for all the HBs, except one: between the O_1 atom of C153 and H2 of PC. Similarly, these HBs are bent for 120°-130°. The most important HBs are the ones between the F and O_2 atoms of C153 and the H3 and H4 hydrogens of PC. Again, upon the excitation these HBs become stronger.

Figs. 4.29 and 4.30 illustrate the orientational preferences between the rings of C153 and of PC for C153 S_0 and S_1, respectively. These preferences are well-defined only for the lactone (#6) and central (#3) rings of C153. The angles α ad β have been defined similarly to the analysis in IL, where the ionic liquid cation and n^{th} ring of C153 mutual orientation was addressed (fig. 4.20). Thus, the angle α corresponds to the above (0°), below (180°) and shifted positions. On the other hand, the angle β gives information either the rings' planes are parallel ($\beta = 0°, 180°$) or perpendicular ($\beta = 90°$).

Clearly, the above and below positions of the nearest neighbour PC molecule with parallel arrangement are the preferred ones when the structure between lactone and central rings of C153 and the ring of PC is considered. This orientation must be supported by the hydrogen bonding that was found important between the hydrogens of PC and the O_2 and F atoms of C153. Upon the excitation, the preferred

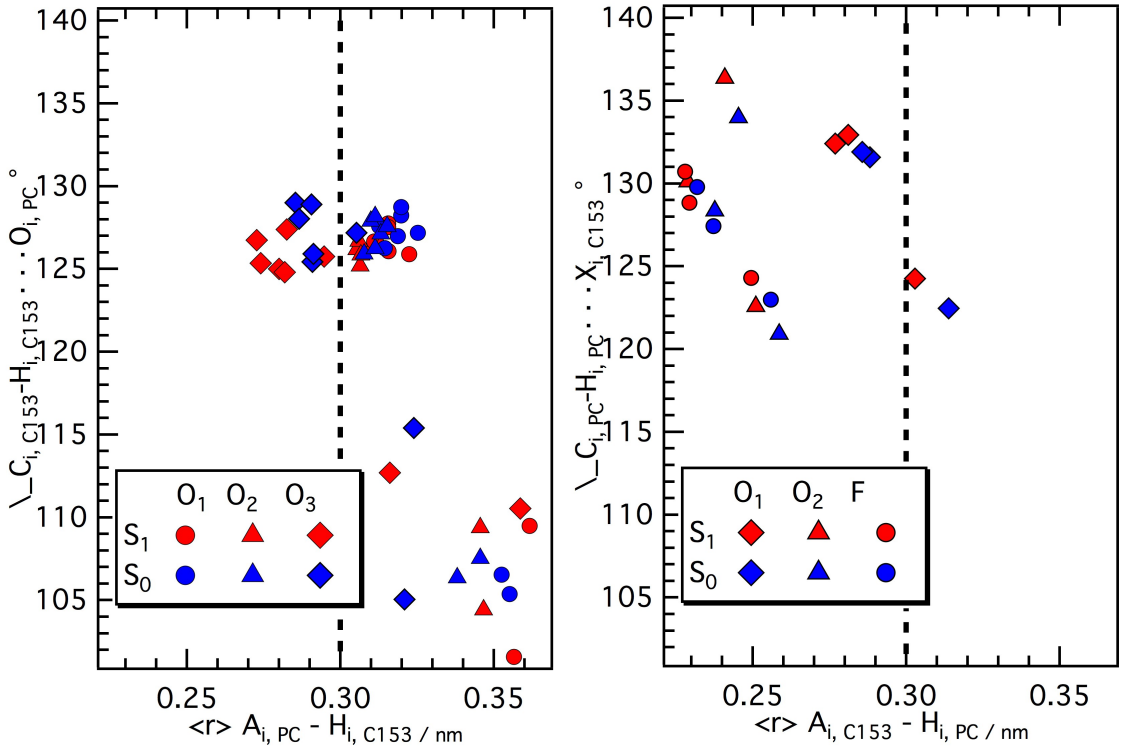

Figure 4.28: Left panel: ∠C-H···A of the HB between the first nearest neighbour RDF between the O_1 (circles), O_2 (triangles) and O_3 (diamonds) atoms of PC and i^{th} carbon atom of C153 C_i as function of mean distance of the first nearest neighbour RDF between the O_1, O_2 and O_3 atoms of PC and the hydrogen atom, linked to the C_i. Right panel: ∠C-H···A of the HB between the first nearest neighbour RDF between O_1 (diamonds), O_2 (triangles) and F (circles) atoms of C153 and i^{th} carbon atom of PC C_i as function of mean distance of the first nearest neighbour RDF between O_1, O_2 and F atoms of C153 and hydrogen atom, linked to the C_i.

arrangement between these C153 ring and PC doesn't change.

Furthermore, the orientation of PC is shifted for approximately 45° with respect to the julolidine rings of C153. This can be explained by the non-planarity of this moiety. In excited state, the above orientation becomes better defined. As the CDFs with the angle β are rather diffuse for the julolidine rings #4 and #5, one can conclude that there is very weak preference for parallel arrangements between these rings and the ring of PC.

Finally, the relative orientation between the central and lactone rings of C153 and PC were investigated. For this, CDFs were calculated and illustrated in fig. 4.31. The first channel was the RDF between the centres of the rings of C153 and the centre of the ring of the PC. The other channel was the ADF for the $\angle\gamma = \angle d_{O_1-C_2(C153)} d_{\#3-C1(PC)}$. Therefore, the vectors $d_{O_1-C_2(C153)}$ and $d_{\#3-C_1(PC)}$ are aligned in parallel and anti-parallel way when $\angle\gamma = 0°$ and 180°, respectively.

The orientation of $d_{O_1-C_2(C153)}$ and $d_{\#3-C_1(PC)}$ is preferentially parallel and antiparallel. However, this preference is rather weak. Upon the excitation, the orientation with $\angle\gamma = 120°$ becomes more important. Taking into account the fact that this orientation is advantageous for H3-F and H4-O_2 HBs, this may be correlated with the fact that in the excited state the HBs are stronger.

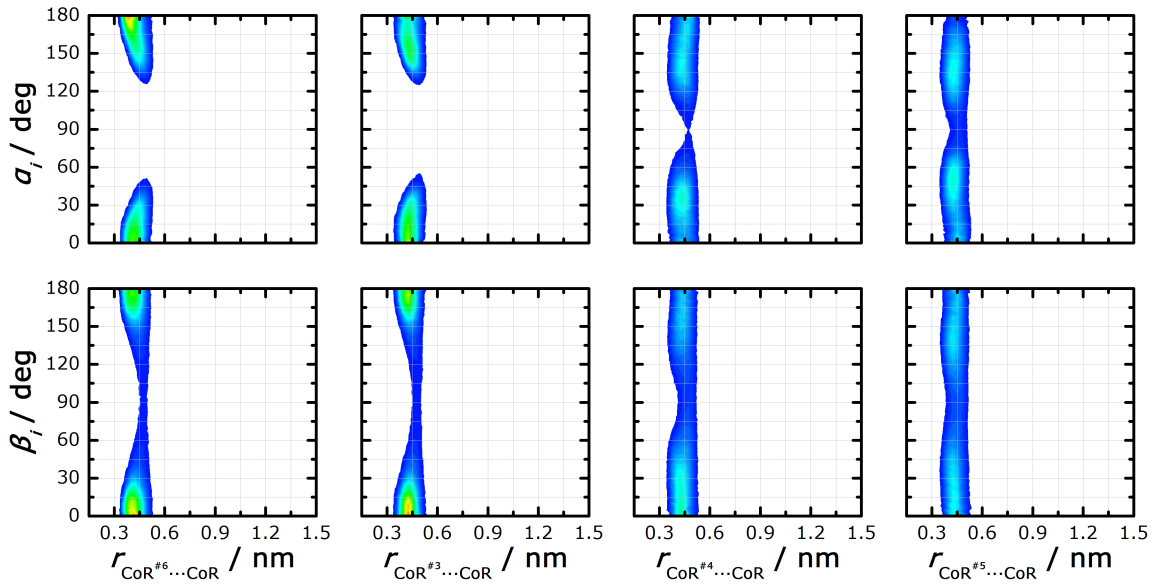

Figure 4.29: Contour plot of combined distribution functions between CoR of C153 in ground state and CoR of PC. The analysis of 8ns trajectory was made. The colour change from blue to red corresponds to the change in intensity from its minimum to its maximum.Minimum and maximum values are the same between the panels.

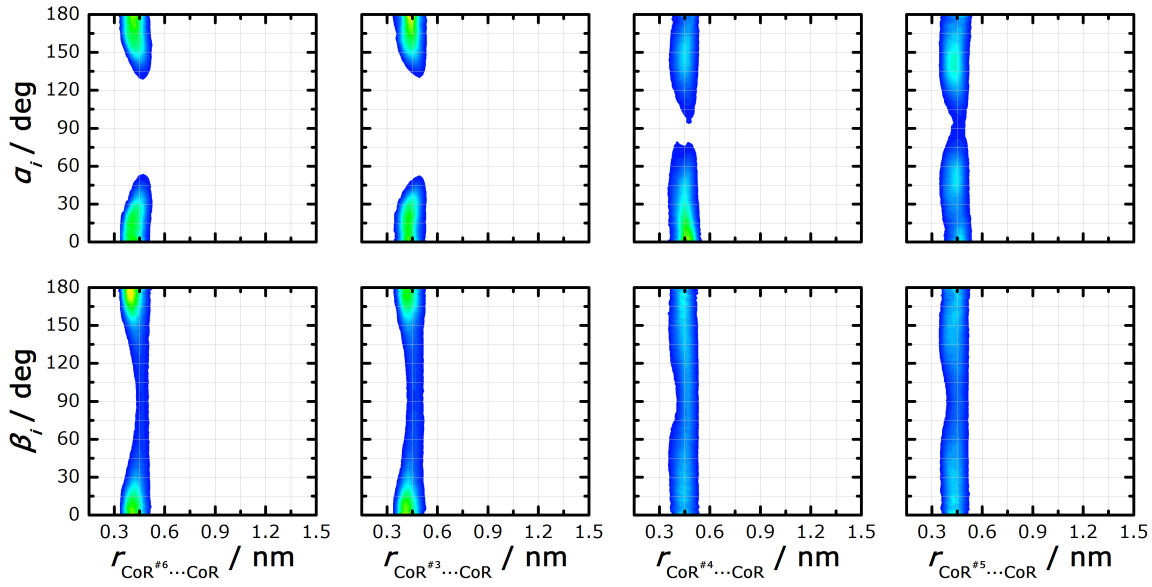

Figure 4.30: Contour plot of combined distribution functions between CoR of C153 S_1 and CoR of PC. The analysis of 8ns trajectory was made. The colour change from blue to red corresponds to the change in intensity from its minimum to its maximum. Minimum and maximum values are the same between the panels and with fig. 4.29.

In conclusion, the structure of the first solvation shell of C153 in PC is rather diffuse. Its most important feature is the hydrogen bonding between the hydrogens of PC and fluorine and oxygen of C153. The preferential orientation of PC molecules to C153 lactone ring is apparently influenced by these HBs. This hydrogen bonding becomes stronger upon the excitation.

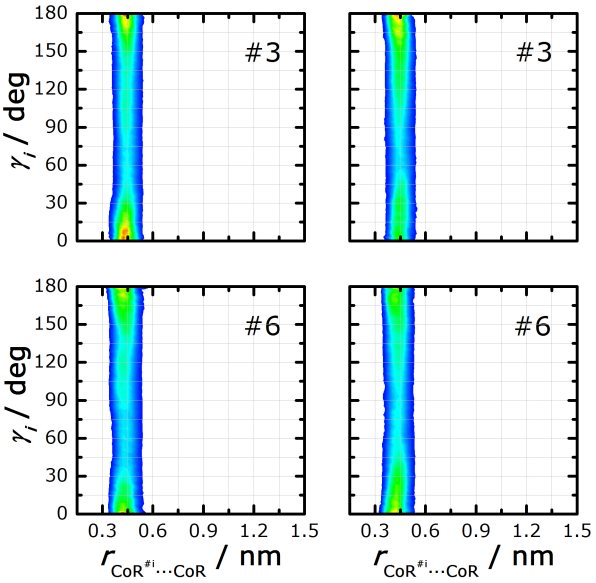

Figure 4.31: Contour plot of combined distribution functions between CoR of C153 S_0 and S_1 and CoR of PC. The analysis of 8ns trajectory was made. The colour change from blue to red corresponds to the change in intensity from its minimum to its maximum. Minimum and maximum values are the same between the panels.

Hydrogen bonding C153-solvent in mixtures

As the analysis of the structure of the solvation shell of C153 in PC and in $BmimBF_4$ have shown, the hydrogen bonding plays a key role in the solute-solvent interactions in these systems. For this reason, the accent was finally made on the calculations of HBs between C153 and the components of the IL/MS mixtures. A similar methodology was applied: the mean distance of the first nearest neighbour RDFs between carbon and acceptor and between hydrogen and acceptor and ∠C-H$\cdots$A of the HB was estimated.

Fig. 4.32 illustrates the result. The analyses of the trajectories of C153 in ground (left) and excited (right) states are presented separately. The contributions of the different classes of interactions were marked as well: HBs between the hydrogens of C153 and the PC, the hydrogens of C153 and the anion, the O_1, O_2 and F atoms of C153 and the hydrogens of the PC and the O_1, O_2 and F atoms of C153 and the hydrogens of the cation. This way, the competition between the components of of the mixture for the hydrogens and for the O_1, O_2 and F atoms of C153 can be addressed.

An examination of the left panel in fig. 4.32 reveals that for C153 S_0, the HBs strength parallels the molar fraction of the PC. The shortest distance is observed for the interactions between C153 and the hydrogens of the PC and between the hydrogens of C153 and the fluorine atom of the anion. Let's first consider the solutions in the PC and in the mixtures with x_{IL}=0.075,0.15 and 0.20. There, only a part of the interactions between the hydrogens of the PC and C153 and between the O_1 and O_2 atoms of PC and C153 can be considered as weak hydrogen bonds. The HBs between the IL and C153 is not present. Contrarily to these systems, in the mixture with x_{IL}=0.65, the HBs between PC and C153 are not present anymore. The hydrogens of C153 are now the subject of the hydrogen bonding with the fluorine

atoms of the anion. The cation has also gained the competition for the O_2 atom of C153.

On the basis of these results, the hypothesis of the preferential solvation of C153 by the IL or by the PC can be ruled out. Indeed, as it is shown in fig. 4.32, on the different sides of the equimolar composition, the PC and the IL exhibit the domination in the hydrogen bonding strength.

Considering the right panel in fig. 4.32, one can note that the general observations that were made for the C153 S_0 (left panel) are conserved for the C153 S_1.Indeed, $< r > A_i - H_j$ is shorter within the dilution of the IL and no preferential solvation can be stated. However, the hydrogen bonding is generally stronger in S_1 than in S_0: the mean distances are shorter. This is particularly important for the interaction between the O_2 atom of C153 and the H2 atom of cation: the $< r > O_{2,C153} - H2_{cat}$ =0.281 nm in S_0 and 0.238 nm in S_1.

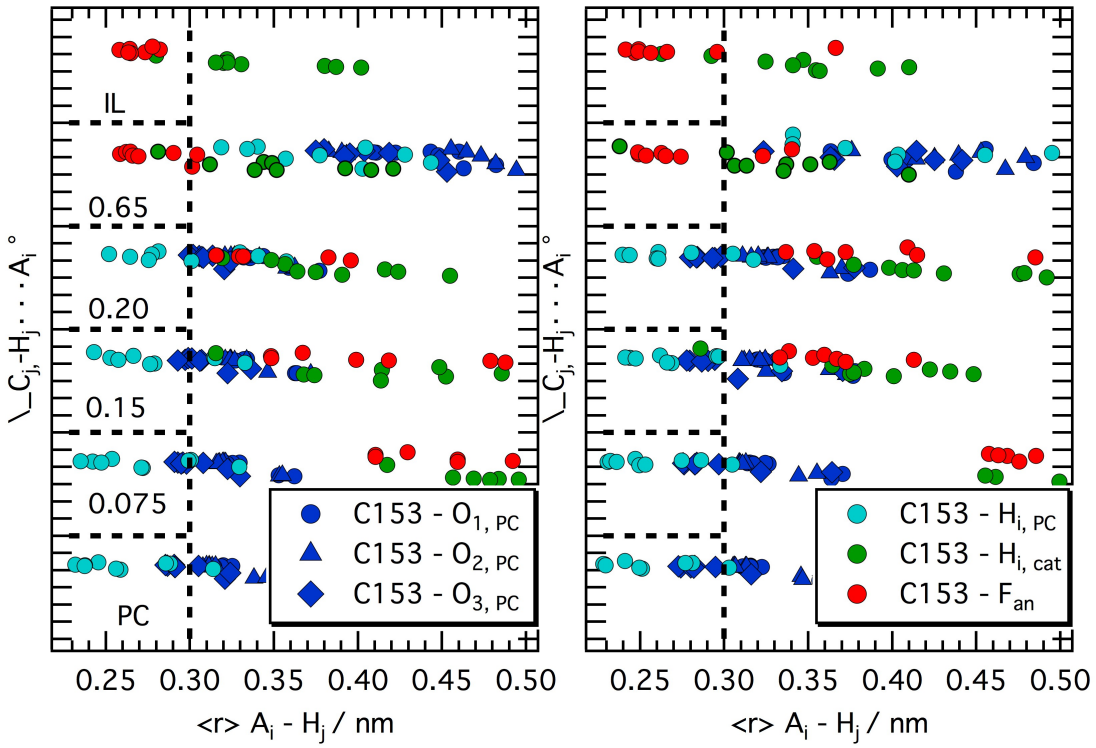

Figure 4.32: The ∠C-H···A of the HB between the first nearest neighbour RDF between the atoms of C153 and the atoms of PC, cation and anion. The left and the right panels correspond to the analysis of C153 S_0 and C153 S_1, respectively. For the sake of clarity, the scale was kept the same for both panels. The dashed lines correspond to the mean distances of 0.3 nm and 180° within x and y, respectively. The curves are plotted with the vertical offset of 180° .

In conclusion, the analysis of the structure of the solvation shell of C153 in $BmimBF_4$/PC mixtures has shown the general strengthening of the solute-solvent hydrogen bonding upon the excitation. This is the main process that can be deduced at the origin of the solvation dynamics in these systems. The reorientation of the cation and of the PC, taking place during the solvation dynamics, is also linked to the HBs strengthening.

Conclusions

The study of the solvation dynamics in $BmimBF_4$/PC mixtures, using the C153 probe, is presented. In order to elucidate the timescale, time components and to get a mechanistic understanding of this process, time-resolved fluorescence measurements (TCSPC and fluorescence up-conversion) and MD simulations were performed.

TRES of C153 in the mixtures change their maximum position with time. The other properties, like assymmetry or FWHM, change little or not at all. The SRFs, calculated from TRES, revealed a complex picture of the multi-regime solvation dynamics, expanded over 6 orders of magnitude: from femtoseconds to nanoseconds. Two or more exponential terms were needed to fit the SRFs, depending on the mixture composition. This complex dynamics was confirmed by the measurements of the time-resolved fluorescence anisotropy. Furthermore, the behaviour of the coupling constant, calculated from the rotational correlation times, follows different regimes of IL/MS mixtures: similar to normal electrolyte solution up to x_{IL}=0.20 and similar to the expanded IL for higher x_{IL}.

The SRFs, calculated from MD simulation, were found to be in good agreement with the experimental data. The subpicosecond solvation was shown to be governed by the interactions between C153 and the PC and between C153 and the anion. In neat IL, anion also dominates the solvation dynamics after 1 ps. In mixtures, the contributions of the interactions C153-cation and C153-anion after 1 ps are similar.

The structure of the solvation shell of C153 was shown to be rather diffuse. The RDFs between the rings' centres of C153 and the anion, the cation, and the PC didn't exhibit any clear features. The relative orientation of the cation ring with respect to the rings of C153 is slightly shifted above/below and parallel for the lactone and the central rings of C153 and diffuse for the julolidine ring of C153. The same arrangement is preferable between C153 and the PC.

The most salient feature of the solvation shell of C153 is the hydrogen bonding between the IL or PC and C153. In the solution in IL, the interaction between the julolidine hydrogens and the fluorine atoms of the anion is the strongest. In the solution in PC, both the distance characteristics of $O_{3,PC}$-$H_{i,C153}$ and $X_{i,C153}$-$H_{i,PC}$ fall into the region of weak hydrogen bonds. Importantly, these hydrogen bonds become stronger upon the excitation. The reorientation of the nearest cation and PC are correlated with this strengthening. In mixtures, multiple possibilities of the hydrogen bonding between C153 and the mixture components creates a competition for the hydrogen atoms and O2 and F of C153. According to the mean distance diagrams, no preferential solvation through this competition can be stated.

Bibliography

[1] R. Sánchez-de Armas, M. n. San Miguel, J. Oviedo, and J. F. Sanz, "Coumarin derivatives for dye sensitized solar cells: a td-dft study," Phys. Chem. Chem. Phys., vol. 14, pp. 225–233, 2012.

[2] A. Rosspeintner, B. Lang, and E. Vauthey, "Ultrafast photochemistry in liquids," Annual Review of Physical Chemistry, vol. 64, no. 1, pp. 247–271, 2013.

[3] B. Dereka, A. Rosspeintner, Z. Li, R. Liska, and E. Vauthey, "Direct visualization of excited-state symmetry breaking using ultrafast time-resolved infrared spectroscopy," Journal of the American Chemical Society, vol. 138, no. 13, pp. 4643–4649, 2016.

[4] E. W. Castner, C. J. Margulis, M. Maroncelli, and J. F. Wishart, "Ionic liquids: Structure and photochemical reactions," Annual Review of Physical Chemistry, vol. 62, no. 1, pp. 85–105, 2011.

[5] M. Mostafavi and T. Gustavsson, Réactions ultrarapides en solution. CNRS Editions, 2006.

[6] J. Lewis and M. Maroncelli, "On the (uninteresting) dependence of the absorption and emission transition moments of coumarin 153 on solvent," Chemical Physics Letters, vol. 282, no. 2, pp. 197 – 203, 1998.

[7] T. Kumpulainen, A. Rosspeintner, and E. Vauthey, "Probe dependence on polar solvation dynamics from fs broadband fluorescence," Phys. Chem. Chem. Phys., vol. 19, pp. 8815–8825, 2017.

[8] X.-X. Zhang, J. Breffke, N. P. Ernsting, and M. Maroncelli, "Observations of probe dependence of the solvation dynamics in ionic liquids," Phys. Chem. Chem. Phys., vol. 17, pp. 12949–12956, 2015.

[9] R. Karmakar and A. Samanta, "Steady-state and time-resolved fluorescence behavior of c153 and prodan in room-temperature ionic liquids," The Journal of Physical Chemistry A, vol. 106, no. 28, pp. 6670–6675, 2002.

[10] M. Sajadi, M. Weinberger, H.-A. Wagenknecht, and N. P. Ernsting, "Polar solvation dynamics in water and methanol: search for molecularity," Phys. Chem. Chem. Phys., vol. 13, pp. 17768–17774, 2011.

[11] N. Ito, S. Arzhantsev, and M. Maroncelli, "The probe dependence of solvation dynamics and rotation in the ionic liquid 1-butyl-3-methyl-imidazolium hexafluorophosphate," Chemical Physics Letters, vol. 396, no. 1, pp. 83 – 91, 2004.

[12] T. Gustavsson, L. Cassara, V. Gulbinas, G. Gurzadyan, J.-C. Mialocq, S. Pommeret, M. Sorgius, and P. van der Meulen, "Femtosecond spectroscopic study of relaxation processes of three amino-substituted coumarin dyes in methanol and dimethyl sulfoxide," The Journal of Physical Chemistry A, vol. 102, no. 23, pp. 4229–4245, 1998.

[13] C. F. Chapman, R. S. Fee, and M. Maroncelli, "Measurements of the solute dependence of solvation dynamics in 1-propanol: The role of specific hydrogen-bonding interactions," The Journal of Physical Chemistry, vol. 99, no. 13, pp. 4811–4819, 1995.

[14] H. Kaur, S. Koley, and S. Ghosh, "Probe dependent solvation dynamics study in a microscopically immiscible dimethyl sulfoxide–glycerol binary solvent," The Journal of Physical Chemistry B, vol. 118, no. 27, pp. 7577–7585, 2014.

[15] V. Nagarajan, A. M. Brearley, T. Kang, and P. F. Barbara, "Time-resolved spectroscopic measurements on microscopic solvation dynamics," The Journal of Chemical Physics, vol. 86, no. 6, pp. 3183–3196, 1987.

[16] J. A. Gardecki and M. Maroncelli, "Comparison of the single-wavelength and spectral-reconstruction methods for determining the solvation-response function," The Journal of Physical Chemistry A, vol. 103, no. 9, pp. 1187–1197, 1999.

[17] R. Fee and M. Maroncelli, "Estimating the time-zero spectrum in time-resolved emmsion measurements of solvation dynamics," Chemical Physics, vol. 183, no. 2, pp. 235 – 247, 1994.

[18] X. Song and D. Chandler, "Dielectric solvation dynamics of molecules of arbitrary shape and charge distribution," The Journal of Chemical Physics, vol. 108, no. 6, pp. 2594–2600, 1998.

[19] M. L. Horng, J. A. Gardecki, A. Papazyan, and M. Maroncelli, "Subpicosecond measurements of polar solvation dynamics: Coumarin 153 revisited," The Journal of Physical Chemistry, vol. 99, no. 48, pp. 17311–17337, 1995.

[20] E. Laitinen, K. Salonen, and T. Harju, "Solvation dynamics study of 4-amino-n-methylphthalimide in n-alcohol solutions," The Journal of Chemical Physics, vol. 104, no. 16, pp. 6138–6148, 1996.

[21] L. Reynolds, J. A. Gardecki, S. J. V. Frankland, M. L. Horng, and M. Maroncelli, "Dipole solvation in nondipolar solvents: Experimental studies of reorganization energies and solvation dynamics," The Journal of Physical Chemistry, vol. 100, no. 24, pp. 10337–10354, 1996.

[22] E. Bart, A. Meltsin, and D. Huppert, "Excited-state solvation dynamics in solid tetraalkylammonium salts," The Journal of Physical Chemistry, vol. 99, no. 22, pp. 9253–9257, 1995.

[23] R. Karmakar and A. Samanta, "Solvation dynamics of coumarin-153 in a room-temperature ionic liquid," The Journal of Physical Chemistry A, vol. 106, no. 18, pp. 4447–4452, 2002.

[24] M. Muramatsu, S. Morishima, T. Katayama, S. Ito, Y. Nagasawa, and H. Miyasaka, "The effect of pre-solvation in the ground state on photoinduced electron transfer in ionic liquids," Journal of Solution Chemistry, vol. 43, pp. 1550–1560, Oct 2014.

[25] M. Muramatsu, Y. Nagasawa, and H. Miyasaka, "Ultrafast solvation dynamics in room temperature ionic liquids observed by three-pulse photon echo peak shift measurements," The Journal of Physical Chemistry A, vol. 115, no. 16, pp. 3886–3894, 2011.

[26] M. Schmollngruber, C. Schröder, and O. Steinhauser, "Polarization effects on the solvation dynamics of coumarin c153 in ionic liquids: Components and their cross-correlations," The Journal of Chemical Physics, vol. 138, no. 20, p. 204504, 2013.

[27] Y. Shim and H. J. Kim, "Dielectric relaxation and solvation dynamics in a room-temperature ionic liquid: Temperature dependence," The Journal of Physical Chemistry B, vol. 117, no. 39, pp. 11743–11752, 2013.

[28] M. Maroncelli, X.-X. Zhang, M. Liang, D. Roy, and N. P. Ernsting, "Measurements of the complete solvation response of coumarin 153 in ionic liquids and the accuracy of simple dielectric continuum predictions," Faraday Discuss., vol. 154, pp. 409–424, 2012.

[29] H. V. R. Annapureddy, Z. Hu, J. Xia, and C. J. Margulis, "How does water affect the dynamics of the room-temperature ionic liquid 1-hexyl-3-methylimidazolium hexafluorophosphate and the fluorescence spectroscopy of coumarin-153 when dissolved in it?," The Journal of Physical Chemistry B, vol. 112, no. 6, pp. 1770–1776, 2008.

[30] S. Daschakraborty and R. Biswas, "Ultrafast solvation response in room temperature ionic liquids: Possible origin and importance of the collective and the nearest neighbour solvent modes," The Journal of Chemical Physics, vol. 137, no. 11, p. 114501, 2012.

[31] S. Daschakraborty, T. Pal, and R. Biswas, "Stokes shift dynamics of ionic liquids: Solute probe dependence, and effects of self-motion, dielectric relaxation frequency window, and collective intermolecular solvent modes," The Journal of Chemical Physics, vol. 139, no. 16, p. 164503, 2013.

[32] D. Chakrabarty, D. Seth, A. Chakraborty, and N. Sarkar, "Dynamics of solvation and rotational relaxation of coumarin 153 in ionic liquid confined nanometer-sized microemulsions," The Journal of Physical Chemistry B, vol. 109, no. 12, pp. 5753–5758, 2005.

[33] S. Daschakraborty and B. Ranjit, "Stokes shift dynamics in (ionic liquid + polar solvent) binary mixtures: Composition dependence," The Journal of Physical Chemistry B, vol. 115, no. 14, pp. 4011–4024, 2011.

[34] S. Daschakraborty and R. Biswas, "Composition dependent stokes shift dynamics in binary mixtures of 1-butyl-3-methylimidazolium tetrafluoroborate with water and acetonitrile: Quantitative comparison between theory and complete measurements," The Journal of Physical Chemistry B, vol. 118, no. 5, pp. 1327–1339, 2014.

[35] D. E. Wetzler, C. Chesta, R. Fernández-Prini, and P. F. Aramendía, "Dynamic solvation of aminophthalimides in solvent mixtures," The Journal of Physical Chemistry A, vol. 106, no. 11, pp. 2390–2400, 2002.

[36] P. Hazra, D. Chakrabarty, and N. Sarkar, "Solvation dynamics of coumarin 153 in aqueous and non-aqueous reverse micelles," Chemical Physics Letters, vol. 371, no. 5, pp. 553 – 562, 2003.

[37] X. J. Jordanides, M. J. Lang, X. Song, and G. R. Fleming, "Solvation dynamics in protein environments studied by photon echo spectroscopy," The Journal of Physical Chemistry B, vol. 103, no. 37, pp. 7995–8005, 1999.

[38] X.-X. Zhang, M. Liang, N. P. Ernsting, and M. Maroncelli, "Complete solvation response of coumarin 153 in ionic liquids," The Journal of Physical Chemistry B, vol. 117, no. 16, pp. 4291–4304, 2013.

[39] J. A. Ingram, R. S. Moog, N. Ito, R. Biswas, and M. Maroncelli, "Solute rotation and solvation dynamics in a room-temperature ionic liquid," The Journal of Physical Chemistry B, vol. 107, no. 24, pp. 5926–5932, 2003.

[40] H. Jin, G. A. Baker, S. Arzhantsev, J. Dong, and M. Maroncelli, "Solvation and rotational dynamics of coumarin 153 in ionic liquids: Comparisons to conventional solvents," The Journal of Physical Chemistry B, vol. 111, no. 25, pp. 7291–7302, 2007.

[41] S. Arzhantsev, H. Jin, G. A. Baker, and M. Maroncelli, "Measurements of the complete solvation response in ionic liquids," The Journal of Physical Chemistry B, vol. 111, no. 18, pp. 4978–4989, 2007.

[42] X.-X. Zhang, M. Liang, N. P. Ernsting, and M. Maroncelli, "Conductivity and solvation dynamics in ionic liquids," The Journal of Physical Chemistry Letters, vol. 4, no. 7, pp. 1205–1210, 2013.

[43] T. Xiao and X. Song, "A molecular debye-hückel theory and its applications to electrolyte solutions," The Journal of Chemical Physics, vol. 135, no. 10, p. 104104, 2011.

[44] X. Song, "Solvation dynamics in ionic fluids: An extended debye–hückel dielectric continuum model," The Journal of Chemical Physics, vol. 131, no. 4, p. 044503, 2009.

[45] X.-X. Zhang, C. Schröder, and N. P. Ernsting, "Communication: Solvation and dielectric response in ionic liquids—conductivity extension of the continuum model," The Journal of Chemical Physics, vol. 138, no. 11, p. 111102, 2013.

[46] L. S. Headley, P. Mukherjee, J. L. Anderson, R. Ding, M. Halder, D. W. Armstrong, X. Song, and J. W. Petrich, "Dynamic solvation in imidazolium-based ionic liquids on short time scales," The Journal of Physical Chemistry A, vol. 110, no. 31, pp. 9549–9554, 2006.

[47] P. Mukherjee, J. A. Crank, P. S. Sharma, A. B. Wijeratne, R. Adhikary, S. Bose, D. W. Armstrong, and J. W. Petrich, "Dynamic solvation in phosphonium ionic liquids: a comparison of bulk and micellar systems and considerations for the construction of the solvation correlation function, c(t)," The Journal of Physical Chemistry B, vol. 112, no. 11, pp. 3390–3396, 2008.

[48] X.-X. Zhang, M. Liang, J. Hunger, R. Buchner, and M. Maroncelli, "Dielectric relaxation and solvation dynamics in a prototypical ionic liquid + dipolar protic liquid mixture: 1-butyl-3-methylimidazolium tetrafluoroborate + water," The Journal of Physical Chemistry B, vol. 117, no. 49, pp. 15356–15368, 2013.

[49] M. Liang, X.-X. Zhang, A. Kaintz, N. P. Ernsting, and M. Maroncelli, "Solvation dynamics in a prototypical ionic liquid + dipolar aprotic liquid mixture: 1-butyl-3-methylimidazolium tetrafluoroborate + acetonitrile," The Journal of Physical Chemistry B, vol. 118, no. 5, pp. 1340–1352, 2014.

[50] B. M. Ladanyi and M. Maroncelli, "Mechanisms of solvation dynamics of polyatomic solutes in polar and nondipolar solvents: A simulation study," The Journal of Chemical Physics, vol. 109, no. 8, pp. 3204–3221, 1998.

[51] D. Roy and M. Maroncelli, "Simulations of solvation and solvation dynamics in an idealized ionic liquid model," The Journal of Physical Chemistry B, vol. 116, no. 20, pp. 5951–5970, 2012.

[52] M. N. Kobrak, "A comparative study of solvation dynamics in room-temperature ionic liquids," The Journal of Chemical Physics, vol. 127, no. 18, p. 184507, 2007.

[53] Z. L. Terranova and S. A. Corcelli, "On the mechanism of solvation dynamics in imidazolium-based ionic liquids," The Journal of Physical Chemistry B, vol. 117, no. 49, pp. 15659–15666, 2013.

[54] S. N. V. K. Aki, J. F. Brennecke, and A. Samanta, "How polar are room-temperature ionic liquids?," Chem. Commun., pp. 413–414, 2001.

[55] M. J. Muldoon, C. M. Gordon, and I. R. Dunkin, "Investigations of solvent–solute interactions in room temperature ionic liquids using solvatochromic dyes," J. Chem. Soc., Perkin Trans. 2, pp. 433–435, 2001.

[56] A. J. Carmichael and K. R. Seddon, "Polarity study of some 1-alkyl-3-methylimidazolium ambient-temperature ionic liquids with the solvatochromic dye, nile red," Journal of Physical Organic Chemistry, vol. 13, no. 10, pp. 591–595, 2000.

[57] C. Reichardt, "Solvatochromic dyes as solvent polarity indicators," Chemical Reviews, vol. 94, no. 8, pp. 2319–2358, 1994.

[58] M. J. Kamlet, J. L. M. Abboud, M. H. Abraham, and R. W. Taft, "Linear solvation energy relationships. 23. a comprehensive collection of the solvatochromic parameters, .pi.*, .alpha., and .beta., and some methods for simplifying the generalized solvatochromic equation," The Journal of Organic Chemistry, vol. 48, no. 17, pp. 2877–2887, 1983.

[59] N. L. Lancaster, "Organic reactivity in ionic liquids: some mechanistic insights into nucleophilic substitution reactions," Journal of Chemical Research, vol. 2005, no. 7, pp. 413–417, 2005.

[60] V. Beniwal and A. Kumar, "Understanding positive and negative deviations in polarity of ionic liquid mixtures by pseudo-solvent approach," Phys. Chem. Chem. Phys., vol. 18, pp. 23853–23863, 2016.

[61] M. Maroncelli and G. R. Fleming, "Picosecond solvation dynamics of coumarin 153: The importance of molecular aspects of solvation," The Journal of Chemical Physics, vol. 86, no. 11, pp. 6221–6239, 1987.

[62] A. Kaintz, G. Baker, A. Benesi, and M. Maroncelli, "Solute diffusion in ionic liquids, nmr measurements and comparisons to conventional solvents," The Journal of Physical Chemistry B, vol. 117, no. 39, pp. 11697–11708, 2013.

[63] T. Köddermann, R. Ludwig, and D. Paschek, "On the validity of stokes–einstein and stokes–einstein–debye relations in ionic liquids and ionic-liquid mixtures," ChemPhysChem, vol. 9, no. 13, pp. 1851–1858, 2008.

[64] A. Stoppa, J. Hunger, G. Hefter, and R. Buchner, "Structure and dynamics of 1-n-alkyl-3-n-methylimidazolium tetrafluoroborate + acetonitrile mixtures," The Journal of Physical Chemistry B, vol. 116, no. 25, pp. 7509–7521, 2012.

[65] I. T. Todorov, W. Smith, K. Trachenko, and M. T. Dove, "Dl_poly_3: new dimensions in molecular dynamics simulations via massive parallelism," J. Mater. Chem., vol. 16, pp. 1911–1918, 2006.

[66] L. Martínez, R. Andrade, E. G. Birgin, and J. M. Martínez, "Packmol: A package for building initial configurations for molecular dynamics simulations," Journal of Computational Chemistry, vol. 30, no. 13, pp. 2157–2164, 2009.

[67] A. Stoppa, J. Hunger, and R. Buchner, "Conductivities of binary mixtures of ionic liquids with polar solvents," Journal of Chemical & Engineering Data, vol. 54, no. 2, pp. 472–479, 2009.

[68] A. Mondal and S. Balasubramanian, "Quantitative prediction of physical properties of imidazolium based room temperature ionic liquids through determination of condensed phase site charges: A refined force field," The Journal of Physical Chemistry B, vol. 118, no. 12, pp. 3409–3422, 2014.

[69] G. Cinacchi, F. Ingrosso, and A. Tani, "Solvation dynamics by computer simulation: A coumarin c153 in 1,4-dioxane," The Journal of Physical Chemistry B, vol. 110, no. 27, pp. 13633–13641, 2006.

[70] M. J. Frisch, G. W. Trucks, H. B. Schlegel, G. E. Scuseria, M. A. Robb, J. R. Cheeseman, G. Scalmani, V. Barone, G. A. Petersson, H. Nakatsuji, X. Li, M. Caricato, A. V. Marenich, J. Bloino, B. G. Janesko, R. Gomperts, B. Mennucci, H. P. Hratchian, J. V. Ortiz, A. F. Izmaylov, J. L. Sonnenberg, D. Williams-Young, F. Ding, F. Lipparini, F. Egidi, J. Goings, B. Peng, A. Petrone, T. Henderson, D. Ranasinghe, V. G. Zakrzewski, J. Gao, N. Rega, G. Zheng, W. Liang, M. Hada, M. Ehara, K. Toyota, R. Fukuda, J. Hasegawa, M. Ishida, T. Nakajima, Y. Honda, O. Kitao, H. Nakai, T. Vreven, K. Throssell, J. A. Montgomery, Jr., J. E. Peralta, F. Ogliaro, M. J. Bearpark, J. J. Heyd, E. N. Brothers, K. N. Kudin, V. N. Staroverov, T. A. Keith, R. Kobayashi, J. Normand, K. Raghavachari, A. P. Rendell, J. C. Burant, S. S. Iyengar, J. Tomasi, M. Cossi, J. M. Millam, M. Klene, C. Adamo, R. Cammi, J. W. Ochterski, R. L. Martin, K. Morokuma, O. Farkas, J. B. Foresman, and D. J. Fox, "Gaussian16 Revision B.01," 2016. Gaussian Inc. Wallingford CT.

[71] M. Brehm and B. Kirchner, "Travis - a free analyzer and visualizer for monte carlo and molecular dynamics trajectories," Journal of Chemical Information and Modeling, vol. 51, no. 8, pp. 2007–2023, 2011.

[72] R. Dennington, T. A. Keith, and J. M. Millam, "Gaussview Version 6," 2016. Semichem Inc. Shawnee Mission KS.

[73] J. J. Dannenberg, "The nature of the hydrogen bond: Outline of a comprehensive hydrogen bond theory," Journal of the American Chemical Society, vol. 132, no. 9, pp. 3229–3229, 2010.

[74] A. Idrissi, B. A. Marekha, M. Barj, F. A. Miannay, T. Takamuku, V. Raptis, J. Samios, and P. Jedlovszky, "Local structure of dilute aqueous dmso solutions, as seen from molecular dynamics simulations," The Journal of Chemical Physics, vol. 146, no. 23, p. 234507, 2017.

[75] G. R. Desiraju and T. Steiner, The Weak Hydrogen Bond In Structural Chemistry and Biology (International Union of Crystallography, Monographs on Crystallography). Oxford University Press, 1999.

Conclusion

In this thesis, a multi-technique experimental and theoretical investigation of the spectroscopic and photophysical properties of the liquid solutions of the indoline derivated dyes D205, D149, D102 and D131 is presented. These dyes present an interest for an application as photo sensitizers in DSSC and have one of the highest efficiencies among the organic dye based DSSC. As solvents, conventional organic solvents, ILs and IL/MS mixtures were used. The latter media are good candidates as solvents for electrochemical devices, possessing interesting properties like low volatility, high thermal stability and high conductivity.

The charge-transfer character of the indoline derivatives was confirmed by the steady-state absorption and fluorescence spectroscopies and quantum chemical calculations. These dyes were shown to have very small dipole moment in the electronic ground state. It increases by 12.5 -16.7 D upon the photo-excitation. Catalan solvent scale was used for the analysis of the steady-state data. The results suggest high importance of solvent polarity, acidity and basicity on the steady-state spectra of these molecules.

Furthermore, TCSPC and femtosecond transient absorption were used to study the photophysics of these dyes. They confirmed the influence of hydrogen bond donor and acceptor ability of the solvent on the equilibrium between the neutral and deprotonated forms of the dyes. Indeed, much shorter excited state lifetime of dyes in protic solvents was observed. With help of the decay associated spectra, the photophysics scheme, different for protic and aprotic solvents was proposed.

The floppy structure of these molecules was associated with their short fluorescence lifetimes. The ultrafast twisting and deactivation is an important feature of the photophysics of the indoline molecules.

Finally, the solvation dynamics was found to play an important role in the photophysics of these dyes. Being relatively well-understood in conventional organic solvents, this process is complex and not clear in ILs and IL/MS mixtures. To study this process, four different fluorescence probes were used: C153, C102, PRODAN and 4-ANMP. After a detailed consideration of the properties of these probes, C153 was proposed as the most suitable probe for the study of the solvation dynamics in IL/MS mixtures.

The time-resolved fluorescence (TCSPC and up-conversion) measurements revealed a multi-regime and complex solvation response in $BmimBF_4$/PC mixtures. The MD simulations, performed for C153 in $BmimBF_4$/PC, show that the weak hydrogen bonding, present between C153 and mixture components, plays a dominant role in the solvation dynamics. Indeed, these HBs become stronger upon the excitation. Translational and rotational motions of the mixture components, correlated with this strengthening, were suggested to be responsible for the solvation dynamics in these systems. The subpicosecond solvation was shown to be governed by the PC

and by the anion. In neat IL, anion also dominates the solvation dynamics after 1 ps. In mixtures, the contributions of the cation and of the anion after 1 ps are similar.

The general conclusions of this work can be formulated as follows:

- The spectroscopic and photophysical properties of the organic dyes are greatly influenced by their environment. The key properties of the solvents are: (i) dipolarity, (ii) acidity (HB donor ability) and (iii) basicity (HB acceptor ability).
- The solvation dynamics in IL/MS mixtures is a multi-regime process, that extends over 6 time scale orders: from femtoseconds to nanoseconds. The strengthening of the hydrogen bonding between the probe and the mixture components and the associated translation and rotation largely determine this process.

Taken together these results, one can model the spectral and photophysical response of the dyes, choosing the appropriate solvent. The influence of the spectral and photophysical of the dyes on the efficiency of the DSSCs is not always clear. The red-shift of the absorption spectra and their larger width help the harvesting of the sun light by the solar cell. Also, longer excited state lifetime is beneficial for the electron injection efficiency. At the same time, the solvation dynamics decreases the energy of the excited state, which decreases the overpotential between the excited state and the conductive band of the semiconductor. On the other side, the solvation dynamics in viscous systems can be much longer than the electron injection. From this point of view, the balance between the charge transport and the decrease of the overpotential by the solvation dynamics must be found in order to construct a perfect solar cell with a high efficiency.

In perspectives, this work can be the basis of the following developments:

- The study of the photophysics of the organic dyes on the semiconductor nanoparticles can provide important details about the influence of the aggregation and of the morphology of the semiconductor surface and may help to reveal the dynamics of the electron injection.
- A comprehensive understanding of the correlation between the spectral and photophysical response of the dyes and the efficiency of the DSSCs must be established. This can be performed on the basis of this work and additional experimental measurements in DSSCs: power conversion efficiency η, open circuit voltage V_{OC}, short-circuit current J_{SC}, fill factor FF and stability tests.

Appendices

Appendix A

Transient absorption

A.0.1 Transient absorption set-up

The scheme of transient absorption set-up is shown in fig. A.1.

A laser system was used for generation of pump and probe pulses. Firstly, femtosecond Ti:sapphire oscillator is pumped by Nd:YVO_4 laser and generates pulses at 76 MHz repetition rate, 100fs width and 10nJ power at 800nm. The beam is stretched, amplified and recompressed with regenerative amplifier (Ti:Sapphire), pumped by Nd:YLF laser. Resulting pulses of 1mJ power, 90fs width, 1kHz repetition rate and 800nm wavelength are split in 90/10 ratio. The first part is injected into Palitra, and the pump pulse of needed wavelength is generated. In this work, 410nm 450nm and 488nm were used to excite indoline dyes solutions. Neutral density filters are used to attenuate pump power in order to prevent the photodegradation of the sample. The second part, about 10% of the light is used to generate a white light continuum in CaF_2 crystal, after passing through the delay line. Two choppers are used to permit the signal acquisition scheme, described below. The polarisation pump and probe beams was set at magic angle, 54.7 degrees. The probe beam is split in two by the periscope, and this way probe (with pump) and reference (without pump) signals are acquired. Single-shot time-resolved spectra are recorded by the CCD camera.

The solution was introduced in the 1mm moving cell, its absorbance at maximum absorption wavelength was maintained to be less than 0.5. Absorbance accuracy of transient spectra (before averaging) is 1mOD. After alignment of the set-up, the CCD camera was calibrated in wavelength using a set of optical filters.

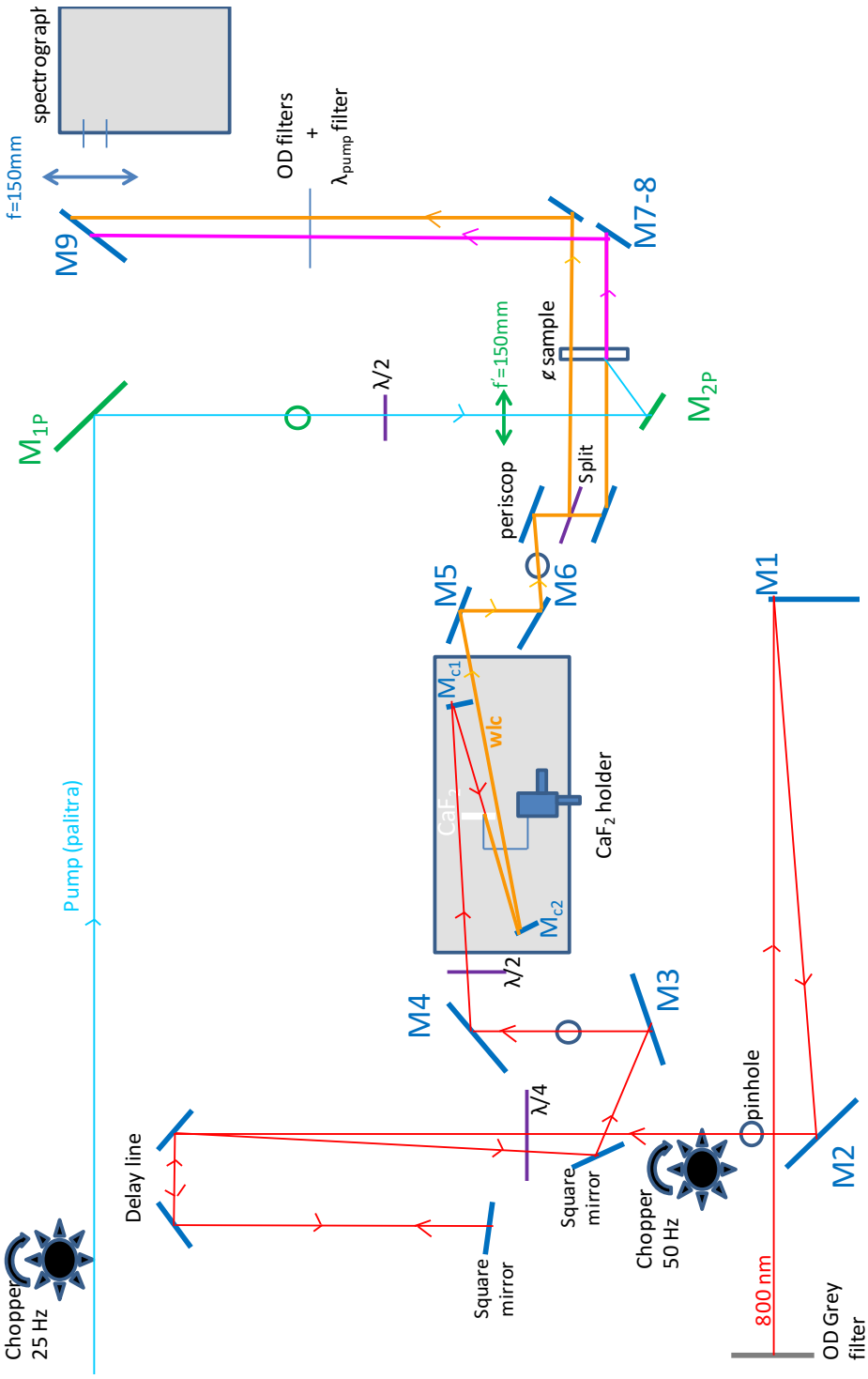

Figure A.1: Transient absorption set-up scheme. The representation was performed by Dr. Miannay F.-A.

A.0.2 Acquisition mode of the transient absorption spectra

During the measurements, 2 cycles (4 forth and back passes) with 300 frames at each delay time were performed. The way of measurement is fully controlled by the software, written by IT agent of LASIR laboratory and based on Labview libraries. Transient spectra are saved for each time delay, being calculated with the equation A.2.

$$\Delta OD = OD^{probe} - OD^{ref} \tag{A.1}$$

$$\Delta OD = -log(\frac{I^{probe}_{pump}(\lambda, \Delta t) - I^{em}(\lambda)}{I^{ref}_{pump}(\lambda, \Delta t) - I^{em}(\lambda)}) + log(\frac{I^{probe}_{0}(\lambda, \Delta t) - I^{stray}(\lambda)}{I^{ref}_{0}(\lambda, \Delta t) - I^{stray}(\lambda)}) \tag{A.2}$$

Intensities, shown in equation A.2 are:

- I^{probe}_{pump} and I^{ref}_{pump} are the intensities of probe and reference beams, when pump is on;
- I^{em} is the intensity of the probe beam, when white light is off, and the pump is on. It represents the fluorescence emission after the excitation of the sample by the pump pulse;
- I^{probe}_{0} and I^{ref}_{0} are the signals if probe and reference beams, when pump is off, cut by the chopper at 25Hz;
- I^{stray} is acquired when both pump and probe beams are blocked.

I^{stray} and I^{em} are measured in the beginning of the measurement and in the end, using the shutters to block pump and probe beams. The rest of the signals are measured at each delay, the pump being blocked by the chopper with two times less frequency than the probe chopper (25Hz and 50 Hz for pump and probe choppers, respectively).

A.0.3 Group velocity dispersion

As shown in [1], refractive index of a transparent condensed material depends on the wavelength. In general, this dependence have exponential character in optic spectral window, refractive index decreasing with the wavelength and is called a dispersion curve.

Due to finite spectral width of the pump and probe pulses, dispersion creates a delay between the red and blue parts of the pulse and results in pulse broadening. Lenses, filters and a sample are the parts of the set-up that are responsible for the pulse broadening.

Group velocity dispersion (GVD) is also visible in the experimental data, as the delay time of different wavelengths is shifted in response to the dispersion curve. As red wavelengths propagate in the media faster than blue ones, it is the blue ones that are first to interact with the excited molecules at negative times, close to zero time. With greater delay between pump and probe, the red wavelengths start to interact with the volume of excited molecules. Thus, blue part of the spectrum comes first and the red part of the spectrum comes the last.

Correction of GVD is not a simple task. In this work, it was performed using a software elaborated in LASIR laboratory. GVD correction consists in shift in time of kinetics at different wavelengths, in the way that they have the time zero at the same time moment. Interpolation is used to compensate the discrete character of the experimental data.

An example of GVD correction is shown in fig. A.2. Non-corrected data is shown on the left panel. The curvature of the time zero wavelength dependence is clearly seen. Corrected data is shown on the right panel. Sellmeier equation (eq. A.3) is used to calculate the dispersion curve from the width of quartz cell, CaF_2 and BK7, used in the set-up scheme for the experiment. In this equation, the coefficients B_i and C_i are experimentally determined for glasses and listed in literature.

$$n^2(\lambda) = 1 + \frac{B_1\lambda^2}{\lambda^2 - C_1} + \frac{B_2\lambda^2}{\lambda^2 - C_2} + \frac{B_3\lambda^2}{\lambda^2 - C_3} \tag{A.3}$$

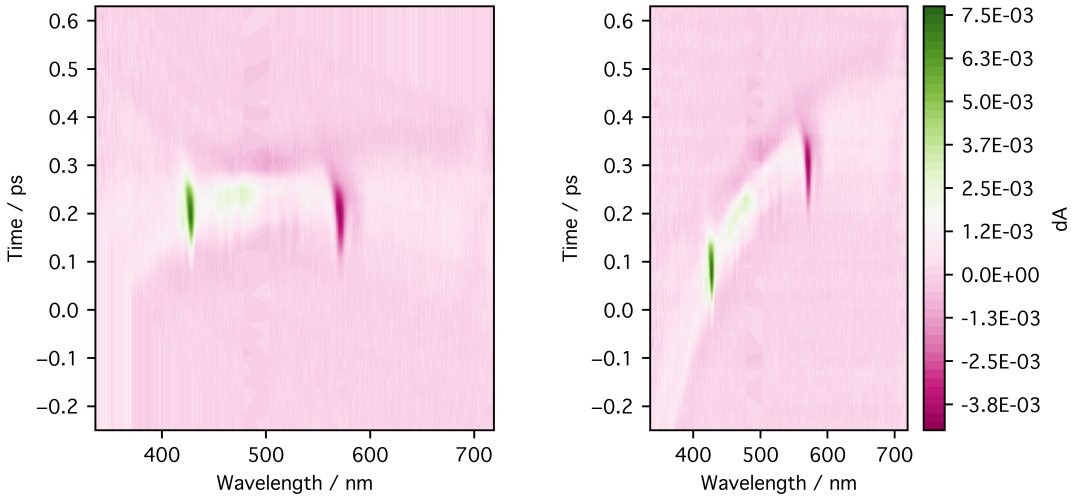

Figure A.2: Corrected (left) and non-corrected (right) for GVD transient absorption signals of neat MeOH, excitation wavelength 488nm.

A.0.4 Time resolution of the transient absorption set-up

One of the methods of the estimation of time resolution of the setup is to record the signal from a long-living specie at the early times, so that the rise is clearly seen. Importantly, the condition that no ultrafast processes affect the signal of the excited state and that the decay of the excited state population can be neglected must be met. Then, the true decay function can be replaced by a step function at early times. Then, the trace must be differentiated and the result is modelled by gaussian function. The full width half maximum of the model must be the estimation of the time resolution. This method is described in the book [1], see page 224, originally used for emission spectroscopy with optical gating methods.

In figure A.3, one can see three kinetics of ruthenium bipyridine chloride solution in acetonitrile at different wavelengths. They were differentiated, as shown on the graph. After, gaussian model was applied (see eq. A.4) in order to extract the estimation of time resolution of the set-up, as it was described above. The *width*

in the equation is linked to the full width half maximum of gaussian as in eq. A.5. Using the following method, the time resolution of transient absorption set-up was estimated to be 115fs.

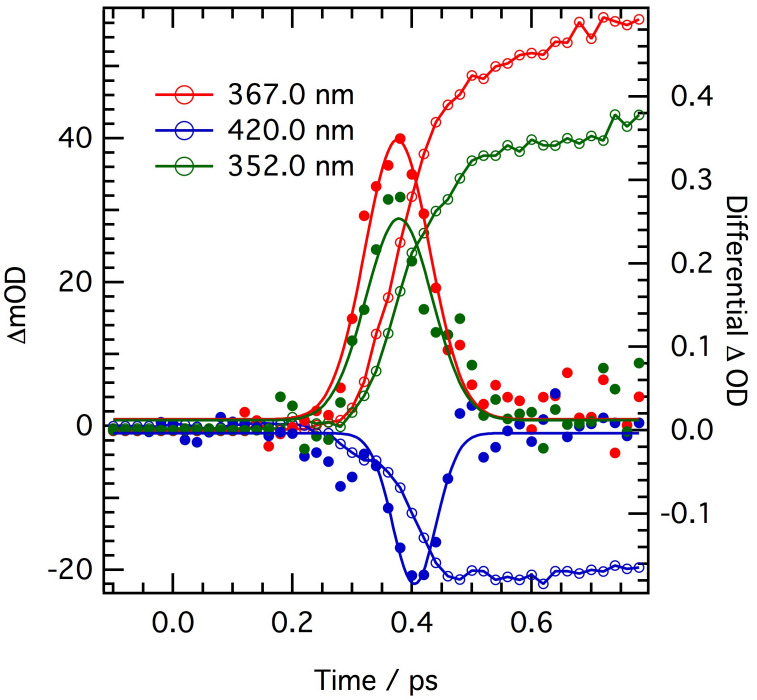

Figure A.3: Ruthenium bipyridine kinetics at three different wavelengths (linked hollows), their differentials as a function of time (full circles) and gaussian model of differentials (solid lines). The colour code corresponds to the wavelength at which the kinetics was recorded. The GVD correction was performed before the treatment. The excitation wavelength was 450nm.

$$y = y_0 + A \cdot \exp\{-\frac{(x - x_0)^2}{width^2}\} \tag{A.4}$$

$$\mathrm{FWHM} = 2\sqrt{\ln 2} \cdot width \tag{A.5}$$

The same solution was used to check the delay line stability. Thus, as the lifetime of the compound lasts for microseconds, in case of perfect stability, one should observe a horizontal kinetics, as shown in fig. A.4.

Another method to obtain the time resolution of the set-up is to measure the cross-correlation of pump and probe pulses. This can be made with a BK7 glass or with the cell filled by neat solvent. In the first case, with BK7 glass, the two-photon absorption takes place: the pump and probe photons are absorbed simultaneously, and a sum-frequency signal is observed in transient spectra at early times. This way to measure the time resolution was tested with the available set-up in LASIR. The result is shown in fig. A.5

As one can see, on this figure, the absorption starts around 488nm, and occurs at smaller wavelengths. This is a direct signature of two-photon absorption: all the signal

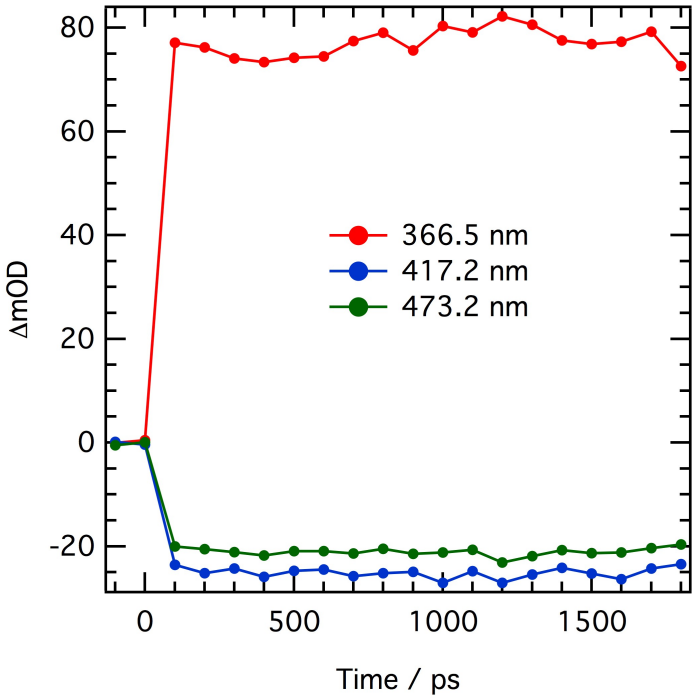

Figure A.4: Ruthenium bipyridine kinetics at three different wavelengths (linked full circles). The colour code corresponds to the wavelength at which the kinetics was recorded. The excitation wavelength was 450nm.

is coming from the sum frequency transitions. The spectrum was corrected for GVD, so the extracted kinetics have maximum at the same time moment. Importantly, like in the method discussed above, the shape of pump and probe pulses in time is assumed to be gaussian function. This choice is approved by the good quality of fits of experimental data, using convolution with gaussian function with a FWHM equal to the time resolution. From the experiments, showed in this work, no direct information about the shape of instrument response function can't be obtained.

Thus, the kinetics are modelled by the gaussian function and the result is given in the legend of the figure: 83, 83, and 90fs from different wavelengths kinetic traces.

Another way of measure, with the cell with solvent was also tested. This configuration of experiment is much closer to the experiment with the solutions of dyes. Thus, it is preferable to use this mode. The transient absorption set-up time resolution was tested with the cells filled by acetonitrile, dimethylsulfoxide, methanol and propylene carbonate. The results are shown in fig. A.6, A.7, A.8 and A.9. In this type of experiment, due to a strong pump intensity, Raman signal can be observed. This is due to the non-elastic scattering of pump light by solvent molecules. A gain or loss in energy (Anti-Stokes and Stokes Raman) of the light is symmetric in energy with respect to the pump pulse energy, and corresponds to the one of the frequencies of molecule vibration. Thus, this kind of signal arises only during the overlap of the probe and pump pulses and can serve as a cross-correlation test.

Analogically to the case with BK7 glass, the spectra were corrected for the GVD. On the top panels of fig. A.6, A.7, A.8 and A.9 the spectra are shown already after the GVD correction. After, Stokes and Anti-Stokes kinetics are extracted

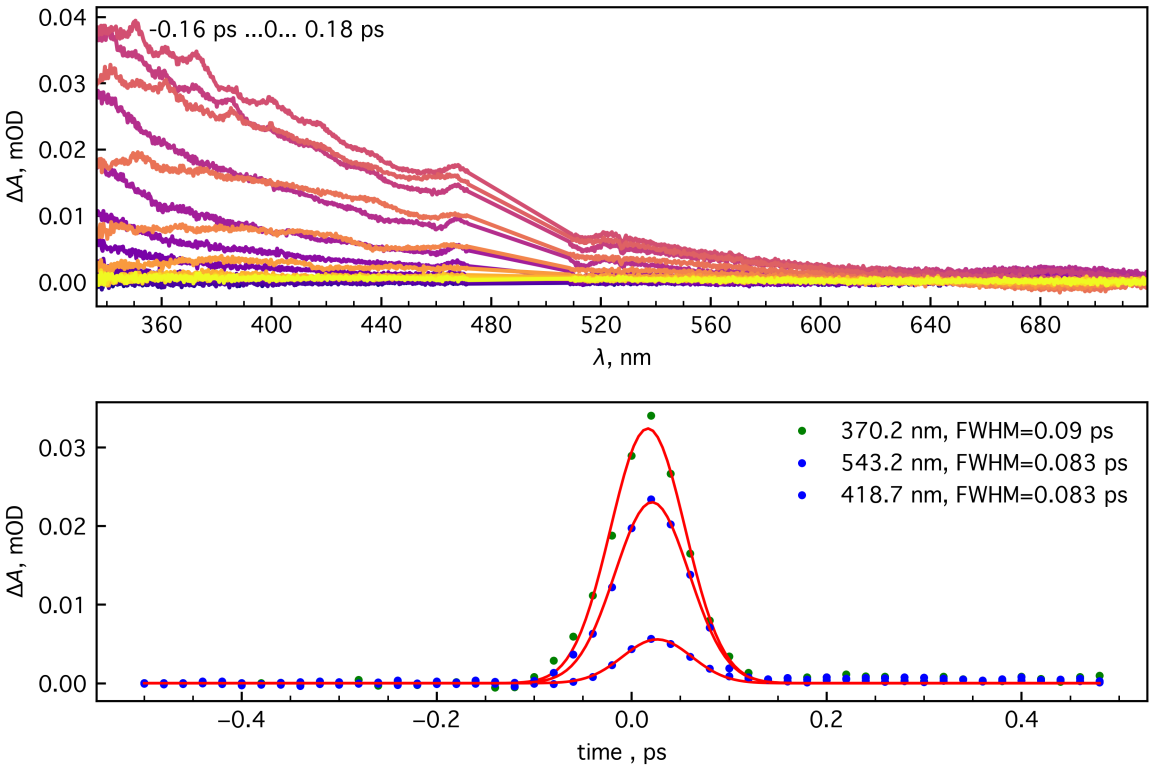

Figure A.5: BK7 test of time resolution of transient absorption set-up. The pump wavelength of 488nm was used. Upper panel shows BK7 transient spectra close to the temporal overlap of probe and pump pulse. Spectra were corrected for GVD. On the lower panel, kinetics at three chosen wavelengths are presented. Legend shows the wavelength and gives the full width half maximum, result of gaussian fit of cross-correlation signal.

Table A.1: Results of transient absorption measurement of cross-correlation in solvent. FWHM of gaussian modelled kinetics, wavelengths of Raman and calculated vibration frequency. Excitation wavelength wavelength was adjusted to 489nm for MeOH and 484nm for DMSO.

		Stokes	Anti-Stokes	Vibration frequency / cm^{-1}
PC	FWHM / ps	0.102	0.101	2981
	λ / nm	571	426	
ACN	FWHM / ps	0.104	0.1	3011
	λ / nm	572.6	425.8	
MeOH	FWHM / ps	0.12	0.104	2955
	λ / nm	572	427.5	
DMSO	FWHM / ps	0.176	0.143	3013
	λ / nm	566.8	422.5	

and modelled by the gaussian function. In view of subtlety of the experiment and measured processes, the results obtained are very close. The results are tabulated and shown in table A.1.

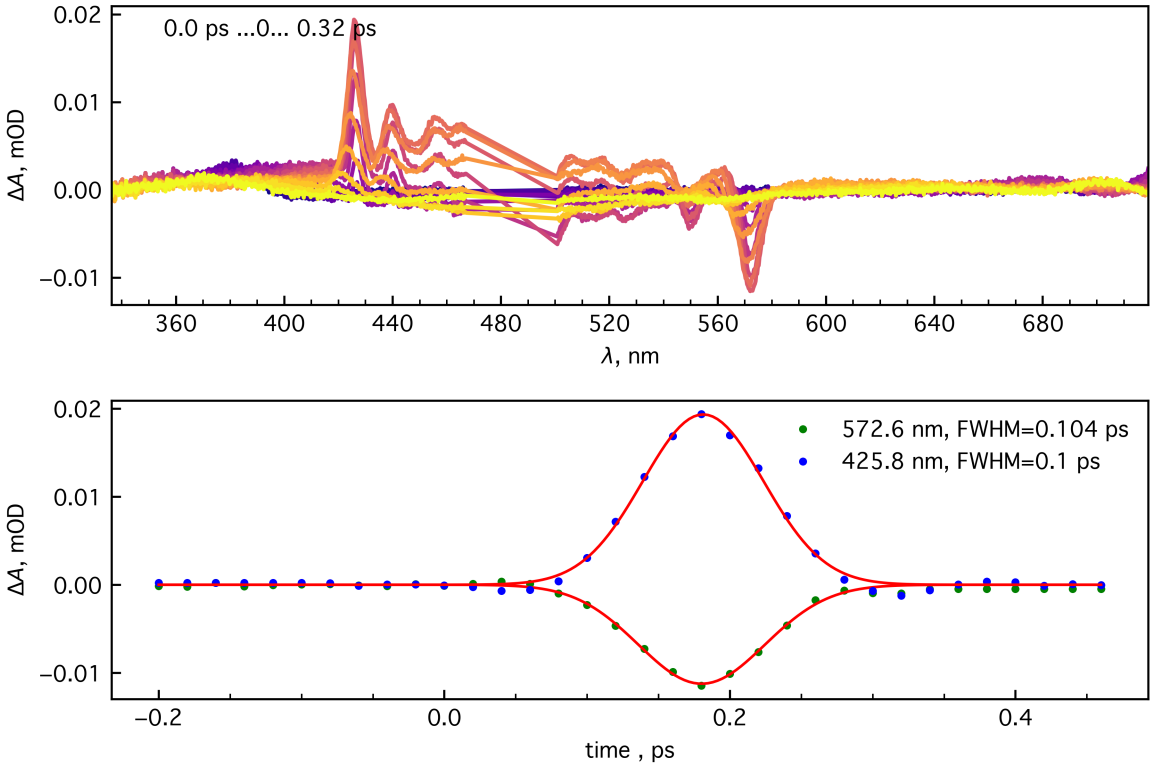

Figure A.6: Solvent test of time resolution of transient absorption set-up. The pump wavelength of 488nm was used. Upper panel shows ACN transient spectra close to the temporal overlap of probe and pump pulse. Spectra were corrected for GVD. On the lower panel, kinetics at three chosen wavelengths are presented. Legend shows the wavelength and gives the full width half maximum, result of gaussian fit of cross-correlation signal.

In regard of the experiments described above, the transient absorption set-up

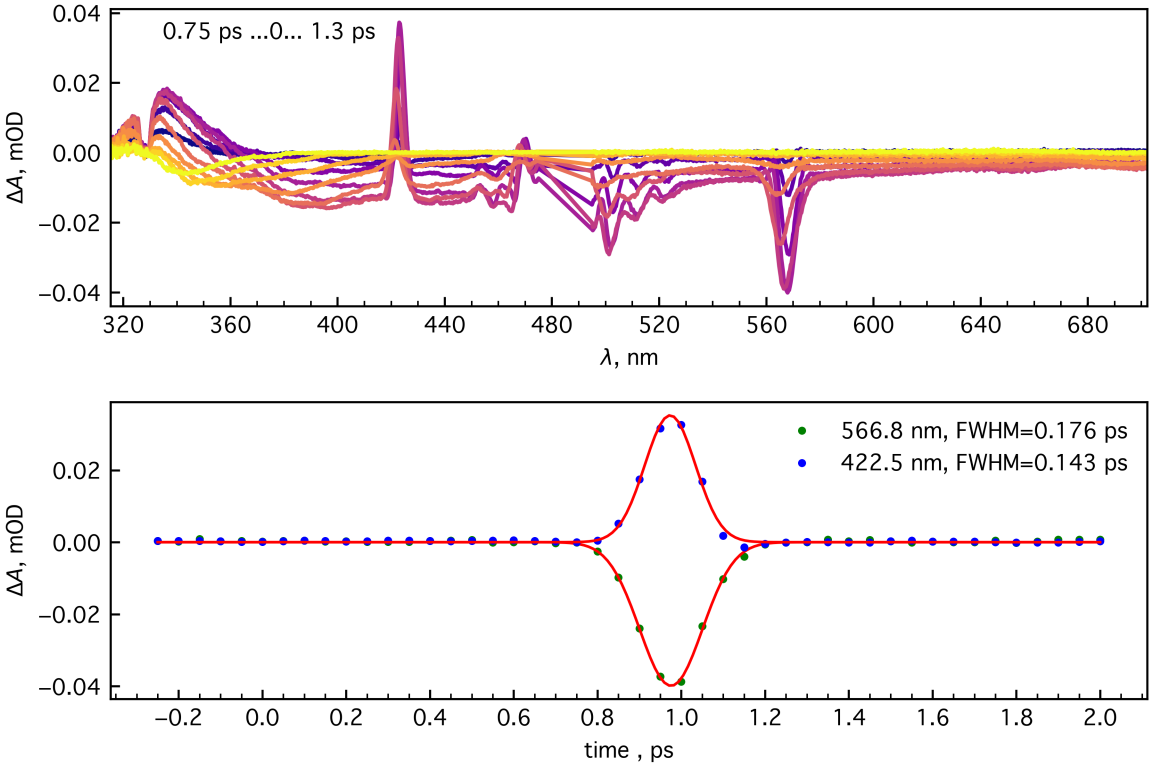

Figure A.7: Solvent test of time resolution of transient absorption set-up. The pump wavelength of 488nm was used. Upper panel shows DMSO transient spectra close to the temporal overlap of probe and pump pulse. Spectra were corrected for GVD. On the lower panel, kinetics at three chosen wavelengths are presented. Legend shows the wavelength and gives the full width half maximum, result of gaussian fit of cross-correlation signal.

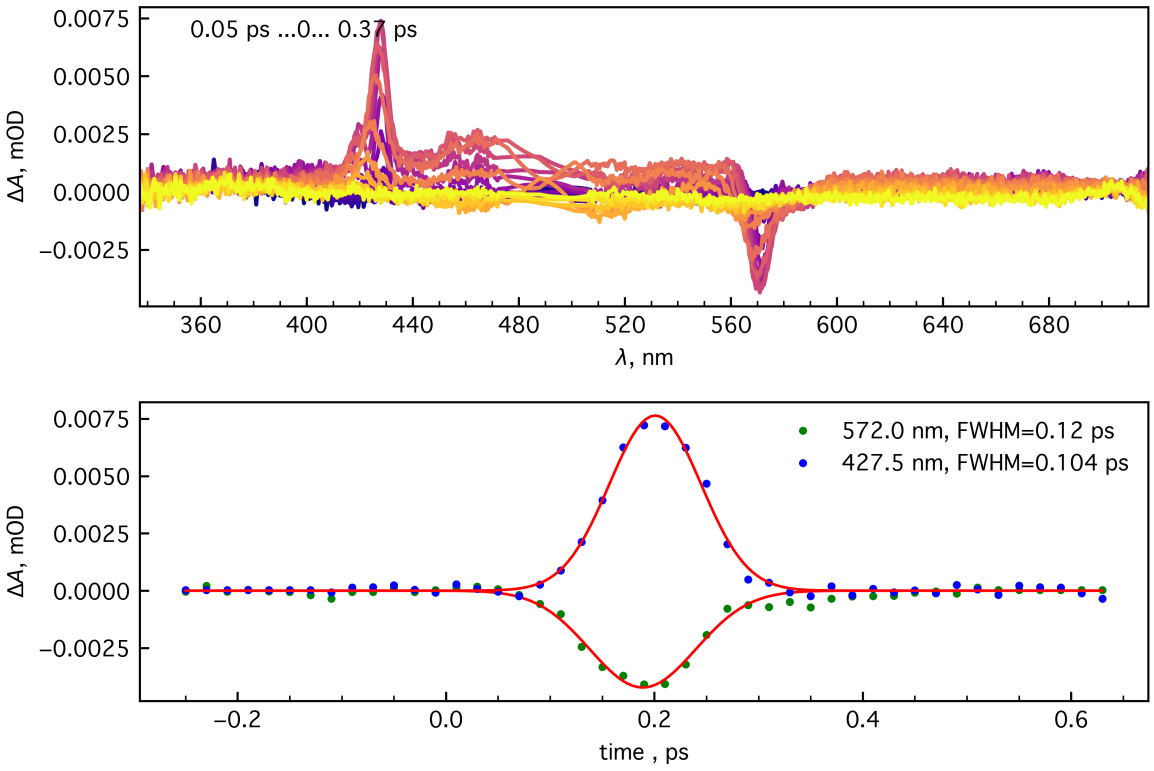

Figure A.8: Solvent test of time resolution of transient absorption set-up. The pump wavelength of 488nm was used. Upper panel shows MeOH transient spectra close to the temporal overlap of probe and pump pulse. Spectra were corrected for GVD. On the lower panel, kinetics at three chosen wavelengths are presented. Legend shows the wavelength and gives the full width half maximum, result of gaussian fit of cross-correlation signal.

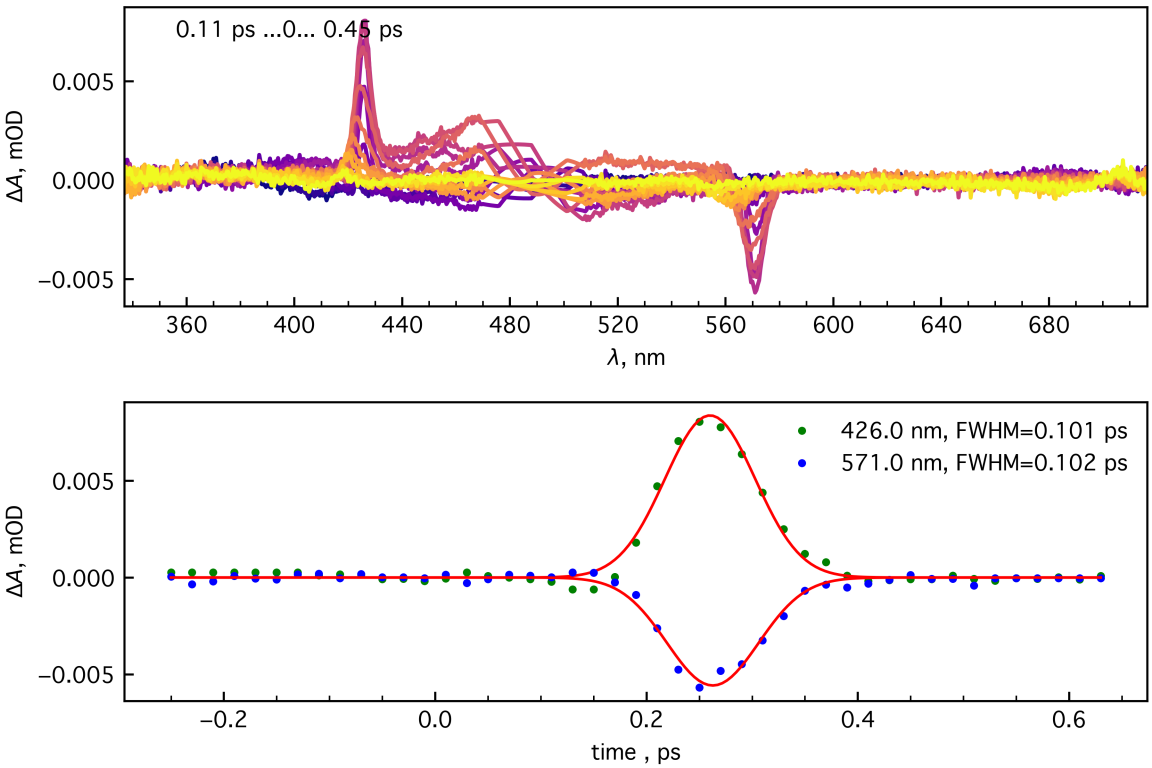

Figure A.9: Solvent test of time resolution of transient absorption set-up. The pump wavelength of 488nm was used. Upper panel shows PC transient spectra close to the temporal overlap of probe and pump pulse. Spectra were corrected for GVD. On the lower panel, kinetics at three chosen wavelengths are presented. Legend shows the wavelength and gives the full width half maximum, result of gaussian fit of cross-correlation signal.

resolution was estimated to be of the order of 120 fs. This value was fixed or optimised in order to obtain the best fit to the experimental data depending on the quality of data. In the frame of experimental shown in the present work, dependence of time resolution on pump wavelength was neglected on the basis of its strong similarity.

Using the equation A.6, taken from [1], one can calculate the width of pump and probe pulses in approximation that they are equal. Using 120fs resolution, obtained by the measurement above, width of the pump and probe pulses was estimated to be 85fs.

$$\Delta t = \sqrt{\Delta t_{pump}^2 + \Delta t_{probe}^2} \tag{A.6}$$

As it is shown in [1], the uncertainty principle states that the product of time and energy uncertainties is limited by Planck constant, divided by two (eq. A.7).

$$\Delta E \Delta t = \frac{h}{2} \tag{A.7}$$

It is clearly seen from this equation that the uncertainties of width and spectrum of the pulse are linked, and one should find the balance between the two. The minimal spectral width of the pulse can be calculated from its temporal shape, using the eq. A.8.

$$\Delta\lambda = \frac{1}{4\pi}\frac{\lambda^2}{c\Delta t} \tag{A.8}$$

If we take the FWHM at the place of uncertainties, we must use the following relation (eq. A.9). Using 120fs FWHM as $\Delta t_{\frac{1}{2}}$, minimal spectral width of 6nm was estimated.

$$\Delta t_{\frac{1}{2}} = 0.88\frac{\lambda^2}{c\Delta\lambda_{\frac{1}{2}}} \tag{A.9}$$

A.0.5 Indoline dyes transient absorption spectra

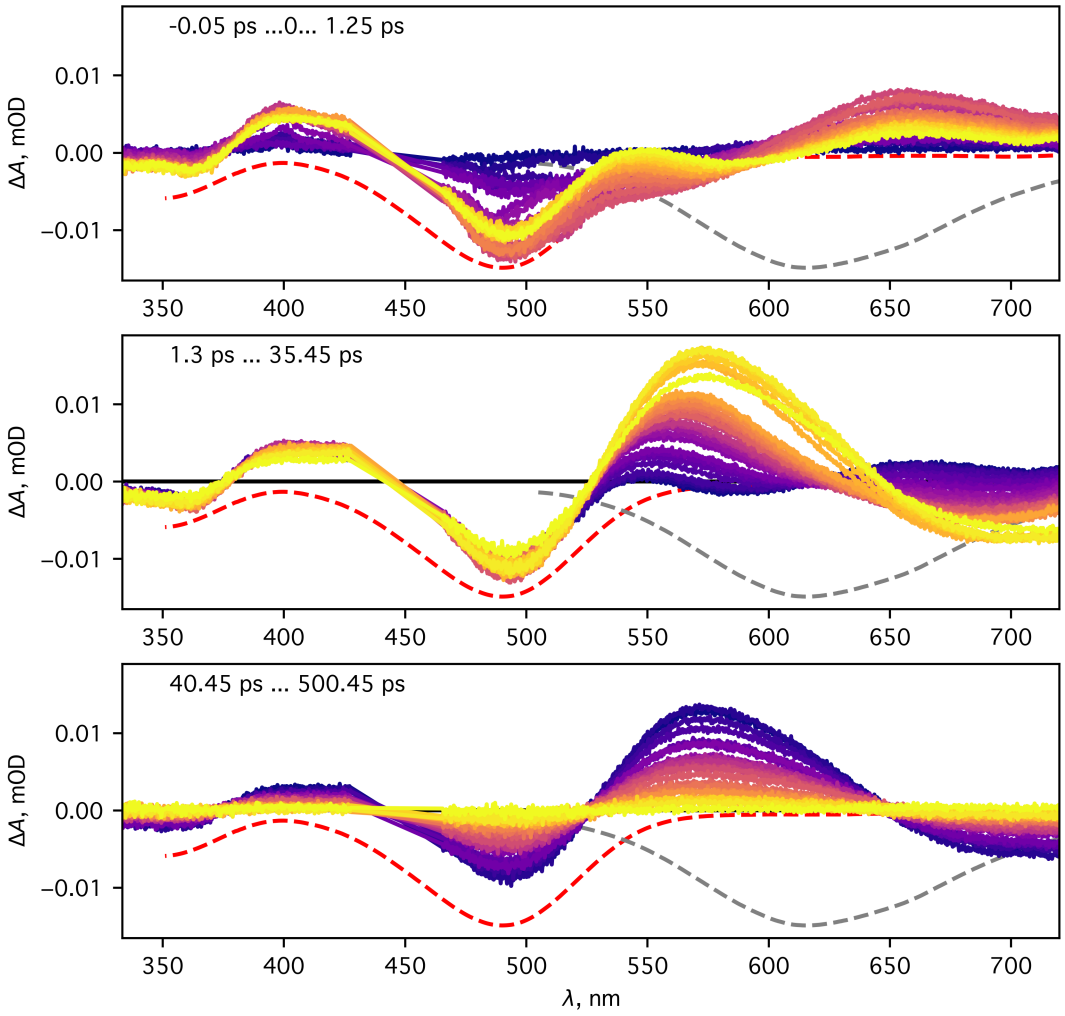

Figure A.10: D102 transient absorption spectra in methanol. The colour gradient 'plasma', from East Bay to yellow colour, was chosen to represent the difference spectra in time ranges, indicated in text boxes in the panels. Red and grey dash lines are used to show inverted steady-state absorption and emission spectra, respectively. Black lines on two lowest panels show the zero difference border.

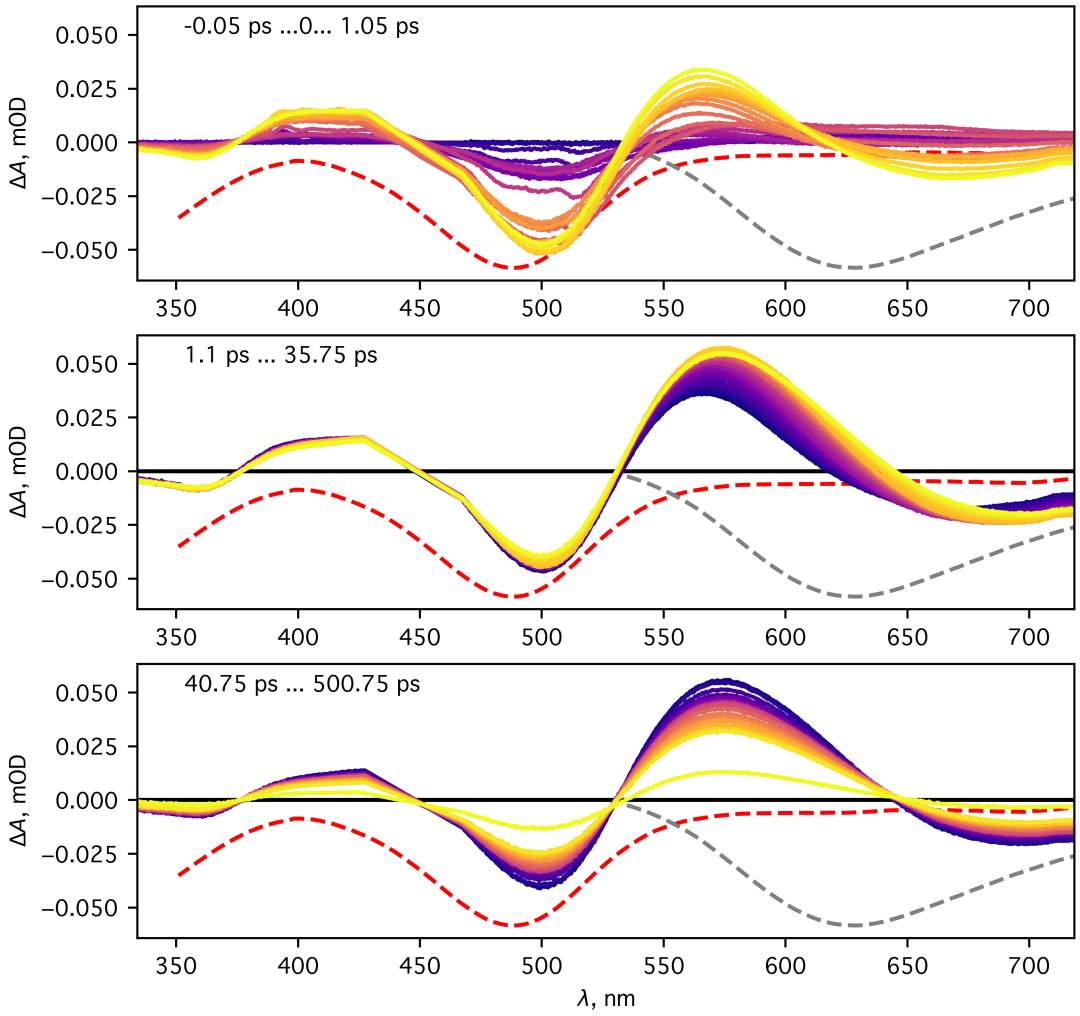

Figure A.11: D102 transient absorption spectra in acetonitrile. The colour gradient 'plasma', from East Bay to yellow colour, was chosen to represent the difference spectra in time ranges, indicated in text boxes in the panels. Red and grey dash lines are used to show inverted steady-state absorption and emission spectra, respectively. Black lines on two lowest panels show the zero difference border.

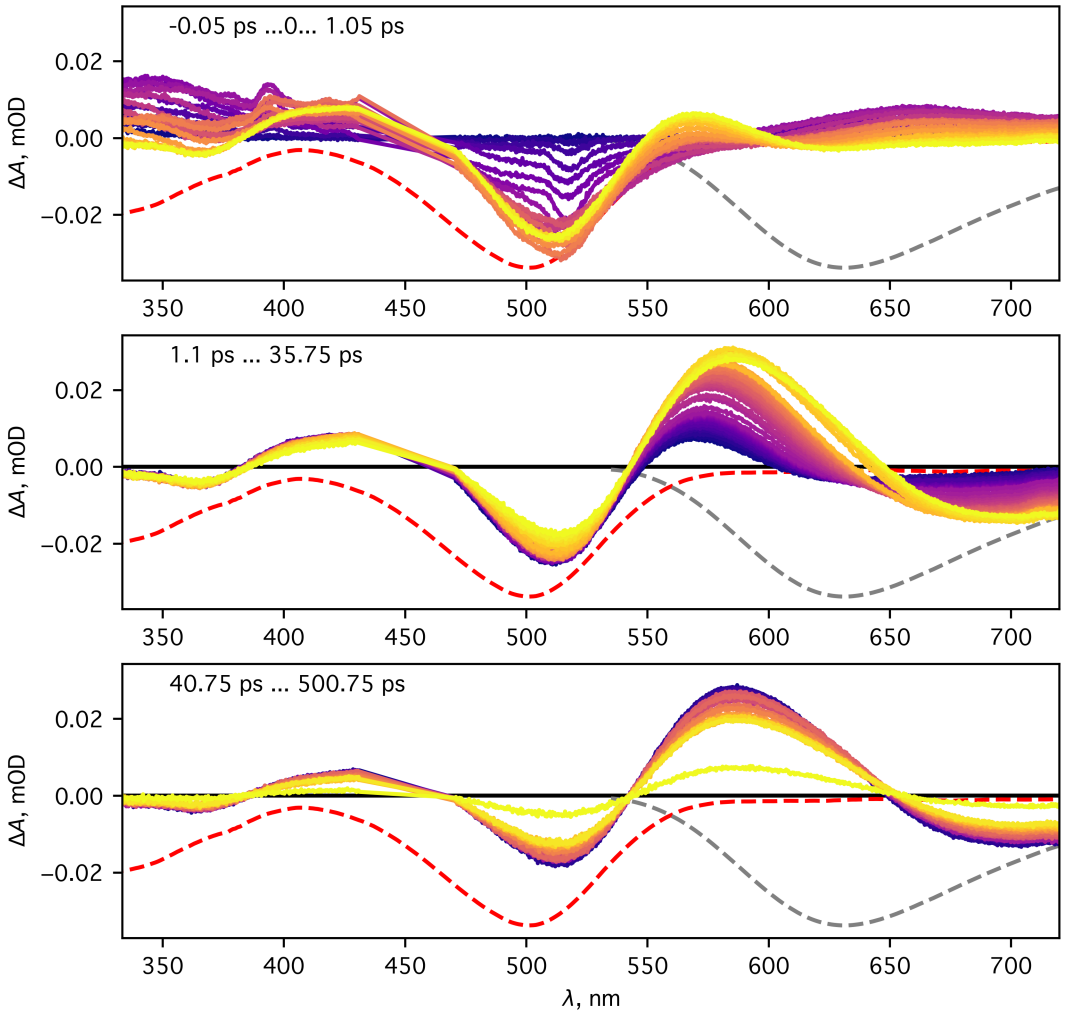

Figure A.12: D102 transient absorption spectra in dimethylsulfoxide. The colour gradient 'plasma', from East Bay to yellow colour, was chosen to represent the difference spectra in time ranges, indicated in text boxes in the panels. Red and grey dash lines are used to show inverted steady-state absorption and emission spectra, respectively. Black lines on two lowest panels show the zero difference border.

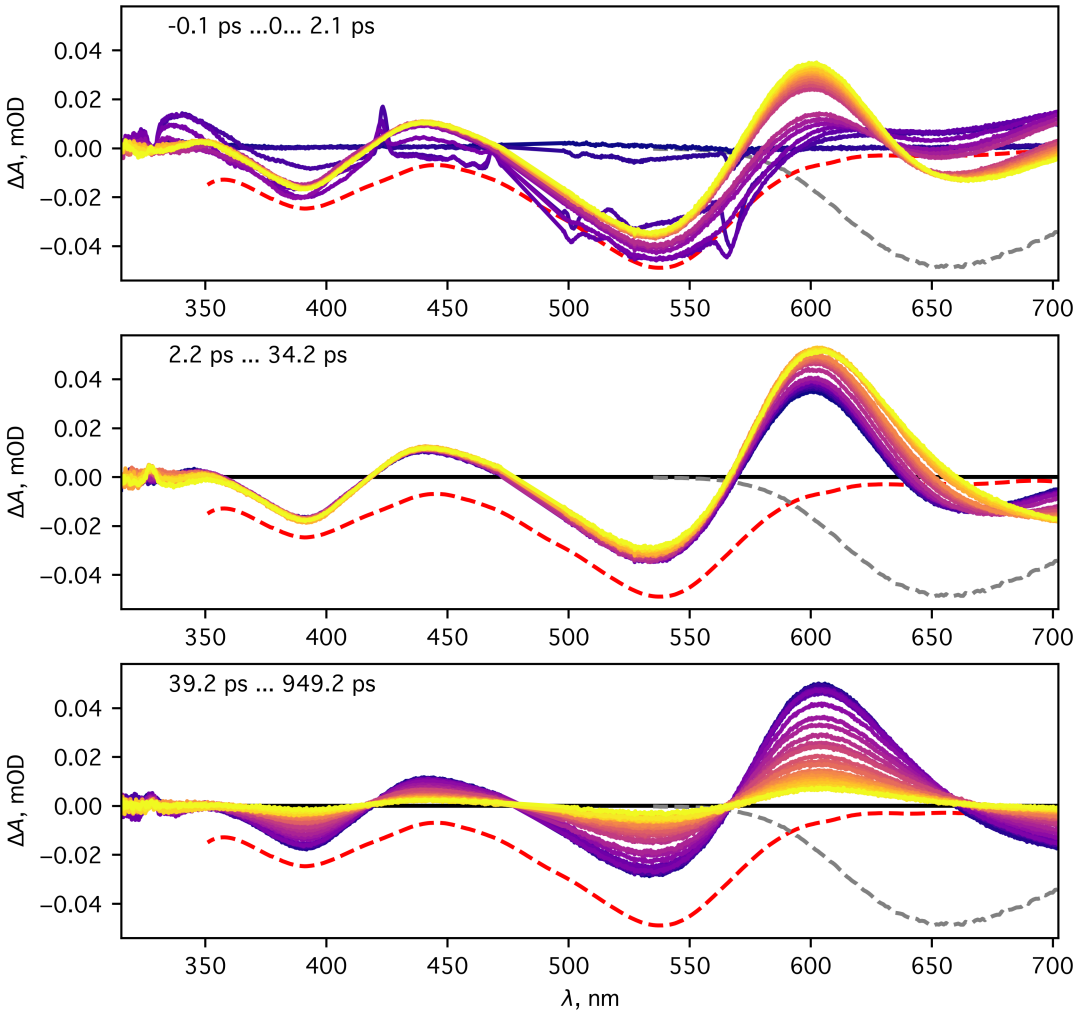

Figure A.13: D149 transient absorption spectra in dimethylsulfoxide. The colour gradient 'plasma', from East Bay to yellow colour, was chosen to represent the difference spectra in time ranges, indicated in text boxes in the panels. Red and grey dash lines are used to show inverted steady-state absorption and emission spectra, respectively. Black lines on two lowest panels show the zero difference border.

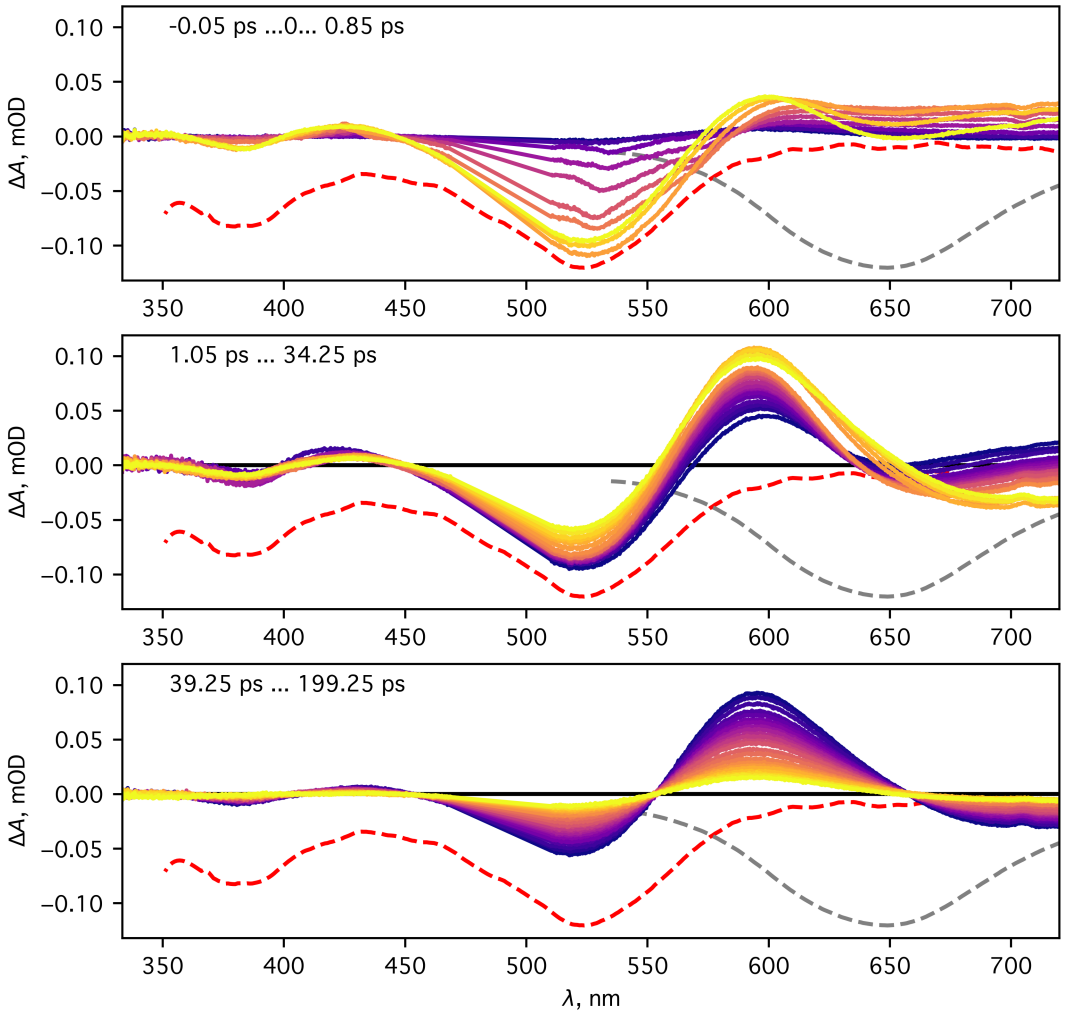

Figure A.14: D149 transient absorption spectra in methanol. The colour gradient 'plasma', from East Bay to yellow colour, was chosen to represent the difference spectra in time ranges, indicated in text boxes in the panels. Red and grey dash lines are used to show inverted steady-state absorption and emission spectra, respectively. Black lines on two lowest panels show the zero difference border.

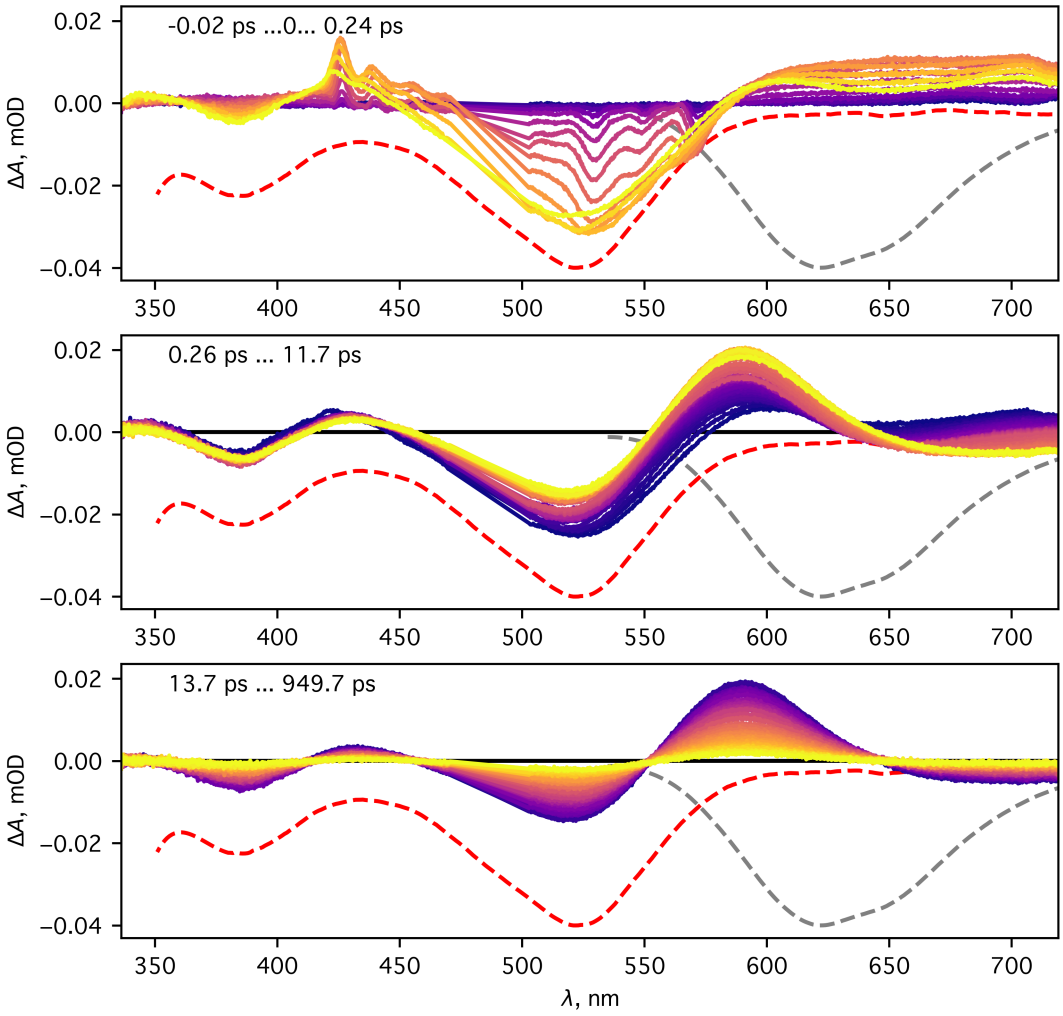

Figure A.15: D149 transient absorption spectra in acetonitrile. The colour gradient 'plasma', from East Bay to yellow colour, was chosen to represent the difference spectra in time ranges, indicated in text boxes in the panels. Red and grey dash lines are used to show inverted steady-state absorption and emission spectra, respectively. Black lines on two lowest panels show the zero difference border.

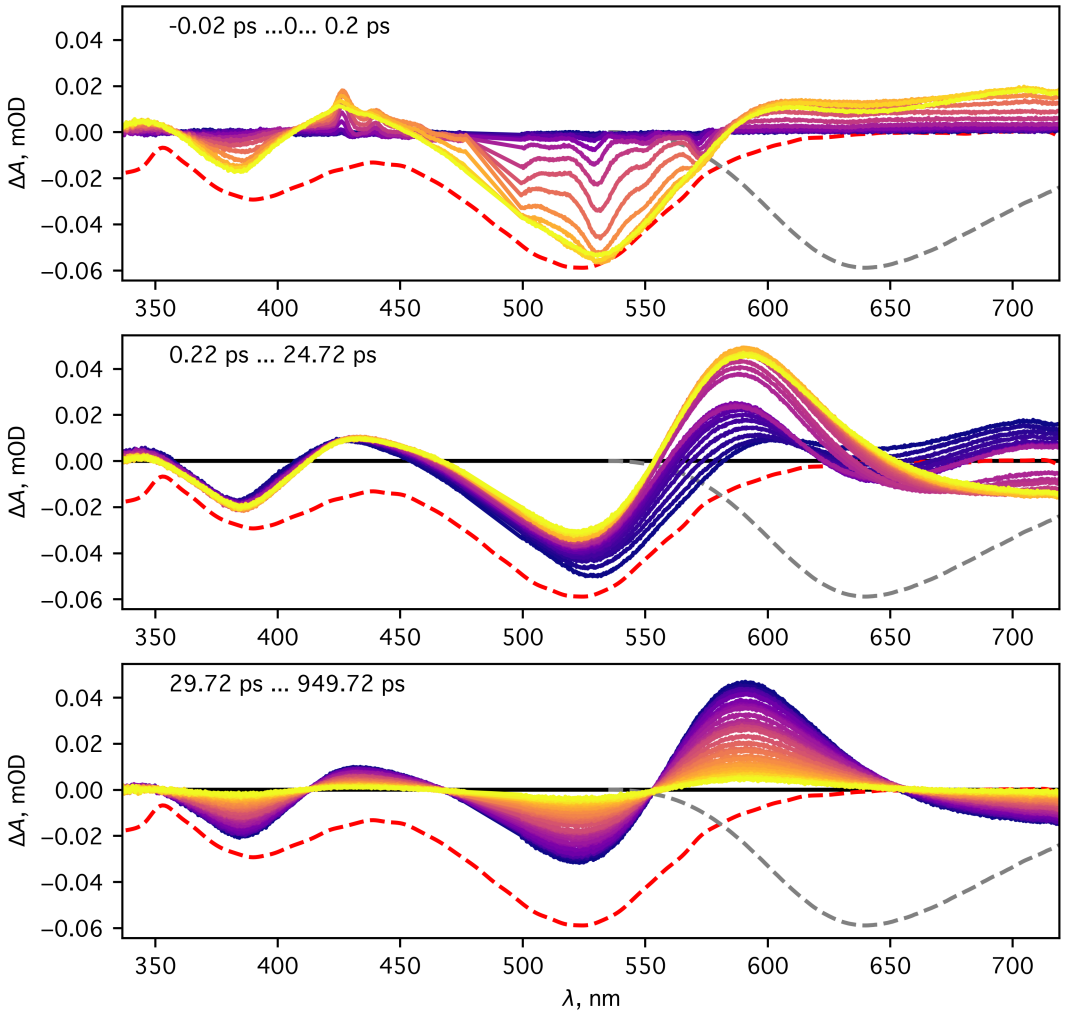

Figure A.16: D205 transient absorption spectra in acetonitrile. The colour gradient 'plasma', from East Bay to yellow colour, was chosen to represent the difference spectra in time ranges, indicated in text boxes in the panels. Red and grey dash lines are used to show inverted steady-state absorption and emission spectra, respectively. Black lines on two lowest panels show the zero difference border. 28.06.2018

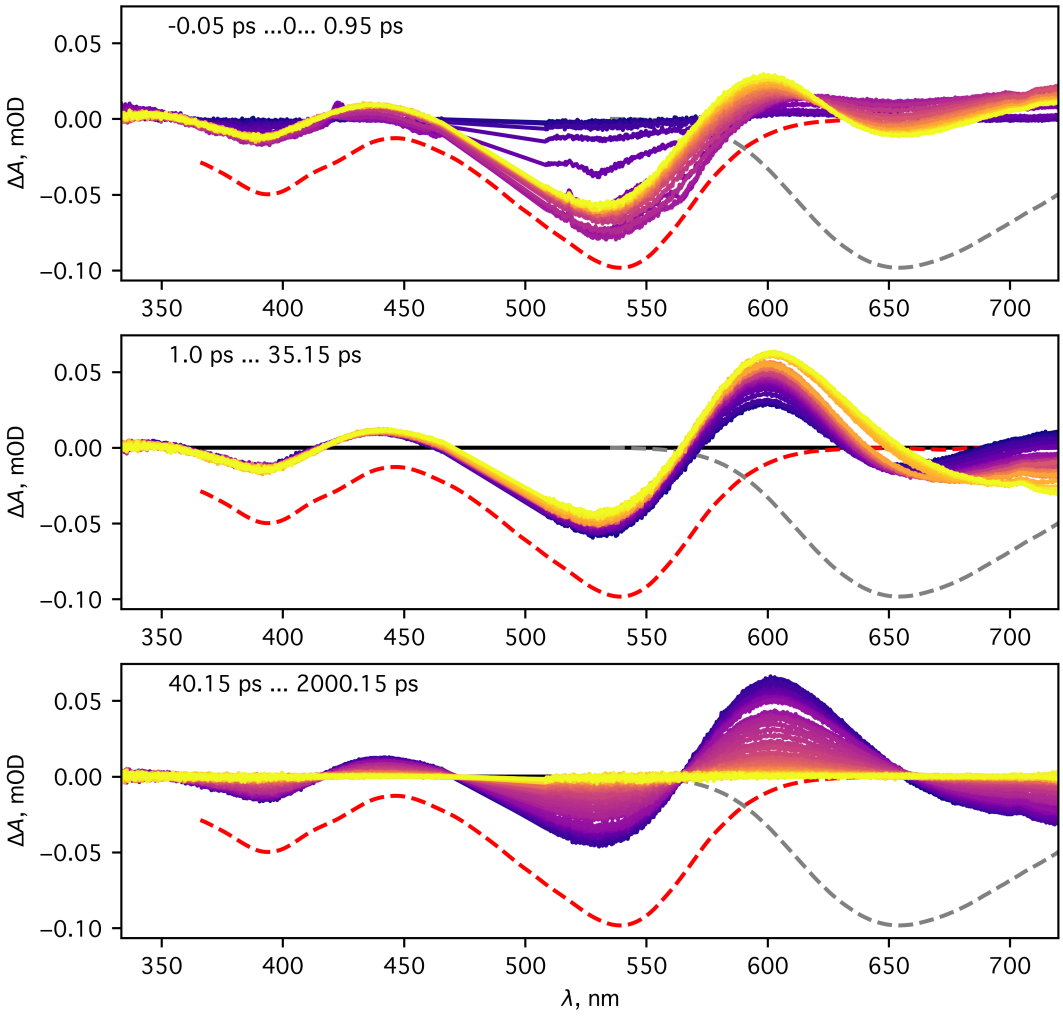

Figure A.17: D205 transient absorption spectra in dimethylsulfoxide. The colour gradient 'plasma', from East Bay to yellow colour, was chosen to represent the difference spectra in time ranges, indicated in text boxes in the panels. Red and grey dash lines are used to show inverted steady-state absorption and emission spectra, respectively. Black lines on two lowest panels show the zero difference border.

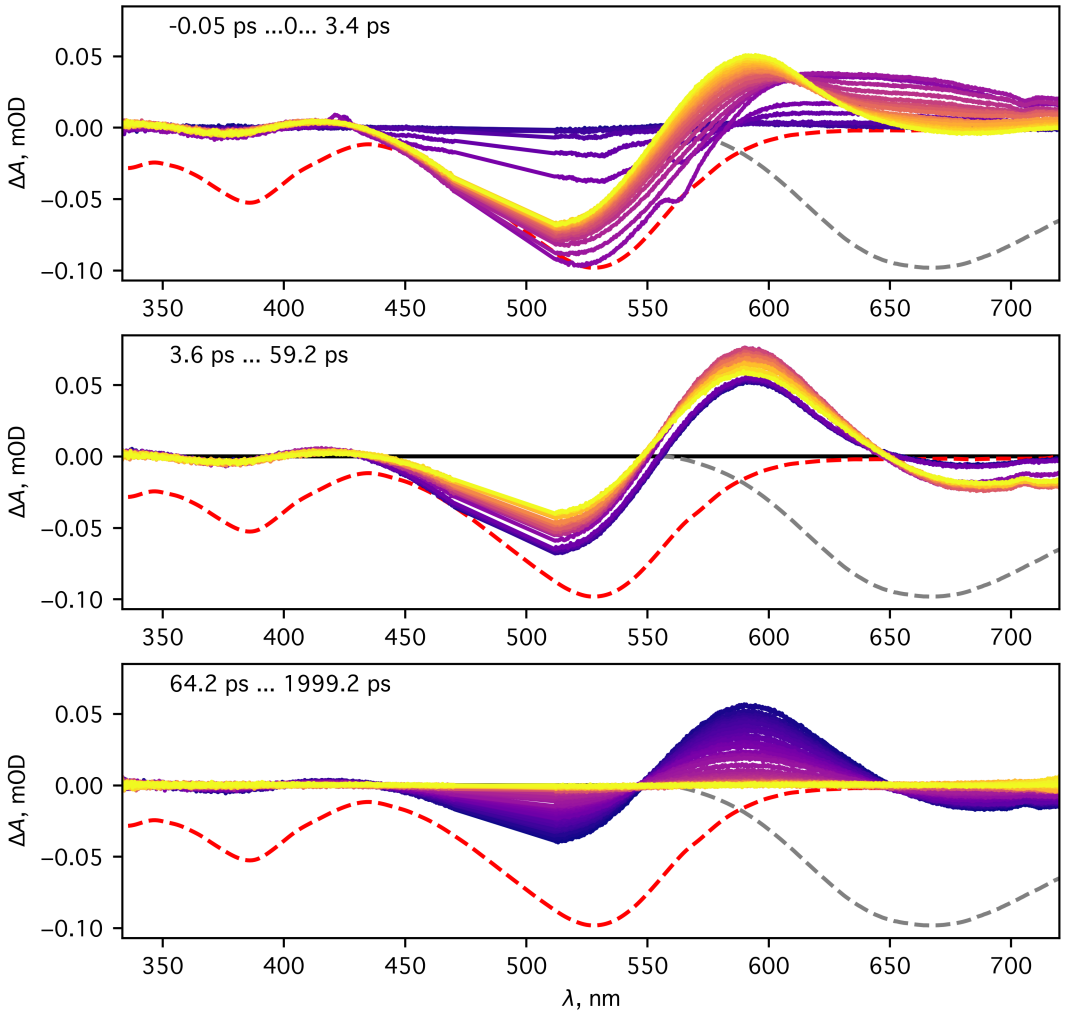

Figure A.18: D205 transient absorption spectra in methanol. The colour gradient 'plasma', from East Bay to yellow colour, was chosen to represent the difference spectra in time ranges, indicated in text boxes in the panels. Red and grey dash lines are used to show inverted steady-state absorption and emission spectra, respectively. Black lines on two lowest panels show the zero difference border.

A.0.6 Indoline dyes decay associated spectra

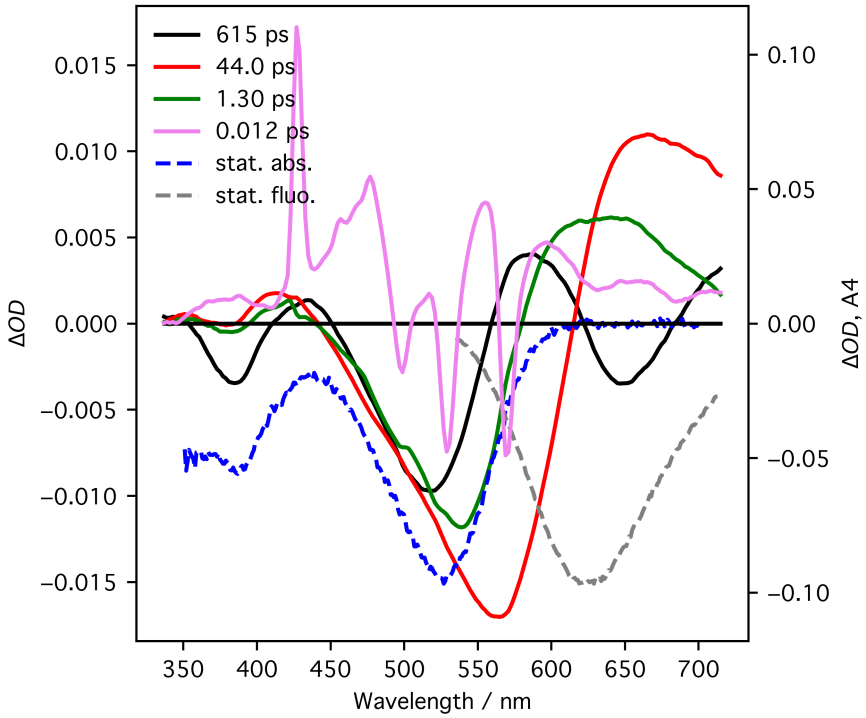

Figure A.19: Decay associated spectra of D149 in PeOH (solid curves). Steady-state absorption and emission are shown as blue and grey dashed curves, respectively.

Appendix B

Probe dependence of the solvation dynamics

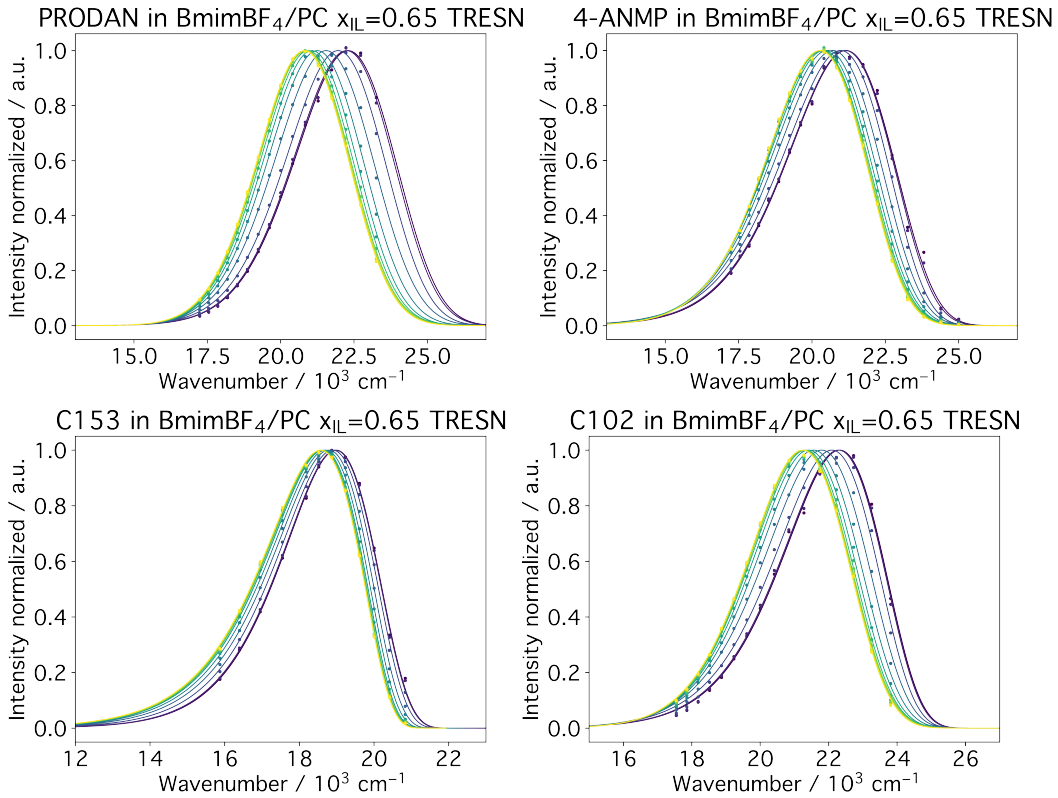

Figure B.1: Normalised TRES of fluorescent probes C153, C102, PRODAN and 4-ANMP in $BmimBF_4$/PC mixture with $x_{IL} = 0.65$. Points are the values reconstructed from TCSPC decays, lines are the lognorm distribution fit results. Data is shown at times (in ns): 0.032, 0.036, 0.064, 0.14, 0.288, 0.532, 0.896, 1.404, 2.08, 2.948, colour varies from blue to yellow with time.

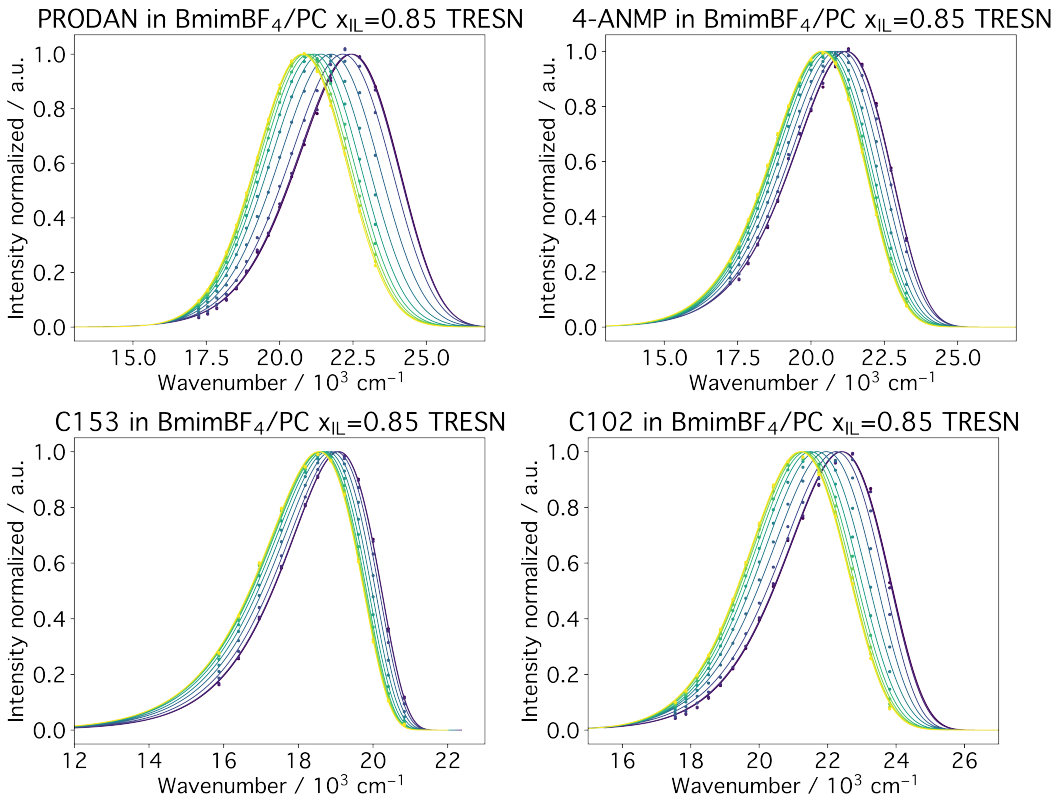

Figure B.2: Normalised TRES of fluorescent probes C153, C102, PRODAN and 4-ANMP in $BmimBF_4$/PC mixture with $x_{IL} = 0.85$. Points are the values reconstructed from TCSPC decays, lines are the lognorm distribution fit results. Data is shown at times (in ns): 0.032, 0.036, 0.064, 0.14, 0.288, 0.532, 0.896, 1.404, 2.08, 2.948, colour varies from blue to yellow with time.

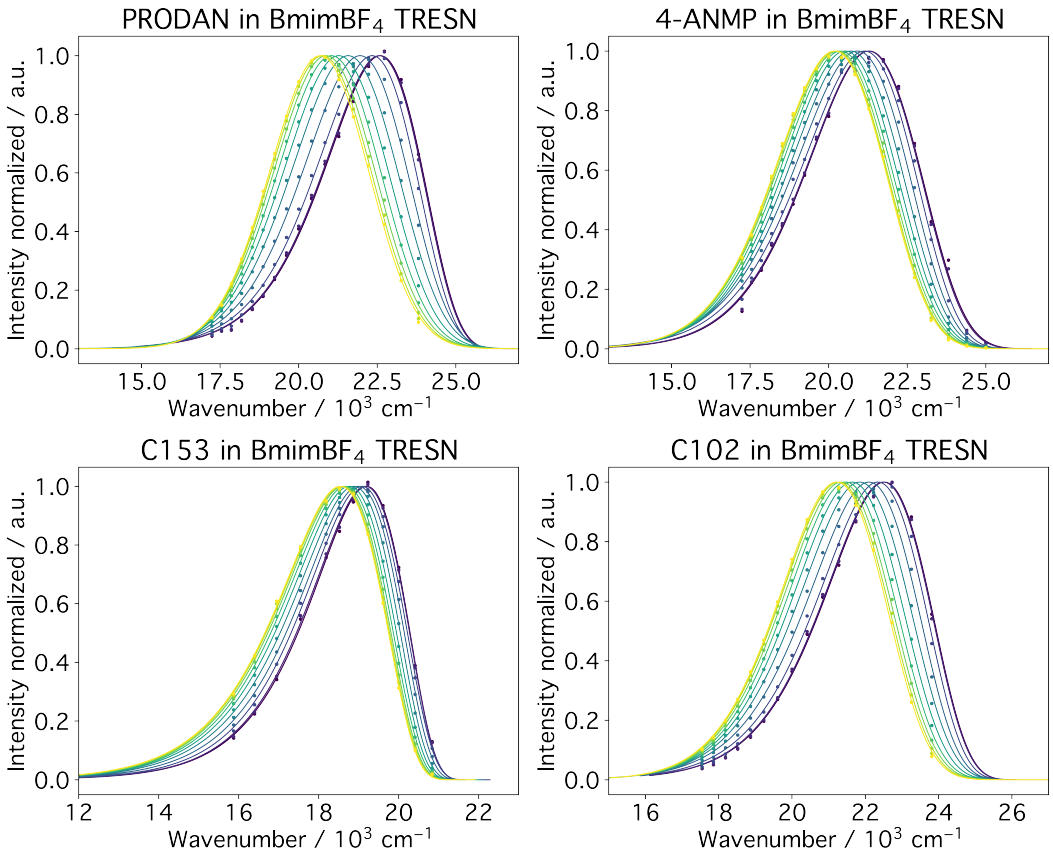

Figure B.3: Normalised TRES of fluorescent probes C153, C102, PRODAN and 4-ANMP in $BmimBF_4$. Points are the values reconstructed from TCSPC decays, lines are the lognorm distribution fit results. Data is shown at times (in ns): 0.032, 0.036, 0.064, 0.14, 0.288, 0.532, 0.896, 1.404, 2.08, 2.948, colour varies from blue to yellow with time.

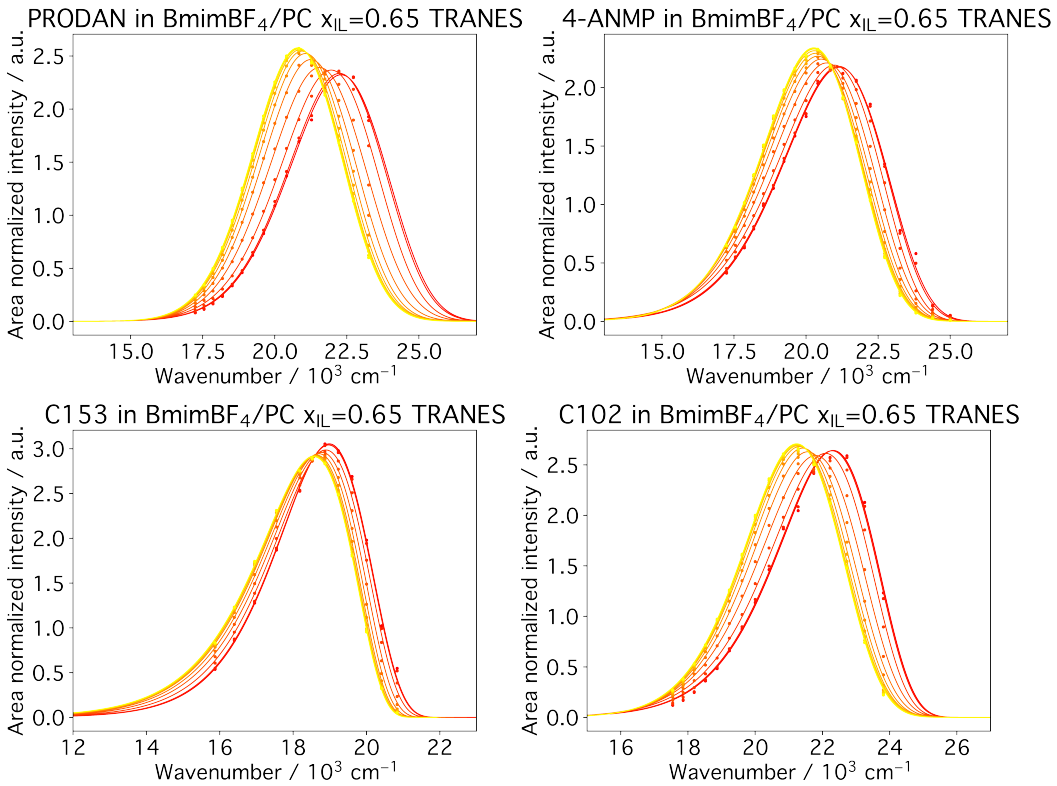

Figure B.4: TRANES of fluorescent probes C153, C102, PRODAN and 4-ANMP in $BmimBF_4$/PC mixture with $x_{IL} = 0.65$. Points are the values reconstructed from TCSPC decays, lines are the lognorm distribution fit results. Data is shown at times (in ns): 0.032, 0.036, 0.064, 0.14, 0.288, 0.532, 0.896, 1.404, 2.08, 2.948, colour varies from red to yellow with time.

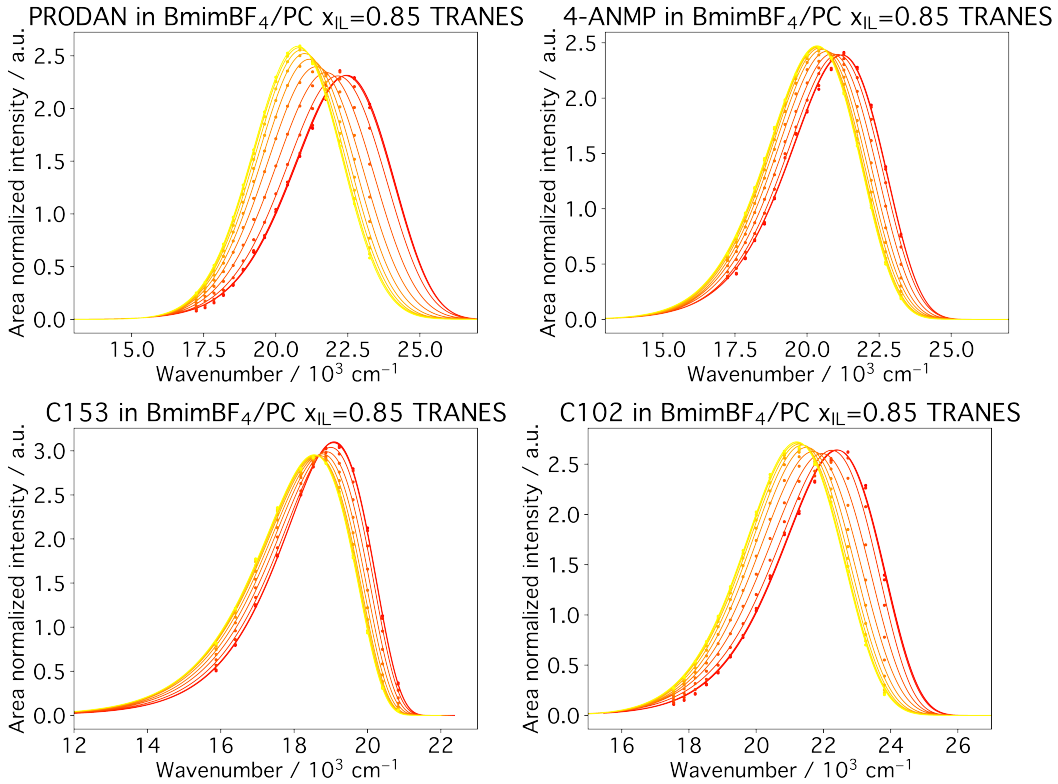

Figure B.5: TRANES of fluorescent probes C153, C102, PRODAN and 4-ANMP in $BmimBF_4$/PC mixture with x_{IL} =0.85. Points are the values reconstructed from TCSPC decays, lines are the lognorm distribution fit results. Data is shown at times (in ns): 0.032, 0.036, 0.064, 0.14, 0.288, 0.532, 0.896, 1.404, 2.08, 2.948, colour varies from red to yellow with time.

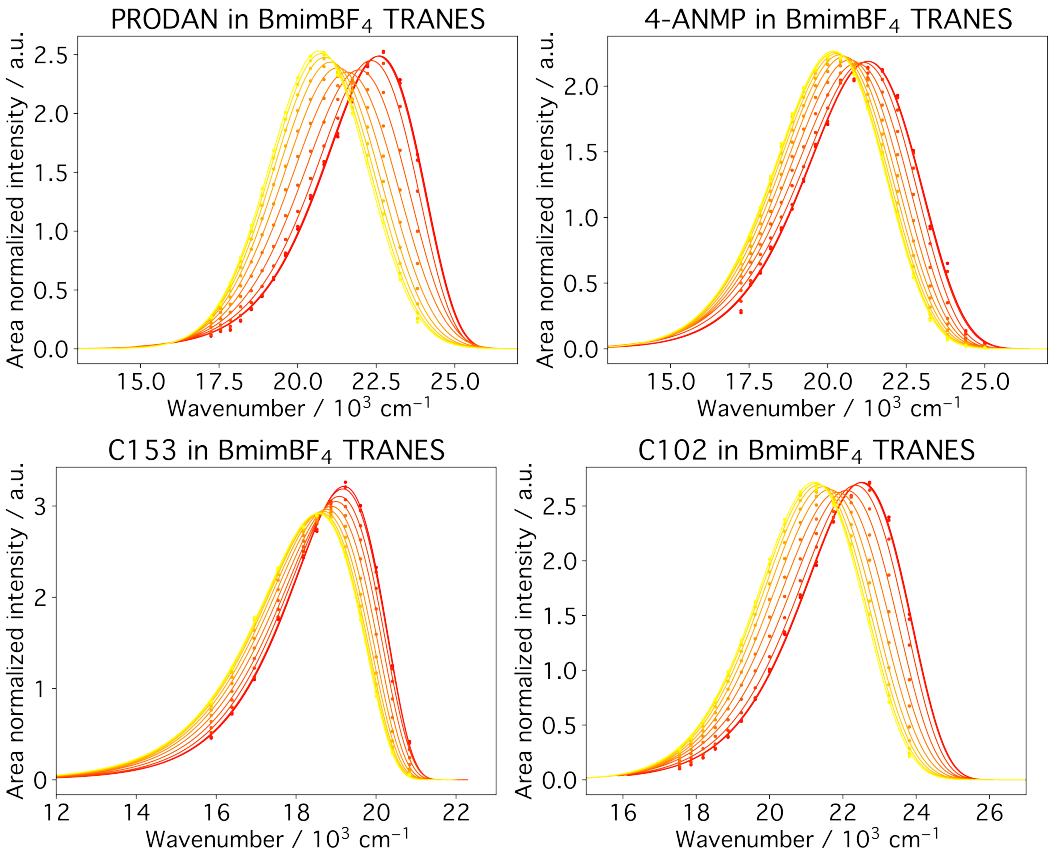

Figure B.6: TRANES of fluorescent probes C153, C102, PRODAN and 4-ANMP in $BmimBF_4$. Points are the values reconstructed from TCSPC decays, lines are the lognorm distribution fit results. Data is shown at times (in ns): 0.032, 0.036, 0.064, 0.14, 0.288, 0.532, 0.896, 1.404, 2.08, 2.948, colour varies from red to yellow with time.

Appendix C

Solvation dynamics

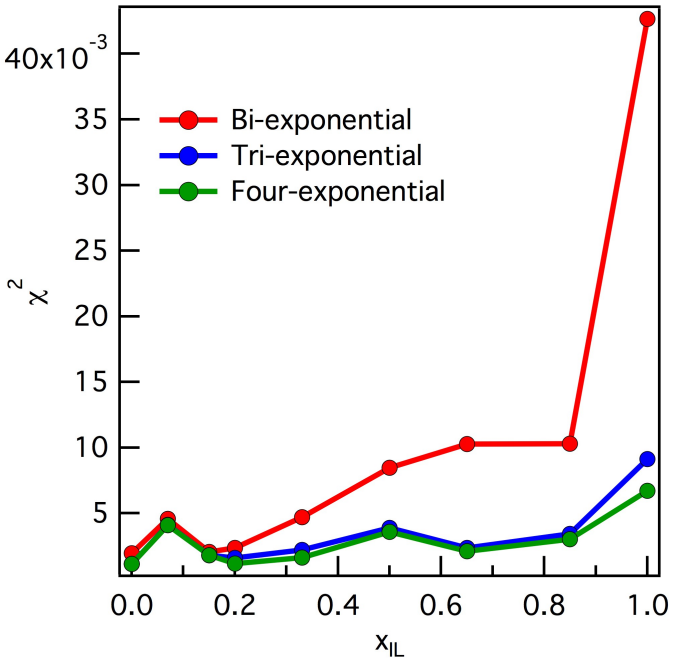

Figure C.1: χ^2 parameters of fit with n-exponential functions of SRFs, obtained with C153 in $BmimBF_4$/PC mixtures. The colour code corresponds to the number of exponentials, as indicated in the legend.

Appendix D

TCSPC set-up: LASIR

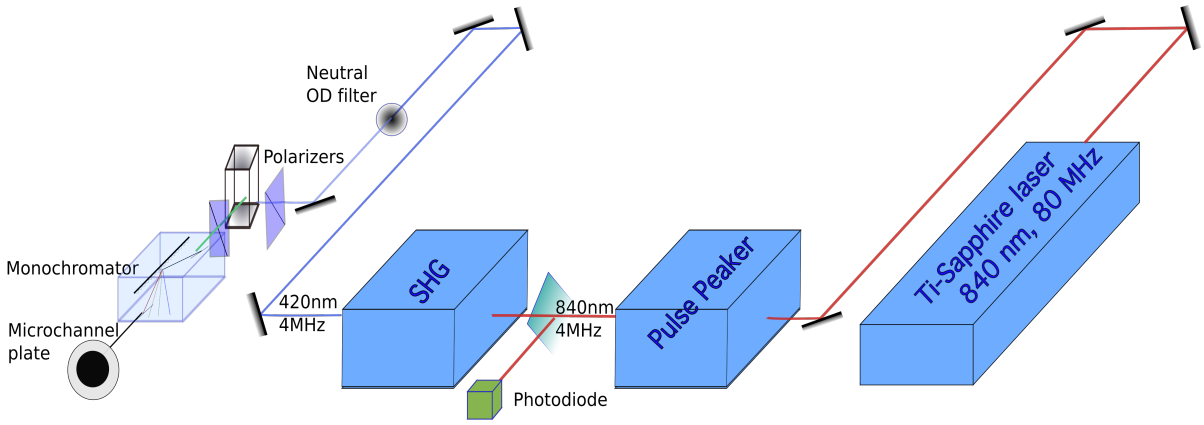

Figure D.1: TCSPC set-up scheme.

The TCSPC set-up is described in the article [2].

Appendix E

Up-conversion set-up: LIDYL

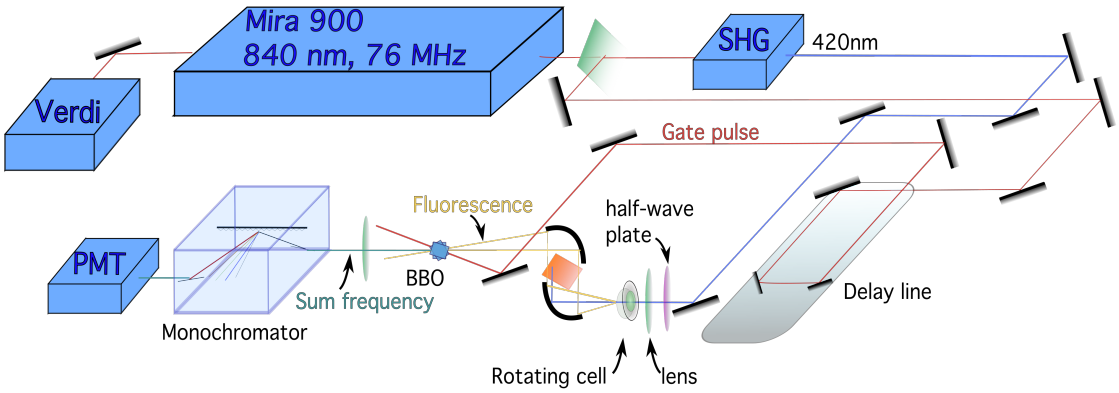

Figure E.1: Fluorescence up-conversion set-up scheme.

The fluorescence up-conversion set-up is described in the article [3].

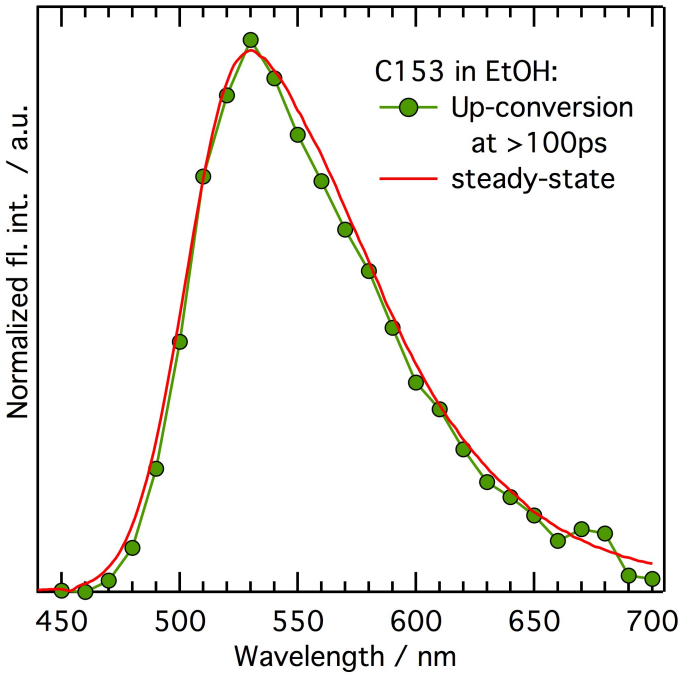

Figure E.2: Wavelength dependency of fluorescence up-conversion set-up sensitivity test: C153 in EtOH steady state (red curve) and time-resolved spectrum at > than 100ps delay time.

Appendix F

Time-resolved fluorescence anisotropy measurements

Time-resolved fluorescence anisotropy measurements were conducted on TCSPC set-up. For this purpose, fluorescence intensity decays were measured at different position of excitation and emission polarisers (fig. D.1): vertical-vertical (VV), vertical-horisontal (VH), horisontal-horisontal (HH) and horisontal-vertical (HV).

The resulting 4 decays were used to calculate the correction factor G (compensation of the polarisation bias of the detection system) and to fit the data simultaneously. Firstly, G-factor was calculated using the equation F.1.

$$G = \frac{\int HV(t)\mathrm{dt}}{\int HH(t)\mathrm{dt}} \tag{F.1}$$

Secondly, the VH and VV decays were fitted simultaneously using iterative reconvolution procedure, using IRF, collected at VV polarisation. During this procedure, the model function is convoluted with IRF and the result is compared to the experimental data. Model function for anisotropy fit is given in equation F.2 [4].

$$\begin{aligned} I_{VV}(t) &= G\int_{-\infty}^{t} IRF_{VV}(t')\frac{1}{3}\sum_{i=1}^{n}\alpha_i \mathrm{e}^{-\frac{t-t'}{\tau_i}}[1+2(R_{INF}+\sum_{j=1}^{m}L_{ij}\beta_j \mathrm{e}^{-\frac{t-t'}{\phi_i}})]\mathrm{d}t' \\ I_{VH}(t) &= \int_{-\infty}^{t} IRF_{VH}(t')\frac{1}{3}\sum_{i=1}^{n}\alpha_i \mathrm{e}^{-\frac{t-t'}{\tau_i}}[1-(R_{INF}+\sum_{j=1}^{m}L_{ij}\beta_j \mathrm{e}^{-\frac{t-t'}{\phi_i}})]\mathrm{d}t' \end{aligned} \tag{F.2}$$

In this equation, the optimzed parametrs are: α_i - Amplitude of the ith fluorescence decay component; τ_i - Lifetime of the ith fluorescence decay component; β_j - Initial anisotropy of the jth anisotropy decay; ϕ_j - Lifetime (correlation time) of the jthanisotropy decay; G-Factor - Ratio of the sensitivities of the detection system for vertically and horizontally polarised light; L_{ij} - Fluorescence / anisotropy component association matrix: L_{ij}=1: lifetime i associated with anisotropy correlation time j, L_{ij}=0: lifetime i not associated with anisotropy correlation time j; R_{INF} - Anisotropy background, also called residual anisotropy. Decay and IRF backgrounds, as well as time shift between IRF and decay are also taken into account (not shown in the equation).

The resulting experimental curves and their fit is shown in fig. F.1.

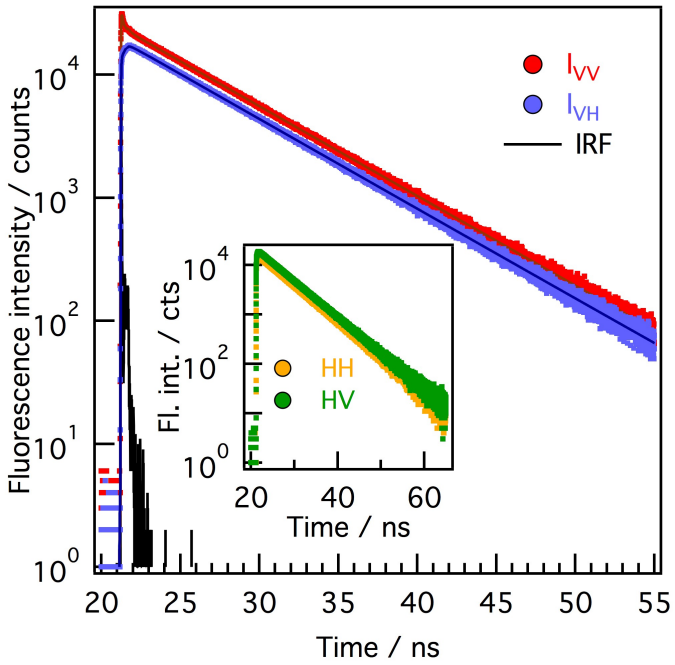

Figure F.1: Fluorescence intensity decays of C153 in $BmimBF_4$/PC mixture with x_{IL}=0.02: VV, VH; inset: HH and HV. Experimental data is shown as dots, and fit curves as solid lines.

Appendix G

Structural formulas of relevant organic molecules

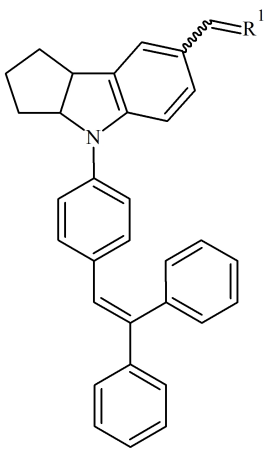

D102 : R^1=

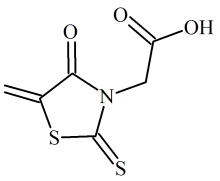

D131: R^1=

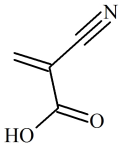

D149 and D205: R^1=

	-R^2
D149	-C_2H_5
D205	-C_8H_{15}

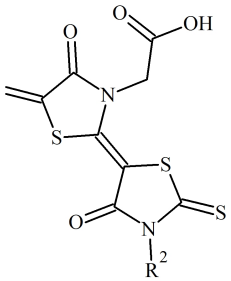

5-ol 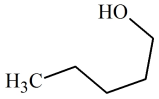

γ-Bl 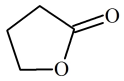

ACN 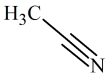

MeOH 

4-ANMP 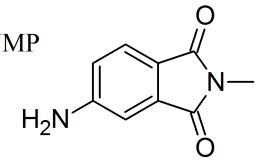

PRODAN 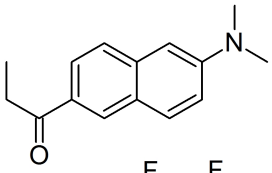

C102 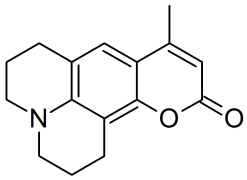

C153 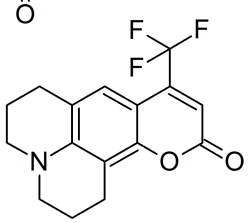

DMSO 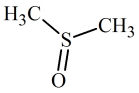

DCM 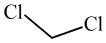

CX 

Bmim$^+$ 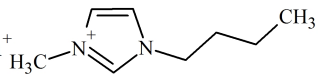

BF_4^- 

TFE 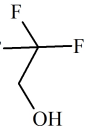

n-3ol 

n-4ol 

PC 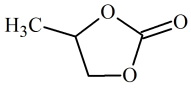

$TFSI^-$ 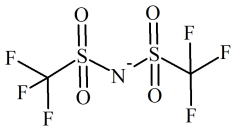

EtOH 

THF 

$CHCl_3$ 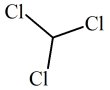

TLN 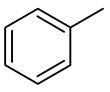

DMF 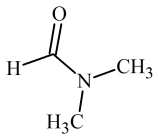

Bibliography

[1] N. Tkachenko, Optical Spectroscopy: Methods and instrumentations. Elsevier Science, 2006.

[2] Y. Smortsova, F.-A. Miannay, H. Oher, B. Marekha, J. Dubois, M. Sliwa, O. Kalugin, and A. Idrissi, "Solvation dynamics and rotation of coumarin 153 in a new ionic liquid/molecular solvent mixture model: [bmim][tfsi]/propylene carbonate," Journal of Molecular Liquids, vol. 226, pp. 48 – 55, 2017. Molecular Liquids Meet Ionic Liquids: From Fundamentals to Applications with Particular Attention to Ionic Liquids.

[3] P. Hébert, G. Baldacchino, T. Gustavsson, and J.-C. Mialocq, "Sub-picosecond fluorescence study of the lds 751 dye molecule in ethanol," Chemical Physics Letters, vol. 213, no. 3, pp. 345 – 350, 1993.

[4] PicoQuant, FluoFit: User's Manual and Technical Data, Version 4.2.